Physics-based simulations of grassfire propagation on sloped terrain at field-scale: A combined wind and slope effect study

Jasmine Joseph Innocent

A thesis submitted in fulfilment of the requirement for the degree of Doctor of Philosophy

Institute for Sustainable Industries and Liveable Cities (ISILC), Victoria University, Melbourne

November 2022

Abstract

The rate of spread of fire *(RoS)* depends on various topographical, weather and fuel parameters. The wind speed and slope of the terrain are among the two major weather and topographical factors that determine the rate of fire spread. These two parameters are investigated in this study to obtain an insight into grassfire behaviour in respect to wind and slope variables, which may then be used to improve operational and empirical models, improve prediction of real wildfires, and subsequently alleviate the risks of wildfire impact.

A fully physics-based modelling study of grassfire behaviour over flat and sloped terrain has been conducted at field-scale. The purpose was to investigate the combined effect of slope and wind on grassfire behaviour and attempt to capture the physical processes governing fire propagation. The simulations are performed using physics-based model, Wildland-urban Interface Fire Dynamics Simulator (WFDS version svn 9977), at driving wind velocities of 12.5, 6, 3, 1 and 0.1 $m.s^{-1}$ and slope angles varying from –30° to +30°. This research primarily analyses the *RoS*, alongside other quantities such as fire isochrones, fire intensity, flame dynamics, mode of fire propagation and heat transfer. Although the focus of this study is to compare quasi-steady fire behaviour with empirical models, an attempt is also made to analyse the dynamic beahviour of fire, as the fire intensity and the expansion of the isochrones even though *RoS* may remain roughly constant.

Slope correction for grassfire propagation in empirical models are presented in two ways: multiplicative and additive. For the former, *RoS* is calculated for no-slope (under the influnce of wind) and then a multiplied by a slope correction factor developed from studies conducted with no-wind conditions (i.e. doubling *RoS* for every 10° slope as given by Noble *et al*. (1980)). For the latter, *RoS* under the influnce of no-wind is determined to which the wind and slope factors are added (Rothermel 1972 model). Within the simulations conducted in this research, the *RoS* and fire intensity are found to have a positive correlation with respect to the slope angles, besides with the wind velocity. *RoS* comparisons have been made with common empirical models: Australian models with 'slope correction' multiplication (CSIRO model and McArthur models MKIII and MKV), and Rothermel models ('Original' and 'Modified' models). At different slope angles and driving wind velocities, different empirical quasi-steady *RoS* broadly matches with particular dynamic maximum, minimum (the upper and lower bounds of instantaneous *RoS* are provided as whiskers to present uncertainty to the averaged *RoS* values) and averaged *RoS* values from this

study. The dynamic nature of grassfire propagation and challenges related to capturing this dynamism in experimental studies are likely reasons for any observed discrepancies.

Within the slope angles and driving wind velocities examined in this study, for higher wind velocities, a second-order polynomial relationship exists between the quasi-steady *RoS* and slope angle, which is also the case for Rothermel models. However, for lower wind velocities, the *RoS*-slope angle relationship is closer to an exponential fit, consistent with the exponential relationship reported with most of the experimental studies that are conducted at no or very low wind speeds. The slope correction for *RoS* in Australian empirical correlations is also exponential, which are likely to be derived from very low wind laboratory-scale slope studies.

The relative *RoS* (*RoS* on any slope divided by *RoS* at a reference slope) results shows that, at higher wind velocities, the relative *RoS* from WFDS are closer to Rothermel models than the Australian correlations. The Rothermel model shows very little slope-effect under the influence of strong wind, whereas, as the wind-velocity reduces, a greater effect can be observed. The opposite is noted for Australian slope function models. It is due to multiplicative nature of Australian correlations compared to Rothermel models' additive nature. Under lower or near zero wind velocities, the Australian model's slope function is closer to the WFDS quasi-steady *RoS* results, whereas there are significant discrepancies in the results for higher wind velocities. Hence, the multiplicative nature of the Australian model's slope function (especially for upslopes at higher wind velocities) may need strong scrutiny.

Generally, the *RoS*, headfire width, fire intensity and flame length are all strongly correlated to wind velocity and slope angle. This study also analyses the *RoS*-fire intensity and fire intensity-flame length relationships. In most cases, the *RoS*-fire intensity relationship is found to be linear (as expected from Byram's correlation for no-slope scenarios). However, the relationship deviates from linearity for higher upslopes. Generally, Byram intensity (Q = fuel load × heat of combustion × *RoS*) was satisfied with approximately 42% fuel load consumed instead of 100% fuel load. A power-law correlation is found between the simulated flame lengths and fire intensities as observed by many previous researchers. However, various researchers proposed different exponents. The flame length results from this study match closest to the empirical model proposed by Anderson *et al.* (1966).

This study also analyses the grass fire propagation with varied ignition fire line widths, at different upslope angles, at 1 $m.s^{-1}$ wind speed. Comparing the pyrolysis region contours for varied ignition fire lines, for higher upslopes, the contour pattern with wider ignition lines appears to give sharper convex curvature. The simulation results, in general, show similarity with the experimentally observed results of Dupuy *et al.* (2011). The narrower the ignition fire line is, the slower is fire propagation and a convergence is obtained at about 30 m ignition line in terms of *RoS*, fire intensity and flame length.

The interaction of wind and fire on a sloped terrain is always complex due to mechanisms of heat transfer and flame dynamics. Heating of unburned vegetation by attached flames may increase the rate of spread. The relative intensities of convective and radiative heat fluxes may change the fire behaviour significantly. This study presents a detailed analysis of flame dynamics, mode of fire propagation and surface radiative and convective heat fluxes on sloped terrain, at various wind speeds. With the increase of slope angles and wind velocity, the plume inclines more towards the ground and becomes elongated in upslope cases, whereas in downslopes, the plume rises from the ground at a shorter distance from the fire line. The flame dynamics results at higher wind velocities indicate that eruptive growth of fires occur in higher upslopes. For higher wind velocities, the flame and near-surface flame dynamics appear to be up-rising, even though the plume is attached. The flame contour results for higher wind velocities indicate that the near-surface flame dynamics are difficult to characterise using the Byram number analysis.

Finally, the heat transfer analyses demonstrated that the convective heat fluxes are more relevant at wind-driven fire propagation and at higher upslopes, whereas, both fluxes are equally significant at lower driving wind velocities compared with higher wind velocities. This tendency agrees with that observed in the literature.

Overall, the finding from this research provide insight into physical and parametric observations with fire isochrone progression, *RoS*, the flame dynamics, mode of fire propagation and heat flux parameters. This can lead to further extensive studies to improve the approach of combined wind and slope effects within operational models.

Acknowledgement

First and foremost, I am extremely grateful to my supervisors, Prof. Khalid Moinuddin and Dr. Duncan Sutherland for their invaluable advice, continuous support, and patience during my PhD study. Their immense knowledge and plentiful experience have encouraged me in all the time of my research study. This endeavor would not have been possible without their enormous support, mentorship, and guidance.

My sincere thanks to research fellow Dr. Nazmul Khan for his insightful suggestions and assistane with the post processing of simualion outputs. I would also express my gratitude to all the members of ISILC at Werribbe campus, especially Assoc. Prof. Paul Joseph, Prof. Vasily Novozhilov, Mr. Amila Wickramasinghe and Dr. Rahul Wadhwani for their kind help and support that made my study a wonderful time. I also wish to acknowledge the support provided by the support team of the NCI (National Computational Infrastructure Australia) in running the simulations. Additionally, I would like to give my gratitude to the whole team at the Bushfire and Natural Hazard CRC throughout my research and the support provided to our research group for this project.

Finally, I would like to express my gratitude to my parents, my husband and children. Without their tremendous understanding and encouragement in the past few years, it would be impossible for me to complete my study. My appreciation also goes out to my family and friends for their encouragement and support all through my studies.

Declaration by Author

I, Jasmine Joseph Innocent, declare that the PhD thesis entitled "Physics-based simulation of grassfire propagation on sloped terrain at field-scale: A combined wind and slope effect study" is no more than 80,000 words in length including quotes and exclusive of tables, figures, appendices, bibliography, references, and footnotes. This thesis contains no material that has been submitted previously, in whole or in part, for the award of any other academic degree or diploma. Except where otherwise indicated, this thesis is my own work.

I have conducted my research in alignment with the Australian Code for the Responsible Conduct of Research and Victoria University's Higher Degree by Research Policy and Procedures.

Signature: 

Date: 14th April 2023

Nomenclature

C	curing index
Cp	specific heat of air (Kj.kg^{-1}.K^{-1})
D_i	diffusion coefficient of the *i*th species
I_R	reaction intensity, (Kw.m^{-2})
F_r	Froude Number (dimensionless)
F	momentum flux
f_b	external force vector excluding gravity
g	gravitational acceleration (m.s^{-2})
H	relative humidity in percent
h	fuel heat content (fuel's heat of combustion), Kj.kg^{-1}
hv	heat of combustion of volatile gas, Kj.kg^{-1}
h_s	fuel bed height from ground level, (m)
h_r	grass (top-surface) roughness
h_c	convective heat transfer coefficient (Wm^{-2}.sec^{-1}),
k	thermal conductivity of species (Wm^{-1}.K^{-1})
k_{sgs}	sub-grid kinetic energy
κ_b	absorption coefficient of solid fuel
K	air temperature in Kelvin (K)
Kr	radiative absorption coefficient of gaseous species
M_C	fuel moisture content, (dimensionless fraction)
M_x	fuel moisture extinction, (dimensionless fraction)
$\dot{m_{vap}}$	evaporation rate
N_c	Byram convection number (dimensionless)
Pf (nx)	Extinction index
Q	fireline intensity (Kw.m^{-1})
Q_f	heat of pyrolysis, (Kj.kg^{-1})
Qig	heat of pre-ignition (Kj.kg^{-1})
Qw	heat of vaporization, Kj.kg^{-1}
Q_{net}	net energy (convection plus radiation) on the fuel surface (Kw.m^{-3})

$\dot{Q}'''_{s,vap}$	endothermic effect of vaporisation of moistur
R	molar gas constant (Kj.kmol^{-1}.K^{-1})
Re	Reynolds number
S_T	fuel total mineral content (dimensionless fraction),
S_e	fuel effective mineral content (dimensionless fraction),
T	ambient temperature, (°C)
T_s	fuel surface temperature (K)
Γ	maximum reaction velocity (m.min^{-1})
Γ'	optimum reaction velocity (m.min^{-1})
$\Gamma' max$	maximum reaction velocity (m.min^{-1})
tan Φ	slope (dimensionless fraction),
U	windspeed at midflame height, (m.min^{-1})
U_{10}	open wind speed at 10 m above the ground, (m.s^{-1})
U_2	open wind speed at 2 m above the ground, (m.s^{-1})
$\overline{U}$	filtered velocities $\bar{u}_i$ ($\bar{u}, \bar{v}, \bar{w}$) in $\bar{x}_i$ directions
Ŭ	integrated radiation intensity (Wm^{-2})
W	fuel weight, (tonnes.ha^{-1})
$\overline{W}$	molecular weight of gas species kg.kmol^{-1}
w_o	Ovendry fuel loading, (kg.m^{-2})
w_s	Fuel bed loading
Wn	Net fuel loading (kg.m^{-2})
$\dot{w}_i$	Production rate of *i*th species during combustion
Y_i	the mass fraction of the *i*th species

Greek letters

ρ	density (kg.m^{-3})
ρ_g	gas density (kg.m^{-3})
$\bar{p}$	filtered background pressure
$\tilde{p}$	pressure perturbation
ħ$_s$	enthalpy
δ	fuel depth, (m)

β_s	the packing ratio
σ_s	the conductivity of air
D_α	diffusivity of species ($m^2.s^{-1}$)
σ	Surface -to-volume ratio
β_{op}	Optimum packing ratio
τ_{ij}	viscous stress tensor (Pa)
μ	molecular viscosity of the fluid ($kg.m^{-1}.s^{-1}$)
μ_{turb}	turbulent viscosity of the fluid ($kg.m^{-1}.s^{-1}$)
$\emptyset_C$	curing coefficient
$\emptyset_M$	Fuel moisture coefficient
$\emptyset_w$	wind factor
$\emptyset_s$	slope factor
ω	vorticity
ρ_p	ovendry particle density ($kg.m^{-3}$)
ρ_b	Ovendry bulk density ($kg.m^{-3}$)
β	Packing ratio
βop	Optimum packing ratio
W_n	Net fuel loading ($kg.m^{-2}$)
$\acute{H}m$	Moisture damping coefficient (dimensionless parameter)
$\acute{\eta}s$	Mineral damping coefficient (dimensionless parameter)
ξ	Propagating flux ratio (dimensionless parameter)
ε	Effective heating number (dimensionless parameter)
Δh_{vap}	latent heat of evaporation ($Kj.kg^{-1}$)
$\dot{m_{pyr}}$	pyrolysis rate
Δh_{pyr}	heat of pyrolysis ($Kj.kg^{-1}$)
$\nabla.\dot{q}''_{sr}$	divergences of the thermal radiation
$\nabla.\dot{q}''_{sc}$	divergences of the convective heat fluxes
$\dot{q}''$	conductive, diffusive, and radiative heat fluxes ($Kw.m^{-2}$)
q'''	heat release rate per unit volume from a chemical reaction ($Kw.m^{-3}$)
$\dot{q}'''_b$	energy transferred to sub-grid scale droplets and particles

$\dot{q}_s''$	convective heat flux
$\dot{q}_r''$	radiative heat flux

Abbreviations

ABL	Atmospheric Boundary Layer
AS3959	Australian Standard 3959
BF	Boundary Fuel
CFD	Computational Fluid Dynamics
CSIRO	Commonwealth Scientific and Industrial Research Organisation
DEFFM	Dry Eucalypt Forest Fire Model
DNS	Direct Numerical Simulation
FCFDG	Forestry Canada Fire Danger Group
FDS	Fire Dynamic Simulator
FFDI	Forest Fire Danger Index
FMC	Fuel moisture content
FE	Fuel Element
GSFM	Grassland Fire Spread Meter
GFDI	Grassland Fire Danger Index Meter
HRR	Heat Release Rate
LES	Large Eddy Simulation
MPI	Message Passing Interface
PDE	Partial Differential Equation
PIV	Particle Image Velocimetry
RANS	Reynolds-averaged Navier–Stokes
RTE	Radiation Ttransport Eequation
RoS	Rate of spread
SAV	Surface-to-volume ratio
SEM	Synthetic Eddy Methodology
WFDS	Wildland-urban Interface Fire Dynamics Simulator
WUI	Wildland Urban Interface

Table of Contents

List of Figures

List of Tables

List of Publications

Journal publications

Jasmine Innocent, Duncan Sutherland, Nazmul Khan and Khalid Moinuddin, 'Physics-based simulations of grassfire propagation on sloped terrain at field-scale: motivations, model reliability, rate of spread and fire intensity.' International Journal of Wildland Fire, 2022 (published online early, January 2023).

Jasmine Innocent, Duncan Sutherland, Nazmul Khan and Khalid Moinuddin, 'Physics-based simulations of grassfire propagation on sloped terrain at field-scale: flame dynamics, mode of fire propagation and the heat fluxes.' International Journal of Wildland Fire, 2022 (published online early, January 2023).

Conference publications

Jasmine Innocent, Duncan Sutherland and Khalid Moinuddin, 'Physical modelling of grassfire propagation on sloped terrain at field-scale under low wind speed.' In Proceedings of 2nd International Conference on Mechanical Engineering and Applied Sciences, 2022. Dhaka, Bangladesh.

Chapter 1. Introduction

1.1 Introduction

Wildland fires are very common phenomena in Australia that occur mostly during the summer season. Wildland fires destroy human life, damage property, and frequently affect the wildland–urban interface (WUI). WUI refers to the zone of transition between unoccupied land and human development, where houses and natural vegetation are mixed (Stewart *et al.* 2007). Two types of WUI are defined: (1) Interface–areas with housing and low-density vegetation within fire's reach (2.4 km or 1.5 miles) of a large, contiguous block of wildland vegetation; (2) Intermix–areas where housing (more than 1 house per 40 acres or 16 ha) intermingles with wildland (non-agricultural) vegetation (Radeloff *et al.* 2005). Figure 1.1 shows pictures of two different WUI areas.

Figure 1.1 – (a) Picture of Interface WUI, taken from Fire Protection Research Colloquium (2009); (b) picture of Intermix WUI, taken from Hermansen-Baez *et al.* (2009)

The lands and communities adjacent to and surrounded by wildland are at risk from the uncontrolled spread of wildfires. Fires within the communities in WUI areas are the most threatening and expensive. Communities residing in the proximity of the WUI may also be impacted by power and water disruptions, contamination caused by fire, effects of smoke on health, and intense radiation.

Figure 1.2 – WUI fire, taken from Hermansen-Baez *et al.* (2009)

On average, 1,200,000 ha burn in Australia annually (Morvan *et al.* 2013). 20% of total accumulated building loss between 1900 to 2003 attributed to bushfire.(McAneney *et al.* 2009). The Black Saturday fire in the state of Victoria in 2009 caused severe damage to Australia ecologically and economically. There were 173 fatalities and 414 injuries, far exceeding the loss of life from any previous bushfires. One million wild and domestic animal deaths were estimated in this fire disaster. The Bushfire Royal Commission established after the fire noted that 316 grass or forest fires were reported on the same day with an estimated fire inTEnsity of 80,000 $kW.m^{-1}$, wind speed over 100 $km.hr^{-1}$ and plume height of 15 km (https:// blacksaturdayfires.com, Royal Commission (2010)

There is a huge economic cost to various nations associated with this uncontrolled spread of fires. A few examples are : (1) the fire in California in October 2007 – an area of 360,000 ha burned, 500,000 people evacuated with an estimated cost of over US$1 billion (http://cdfdata.fire.ca.gov/incidents/incidents_archived?archive_year=2007,http://www.nusinstitute.org/Research/Briefs/Economic-Impact-Fires-07); (2) the European heat event in 2018 – a series of deadly fire events in many parts of Europe caused 103 fatalities, destroyed more than 4000 buildings and cost €33.7 million (https://www.worldweatherattribution.org/attribution-of-the-2018-heat-in-northern-europe/, https://www.theguardian.com/world/2018/jul/22/heatwave-northen-hemisphere-uk-algeria-canada-sweden-whats-the-cause); (3) the California wildfire

season of 2020 – by the end of the season, 9917 fires had burned out 1,779,730 ha, making 2020 the largest wildfire season recorded in California's modern history, with an estimated cost over US$12 billion (California fires in 2020, by the numbers - CalMatters); (4) the Black Saturday fires in Australia in February 2009 – more than 450,000 ha burned, 3500 buildings including more than 2000 houses destroyed; these fires resulted in widespread economic, social and environmental destruction with a net estimated cost of AU$942 million (Fire Australia Article (bushfirecrc.com), https:// blacksaturdayfires.com); (5) intense bushfires occurred in many parts of Australia recently in the 2019–2020 bushfire season, known as Black Summer. The fires burnt an estimated 18.6 million ha, destroyed over 5900 buildings, killed 34 people and 400 deaths attributed to smoke related after affects, costing over AU$103 billion in property damage and economic losses ((https://naturaldisaster.royalcommission.gov.au (Royal commission into Natural Disaster Arrangments,2020), Black Summer bushfires, VIC, 2019-20 (aidr.org.au), Black Summer bushfires, NSW, 2019-20 (aidr.org.au)).

Figure 1.3 – Images from the Black Saturday bushfire, Australia, in 2009 (https://www.abc.net.au/news/2016-11-29/, https://blacksatudayfires.com)

Wildfires are becoming more intense and more frequent, retaliating communities and ecosystems in their path. Sullivan *et. al* (2022) quoted from the report by United Nations Environment Programme (UNeP) that "the risk of wildfires pose to people and the environment is increasing due to numerous factors, including, but not limited to, climate change". Sullivan *et al.* (2022) noted that climate change and land-use change are making wildfires worse and anticipates a global increase of extreme fire events in areas previously unaffected. The effects of climate change will

increase the frequency of wildfire in upcoming decades (Jolly *et al.* 2015). Climate change contributed to the record-breaking drought and weather conditions leading to the bushfires' unprecedented range across Australia (Climate Council report 2020, https://www.climatecouncil.org.au). The drying effect makes vegetation to ignite and burn more easily (more flammable) and therefore more likely to support extreme fire behaviour. It also makes vegetation more susceptible to spot fires ahead of main fires (created by landing of burning firebrands) when weather conditions worsen (such as high temperature, low relative humidity, and strong wind). National Interated Drought Information System (NIDIS) report 2022 states that drought combined with warming temperature, can result in decreased snowpack and streamflow, increased evaporative demand, dry soils, and large-scale tree deaths, which results in increased potential for large wildfires (https://www.drought.gov/sectors/wildfire-management). With global temperature on the rise, there is looming potential for large fires persist to the future. An integrated wildfire management is key to adapting to present and impending changes in global wildfire risk.

The number of homes at risk of fire in the WUI is likely to increase owing to the growing number of people moving into fire-prone areas (US Government Accountability Office (GAO) studies https://www.gao.gov/products/gao-15-772 Report GAO-15-772, publised in 2015). A similar increasing trend may prevail in other countries too. With urban growth, increasing numbers of people in Australia are living in rural/urban interface communities in suburbs and rural sub-divisions in close proximity to bushland, with a greater population potentially being exposed to bushfire risk (Norman *et al.* 2009). According to an SGS economic and planning analysis report (Gorrey and Wade 2019, sgsep.com.au), in the decade 2008–2018, the number of people in New South Wales (NSW) living in areas of very high and high risk of bushfires increased by 29,000. In Victoria, the number of people having moved to bushfire-prone areas increased by 111,000 during this period (https://www.planning.vic.gov.au). Currently, close to a quarter of all dwellings in the Australian Capital Territory (ACT) are located in areas identified as bushfire-prone and the population continues to grow in these areas (https://esa.act.gov.au).

Norman *et al.* (2009) pointed out that urban growth can increase disaster risk, and the projected impacts of climate change will further potentially expose more people to risk. An integrated approach to three areas – spatial planning, bushfire risk management and climate change – can provide a significant degree of risk reduction (Norman *et al.* 2009). Hence, fire propagation and

fire behaviour studies are important, though these are difficult since fire dynamics depend on various factors.

Researchers in the field of wildland fire predictive services have two principal objectives: (1) to quantify fire danger, thereby developing fire danger rating systems, and (2) to develop models that enable the accurate prediction of fire spread in wildland (Perry 1998). Estimation of fire intensity, rate of fire spread and smoke transport are important as these studies have a number of applications such as: providing means by which communities can assess and/or reduce their risk to WUI fires, helping in planning the risk from fire spread, planning smoke-free evacuation routes, and helping in the management of firefighting and evacuation logistics (Mell *et al.* 2007)

The magnitude, severity and rate of fire spread are the result of a number of complex physical and chemical processes. According to Sullivan (2009a), 'Wildland fire is a complicated combination of energy released owing to chemical reactions in the process of combustion and the transport of that energy to surrounding unburnt fuel and the subsequent ignition of that fuel'. The spread of fire is affected by a number of environmental variables (McArthur 1967). Fire behaviour depends on various topographical, weather, and fuel factors, as shown in Figure 1.4. Topographical considerations are the slope of the terrain and the bearing of the slope (e.g. in Australia, south-facing slopes tend to have less severe fires because they receive less sun and have a higher overall fuel moisture content). The weather factors are wind speed, relative humidity, temperature, soil moisture and atmospheric stability. The fuel factors are fuel type (includes fules with different thermo-physical and flammability properties), fuel height, density, and moisture content. Various fuel/vegetation species may have different thermo-physical and flammability properties.

Figure 1.4 – Fire behaviour triangle with major factors determining rate of fire spread outlined in red (courtesy: https://www.weatherstem.com)

Anecdotal evidence (https://www.planning.vic.gov.au, https://www.fire.nsw.gov.au) suggests that the two parameters highlighted in Figure 1.4 are among the major factors that determine the rate of fire spread. These two parameters are investigated in the present study to obtain insight into grassfire behaviour in relation to wind and slope variables.

1.2 Overview of fire modelling studies

Sullivan (2009a, b, c) divides the modelling approaches into three categories: physical and quasi-physical models (Sullivan 2009a), empirical and quasi-empirical models (Sullivan 2009b) and simulation and mathematical analogue models (Sullivan 2009c).

A considerable number of field-based studies (Cheney *et al.* (1998) Burrows (1994)) have been carried out in Australia since the pioneering outdoor fire experimental studies by McArthur in the 1950s and early 1960s (McArthur 1966, 1967). These experimental studies extended the understanding of fire behaviour of various fuel types. Empirical models have been developed over time based on these experimental studies to describe fire behaviour related to weather and fuel variables, where such knowledge did not previously exist. Empirical and semi-empirical models are based on statistics, observations and experimental studies or some form of physical framework on which the statistical analysis is based. Over the years, empirical fire behaviour models and

relationships have been made available to end users for operational implementation. Commonly used operational models rely on these empirically derived relations to predict fire spread rate. Examples of such operational models used in Australia are: the McArthur Fire Danger Meter (Noble *et al.* 1980) and CSIRO Grassland Fire Spread Meter (GSFM) (Cheney *et al.* 1998). These operational models provide fire prediction quickly, can easily be applied and are user friendly. However, these empirical/operational models predict the steady-state rate of fire spread and are unable to include the transient and dynamic behaviour of fire (Sharples 2017, Taylor *et al.* 2004).

With improved computational resources in the last 30 years, fire modelling studies started using computer simulations to undertake calculations and implemented methods other than those directly related to observations and experimental measurements. A wide range of modelling work was conducted in wildland fire during the period 1990–2007 for the prediction of fire spread in wildland areas. Two-dimensional mathematical analogue models were developed in late 1990s and early 2000s (Perry 1998). Simulation and mathematical analogue models are two-dimensional application models that simulate fire propagation across a modelled landscape. These methods are mathematical in nature and provide an analogue of fire behaviour instead of the single-dimensional predictions used with early fire models. Many of these approaches started using computer simulations to undertake calculations on mathematical concepts and implemented methods other than those directly related to observations and measurements.

In recent years, advancements in computational power have led to the development of three-dimensional Computational Fluid Dynamics (CFD) models to simulate fire spread across a landscape. Transient fire behaviours (fire–fuel and fire–atmospheric interactions) are included in these models (Mell *et al.* 2007). These models incorporate the transfer processes in fire spread such as mass transfer, heat transfer, combustion and pyrolysis of fuel, and discretise their mathematical differential equations. These equations are then solved numerically using CFD methods (Mell *et al.* 2007).

The three modelling approaches, empirical, mathematical analogue and physics-based, are detailed in the following sections.

1.2.1 Empirical and semi-empirical models

These models are predominantly based on statistics, observations, and experimental studies. One of the empirical models for Australian vegetation is the McArthur model for grassland (McArthur 1966, 1967). Another empirical grass fire spread model, termed the CSIRO model, proposed by Cheney *et al.* (1998), is widely used in Australian operational platforms (CSIRO Grassland Fire Spread Meter, GSFM).

The equations related to the McArthur models, CSIRO model and Rothermel model in the field of grassfire propagation are detailed in Chapter 2, Section 2.1.

Figure 1.5 shows images of the MacArthur Fire Danger Meter, based on the McArthur model (McArthur 1966, 1967). Figure 1.5(a) is an image of the McArthur Forest Fire Danger Index (FFDI) meter. The risk inputs for the meter are wind speed, air temperature, humidity, soil moisture (drought factor), and last rain event (rainfall till 9 am on the day). Figure 1.5(b) represents a Grassland Fire Danger Index Meter (GFDI), which is simpler than the FFDI meter and only uses wind speed, air temperature, relative humidity and grass dryness (given by a 'degree of curing' index). These meters were used by firefighters on the ground to quantify fire spread rate by turning the meter to the correct inputs and reading off the computed fire danger index and rate of spread.

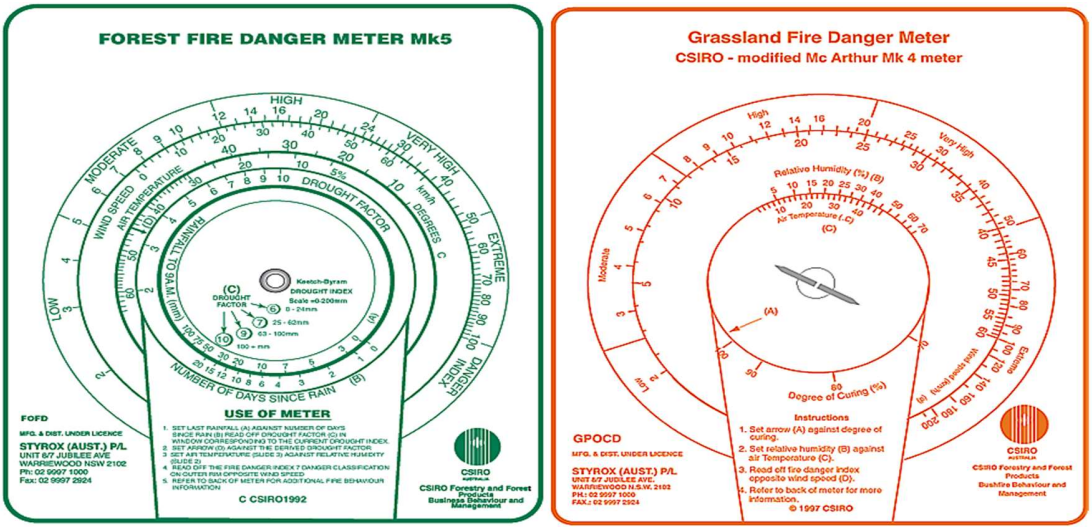

(a) *MKV McArthur Forest Fire Danger Index meter (FFDI)*

(b) *MKV McArthur Grassland Fire Danger Index meter (GFDI)*

Figure 1.5 – McArthur fire danger meters

Another model, the Dry Eucalypt Forest Fire Model, DEFFM, was developed by CSIRO researchers to predict the rate of spread of fire on dry eucalypt forest (Gould *et al.* 2008). They conducted a field-scale study named 'Project Vesta' (initiated in 1996) aimed at developing an improved model for fire propagation in eucalypt forests. Experimental burns were conducted at two sites in Western Australia consisting of 200 × 200 m plots of eucalypt forest. They examined the results, tested against data from experimental fires and well-documented wildfires and then analysed the relationship of rate of fire spread with wind speeds and fuel characteristics for dry eucalypt forest. This empirical model predicts fire spread rate based on estimates of wind speed, dead fuel moisture content and visual assessment of fuel characteristics. This model included algorithms to predict fire behaviour, with fuel characteristics described using a numeric fuel hazard score (from 0 to 4) or fuel hazard rating (Low to Extreme).

It should be noted that most of the experimental studies found in the literature are of laboratory scale. Empirical models are computationally cheap to implement and only require few parameters, which makes them user-friendly. These models predict the steady state or constant rate of fire spread and are unable to include fire–fuel–atmospheric interactions. The experimental fires used to develop these models were small fires relative to real observed wildfires. Hence, the empirical models often provide only crude predictions of fire behaviour and can have large errors (e.g ± 50% in the rate of spread) in realistic conditions (Cruz *et al.* 2015).

1.2.2 Mathematical analogue models

These are two-dimensional application models to simulate fire propagation across a modelled landscape (Sullivan 2009c). These methods are mathematical in nature and provide an analogue of fire behaviour instead of the single-dimensional predictions used with early fire models. Many of these approaches started using computer simulations to undertake calculations on mathematical concepts and implemented methods other than those directly related to observations and measurements. Huygens' wavelet principle is used in most of these models to define fire spread in the form of light waves (Anderson *et al.* 1982). This principle describes the propagation of light waves, in which each light wave becomes the source of subsequent light waves. It is assumed that each point on a fire perimeter is a theoretical source of new fire, producing another set of fire spread waves. Anderson *et al.* (1982) applied Huygens' wavelet principle and demonstrated elliptical spread at each point of the fire contour. They coupled the wavelet principle with constant

wind and changed wind speed conditions to generate mathematical equations for homogeneous flat terrain fire, with some suggestions made for non-uniform and variable topographical conditions.

One of the popular models is AUSTRALIS, developed by CSIRO (Kelso *et al.* 2015). In this model, each cell represents an area within the landscape and contains information about the fuel and topography of the area. This model is a 'cellular automata' model where fire spread between cells is governed by a series of rules that determine the state of a cell as burning, burnt, or unburnt. When a cell ignites and conditions are favourable for fire, some of its neighbouring cells will also catch alight, and fire spreads from one cell to another, simulating wildfire spreading across a landscape (Dunn and Milne 2004). Other mathematical analogue models are: FARSITE (Finney 2004) used by Federal and State land management agencies in the US, and the Canadian Wildland Fire Growth Model Prometheus, which is based on the Canadian Fire Behaviour Prediction system (Forestry Canada Fire Danger Group (FCFDG 1992).

Another prominent mathematical analogue model is called BEHAVE, which uses the Rothermel model – a widely used semi-empirical fire spread model based on observations of US vegetation (Rothermel 1972, Rothermel and Burgan 1984) –, within its mathematical formulations.

There are many operational implementations of semi-empirical and mathematical analogue models in Australia such as CALM Spinifex (Western Australia (WA) Department of Conservation and Land Management) and PHOENIX (an implementation of modified forms of the CSIRO grassland model and McArthur fire model, other models for smoke transport and other phenomena), used by the Country Fire Authority (CFA) Victoria and NSW Rural Fire Services. SPARK is another operational tool developed by CSIRO researchers to simulate fire propagation. SPARK employs a level set method (a conceptual framework for using level sets as a tool for numerical analysis of surfaces and shapes) to capture the fire front curvature and includes the effect of ember attacks through a sophisticated spot-fire modelling framework (Data 61 projects, CSIRO website: http://research.csiro.au/data61).

1.2.3 Physics-based models

In physics-based models, the transfer processes in fire spread are identified, converted to mathematical differential equations and then solved numerically using methods from CFD (Mell

et al. 2007). The modelling starts from the thermal degradation of vegetation and goes through a set of conservation equations of the coupled system formed by the vegetation and the surrounding gaseous medium to finally end with the development of turbulent flame inside and above the vegetation layer (Shamseddin 2019).

Some of the common implementations of physics-based models are: FIRETEC and FDS (Fire Dynamics Simulator). FIRETEC was developed at the Los Alamos National Laboratory in the USA. It is a coupled, three-dimensional (3D), multiphase wildland fire model (Linn *et al*. 2002). FIRETEC is coupled to the HIGRAD atmospheric model (Linn *et al*. 2002). FDS was released in 2000 by the US National Institute of Standards and Technology (NIST), in collaboration with VTT Technical Research Centre, Finland (McGrattan 2006, McGrattan *et al*. 2013). Wildland–Urban Interface Fire Dynamics Simulator (WFDS), developed by Mell *et al.* (2007), Mell *et al.* (2009), is an extension of FDS version 4 (McGrattan 2006) and then was made compatible with FDS version 6.0 (Perez-Ramirez *et al*. 2017). FIRESTAR3D is another 3D physics-based model developed to predict wildfire behaviour (Morvan *et al.* 2018). The methodologies used in FIRESTAR3D is similar to that used in FDS.

1.2.3.1 Advantages of physics-based models

There are many advantages of physics-based models over empirical and mathematical models; for example, these 3D models include fire–fuel and fire–atmospheric interactions and identify the transfer process in fire spread. These models are likely to discharge finer and detailed prediction than analogue models due to their ‘multiphase’ modelling approach, which attempts to comprehensively capture the physical processes governing fire behaviour (from pyrolysis, combustion and turbulence to smoke and heat transport) and operates over a wide range of conditions. They are highly suitable models for fire management planning and research applications owing to their detailed consideration of fuel, combustion and heat transfer mechanisms (Sullivan 2009a), though it will take years for land managers to adopt these models for planning. However, the use of physics-based models as an operational tool in wildfire management is not very feasible at present, owing to their requirement of vast computational resources, high-resolution data, and longer computational time.

1.2.3.2 Significance of physics-based modelling in the future

Fire services and authorities make considerable use of computer models to quantify fire spread rate to help in developing planning tools, strategise smoke-free evacuation routes and help in management of firefighting and evacuation logistics. However, current operational (computer) models are based on empirical modelling and there may be the limitations mentioned previously. For these reasons, physics-based models are likely to underpin the next generation of wildland fire models to be used as planning tools in operational applications. Although currently physics-based models are computationally expensive and take several hours to complete simulations, in the future, computational power will improve, such that physics-based models can habitually be used to improve operational models and hence forecasting of fire behaviour.

1.3 Research opportunities

In Australia, vegetation type is broadly classified into seven categories: (a) forest, (b) woodland, (c) shrubland, (d) scrub, (c) mallee, (f) rainforest, and (g) grassland (Australian Standard AS3959, 2018). Considering fuel type, almost 70% of Australia is covered with shrublands and grasslands (Metcalfe and Bui 2016). Similarly, grassland covers a significant landmass in wildfire-prone countries. In the present research, we limit our investigation to grassland fire behaviour. Grassfires can start and spread quickly and are extremely dangerous. Grass is a fine fuel that burns more quickly than bush or forests. Grassfires tend to be less intense and produce fewer embers than bushfires; however, they still generate enormous amount of radiant heat (Norman *et al.* 2009).

Wind is an important weather parameter that significantly impacts fire propagation. Wind speed is the dynamic force that drives the fire front forward. The interaction between the fire and wind field above the fire zone influences the fire behaviour and flame characteristics. Grasslands are often found on terrains with slope. The topography, slope, can have a significant influence on the way the fire behaves. There have been a considerable number of experimental studies(Burrows (1994), Weise and Biging (1997), Taylor *et al.* (2004), conducted to develop rate of spread (*RoS)* models as a function of different weather conditions and fuel parameters. However, topographical (slope) effects have been less studied, especially outside the laboratory scale and in combination with driving wind velocities. This topographic feature can increase or decrease fire spread rate, relative to level of terrain, depending on whether the slope is upward- or downward-directed. Australian practitioners currently use a ‘rule of thumb’ stating that the *RoS* of fire doubles for every 10°

upslope or halves with every 10° of negative slope (McArthur 1966, 1967, Noble *et al.* 1980). There appears to be little empirical evidence for this other than the knowledge of experienced practitioners and/or very-low-velocity laboratory-scale experiments. In Section 2.1.4, criticism of slope correction to fire spread rate is discussed. Furthermore, the combined effect of slope and wind on *RoS* is not well studied.

Pyrolysis and combustion of fuel, interaction of the fire with a turbulent atmosphere, wind and topographical effects, all these attributes are important in determining the behaviour of fire. Norman *et al.* (2009) state 'Most of the research studies in bushfire behaviour have focused on prediction of forward rate of spread, flame dimensions and likelihood of fire brands being thrown ahead of the fire to start spot fires; however, the physical behaviour involved in fire propagation is not applied'. Again, the empirical models may not be inclusive of much of the physical behaviour involved in fire propagation, especially in sloped terrain environments.

There is a need to investigate these aspects and underlying physical mechanisms using a physics-based modelling approach. Therefore, in this study, the physics-based model WFDS is used, with rigour, to investigate the combined effect of slope and wind on grassfire behaviour. In particular, this research focuses on fire propagation in grassland with sloped terrain (upslopes and downslopes) at different driving wind velocities.

1.4 Aim and objectives of the study.

The end goal of this study is to improve the knowledge of fire spread in grassland and thereby provide insight into and improvement to current empirical models used for fire behaviour prediction, so that risks and losses associated with bushfires can be reduced.

A set of field-scale simulations are performed, using physics-based model WFDS, with varying wind speeds and slope angles (both upslopes and downslopes), to investigate the combined effect of slope and wind on grassfire behaviour. The simulations are performed to obtain insight into grassfire behaviour that can then be used to improve empirical models, improve prediction of real wildfires, and subsequently mitigate the risks of wildfire impact.

The simulations are conducted through a systematic modelling approach. First, the study ensures that the result is ignition intensity-independent, and grid- and domain-converged, and that the atmospheric boundary layer is properly established upstream of the burnable grass plot before the

fire line is ignited. Simulations are then performed with driving wind velocities of 12.5, 6, 3, 1 and 0.1 $m.s^{-1}$ and slope angles varying from –30° to +30°.

The study then analyses the *RoS*, head fire width, fire isochrones and location of the fire front, fire intensity, mode of fire propagation, flame dynamics, flame length, and heat flux parameters. *RoS* is then compared with the results derived from empirical models in the literature: the McArthur MKIII and MKV models, CSIRO model, and Rothermel 'Original' and 'Modified' models.

In summary, this study seeks to answer:

- What effect do the upslope and downslope have on the *RoS* and how does that compare with operational models?
- What is the effect of relative *RoS* at each of the driving wind velocities and how does that compare with Australian slope function (rule of thumb) and the Rothermel model variations?
- What effect does the driving wind velocity have on the *RoS*, fire front and fire intensity as the slope angle varies?
- What effect does the driving wind velocity have on the flame parameters (flame attachment–detachment behaviour, flame length) and mode of fire propagation (wind-driven or buoyancy/plume-driven), as the slope angle varies?
- What is the relative contribution of radiative and convective heat transfer in sloped terrain at different driving wind velocities?

Chapter 2. Literature review

This chapter discusses the different fire modelling studies in the literature and provides an overview of previous studies in the field of grassfire propagation on slopes, both empirical/experimental studies and physics-based modelling studies.

2.1 Empirical modelling studies – Prediction of RoS

The empirical or semi-empirical models for grassfire propagation aim to predict the quasi-steady *RoS*, and some of the models predict flame height and fire intensity as well. *RoS* on no slope under the influence of a driving wind velocity or on slope with no driving wind velocity is taken as the base case to develop these models. Then slope and/or wind corrections are either added or multiplied to obtain the *RoS* for sloped terrain. In this section, empirical models of *RoS* with such corrections are discussed.

2.1.1 Rate of spread of fire (*RoS*) on no slope

Commonly used empirical models for Australian grassland to derive *RoS* on no slope are: the McArthur models Mark III and Mark V (McArthur 1966, 1967) and CSIRO model (Cheney *et al.* 1998).

2.1.1.1 McArthur models

One of the empirical models for Australian vegetation is the McArthur model for grassland (McArthur 1966, 1967). The McArthur model was mostly developed from experimental studies, a well-recorded Victorian bushfire (1939), and other bushfire case studies. This model quantifies *RoS* in grassland, and is included in the Australian Standards (AS3959 2018) to describe the effect of weather and fuel variables on fire spread (Cheney *et al.* 1998). Noble *et al.* (1980) presented a set of equations for the Mark III and Mark V versions of McArthur's grassland fire danger meter.

The *RoS* (km.h^{-1}) is proposed as a function of the grassland fire danger index (GFDI) as given by eqn (2.1):

$$RoS = C1\, f(C, T, H, U_{10}, W), \qquad 2.1)$$

where U_{10} is the open wind speed at 10 m above the ground, T is the air temperature (°C), H is the relative humidity in percentage, C is the curing index (The proportion of dead fuel material in

a grassland is typically described as curing level or curing index , represented as a percentage), W is the fuel weight (tonnes.ha^{-1}) and $C1$ is an empirical constant.

The equation for *RoS* in the MKIII and MKV models (Noble *et al.* 1980) is

$$RoS = 0.13\text{GFDI} \tag{2.2}$$

The GFDI equation in the MKIII model is

$$\text{GFDI} = 2.0\ exp\left(-23.6 + 5.01\,ln(C) + 0.0281T - \left(0.226\sqrt{H}\right) + 0.633\sqrt{U_{10}}\right) \tag{2.3}$$

The MKV model includes fuel moisture content (M_C) in the GFDI equation, as given by eqns (2.4) and (2.5):

$$\text{GFDI} = 3.35W\ exp(-0.0897M_C + 0.0403U_{10}\ ), when\ M_C < 18.8\%, \tag{2.4}$$

$$\text{GFDI} = 0.299Wexp(-1.686Mc + 0.0403U_{10}\ )(30 - M_C), when\ 18.8\% < Mc < 30\%, \tag{2.5}$$

where M_C is

$$M_C = \frac{97.7 + 4.06H}{T + 6} - 0.00854H + \frac{3000}{C} - 30 \tag{2.6}$$

2.1.1.2 CSIRO model

The CSIRO empirical fire spread model proposed by Cheney *et al.* (1998) is widely used in Australian operational platforms. This model is based on field experiments conducted in annual grasses of the Northern Territory (NT) (an annual plant is a plant that completes its life cycle, from germination to the production of seed, within 1 year, and then dies) and documented wildfire observations. This model adds a fuel load coefficient in determining *RoS*, which is given by eqn (2.7):

$$\begin{aligned} RoS = \{&(0.054 + 0.209U_{10})\emptyset_M\ \emptyset_C\ , U_{10} \le 5\ km.h^{-1}, \\ &(1.1 + 0.715(U_{10} - 5)^{0.844})\emptyset_M\ \emptyset_C\ , U_{10} > 5\ km.h^{-1}\ \}, \end{aligned} \tag{2.7}$$

where $\emptyset_M$ and $\emptyset_C$ are the coefficients of fuel moisture and curing, respectively.

$$\emptyset_M = exp(-0.108M_C), \quad when\ M_C < 12\%, \tag{2.8}$$

$$\emptyset_C = 1.12/\ [\ (1 + 59.2exp\ (-0.124(C - 50))\ ], \tag{2.9}$$

2.1.2 Slope correction

For slope, McArthur (McArthur 1966, 1967) proposed a rule of thumb that for every 10° of positive slope, the rate of fire spread approximately doubles, or halves with every 10° of negative slope. Noble *et al.* (1980) presented a set of equations for slope correction factors. The equations for a fire burning on uphill and downhill terrains are given by eqns (2.10) and (2.11):

$$Uphill, RoS_{corr} = RoS\, e^{0.069 slope}\,, \tag{2.10}$$

$$Downhill, RoS_{corr} = RoS\, e^{-0.069\, slope}, \tag{2.11}$$

where RoS is the forward wind-induced rate of spread (km.h^{-1}), RoS_{corr} is corrected RoS for slope and $slope$ is the effective slope of the terrain expressed in degrees. The correction is considered valid up to ± 20° slope (McArthur 1967, Sharples 2017).

Thus, in Australia, for slope, the empirical and operational models are multiplicative: the McArthur (McArthur 1966, 1967) and CSIRO (Cheney *et al.* 1998) models for flat surface multiplied with the slope correction factor.

2.1.3 Rothermel model

The Rothermel surface fire spread model (Rothermel 1972) is a semi-empirical model and is widely used in US fire management systems. This model is based on theoretical analysis combined with several experimental correlations and well-recorded wildfire data. The RoS for no-wind and no-slope is derived from the ratio of heat source to heat sink established from the fuel parameters and the moisture content (Andrews *et al.* 2013). This approach is additive in relation to wind and slope, in contrast to the Australian multiplicative approach. The packing ratio and surface-to-volume ratio are the two important components of this model.

The RoS (RoS_{corr}) is given by eqn (2.12):

$$RoS_{corr} = RoS_0\,(1 + \emptyset_w + \emptyset_s\,), \tag{2.12}$$

where RoS_0 is the fire spread rate when there is no wind and no slope involved, and $\emptyset_w$ and $\emptyset_s$ are the factors for wind and slope, respectively. This model is considered applicable up to 0–37° upslope angles.

2.1.3.1 'Original' Rothermel model

The equations used with the 'Original' Rothermel model are detailed in eqns (2.13) to (2.31) (Rothermel 1972, Wilson 1980, 1990, Weise and Biging 1997, Andrews 2018).

The *RoS* is calculated from three data sets:

- fuel particle properties – heat content, mineral content, particle density
- fuel arrangements – fuel load, surface-to-volume ratio (SAV), depth of fuel bed, dead fuel moisture extinction
- environmental parameters – fuel moisture content, ambient temperature, wind velocity, slope steepness.

Rate of spread *RoS* (m.sec^{-1}) is given by eqn (2.13):

$$RoS = \frac{I_R \xi \, (1 + \emptyset_w + \emptyset_s)}{\rho_b \, \varepsilon \, Q_{ig}}, \tag{2.13}$$

where

I_R ReACtion Intensity (kW.m^{-2}),
ξ Propagating flux ratio (dimensionless parameter),
$\emptyset_w$ Wind factor,
$\emptyset_s$ Slope factor,
ρ_b Bulk density (kg.m^{-3}),
ε Effective heating number (dimensionless parameter),
Q_{ig} Heat Of pre-ignition (kJ.kg^{-1}).

Eqns (2.14) to (2.31) define each of the above terms. The parameters used in these equation are:

w_o oven-dry fuel loading (kg.m^{-2}),
δ fuel depth (m),
β_s packing ratio,
σ surface-to-volume ratio (cm^{-1}),
M_C fuel moisture content (dimensionless fraction),
M_x fuel moisture extinction (dimensionless fraction),
U windspeed at midflame height (m.min^{-1}),
tan θ slope (dimensionless fraction),

Γ'	optimum reaction velocity (m.min^{-1}),
h	fuel heat content (fuel heaT of combustion) (kJ.kg^{-1}),
W_n	net fuel loading (kg.m^{-2}),
$ήM$	moisture damping coefficient (dimensionless parameter),
$ήS$	mineral damping coefficient (dimensionless parameter),
ρ_p	oven-dry particle density (kg.m^{-3}),
β_{op}	optimum packing ratio,
S_T	fuel total mineral content (dimensionless fraction),
S_e	fuel effective mineral content (dimensionless fraction),
h_v	heat of combustion of volatile gas (kJ.kg^{-1}),
T	ambient temperature (°C),
Q_f	hEAt of pyrolysis (kJ.kg^{-1}), and
A, B, C, E	dimensionless parameters.

reaction iNTensity I_R (kW.m^{-2})

$$I_R = \frac{1}{60}(\Gamma' \; W_n \; h \; ήM \; ήs), \tag{2.14}$$

optimum reaction velocity Γ' (m.min^{-1})

$$\Gamma' = \Gamma'_{max} \left[\frac{\beta_s}{\beta_{op}} exp\left(1 - \frac{\beta_s}{\beta_{op}}\right)\right]^A, \tag{2.15}$$

maximum reaction velocity Γ'_{max} (m.min^{-1})

$$\Gamma'_{max} = (0.0591 + 2.926\sigma^{-1.5})^{-1}, \tag{2.16}$$

packing ratio β_s

$$\beta_s = \frac{\rho_b}{\rho_p}, \tag{2.17}$$

oven-dry bulk density ρ_b (kg.m^{-3})

$$\rho_b = \frac{w_o}{\delta}, \tag{2.18}$$

optimum packing ratio β_{op}

$$\beta_{op} = 0.20395\sigma^{-0.8189}, \tag{2.19}$$

dimensionless parameter A

$$A = 8.9033\sigma^{-0.7913} \tag{2.20}$$

net fuel loading W_n (kg.m^{-2})

$$W_n = w_o(1 - S_T), \tag{2.21}$$

moisture damping coefficient (dimensionless parameter), $\acute{\eta}M$

$$\acute{\eta}M = 1 - \left(2.59 * \frac{M_C}{M_x}\right) + 5.11\left(\frac{M_C}{M_x}\right)^2 - 3.52\left(\frac{M_C}{M_x}\right)^3, \tag{2.22}$$

mineral damping coefficient (dimensionless parameter), $\acute{\eta}S$

$$\acute{\eta}S = 0.174{S_e}^{-0.19}, \tag{2.23}$$

propagating flux ratio (dimensionless parameter), ξ

$$\xi = (192 + 7.9095\sigma)^{-1} exp[(0.792 + 3.7597\sigma^{0.5})(\beta_s + 0.1)], \tag{2.24}$$

wind coefficient (dimensionless parameter), Φ_w

$$\emptyset_w = C(3.281U)^B \left(\frac{\beta_s}{\beta_{op}}\right)^{-E}, \tag{2.25}$$

dimensionless parameter C

$$C = 7.47\, exp(-0.8711\sigma^{0.55}), \tag{2.26}$$

dimensionless parameter B

$$B = 0.15988\sigma^{0.54}, \tag{2.27}$$

dimensionless parameter E

$$E = 0.715\, exp(-0.01094\sigma), \tag{2.28}$$

slope factor (dimensionless parameter), $\emptyset_s$

$$\emptyset_s = 5.275{\beta_s}^{-0.3}(tan\,\Phi)^2, \tag{2.29}$$

effective heating number (dimensionless parameter), ε

$$\varepsilon = exp\left(-\frac{4.528}{\sigma}\right), \tag{2.30}$$

heat Of pre-ignition (kJ.kg^{-1}), Q_{ig}

$$Q_{ig} = 581 + 2594M_C. \tag{2.31}$$

2.1.3.2 'Modified' Rothermel model

Wilson (1990) presented as modified version of the Rothermel model, which is detailed in Weise and Biging (1997). This model incorporates an extinction index $Pf_{(nx)}$, which is a function of heat of vaporisation Q_w and fuel moisture content M_C.

The equations used with the 'Modified' Rothermel model are detailed in eqns (2.32) to (2.46).

rate of spread RoS (m.sec^{-1})

$$RoS = \frac{(\xi\ h_v\ w_o\ \Gamma\ \eta M)(1 + \emptyset_w + \emptyset_s)}{[\rho_b\ \varepsilon\ (Q_f + M_C \emptyset_w)]}, \tag{2.32}$$

propagating flux ratio (dimensionless parameter), ξ

$$\xi = 1 - exp(-0.17\sigma\beta_s), \tag{2.33}$$

packing ratio β_s

$$\beta_s = \frac{\rho_b}{\rho_p}, \tag{2.34}$$

oven-dry bulk density (kg.m^{-3}), ρ_b

$$\rho_b = \frac{w_o}{\delta}, \tag{2.35}$$

optimum packing ratio β_{op}

$$\beta_{op} = 0.20395\sigma^{-0.8189}, \tag{2.36}$$

maximum reaction velocity Γ (m.min^{-1})

$$\Gamma = 0.34\sigma\ (\sigma\ \beta_s \delta)^{-0.5}\ exp\left(-\sigma\frac{\beta_s}{3}\right) Pf_{(nx)}, \tag{2.37}$$

extinction index $Pf_{(nx)}$

$$Pf_{(nx)} = \frac{ln\left(\sigma\ \beta_s\ \delta\ \frac{h_v}{Q_w}\right)}{(M_C + \frac{Q_f}{Q_w})}, \tag{2.38}$$

heat of VAporisation Q_w, (kJ.kg^{-1})

$$Q_w = 4.18(100 - T + 540), \tag{2.39}$$

moisture damping coefficient (dimensioNLess parameter), ηM

$$\eta M = exp\left(-\frac{M_C}{M_x}\right), \tag{2.40}$$

wind coefficient (dimensionless parameter), $\emptyset_w$

$$\emptyset_w = C(3.281U)^B \left(\frac{\beta_s}{\beta_{op}}\right)^{-E}, \quad (2.41)$$

dimensionless parameter C

$$C = 7.47\exp(-0.8711\sigma^{0.55}), \quad (2.42)$$

dimensionless parameter B

$$B = 0.15988\sigma^{0.54}, \quad (2.43)$$

dimensionless parameter E

$$E = 0.715\exp(-0.01094\sigma), \quad (2.44)$$

slope factor (dimensionless parameter), $\emptyset_s$

$$\emptyset_s = 5.275{\beta_s}^{-0.3}(\tan\Phi)^2, \quad (2.45)$$

effective heating number (dimensionless parameter), ε

$$\varepsilon = \exp\left(-\frac{4.528}{\sigma}\right). \quad (2.46)$$

2.1.4 Criticism of slope correction

Sharples (2008, 2017) comprehensively reviewed wind slope correction for empirical fire models. Sharples (2008) examined a range of mathematical and empirical/semi-empirical models employed for wind -slope correction of wildfire rate of fire spread. He comprehensively reviewed various models that implied additive and multiplicative approaches in relation to slope and wind correction. McArthur (McArthur 1966, 1967) and Rothermel (Rothermel 1972) models were reviewed along with different mathematical and physical models: the models proposed by McAlpine *et al.* (1991), Nelson (2002), McRae (2004), Pagni and Peterson (1973), and Morandini *et al.* (2002). Overall, he obseved that the additive vector (in which the effects of wind and slope are combined in a vectorial manner) methods tend to give the most reliatsic wind-slope correction results. Again, he denoted that 'dynamic effects' can create fire behaviour that may not be accounted in these models and warranted furthur studies incorporating fire-topograhy-atmospheric interactions, to evalulate and refine wind-slope correcrion methods. Sharples (2017) pointed out that McArthur might not have advocated the use of eqn (2.11), which may have been adopted out of a combination of loose reasoning and convenience. Sharples also noted that the

operational models based on empirical modelling are developed with a quasi-steady state assumption, which may not be the case with real wildfire propagation.

Cruz and Alexander (2013) reviewed the performance of operational fire models, based on *RoS*, used by fire and emergency service analysts on seven vegetation types found in Australia. Whilst, their study did not specifically cite the ramifications of slope and wind correction factors, they found that, on average, most of the fire models have a mean absolute error of 20–80% in estimating the predictive rate of fire spread. They noted that the differences in prediction are due to assumptions and the limitation of these models.

To test the empirical models discussed above, some laboratory studies were conducted, predominantly with no-wind or very low wind conditions.

Sullivan *et al.* (2014), based on several laboratory experiments, examined fire spread on negative slopes and showed that significant underprediction can occur with the use of eqn (2.11). For a slope of –20°, the underprediction was by a factor of three. Sharples (2017) interpreted Sullivan *et al.* (2014) as implying that the value of *RoS* for a negative slope situation should never be less than 60% that of the zero-slope condition. Sullivan *et al.* (2014) also questioned the basis for McArthur's rule of thumb as it is only described as the result of 'experimental fire studies' in McArthur (1967) and showed that on upslopes, it significantly overestimates RoS_{corr} compared with the US model BEHAVE (Rothermel and Burgan 1984) based on the Rothermel model (Rothermel 1972).

Burrows (1994) conducted multiple laboratory and field experiments using uniform jarrah forest litter fuels (in jarrah forest, Western Australia) under low (about 1.8 $m.s^{-1}$ and below) and zero wind conditions and compared the *RoS* values against fuel moisture content, wind speed and slope. He observed an exponential relationship between *RoS* and slope angle at zero wind conditions and found that his experimental results roughly matched eqns (2.10) and (2.11) in the range of ±15°.

Weise and Biging (1997) found the opposite of Burrows (1994) in their laboratory experiments using a tilting wind tunnel. The experiments were conducted under no-wind conditions and low wind speeds ranging from 0.4 to 1.1 $m.s^{-1}$ and with five slope angles (+15%, +30%, 0, –5% and –30%). Their fuel beds were composed of vertical paper birch (*Betula papyrifera*) sticks and a shallow layer (<0.5 cm) of evenly distributed coarse aspen (*Populus tremuloides*) excelsior (wood

wool). They compared the mean observed *RoS* values from experimental fires with the values derived using various empirical models and found that agreement between their observed *RoS* and that predicted by the McArthur models was poor but was good with the Rothermel model.

Viegas (2004) analysed wind- and slope-induced convection effects on fire propagation using an analytical model that determined reference rate of spread values. He then compared these with data from his experimental studies. A series of experimental studies were conducted on fuel beds (16 × 1.6 m inclined up to 40° in 5° steps) composed of dead needles of *Pinus pinaster* with arbitrary wind conditions. Wind speeds of 5 and 11 $m.s^{-1}$ were generated using axial flow fans. The data recorded by the video images were analysed. The analytical model based on additive effect of slope and wind showed good predictions for the fire front spread directions and reasonably agreed with the rate of fire spread. Also, the *RoS* values were found to be in good agreement with the additive concept proposed by Rothermel (1972). However, this study covered only a limited range and large-scale experiments are warranted to understand the effect of wind and slope on fire front movement, shape and length.

The various empirical and analytical models discussed above are found to be harmonious to some degree under certain conditions, however, they disagree in terms of the approach and the conditions the model will work under. From these discussions, it appears that the notion of obtaining quasi-equilibrium *RoS* for a flat surface as a function of wind and then adding or multiplying the slope correction may not be accurate. Moreover, these models do not include the dynamic nature of fire propagation and may not be inclusive of much of the physical behaviour involved in fire propagation, especially on sloped terrains.

2.2 Other experimental studies

This section details other experimental studies conducted with and without slopes that investigated flame characteristics, interaction between the plume and terrain, heat transfer mechanisms and mode of fire propagation. Again, most of these experimental studies were performed with mild or no-wind conditions.

2.2.1 Flame characteristics, plume and flame attachment

Mendes-Lopes *et al.* (2003) carried out a set of experiments in a dedicated burning tray (1.0 × 0.7 m bed of *Pinus pinaster* needles) in a wind tunnel set up with varying wind velocities of 0, 1, 2, 3 $m.s^{-1}$, fuel moisture content (10% and 18%) and slope angles of –15°, –10°, –5°, 0°, +5°, +10° and +15°. Each of these experimental fires was video recorded. They analysed the flame parameters (flame length, height and angle) and *RoS* of both headfire and backing fire from the mean of each set of results. The *RoS* was obtained by fitting a straight line to the data points with *RoS* represented by the slope value of the straight line (goodness of fitting is represented by an R^2 value) from the least-square regression method. Analysis of variance (a statistical method) was carried out for *RoS* to examine the combined effect of wind velocity, slope and fuel moisture content. A similar analysis technique was used on the flame geometry to determine flame parameters. Their experiments revealed that rate of spread increases with upslope; however, the rate of spread is very low for back-wind and/or downslope conditions. They observed the strongest influence on *RoS* is by far wind velocity, followed by fuel moisture content, then slope. Because of the much stronger influence of wind velocity on rate of spread, wind velocity was chosen as the leading independent variable. They also noted that the wind-driven flames bend over, increasing radiative heat transfer to the fuel, which is also heated by the convective heat transfer from the hot gases emanating from the flame. For upslope and wind-driven flames, the proximity of the flame and fuel due to the slope further increased heat transfer to the fuel bed. These experiments conducted at low wind velocities showed vertically oriented flames due to buoyancy forces.

Viegas (2004) and Dold and Zinoviev (2009) in their experimental studies observed a rapid increase in *RoS* for fires burning on steep slopes, despite burning under persistent environmental conditions. This rapid acceleration of fires has been termed as ‘fire blow-up’ or ‘fire eruption’. Sharples (2017) stated that eruptive beahviour occurs due to an interaction between the slope of the terrain and the fire’s plume. According to Sharples (2017), for steep slopes, a localized pressure deficit can form immediately upslope, ahead of the fire, and this causes the flames and plume to attach to the terrain surface.

Dold and Zinoviev (2009) conducted a series of laboratory experiments (using a uniform layer of loosely packed straw as fuel) on upslope scenarios (upslope angles of 15°, 20°, 25°, 30° and 35°) along with a field experiment on a 40 × 25 m plot (containing Mediterranean shrubs), at +23°

slope. They used straight-line fires in mild or negligible wind conditions. They observed eruptive growth of fire and flame attachment at a slope of +23° with the field experiment, and closer to +30° in the laboratory experiments for the vegetation type they used. They found that for low driving wind velocity (their experiments were conducted at a low ambient wind speed of 1.6 ± 1 $m.s^{-1}$) for fires burning above 20° slope, the interaction of wind and topographical effects (such as slope) can have significant implications on plume behaviour.

Dupuy *et al.* (2011) conducted a set of laboratory fire experiments (in Pinus halepensis fuels beds, 1 $kg.m^{-1}$) to test the effect of slope and fuel bed width on fire behaviour such as rate of fire spread, fuel consumption, flame residence time and flame geometry. The experiments were conducted under no-wind conditions, at upslope angles of 0º, 10º, 20º and 30º and fuel bed width of 1,2 and 3 m. Experiments were conducted on a 10 m long and 4 m wide inclinable table (angle of inclination varied from 0º to 30º) with a burnable area of 9 m long and 3 m wide. The fires were ignited along the entire width of fuel bed and camera recordings were used to examine fire line contour and flame geometry. They observed that the fire line shape greatly influenced by slope. Curvature shaped fire isochrones were observed for higher upslopes and in 20º the fire contour changed to a pointed V- shape and remain in the shape beyond 3 or 4 m. The rate of spread was found to increase with increase in slope angle and with fuel bed width. However, fuel bed width had a significant effect on rate of spread only at the higher upslopes 20º and 30º (notable effect at 3m- wide fuel bed), whereas, the slope effect was significant for all fuel bed widths. They observed that slope effect on rate of fire spread at the 30º slope angle was underestimated by empirical models: Rothermel model (Rothermel 1972), the Canadian Fire Behaviour prediction model (Forestry Canada Fire Danger Group (FCFDG 1992), which is based on Rothermel studies and the McArthur model (McArthur 1966, 1967. In particular, for 3m -wide fuel bed cases the underestimation was by a factor of 2. Flame lengths were correlated closely with fire line intensity but found to be exceeded those predicted by usual correlations (Alexander and Cruz (2012, 2021)). For 30º upslope, the fire line changed towards a pointed shape, however, observed an unstable shape towards the end of fuel bed and they hypothesised this to the air entrainment from the lateral sides of fuel bed area. They called for further investigation including flow diagnostics, and field scale experiments to assess the effect of slope and fire width on upslope fires.

Chen *et al.* (2018) performed a series of fire spread experiments on a pine needle board (6 × 1.8 m fuel bed) under slope conditions of +5° to +30°, at no-wind conditions, to study the effect of slope angle on flame propagation. Fire spread rate, temperature and radiative heat flux were measured from the experiments along with flame parameters. The results showed significant increase in flame length from the slope angle +20°. For higher slope angle cases, the flame was observed to be tilted to the unburnt portion of the fuel bed owing to unbalanced air entrainment pushing the flame towards the unburned region. They noted that this behaviour intensified the radiative heat flux from the flame onto the fuel bed surface, leading to an increase in fire spread rate. The flame attachment contributed significantly to elevating the fire spread rate on higher slope angles. Their results showed that radiation heat flux increased with slope angle, increasing rapidly for slope angles above +20°. Chen *et al.* (2018) then performed numerical simulations using a physics-based fire model and compared the experimental results with simulation results and empirical models in the literature. Their simulation study is detailed in Section 2.3.1- Physics-based modelling of fire propagation on slope -.

Sánchez-Monroy *et al.* (2019) conducted laboratory-scale experiments involving uniform coarse excelsior (shredded aspen, *Populus tremuloides*) heartwood, with no wind imposed, for sloped fuel beds, accompanied by numerical simulations using a physics-based model. Coarse excelsior heartwood was selected as fuel (approximately 2.5 × 0.8 mm cross-section) with three different fuel bed depths (2.54, 7.62 and 15.24 cm) and packing ratios (0.005, 0.01 and 0.03). The experiments were designed with fuel bed slopes ranging from –16° to +45°. Rate of fire spread and flame geometry (such as flame length, height, angle) were measured in each of the experimental tests. They observed that radiative heat transfer is the dominant mechanism of heating for slope angles between 0° and 20°, and the convection heat transfer mechanism starts to be relevant and becomes more important than radiation for slopes of 31° and 45°. Their findings were similar to the results obtained by Morandini and Silvani (2010), in their field-scale experiments (detailed in Section 2.2.2). Sánchez-Monroy *et al.* (2019) then performed computer simulations using the physics-based WFDS model and compared the plume attachment, fire front shape, *RoS* and flame properties observed from experiments with the simulation results. Their simulations study is discussed in Section 2.3.1- Physics-based modelling of fire propagation on slope.

The interaction between wind and topography will remarkably affect heat transfer from the burning zone into unburnt fuel (Apte *et al.* 1991, Cobian-Iñiguez *et al.* 2019). Dold and Zinoviev (2009), Dupuy *et al.* (2011) and Sánchez-Monroy *et al.* (2019) in their separate studies with laboratory experiments observed that flame or plume attachment leads to enhanced preheating of fuels upslope, ahead of the fire and a resulting acceleration of the fire spread. If such phenomena occur, convective heat transfer significantly increases.

It is therefore important to understand how the plume and flame attachment behaviour occurs.

2.2.2 Fire propagation studies – modes of propagation

Fire propagation is often characterised as either in a wind-driven or buoyancy-driven mode (Apte *et al.* 1991). Apte *et al.* (1991) conducted experimental studies over horizontal surfaces of polymethylmethacrylate (PMMA) in a wind tunnel set-up with wind speeds ranging from 1 to 2.1 $m.s^{-1}$. Their experiments showed that the fire spreads initially in a boundary layer mode, during which the heat fluxes are nearly constant. Transition to plume- or buoyancy-driven mode occurred earlier at lower wind velocities, accompanied by a rapid increase in the heat fluxes. As the fire progressed, radiation increasingly became the dominant mode of heat transfer from the flame to the fuel surface. They used the Froude number vs flame length to analyse the two different modes of fire propagation. The Froude number (F_r) is a dimensionless number used to predict fire spread regime, and is the ratio between two forces: the inertia due to the wind flow and the buoyancy forces resulting from the gradient of density between the interior of the plume and the ambient air (Apte *et al.* 1991, Morvan *et al.* 2013, Moinuddin *et al.* 2018).

$$\mathrm{F_r} = \frac{U_{10}}{\left\{\frac{gQ}{\rho_g C_g T_s}\right\}^{⅓}}, \tag{2.47}$$

where U_{10} = average wind velocity ($m.s^{-1}$), g = gravitational acceleration ($m.s^{-2}$), Q = fire line intensity ($kW.m^{-1}$), ρ_g = gas density ($kg.m^{-3}$), C_g = gas heat capacity ($kJ.kg^{-1}.K^{-1}$), T_s = fuel surface temperature (K). $F_r < 1$ indicates a plume- or buoyancy-dominated fire, while $F_r > 1$ indicates a wind-driven fire.

The Byram convection number, N_c, is another dimensionless parameter used to quantify the mode of fire propagation into wind-driven or buoyancy-driven fire mode (Mell *et al.* 2018, Morvan and Frangieh 2018).

$$N_c = \frac{2gQ}{(U_{10} - RoS)^3 \rho_g C_p T} \quad , \tag{2.48}$$

where U_{10} = wind velocity (10-m open wind speed in a zone not affected by the fire front; $m.s^{-1}$), RoS = rate of fire spread ($m.s^{-1}$), Q = fire line intensity ($kW.m^{-1}$), T = ambient temperature (K), g = acceleration due to gravity (9.8 $m.s^{-2}$), ρ_g = gas density (1.2 $kg.m^{-3}$), C_p = specific heat of air (1.0 $kJ.kg^{-1}.K^{-1}$) . If $N_c > 10$, the fire is buoyancy-driven, and if $N_c < 2$, the fire is wind-driven. At intermediate N_c values, the fire is neither buoyancy-driven nor wind-driven. However, as N_c is dimensionless, discretion is available in choosing the velocity at any relevant height to analyse the mode of fire propagation.

Morvan and Frangieh (2018) analysed a large set of wildfire experimental data (both field and laboratory scale) from the literature to understand the role of *RoS* and wind velocity on fire propagation. They used Byram number analysis to investigate the existence of two regimes of fire propagation (wind-driven fire vs plume-dominated fire) and hypothesised that heat transfer in buoyancy-driven fires is dominated by radiation, and by convection in wind-driven fires. This hypothesis is untested at large experimental scales; however, there are experimental measurements of heat fluxes in laboratory-scale fires (Dupuy and Maréchal (2011).

Dupuy and Maréchal (2011) conducted laboratory fire experiments under no-wind conditions (in *Pinus halepensis* fuels beds) to understand the role of radiation and convection heat transfer with slope on fire spread. In their experiments, they measured fuel temperature and gas temperature simultaneously at the same location (using infrared camera and thermocouples, respectively) and measured the incident radiant heat flux received by a small fuel bed volume ahead of the fire line. These measurements were used to compute heat transfer for each slope angle (0º, 10º, 20º and 30º). Overall, they found radiative heating dominated the heat transfer mechanism for the slopes between 0º and 20º, but close to the fire line (< 10 cm), the flux due to convective heating was also significant, reaching one-third the net heat flux at 20º slope angle. When the slope angle increased from 20º to 30º, the rate of spread rose by a factor of 2.5 owing to a marked increase in convective heating, while radiative heat flux remained constant or decreased slightly (Dupuy and Maréchal

2011). This may be due to so-called eruptive behaviour where the plume and flame attach to the slope (Sharples 2017). Based on Byram number (N_c) analysis (eqn (2.48)), data and trend presented here, all the fires presented by Dupuy and Maréchal (2011) are likely buoyancy-driven fires.

Tihay *et al.* (2014) conducted experiments at laboratory scale (needles of Pinus pinaster on a 2 m × 2 m combustion table) under no-slope and +20º slope, at no-wind conditions. The experiments were conducted with different fuel loads of 0.6, 0.9 and 1.2 $kg.m^{-2}$ and fires were ignited along the entire width of fuel bed. They investigated the heat release rate (HRR) using oxygen consumption calorimetry, mass loss rate (MLR), geometry of fire front using camera recording and heat fluxes using heat flux transducers, to understand the effect of slope on fire behaviour. They did not observe a quasi-steady state HRR (and MLR) at 20º slope (at this slope the fire front turned out to a V-shape (a pointed convex) pattern as the fire progressed though the fuel bed), compared with no-slope condition, for all three fuel loads (higher the fuel load, less occurrence of steady state). They demonstrated that the HRR over time can be estimated mathematically with the fuel load and the time derivative of burnt surface area. Their heat flux measurements showed that, for a 20º slope, convection represented the major fraction of heat transfer (between 61.1% and 74.9% of the total heat transfer and the remaining fractions were represented by radiative heat transfer) and convection fraction increased with increase in fuel load.

Morandini and Silvani (2010) conducted five field-scale experimental fires (ignition line 20–30 m) in the Mediterranean region with various vegetation properties, wind conditions (< 5 $m.s^{-1}$) and topography to examine heat transfer ahead of the fire front. The temperature and heat fluxes were measured (using an intrusive sensor system comprising a heat flux gauge, transducers, thermocouples) at the top of the vegetation as the fire progressed. The results showed the existence of two different fire spread regimes that were either dominated by radiation or governed by mixed radiant–convective heat transfer. For higher fuel loads, plume-dominated propagation was observed by way of the buoyancy forces generated by the fire and radiation was observed to be the dominant heat transfer mechanism ahead of the fire front. The second regime, wind-driven, occurred for lower fuel loads, where the flow is governed by inertial forces due to wind; preheating of unburned fuel occurred due to both radiative and convective heat transfer. Their study demonstrated that neither the Froude number, F_r, (eqn (2.47)) nor the convection number, N_c, (eqn (2.48)) – used in the literature to predict fire spread regimes – reflect the observed behaviour of

wind-driven fires. They noted that in a wind-driven fire regime, convective heat transfer becomes significant owing to the interaction of the fire plume with unburned vegetation and should be taken into account when managing safety zones.

Nelson (2015) questioned Morandini and Silvani (2010) that the influence of slope on fire behaviour was not accounted for in their studies while determining the F_r and N_c values and, thus, the conclusion of Morandini and Silvani (2010) is questionable. Nelson (2015) re-analysed the experimental data of (Morandini and Silvani 2010) based on a triangular flame model described by Anderson *et al.* (2006). The slope angle, flame height, flame tilt angle and flame half-depth from the experimental data were used to construct a triangular flame model. Nelson (2015) then compared the F_r and N_c computed from the triangular flame model with the corresponding parameters from Morandini and Silvani (2010). He pointed out that Morandini and Silvani (2010) omitted the slope effect while computing F_r and N_c and observed that their calculated F_r and N_c exceeded the corresponding variables reported by Morandini and Silvani (2010) by a factor of 3 when slope effects were included in the analysis. Nelson (2015) reinstated the need to include slope effects in determining wind–slope-aided fire propagation and this warrants further studies about the accepted norm of stipulating the transition from buoyancy-dominated to wind-driven fire as wind speed and slope angles increases.

As part of their continuing study, Morandini *et al.* (2018) conducted a series of fire spread experiments, with no wind, across a porous bed of excelsior (fuel bed 21 m^2, fuel load 0.2–0.6 $kg.m^{-2}$) in a large-scale laboratory facility under no slope and 30° upslope with a line fire. The velocity field flow patterns inside the spreading flame (within the fire plume and on both sides of the flame) with respect to the fire front were measured using a PIV system (Particle Image Velocimetry, a laser optical method using computer-controlled cameras and videos, used for flow visualisation and diagnostics), heat fluxes were measured using heat flux microsensors and gas temperature using thermocouples. From the data collected from this experiment, they found that the increase of the rate of spread with increasing slope could be attributed to a major change in flame dynamics. Under no-slope conditions, preheating of the fuel particles was dominated by radiation from the flames. However, under 30° upslope condition, they noted a substantial increase of air entrainment at the burnt side of the fire compared with no slope. They observed a convective heat transfer mechanism in the downstream area that resulted from the interaction between

upstream air entrainment and the fire-generated buoyancy forces. Their heat flux measurement data confirmed the existence of such convective mechanisms for upslope conditions, and that the downstream heating of the unburnt fuel depends on both radiative and convective heat transfer mechanisms. They also noted that the rate of heat transfer ahead of the fire front increased with increase of slope and fuel load.

2.3 Physics-based modelling studies in the field of grassfire propagation

A physics-based modelling approach has recently been used to study several different fire scenarios including fire spread on grass, fire transition from grass to a canopy, firebrands (spotting in wildfires), backing fire, and fire on slopes. These are versatile models and becoming accepted as insightful and valid tool to investigate fire behaviour including wildfires. (Mell *et al.* 2007, Pimont *et al.* 2012, Moinuddin *et al.* 2018, Sánchez-Monroy *et al.* 2019, Sutherland *et al.* 2020).

The following sections discusses some of the physics-based modelling studies found in the literature, in relation to wildfire propagation, with and without slope. The section also includes studies that reinforce the potential of the fully physical fire model WFDS to simulate wildfire in conditions like real fire scenarios.

2.3.1 Physics-based modelling of fire propagation on slope

In the area of physics-based modelling of surface fire propagation on slopes, Linn *et al.* (2007) used a Reynolds-averaged Navier–Stokes (RANS)-based HIGRAD/FIRETEC model (a coupled atmospheric transport and wildfire model) to study fire propagation through forests (with tall grass underneath) on hills, canyons and ridges. A set of simulations were conducted on a domain of 640 × 320 m size, at two different wind speeds of 6 and 12 $m.s^{-1}$, with five different idealised topography scenarios (Flat, Hill, Canyon, Upcan and Ridge). They studied the effect of both the fuel structure and slope on the *RoS* and shape of the fire. They observed that both the fuel structure and slope affected the fire spread rate (which is obvious) and shape of the fire. However, their study was not free of discretisation, numerical effects such as grid convergence was not presented and hence convergence of results was unknown. Again, the simulation modelling was not validated against any experimental measurement.

Pimont *et al.* (2012) used the LES (Large Eddy Simulation) version of HIGRAD/FIRETEC to simulate typical Mediterranean vegetation fire grassfires with different slopes (–60% to 100%), wind (1, 5 and 12 $m.s^{-1}$) and ignition length (20 and 50 m). The vegetation structure is known as garrigue, which is a type of low shrubland or heath and Pimont *et al.* (2012) described the vegetation structure as composed by patches of shrubs (75%) and grass (25%). They observed reasonably good agreement with BEHAVE (US model) and the Canadian Forest Fire Behaviour Prediction System (CFFBPS) (FCFDG 1992), which incorporates the Rothermel model; however, agreement with McArthur model was poor except for few cases. The study of Pimont *et al.* (2012) was conducted with a simplified spatially constant wind flow condition that was dictated by the comparison with empirical laws. These laws are based on wind profiles that depend on the leaf area index (LAI) of the stand to set initial flow profile conditions in order to avoid LES of precomputation of ambient wind (i.e. a significant computational cost). Given that a simplified wind field was used and there was no grid convergence study, a further investigation of surface fire propagation on sloped terrain is warranted with dynamic wind field and appropriate grid resolution.

Chen *et al.* (2018) developed an in-house LES-based fire model termed the Pyrolysis model. Contrasting with the HIGRAD/FIRETEC coupled model, this model was specifically designed for flame propagation of a laboratory-scale fire scenario and incorporated detailed combustion chemistry. This model included sub-modelling components to address solid pyrolysis, gas-phase combustion, radiation heat transfer, soot formation and turbulence. The mesh system adopted in this study used very fine rectangular grids, size of 0.05 m. As a result, the model needed very high computational resources and grid convergence study was not presented. Chen *et al.* (2018) performed numerical simulations on a series of fire spread experiments (discussed in Section 2.2.1), at no wind conditions, and compared the experimentally observed rate of spread, radiative heat flux and flame propagation characteristics with the simulation results. The model predictions were in good agreement with the experimental data, and the fire spread rate and temperature predictions were within 12% accuracy in comparison with the experimental results. The simulations were able to replicate the fire front region (smoke and gas temperature contours) for different slope conditions. They also compared the prediction from their fire model with three empirical models: the Rothermel model, Australian forest fire model (based on McArthur models) and the Canadian Forest Fire model (which incorporates the Rothermel model) (FCFDG 1992),

and found that these three empirical models significantly underestimated the *RoS* for slope angles higher than +20° relative to the model prediction

Eftekharian *et al.* (2020) investigated terrain slope effects on wind enhancements using a CFD model, FireFOAM, which employs an LES scheme. They used a computational domain size of 34 × 9 × 15 m with a line fire bed (0.3 m depth and 9 m width) and simulations performed with slope angles –20° to +20°. They performed grid convergence study using three grid sizes; coarse, medium and fine girds and medium grid (127 × 527 × 130 mm) was chosen for the simulations. The simulation results were validated against two sets of experimental data of their previous work (Eftekharian *et al.* (2019) and obtained a reasonable agreement against experimental data. They found that the strongest fire-induced pressure gradient occurs in the low-density region immediately downstream of the fire source, causing maximum wind enhancement, and wind enhancement gradually decays longitudinally along the plume line further downstream of the fire. They observed that an upslope terrain reinforces the Coanda effect (reaction to the pressure difference induced by changes in the capacity for entrainment of air upslope and downslope of the fire, considered the main cause of plume attachment to the ground) and intensify attachment of the plume to the ground, whereas the downslope conditions weaken the Coanda effect and reduce the flow's tendency to attach to the ground downstream of the fire source.

2.3.2 Physics-based modelling studies using FDS/WFDS – with and without slope.

WFDS/FDS are fully 3D models with an underlying LES-based hydrodynamic and turbulence model (Mell *et al.* 2007, McGrattan *et al.* 2015). WFDS modelling includes fire propagation through vegetative fuel such as trees, grasslands and shrublands.

Mell *et al.* (2007) used the physics-based model WFDS and simulated the experimental grass fires of (Cheney *et al.* 1993) (Australian grassland experiments conducted in the Northern Territory, named F18, F19 and C064) and demonstrated how well WFDS reproduces the experimentally observed results. Fuels in these experiments were open grasslands, continuous and normally fully cured. For grassfire modelling, they used two computational grids: one for the gas phase that resolves the fire plume and another for the vegetative fuel bed that resolves heat transfer and thermal degradation. Their study was conducted with WFDS version 4.0. Grid sensitivity and Atmospheric Boundary Layer (ABL) development were not rigorously conducted in this study.

Figure 2.1 shows a photograph taken during the experimental fire and a snapshot of the WFDS simulation to show that WFDS can qualitatively predict the behaviour observed experimentally. Mell *et al*. (2007) simulated 16 fires (four different ignition line lengths and four different wind speeds of 1, 3, 4 and 5 $m.s^{-1}$) and discussed in detail the effect of wind, fire head width and residence time of head fire and mass loss rate on fire spread. WFDS simulations showed similarity with experimentally observed fire spreads and previously used empirical relations.

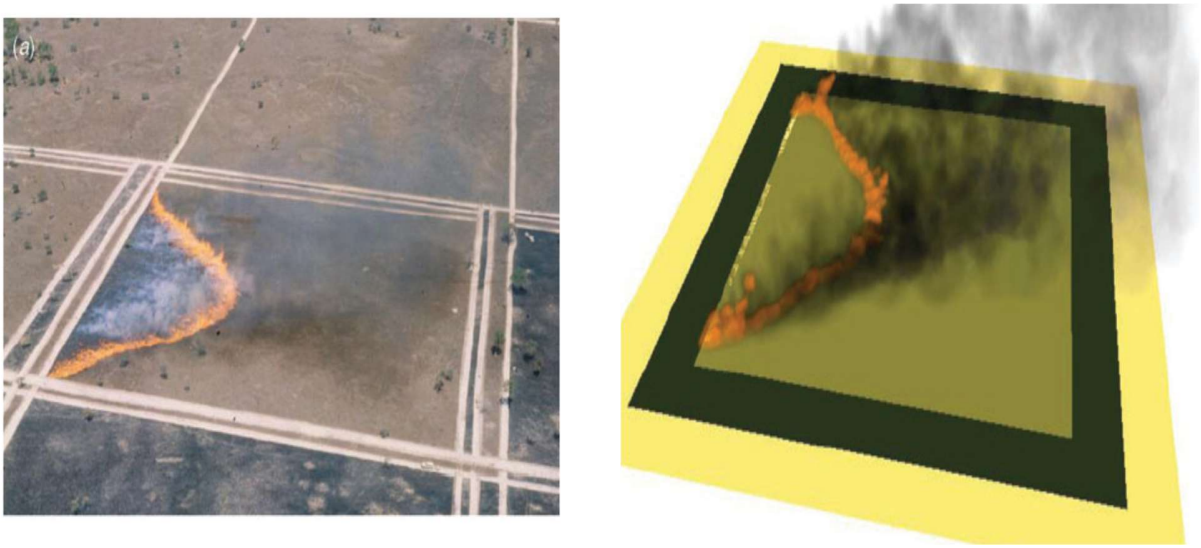

(a) Photograph of fire perimeter taken during experiment F19 at 56 s

(b) Snapshot of WFDS simulation of the same experimental fire

Figure 2.1 – Qualitative comparison between experimental fire and WFDS modelling studies (Mell *et al*. 2007)

Morvan *et al.* (2013) used WFDS to study the interaction of a forward-propagating head fire (in the direction of the prevailing wind) with a backing fire travelling in the opposite direction to the wind. A set of simulations were conducted on flat terrain (20 m width × 50 m length grassland plot) with wind speeds ranging from 1 to 10 $m.s^{-1}$ with both head fire and backfire ignition scenarios (stand-alone and combined scenarios). They compared the *RoS* vs wind velocity obtained for standalone fire simulations with various empirical models and experimental observations from the literature. For moderate wind speed conditions (up to 8 $m.s^{-1}$), the results obtained using physics-based WFDS and FIRESTAR2D models (Morvan *et al.* 2009) were found to be in relatively good agreement with empirical models and experimental data. However, for strong wind conditions (> 8 $m.s^{-1}$), all models (except FIRESTAR) underpredicted the *RoS* in comparison with

experimental data. The results with the combined ignition scenario (both the head fire and a secondary fire ignited together on the downwind side) highlighted that both head fire and backfire can interact via two mechanisms: the head fire acts on the backfire as a screen and reduces the direct action of the wind flow on the backfire for a relatively larger distance (>10 m), and the gas entrainment generated in the vicinity of the head fire causes the backfire to incline towards the forward fire front for shorter distances (nearly equal to 10 m). Though this study focused on the interaction between head fire and backfire, generally, it demonstrated that the fully physical fire model WFDS has the potential to simulate the interaction between two fire fronts in conditions like a real fire scenario.

Moinuddin *et al.* (2018) performed grassfire simulations of the C064 grassland experiment conducted in the Northern Territory by Cheney *et al.* (1993) with WFDS version 6.0 and with adequately resolved grid and developed ABL. They conducted precursor simulations without grass burning until an appropriately mapped wind profile was obtained over the length of the domain. The longitudinal velocity profiles obtained at various downwind locations were analysed to ensure that ABL was developed with a steady-state velocity profile. They also performed domain and grid convergence studies to obtain domain- and grid-converged results. Simulations were conducted on flat terrain with a grass plot size 104 × 108 m (mimicking the grass plot size of the C064 experiment), at varying inlet wind velocities (U_2) of 3, 6, 6.5, 7.5 and 10 m.s^{-1}. The results were then validated against experimental results of Cheney *et al.* (1993), and it was found quantitatively that the fire line progression was well predicted. The *RoS* vs wind velocity (U_{10}) from their study is shown in Figure 2.2. The experiments were conducted under a range of fuel and weather conditions ('Natural', 'Cut' and 'Wildfire' shown in Figure 2.2 refers to different fuel/grass conditions (Moinuddin *et al.* (2018)).

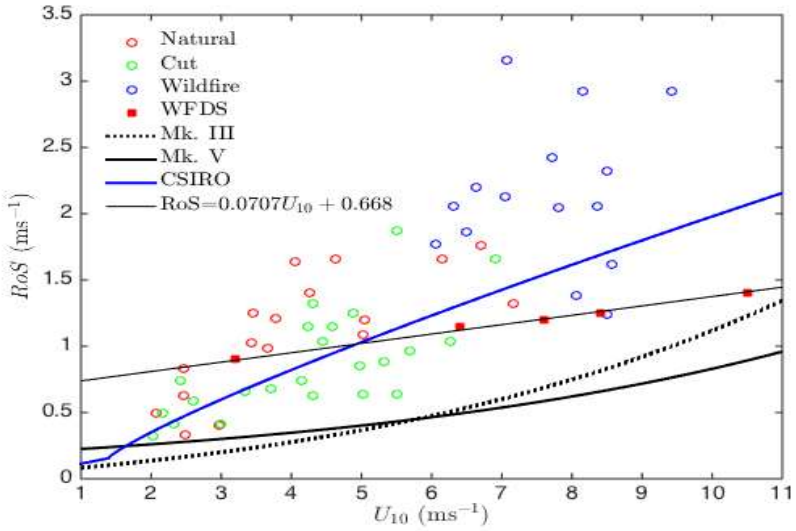

Figure 2.2 – Effect of driving wind velocity on fire spread rate (Moinuddin *et al.* 2018): WFDS simulation results compared with various operational models, with experimental results obtained by Cheney *et al.* (1993) in the background

The *RoS* was found to be linearly correlated with 10-m open wind velocity as demonstrated in Figure 2.2. Moinuddin *et al.* (2018) then compared their WFDS *RoS* values with the results obtained from the various empirical models as shown in Figure 2.2. The experimental observations in the background are from Cheney *et al.* (1998). The CSIRO model prediction is derived from the same experimental data set while the two McArthur model (MKIII and MKV) predictions were derived from a dataset of lower wind speed range. They also studied the effect of grass height on *RoS* and found that as the grass height increases (bulk density was kept constant), the fire propagation mode changes from boundary layer to plume- or buoyancy-driven mode.

Sánchez-Monroy *et al.* (2019) conducted a validation study for WFDS (version compatible with FDS 6.0) for sloped fuel beds with no wind imposed through comparison with results obtained from laboratory experiments. In their laboratory-scale experiments (discussed in Section 2.2.1), they measured fire rate of spread and flame geometry. The results were then compared with numerical simulations using WFDS. Simulations were conducted with two of the fuel bed depths (7.62 and 15.24 cm) and with slope angles ranging from 0° to +45°; the domain height ranged from 1.68 to 6 m. They assessed two approaches to implement slope: (1) by changing the geometry of the fuel bed, (2) by modifying the gravity vector to mimic the effect of sloped terrain. They

found the first approach agreed with their observed experimental fire behaviour better than the second approach and hence selected the first approach to implement slope. *RoS* and flame characteristics (length, height, depth and angle) obtained from simulation outputs were analysed and compared with the experimental results (Section 2.2.1). The temperature contours (along the *x*–*z* plane of symmetry) and fire front shapes were analysed to study the plume attachment behaviour. The experimental trends were found to be replicated well by the WFDS simulations and proved that the model could reproduce the observed trends of fire behaviour.

Their simulation studies were performed on upslopes (only), with no driving wind velocity imposed at the inlet, and grid cell sizes of 1 to 2 cm were chosen in the simulations based on grid resolution studies. With a changed fuel bed geometry approach, their study had lateral wind entrainment to the fire (from the sides and underneath the ramp) and entertainment increased with increase in surface inclination.

2.4 Dynamic fire propagation

Dynamic fire propagation arises from the complex interaction between the terrain, the atmosphere and the fire, and the effects produced by dynamic fire propagation cannot be predicted by current operational fire spread models (Sharples 2017). Cruz and Alexander (2013) noted that one of the uncertainties associated with accurate prediction of fire spread rate is the dynamic mechanism associated with fire and the surrounding environment.

The empirical fire spread models are usually applied assuming a constant wind speed and hence predict a quasi-steady state fire spread rate (Taylor *et al.* 2004; Sharples *et al.* 2011). Taylor *et al.* (2004) examined fire spread and flame temperature in a series of crown fire experiments conducted in the Northwest Territories, Canada. This study was conducted to analyse the temporal and spatial variation in fire spread rate in relation to wind speed. Their observed rate of spread suggested that fire spread rate was highly variable in terms of both the time and distance scale (fires spreading over 75–100 m for 1.5–10 min). In the crown fire experiments, they observed considerable variation in rate of spread within a distance of 150 m over a period of 1.5–10 min. They noted that the variation in rate of spread (and hence fire intensity) may be of the same order of magnitude as the variation that would be expected over burning periods of 1 h and thousands of metres. They attributed this observed variation to the dynamic nature of fire behaviour.

Cruz and Alexander (2013) analysed and compiled 49 fire spread models datasets involving 1278 observations (mostly the *RoS* models derived from experimental fires) in seven different fuel type groups. The data covered a wide range of fuel species and fire propagation regime types (surface fires, crown fires). They analysed the models' performances in terms of predicting rate of fire spread against independent data derived from field observations to summarise their findings. A mean absolute percentage error of 42% under-prediction and 140% over-prediction were observed for *RoS* values obtained from fire spread models for grassland fires. They associated these uncertainties or discrepancies in predicting the *RoS* with the ineffectiveness of current empirical models to predict dynamic fire propagation.

The abovementioned experimental and statistics studies attributed the discrepancies in fire spread rate to the 'dynamic nature of fire', which they portray as a complex and ambiguous concept. Sharples (2017) pointed out that the operational models are developed with quasi-steady state assumptions, which may not be the case in real wildfire propagation, and this may be the reason for such differences between predictions and observations. The empirical models based on experimental studies assume that for a given set of input parameters, such as wind speed, relative humidity, temperature and fuel characteristics, a fire will exhibit a steady or constant rate of spread. The dynamic behaviour of fire and its ramifications on fire propagation are not quite accounted for in such empirical fire models (Sharples *et al.* 2011; Sharples 2017).

This 'dynamic behaviour of fire propagation' is a recent paradigm of research where researchers attempt to comprehensively capture the physical processes governing fire behaviour. This unsteady behaviour of fire spread occur because of a combination of different driving factors, such as, changes in vegetation and wind (direction and velocity) over time and slope of the terrain as fire spreads. Sharples *et al.* (2011) highlighted the role of environmental factors such as modification of fire weather conditions by the topography, and coupling between terrain, fire and atmosphere, that can significantly affect the dynamic nature of fire propagation. This result in the potential of fire to propagate laterally along certain terrain elements such as slope (Sharples *et al.* 2011).

Hilton *et al.* (2016) noted that the combination of various processes driving fire propagation (heat transfer mechanisms and transport of burning material) and their interactions with environmental conditions governs the dynamic variation of the fire front in shape and fire spread rate. They

conducted simulations using a two-dimensional computational method, the Level Set method (a conceptual framework for using level sets as a tool for numerical analysis of surfaces and shapes), to analyse the dynamic evolution of a wildfire's progression. They compared the fire curvature effect from the level set simulations with the fire isochrones from an experiment conducted in a large combustion wind tunnel known as the CSIRO Pyrotron (Sullivan *et al.* 2013).They found that inclusion of some aspect of fire perimeter shape for a given forward rate of spread can improve prediction of the dynamic nature of fire propagation and concluded that incorporating the dynamic effects in a computationally efficient way may lead to improved prediction capability for empirical models.

Sutherland *et al.* (2020) used WFDS to study the effect of ignition protocol on the development of grassfires. They used an identical domain size, configuration and grid resolution to that of Moinuddin *et al.* (2018). Simulations were performed with varied U_{10} wind velocities (2.7, 6.2 and 10.7 m.s^{-1}), ignition times and ignition line lengths. Two different ignition protocols – an inward ignition protocol and an outward ignition protocol – were used to study the effect of ignition protocol on fire spread behaviour. They considered the fire spread as dynamics and presented the *RoS* as a function of time and of distance by differentiating the fire front location data. They observed fluctuations (accelerations and decelerations) in fire spread rate that deviated from quasi-steady conditions that they attributed to dynamic behaviour of fire.

Moinuddin *et al* (2021) in their recent study using WFDS investigated the effect of relative humidity and fuel moisture content (M_c) on the rate of spread of grassfire as well as on the mode of fire propagation. The simulations were performed using fine grid resolution over a domain 960 m long, 640 m wide and 100 m high (with a 104 × 108 m burnable grass plot), at an inlet wind speed U_2 of 6, 4 and 3 m.s^{-1}. Four sets of simulations were performed: three sets with 210 mm tall grass and one set with 175 mm tall grass. They validated the WFDS simulations with Synthetic Eddy Methodology (SEM) and roughness, against the C064 field-scale grassfire experiment of Cheney *et al.* (1993) on a flat terrain and good agreement was observed. They measured both the quasi-steady and dynamic *RoS* values at different percentage moisture contents and compared the results against *RoS* values derived from empirical models in the literature. Overall, the simulated *RoSs* were found to be closer to the prediction of Cheney *et al.* (1998) compared to other

empririal models considered and the relationship between *RoS* and relative humidity (hence fuel moisture) was found to be linear.

These studies demonstrated that 'dynamic fire behaviour' have important consequences on understanding fire spread and obtaining accurate fire predictions. Therefore, it is important to investigate this aspect, which accounts for the coupling of fire, fuel, weather and topography, effectively.

2.5 Research gap

Most of the experimental studies found in the literature are at laboratory scale. Empirical models are computationally cheap to implement and require only few parameters, which make them user-friendly. However, empirical and semi-empirical models are by and large considered valid in the range of conditions in which they were developed (often in benign conditions) and are highly dependent on the conditions in which the source data were obtained for modelling (Cruz *et al.* 2017, Mell *et al.* 2018). The primary objective of operational (empirical) fire spread models is to predict the rate of spread of fire once it has reached a quasi-steady state and these models may not include the physical behaviour involved in fire spread, such as fire plume attachment (Sharples 2017) and the different modes of fire propagation (Apte *et al.* 1991, Mell *et al.* 2018). Furthermore, the combined effect of slope and wind on *RoS* is not well studied at field scales.

Again, in the literature, experimentally, the aspects of flame dynamics and preheating of virgin fuels ahead of the firefront via heat fluxes related to surface fire on slope were mostly investigated at laboratory scale. In some studies, aspects were studied theoretically. Furthermore, mode of fire propagation for this kind of fires has not been investigated in detail.

The 3D physics-based models have shown their capability in simulating real experimental wildfire cases. These models provide an insight into the dynamic behaviour of fire propagation (from pyrolysis, combustion and turbulence to smoke and heat transport) and operate under a wide range of conditions. These simulations can also be realiably used to investigate flame parameters, mode of fire propagation and radiative and convective heat transfer process. The information gained from these models helps in understanding the physics involved in fire propagation and helps to improve the empirical and semi-empirical fire models that are used by fire and emergency services (Mell *et al.* 2007, Hoffman *et al.* 2015, Hilton *et al.* 2016, Sharples 2017, Morvan *et al.* 2018,

Sutherland *et al.* 2020, Moinuddin *et al.* 2021). Owing to a lack of computational resources, many past field-scale physics-based modelling studies were not grid-converged.

The present study investigates the combined effect of slope (upslopes and downslopes) and driving wind on grassfire behaviour. Simulations are performed using the versatile physics-based model WFDS, a fully 3D model, which includes sub-models to capture the fire–fuel and fire–atmospheric interactions. WFDS includes fire propagation through vegetative fuel such as trees, grasslands and shrublands and has been rigorously validated for various scenarios including surface fires propagating in grassland. This study follows the same WFDS model used by Moinuddin *et al.* (2018) on flat terrain at field scale under different driving wind velocities and Sánchez-Monroy *et al.* (2019) on slope (but no wind condition) at laboratory scale. Driving wind velocities of 0.1, 1, 3, 6 and 12.5 $m.s^{-1}$ are applied at the inlet for each of the slope angles. Moreover, the simulations are conducted at field scale with fine grid resolutions and an appropriately developed wind field. Furthermore, this study follows the new paradigm of research, 'dynamic fire behaviour', attempting to capture the physical processes governing fire propagation. Gravity vector approach is used to implement slope (which saves computational time) and therefore does not include a lateral wind entertainment scenario. In this study, an idealised slope situation is considered. We understand that the situation may be complex in a real fire scenario, with potentially the existence of different physical behaviour on different segments of sloped terrain and that furthermore the velocity range may also alter the physical behaviour of a fire.

Chapter 3. Model description and methodology

3.1 Overview of FDS/WFDS modelling

The physics based WFDS model includes sub-models in its multi-phase modelling approach: a fuel (vegetation) sub-model, thermal degradation (pyrolysis) sub-model, combustion sub-model, hydrodynamics/turbulence sub-model and heat transfer sub-model. This is illustrated in Figure 3.1.

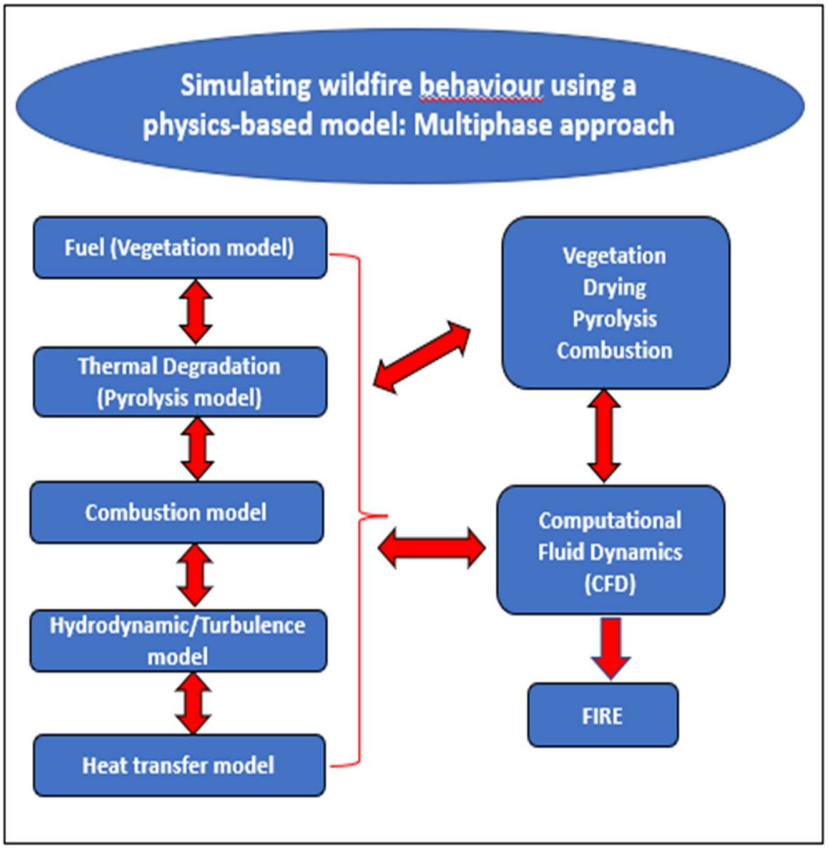

Figure 3.1 – Sub-models used in FDS/WFDS; courtesy, Morvan and Dupuy (2004)

Numerical methods of CFD are employed in each of these sub-models to solve the equations governing the conservation of momentum, mass and energy, pyrolysis, and gas-phase combustion and heat transfer equations. Once the domain is divided into cells, the differential form of the governing equations (partial differential equations, PDEs) is discretised at each cell to generate a large system of algebraic equations. These equations (approximated using second-order finite differences on a collection of three-dimensional grids) are numerically solved to obtain the values

of all the required variables at all the cell centres with the application of initialisation and boundary conditions. For simulations that use multiple meshes, the equations are processed in parallel using Message Passing Interface (MPI) libraries.

An overview of the relevant equations used in the modelling of mass, momentum and energy transport are discussed in the sections below. Absolute details of every equation can be found in (Mell *et al.* 2009, McGrattan *et al.* 2015, Perez-Ramirez *et al.* 2017, Sánchez-Monroy *et al.* 2019).

It should be noted that hydrodynamic/turbulence modelling transposes many of the governing equations. There are two main modelling techniques used in the numerical simulation of turbulence in WFDS, which are direct numerical simulation (DNS) and the Large Eddy Simulation (LES). These are briefly discussed here.

DNS is a numerical method where all turbulence scales (eddies) are resolved by numerical methods. It is a very successful research tool to provide in-depth information that is difficult to obtain through experiment; however, DNS requires vast computational resources. A very fine numerical grid size of the order of < 1 mm is required in the DNS approach for fire modelling. Hence, this method is limited to flows with a low Reynolds number and simple geometries and is suitable to model fundamental fluid and/or heat flows, and very small-scale combustion.

By default, WFDS uses LES methodology to model turbulence. LES spatially filters the momentum equation, resolves larger eddies during numerical simulations and models the effects of smaller eddies on larger eddies. The large range of length scales involved in modelling the behaviour of bushfires presents severe challenges because they cannot all be resolved. To overcome this, LES captures the features of large eddies in the flow and the effects of the smallest structures in the flow on large eddies are approximated. As a result, the variables appear as filtered variables. LES modelling is detailed in Section 3.2.2.2.

3.2 Governing equations

3.2.1 Conservation of mass (continuity equation) and species

In the FDS/WFDS model, density is solved by the conservation of mass or continuity equation by modelling the mass and species transport. The combustion process in fire involves multiple fuel gases; however, to make the computation process fast and effective, six gaseous species (fuel, O_2,

CO_2, H_2O, CO, N_2) and soot particles are tracked in the process. FDS solves the mass density of each species. The mixture mass density is then obtained by the summation of each species' density. If multiple fuels and products are formed, they are grouped together as a 'lumped species' and the transport equation for each of the lumped species has the same form as the transport equation for a single species (Wadhwani 2019).

The species equation is:

$$\frac{\partial(\rho Y_i)}{\partial t} + \nabla \cdot (\rho \overline{U} Y_i) = \nabla \cdot (\rho D_i \nabla Y_i) + \dot{w}_i , \quad (3.1)$$

where Y_i and D_i are the mass fraction and diffusion coefficient of the ith specieIhere i = 1,2,3 ... *Ns,* ρ = density, t = time, $\overline{U}$ = filtered velocities $\bar{u}_i$ $(\bar{u}, \bar{v}, \bar{w})$ in $\bar{x}_i$ directions, respectively, and $\dot{w}_i$ = production rate of ith species during combustion.

The mass density is obtained from eqn (3.2):

$$\rho = \Sigma \rho_i Y_i . \quad (3.2)$$

The summation of species equation over all *Ns* species gives the mass or continuity equation:

$$\frac{\partial \rho}{\partial t} + \nabla . \rho \overline{U} = \Sigma \dot{w}_i , \quad (3.3)$$

where the term $\frac{\partial \rho}{\partial t}$ describes the rate of change of mass or density change with time. The second term $\nabla . \rho \overline{U}$ defines the net mass flow through the surface of the computational cell and $\dot{w}_i$ is the production rate of the ith species during combustion.

3.2.2 Conservation of momentum and turbulence sub-models

In WFDS, hydrodynamic/turbulence modelling includes the modelling of conservation of momentum, based on the momentum equation (also known as the Navier–Stokes equation).

3.2.2.1 Momentum equation

The momentum equation is:

$$\frac{\partial \rho \overline{U}}{\partial t} + \nabla . (\rho \overline{U} \overline{U}) = -\nabla \bar{p} + \nabla . \tau_{ij} + \rho g + \nabla . \tau_{turb} + f_b . \quad (3.4)$$

The left-hand side terms represent the change in momentum and inertial forces and the right-hand side denotes forces from pressure, viscous shear stress, gravity and filtered turbulence.

In eqn (3.4), ρ = density, g = gravity, $\bar{p}$ = filtered background pressure, τ_{ij} = viscous stress tensor (defined in eqn (3.5)), τ_{turb} = filtered turbulence (defined in eqns (3.7) – (3.10)) and f_b = any external force vector except gravity; the influence of the grass fuel bed on the wind is approximated by a drag force (in the first grid cell above the boundary) as a function of the drag coefficient:

$$\tau_{ij} = \mu\left(2\overline{S_{ij}} - \frac{2}{3}(\nabla.\bar{U})\delta_{ij}\right), \tag{3.5}$$

where μ = molecular viscosity of the fluid, $\overline{S_{ij}}$ = strain rate tensor (defined in eqn (3.6)) and δ_{ij} = Kronecker delta, which = 1 when $i = j$; otherwise 0, and

$$\overline{S_{ij}} = \frac{1}{2}\left(\frac{\partial \bar{u}_i}{\partial x_j} - \frac{\partial \bar{u}_j}{\partial x_i}\right). \tag{3.6}$$

3.2.2.2 Turbulence sub-model

The LES sub-model incorporates the turbulence effect in the simulation where large-scale motions are resolved, and the smaller-scale motions are modelled with an eddy viscosity approach. That is, the diffusive action of unresolved turbulent motion acts like an additional viscosity term. Models such as the Smagorinsky model (used as the default in previous editions of FDS/WFDS) (Samgorinsky 1963), and Deardorff turbulence model (Deardorff 1972) filter the small-scale eddies during the numerical simulation by time- and spatial-averaging. In Version 6 of FDS (McGrattan *et al.* 2013), the default LES model is based on the Deardorff turbulence model (Deardorff 1972), with the turbulence τ_{turb} (filtered turbulence; sub-grid-scale Reynolds stress) defined as per eqns (3.7) – (3.10):

$$\tau_{turb} = \mu_{turb}\left(2\overline{S_{ij}} - \frac{2}{3}(\nabla.\bar{U})\delta_{ij}\right), \tag{3.7}$$

$$\mu_{turb} = \rho C_v \Delta\sqrt{k_{sgs}}\,, \tag{3.8}$$

$$k_{sgs} = \frac{1}{2}((\bar{u} - \hat{\bar{u}})^2 + (\bar{v} - \hat{\bar{v}})^2 + (\bar{w} - \hat{\bar{w}})^2)\,, \tag{3.9}$$

$$\Delta = (\delta x.\delta y.\delta z)^{\frac{1}{3}}\,, \tag{3.10}$$

where μ_{turb} = turbulent viscosity of the fluid, $\overline{S_{ij}}$ = strain rate tensor (defined in eqn (3.6)), k_{sgs} = sub-grid kinetic energy. $\bar{u}$ is the average value of u at the grid centre (representing the LES filtered velocity at length scale Δ, the filter scale), $\hat{\bar{u}}$ = weighted average of $\bar{u}$ over the adjacent

cells (representing a test-filtered field at length scale 2Δ), and similarly for $\hat{\tilde{v}}$ and $\hat{\tilde{w}}$. In the above equations, C_v = 0.1 is a constant coefficient and Δ is the filter scale.

The flows encountered in bushfiresare highly turbulent. In WFDS, there are two ways by which realistic turbulence can be generated for windfields; (1) by creating a perturbation or tripping near the inlet (as done in Moinuddin *et al.* (2018) and (2) the Synthetic Eddy Method (SEM), introduced by (Jarrin.N *et al.* 2006). Using SEM, an inlet turbulent profile can be implemented. SEM views the turbulence as a superposition of coherent structures. To calculate fluctuating component in the boundary conditions for the velocity field, a number of coherent structures are introduced in the computational domain and are defined by a shape that encircles the structure's spatial and temporal characteristics (Jarrin.N *et al.* 2006). 'Eddies' are injected into the flow at random positions on the boundary and emerge with the mean flow over a short distance near the boundary equivalent to the maximum eddy length scale. Once the eddy passes through this region, it is recycled at the inlet of the boundary with a new random position and length scale. The eddies are idealised as velocity perturbations over a spherical region in space with a diameter (eddy length scale) selected from a uniform random distribution. The selection procedures guarantee that prescribed first- and second-order statistics (including Reynolds stresses) are satisfied (Jarrin.N *et al.* 2006). SEM requires shorter ground to travel to generate realistic ABL, before the ignition line. Therefore, in this study we used SEM to generate a turbulent windfield.

In the present study, the turbulence effect in the simulations is modelled using the default Deardorff LES technique, which is simple but reliable and a computationally better model to be used for large field-scale grassfire simulations. Turbulence is introduced at the domain inlet using SEM. The parameters (characteristic length scale, number of eddies, velocity scale/fluctuations) used to invoke the eddies are shown in the input file of one of the simulations in Annexure B.

3.2.3 Modelling of conservation of energy

FDS does not explicitly solve the energy conservation equation (McGrattan *et al.* 2015) owing to a low Mach number approximation. For computational simplicity, FDS solves energy conservation implicitly by coupling the ideal gas equation for temperature and Poisson equation for pressure. The ideal gas equation is:

$$\overline{p} = \frac{\rho RT}{\bar{W}}, \tag{3.11}$$

where $\overline{p}$ = filtered background pressure, R = molar gas constant, 8.3145 kJ.kmol^{-1}.K^{-1}, T = vegetation surface temperature (K) and $\overline{W}$ = molecular weight of gas species (kg.kmol^{-1}).

The spatially and temporally resolved pressure, p, can be broken down into a 'background' pressure $\overline{p}(z,)$ and a 'perturbation' pressure $\tilde{p}(x,y,z,t)$. z is the spatial coordinate in the direction of gravity, which includes the stratification of the atmosphere in the background pressure. The fluid motion is driven by perturbation, $\tilde{p}$. The low Mach approximation relates the internal energy, e, and enthalpy, $ħ_s$, in terms of thermodynamic (background) pressure as shown in eqn (3.12).

$$ħ_s = e + \frac{\overline{p}}{\rho} \tag{3.12}$$

The energy conservation equation in WFDS may then be written in terms of the enthalpy, $ħ_s$.

$$\frac{\partial}{\partial t}\left(\rho ħ_s\right) + \nabla.\left(\rho ħ_s \overline{U}\right) = \frac{D\bar{p}}{Dt} + \dot{q}''' - \dot{q}_b''' - \nabla.\dot{q}'' \tag{3.13}$$

The term $\dot{q}'''$is the heat release rate per unit volume from a chemical reaction. The term $\dot{q}_b'''$ is the energy transferred to sub-grid-scale droplets and particles. The term $\dot{q}''$ represents the conductive, diffusive and radiative heat fluxes:

$$\dot{q}'' = -k\nabla T - \sum_\alpha ħ_{s,\alpha}\rho D_\alpha \nabla Z_\alpha + \dot{q}r'' \,, \tag{3.14}$$

where k is the thermal conductivity of species and D_α is the diffusivity of species α.

The Poisson equation for pressure is:

$$\nabla^2 H = -\frac{\partial(\nabla.\overline{U})}{\partial t} - \nabla.F \,, \tag{3.15}$$

where

$$F = -\overline{U}\times\omega - \tilde{p}\,\nabla\left(\frac{1}{\rho}\right) - \frac{1}{\rho}\left[(\rho-\rho_0)g + f_b + \nabla.\tau_{ij}\right], \tag{3.16}$$

$$\mathrm{H} = (\bar{p} + \tilde{p} - \rho g h_s), \tag{3.17}$$

where h_s = the height from ground level (m), g = gravitational acceleration (m.s^{-2}), F = momentum flux, ω = vorticity, ρ = instantaneous density (kg.m^{-3}) and ρ_0 = density at the initial temperature (kg.m^{-3}), $\overline{p}$ = filtered background pressure, $\tilde{p}$ = pressure perturbation, f_b = external force vector excluding gravity, and τ_{ij} = viscous stress tensor (Pa).

3.2.3.1 Gas-phase radiative heat transfer sub-model

The radiation transport equation (RTE) is solved using a Finite Volume heat transfer method based on (Raithby and Chui 1990). It consists of a set of complicated equations. Only the final form of the radiation transfer equations is given by eqn (3.18) and eqn (3.19). More details can be found in (McGrattan 2006, Mell *et al.* 2009, McGrattan *et al.* 2015, Perez-Ramirez *et al.* 2017, Sánchez-Monroy *et al.* 2019).

$$\hat{\mathrm{S}}.\nabla\bar{\mathrm{I}}(x,\hat{\mathrm{s}}) = Kr\,[\mathrm{I_b}(\check{\mathrm{T}}) - \bar{\mathrm{I}}(x,\hat{\mathrm{s}})] + K\mathrm{r_{b,e}}\,[\mathrm{I_b}(\mathrm{T_e}) - \bar{\mathrm{I}}(x,\hat{\mathrm{s}})]\,. \tag{3.18}$$

Integrating the RTE (eqn 3.18) over all solid angles gives the equation for conservation of radiant energy:

$$\begin{aligned}\nabla.q_{\mathrm{r}}(\mathrm{x}) &= Kr\,[4\pi\mathrm{I_b}(\check{\mathrm{T}}) - \check{\mathrm{U}}_{(\mathrm{x})}] + K\mathrm{r_{b,e}}\,[4\pi\mathrm{I_b}(\mathrm{T_e}) - \check{\mathrm{U}}_{(x)}]\,, \\ &= Kr\,[4\pi\mathrm{I_b}(\check{\mathrm{T}}) - \check{\mathrm{U}}_{(\mathrm{x})} + (\nabla.q_{r:b})v_b\end{aligned} \tag{3.19}$$

The second term in eqn (3.19) is the radiation heat transfer term. $Kr_{b,e}$ is the radiation absorption coefficient ($\mathrm{m^{-1}}$) due to sub-grid vegetation (eqn (3.20))

$$K_{b,e} = \frac{\sigma\beta_s}{4}\,, \tag{3.20}$$

where spectral $\bar{\mathrm{I}}(x,\hat{\mathrm{s}})$ = spectral radiation intensity, $\mathrm{I_b}(x,\hat{\mathrm{s}})$ = blackbody radiation intensity, Kr = radiative absorption coefficient (function of mass fraction and temperature of given mixture of participating gaseous species), $\check{\mathrm{U}}$ = integrated radiation intensity ($\mathrm{W.m^{-2}}$), q_{r} = radiative heat flux vector ($\mathrm{kW.m^{-2}}$), and $\hat{\mathrm{s}}$ = unit vector in the direction of radiation intensity, $\mathrm{T_e}$ = Temperature of the thermally thin fuel elements in gas phase, σ = surface-to-volume ratio and β_s = packing ratio of the fuel particles.

A large number of validation and verification tests have been conducted to test the radiation solver and the overall FDS modelling system into which WFDS is integrated (Mell *et al.* 2009). FDS uses approximately 100 discrete angles for the gas phase (McGrattan *et al.* 2013). The most important radiation parameter is the fraction of energy released from the fire as thermal radiation, commonly referred to as the radiative fraction. The simulations conducted in the present study describe the radiative fraction (radiation loss) as 35% (default value) (McGrattan *et al.* 2013).

3.2.4 Fuel (vegetation) sub-models

There are two ways of modelling vegetative fuels (such as trees, grasses, decorative plants) in FDS/WFDS, namely the FE (Fuel Element) and BF (Boundary Fuel) models.

The Fuel Element (FE) model is used for vegetation that occupies a specified volume (raised fuel) such as trees. This requires sufficient gas-phase grid resolution that temperature gradients and conjugate heat transfer between the gas and solid phases in the bulk fuel bed are resolved (Moinuddin *et al.* 2018). In this method, the interaction between the two phases is represented using volume source/sink terms in mass, energy and momentum balance equations. The FE model requires finer grids to achieve numerically converged solutions.

The Boundary Fuel (BF) model is used for surface fuels such as grasslands (Mell *et al.* 2007). In the BF method, the energy conservation for the vegetative fuel layer is solved in its own computational grid, which interfaces with the computational grid of the gas phase. In this case, the interactions between the two phases (i.e. solid fuel layer and surrounding atmosphere) are limited to heat and mass flow at the interface between the two phases (Wadhwani 2019). The BF model uses a separate vertical computational grid, resulting in vertical conductive heat transfer in the thermally degrading fuel bed. It is to be noted that this assumption is mainly valid at the heading fire front, and less along the flank fires where the heat exchanges between the gas phase and the solid phase might not be unidimensional. The horizontal grid is the same as the gas phase. The assumptions leading to the BF model are most consistent with large fires for which the majority of the heat release occurs above the fuel bed, resulting in predominantly vertical radiant heat transfer in the thermally degrading fuel bed (Moinuddin *et al.* 2018).

The BF model is computationally less intensive owing to the coarser gas-phase grid (Mell *et al.* 2007, McGrattan *et al.* 2013). The BF method is used for large-scale wildfire modelling and is available in FDS/WFDS model versions. This method is typically used to describe surface fuel (vegetation) for wildfire simulation as this method defines thermally thin vegetation that does not need to be resolved (Morvan and Dupuy 2004). Again, the BF model is a validated method for grassland fire simulations (Moinuddin *et al.* 2018). Therefore, following Moinuddin *et al.* (2018), the Boundary Fuel (BF) vegetation sub-model is used in this study to model the vegetation.

3.2.5 Pyrolysis (thermal degradation) sub-models

There are two thermal degradation (pyrolysis) sub-models used in FDS, which are derived based on empirical studies. They are called the Linear and Arrhenius models. Each degradation model can be used with each vegetation model and hence four different implementations can be simulated.

The Linear model assumes a two-stage endothermic thermal decomposition: water evaporation and then solid fuel pyrolysis. The equation for water evaporation is:

$$\dot{m_{vap}} = \frac{\dot{Q_{net}}}{\Delta h_{vap}}, \qquad \text{when } T_s = 373 \text{ K}, \tag{3.21}$$

where T_s is the vegetation surface temperature, $\dot{m_{vap}}$ is the evaporation rate, Q_{net} is the net energy (convection plus radiation) on the fuel surface and Δh_{vap} is the latent heat of evaporation. The temperature-dependent mass loss rate expression of (Morvan and Dupuy 2004) is used to model the solid fuel degradation. This model assumes that the pyrolysis begins at T_0 and terminates at T_1. The equation for pyrolysis rate is:

$$\dot{m_{pyr}} = \frac{\dot{Q_{net}}}{\Delta h_{pyr}} \; x \; \frac{T_s - T_0}{T_1 - T_0}, \qquad if \; T_0 \leq T_s \leq T_1, \tag{3.22}$$

where $\dot{m_{pyr}}$ is the pyrolysis rate and Δh_{pyr} is the heat of pyrolysis (also known as heat of reaction). In this study, T_0 and T_1 are taken as 400 and 500 K, respectively, following (Morvan and Dupuy 2004). The solid fuel is represented as a series of layers that are consumed from the top down until the solid mass reaches a predetermined char fraction. At this point, the fuel is considered consumed. Char oxidation is not accounted for in these simulations. This is because significant char oxidation occurs only at material temperature much greater than that achieved in these simulations.

In the second model, the Arrhenius approach, moisture loss and vegetation degradation are based on Arrhenius expressions as used in (Morvan and Dupuy 2001). The reaction equations obtained from Arrhenius expressions cover three stages: water evaporation, pyrolysis and char oxidation. In this model, drying and pyrolysis occur according to a three-step mechanism: (1) endothermic drying reaction; (2) endothermic global pyrolysis reaction; and (3) exothermic global char oxidation reaction. The Arrhenius equation involves three kinetic parameters in pyrolysis: pre-

exponential factor A (s^{-1}), activation energy E ($kJ.mol^{-1}$) and reaction order n. The Arrhenius model detailed equations can be found in (Morvan and Dupuy 2001, Porterie *et al.* 2005, McGrattan *et al.* 2015).

Compared with the Linear model, the Arrhenius model requires significantly more user-supplied parameters that are difficult to measure accurately for wildland fuels, and these parameters vary considerably with species (Moinuddin *et al.* 2018). With the Linear model, ignition and sustained burning occur over a lower gas-phase temperature range and, hence, coarser gas-phase grid resolutions may be sufficient. Hence, following (Moinuddin *et al.* 2018), the Linear pyrolysis sub-model is used to model the thermal degradation of vegetation (pyrolysis) in a boundary fuel (BF) vegetation model. The physical and thermal parameters of fuel used in this study (with a Linear pyrolysis sub-model and a boundary fuel vegetation model) are mentioned in the Section 4.2.

3.2.6 Heat transfer to solid fuel

To compute the temperature and reaction inside solids, WFDS solves a one-dimensional heat transfer equation numerically. The heat transfer sub-models used in FDS/WFDS are: the one-dimensional conductive heat transfer model, simple convective heat transfer model and radiative heat transfer model.

The modelling of solid objects in FDS is presented in detail in (McGrattan 2006, McGrattan *et al.* 2015). A brief description of the modelling of the one-dimensional heat transfer equation for solid fuel in a vegetative fuel bed (fine wildland fuels such as grass, shrubs are considered thermally thin fuel) at surface temperature T_s is given by eqn (3.23) (Moinuddin *et al.* 2021):

$$\beta_s \rho_s c_s \frac{\partial T_s(x,y,z,t)}{\partial t} = -\nabla . \dot{q}''_{sr} - \nabla . \dot{q}''_{sc} - \dot{Q}'''_{s,vap} - \dot{Q}'''_{s,kin}, \quad (3.23)$$

where β_s = packing ratio, ρ orρ_s = density, c_s = specific heat of the fuel, $\nabla . \dot{q}''_{sr}$ = divergences of the thermal radiation and $\nabla . \dot{q}''_{sc}$ = divergences of the convective heat fluxes, on the solid fuel elements within the bulk vegetative fuel bed, $\dot{Q}'''_{s,vap}$= endothermic effect of vaporisation of moisture (related to eqn (3.21)), $\dot{Q}'''_{s,kin}$ = contribution of heats (endothermic and exothermic) associated with the thermal degradation/pyrolysis of the solid (related to eqn (3.22)).

The radiative heat flux $\dot{q}_r''$ can be found by estimating the absorption coefficient, κ_b, of the bulk fuel bed, which is related to field measurements of the average surface-to-volume ratio,σ, and packing ratio, β_s, of the fuel particles.

$$\kappa_b = \frac{1}{4}\beta_s\sigma = \frac{1}{4}\frac{w_s\sigma}{\rho_s h_s}, \tag{3.24}$$

where w_s, h_s are the fuel bed loading and fuel bed height, and ρ_s = density of fuel.

$\nabla.\dot{q}_{sr}''$ in eqn (3.23) is the second term (radiation heat transfer term) of the right-hand components of eqn (3.19). The convective heat transfer, $\dot{q}_s''$, of twig, grass, or other materials is obtained using an empirical correlation (involving σ_s, the conductivity of air and β_s, the packing ratio), where the fuel particles are modelled as a collection of cylinders:

$$\nabla.\dot{q}_{sc}'' = \beta_s\sigma_s\, h_c\, \Delta T\,, \tag{3.25}$$

where h_c is the convective heat transfer coefficient ($Wm^{-2}.s^{-1}$), ΔT is the difference between the vegetation and the gas temperature (taken at the centre of the grid cell abutting the boundary fuel surface). h_c is calculated as shown in eqn (3.26) (Porterie *et al.* 1998):

$$h_c = 0.5\, k(T_g)\frac{0.683(Re)^{0.687}}{2/\sigma_s}, \tag{3.26}$$

where $k\,(T_g)$ is the thermal conductivity of the gas as a function of gas temperature, and the Reynolds number (R_e) is calculated as per eqn (3.27), where ρ_g is the gas density and μ is the molecular viscosity.

$$R_e = \frac{4\rho_g\sigma_s}{\mu}. \tag{3.27}$$

3.2.7 Combustion sub-models

Combustion can be modelled in two ways: 'finite rate' and 'mixing controlled' approaches. By default, the mixing-controlled method is used in WFDS where the reaction of fuel and oxygen is infinitely fast and controlled only by mixing. In the present study, the default and commonly used mixing controlled combustion sub-model is used. The second method consider that the reaction is finite rate. The approach usually requires very fine grid resolution that is not practical for large-scale fire applications such as wildfire modelling. The finite rate approach is not discussed in this study and more details on this method can be found in (McGrattan *et al.* 2013).

In the mixing-controlled method, infinitely fast mixing control reactions occur where the single fuel species (composed primarily of C, H, O and N) reacts with O_2 to form H_2O, CO_2, Soot and CO. The FDS/WFDS inbuilt empirical calculations determine the rate of mixing of fuel and oxygen within a given mesh cell, at a given time step, wherein only the mixed composition can react within each computational cell (McGrattan *et al.* 2013). Eqn (3.28) shows the reaction formulae.

$$C_xH_yO_zN_v + a_{O_2}O2 \rightarrow a_{CO_2}CO_2 + a_{H_2O}H_2O + a_{CO}CO + a_sSoot + a_{N_2}N_2 \qquad (3.28)$$

FDS/WFDS calculate the stoichiometric coefficients, a_{CO_2}, a_{H_2O}, a_{CO}, a_s and a_{N_2}, automatically from the chemical formula of the fuel along with the yields of CO and soot, and the volume fraction of hydrogen in the soot (McGrattan *et al.* 2013). FDS/WFDS regulates the rate at which the fuel and oxygen mix within a given mesh cell at a particular time step. The unmixed fraction of fuel is represented by a variable ζ, ranging from zero to one, at every time step, and is represented by eqn (3.29):

$$\frac{d\zeta}{dt} = -\frac{\zeta}{\tau_{mix}}, \qquad (3.29)$$

where τ_{mix} = mixing time scale. By default, if the cell is initially unmixed, the combustion is considered as non-premixed and ζ is taken as 1, whereas if the cell is initially mixed, the combustion is considered as premixed and ζ is taken as 0. The amount of combustion products (CO_2, H_2O, CO and soot) formed is determined by using the chemical formation of the fuel. The heat release rate per unit volume, $\dot{q}'''$, is derived by adding the species' (combined) mass production rates multiplied by their corresponding heat of formation.

$$\dot{q}''' = -\sum_{\alpha} \dot{m}_{\alpha}''' \ \Delta H_{f,\alpha}, \qquad (3.30)$$

where $\dot{m}_{\alpha}'''$= lumped species mass production, $\Delta H_{f,\alpha}$ = heat of formation for α^{th} species.

3.3 Summary

In this chapter, the underlying physics, chemistry and governing equations used in FDS/WFDS model and the sub-models that are explicitly applied in the simulations conducted in this study were discussed. In summary, a linear pyrolysis sub-model was adopted to model the thermal degradation of vegetation with a boundary fuel/vegetation method. The turbulence effect was

modelled using the default Deardorff LES technique with turbulence introduced at the domain inlet using SEM. The specific radiative and convective sub-models developed for vegetative fuel were used to model the heat transfer and default mixing-controlled sub-model was used to model the combustion.

Chapter 4. Grassfire propagation on sloped terrains at higher wind velocities

This chapter discusses and analyses the simulations conducted at different slope angles (both upslopes and downslopes), with higher and medium nominal driving wind velocities (U_{10}) of 12.5, 6 and 3 m.s^{-1}. Section 4.1 includes the numerical implementation detailing the simulation set-up; Section 4.2 present the parameters and variables used in the simulations; Section 4.3 discusses the sensitivity studies, model reliability and accuracy; and Section 4.4 presents the list of simulations conducted in this study followed by the results, detailed analysis, and discussion.

4.1 Simulation set-up

The model is set up in a rectangular block of 360 × 120 × 60 m dimensions as shown in Figure 4.1. A burnable grass plot (dark green region) of 80 m × 40 m is chosen, with a line fire set up at the beginning of this section. For higher upslopes, +30°, +25° at 12.5 m.s^{-1} and +30° at 6 m.s^{-1}, the simulations are repeated with longer grass plot of 120 m × 40 m section.

The distance of the ignition line from the inlet is 160 m, the bordering subdomains (both sides) are 80 m (40 m on each side) and the distance from the burnable grass plot to the outlet is 120 m.

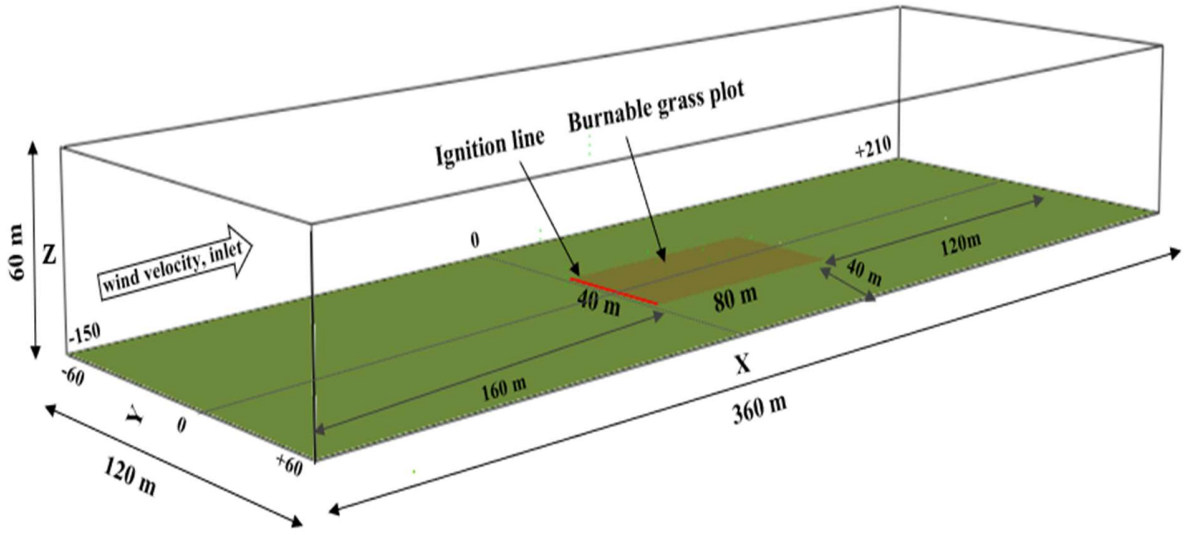

Figure 4.1 – Geometry of the domain: size 360 × 120 × 60 m with burnable grass plot 80 × 40 m (dark green region)

To model the wind field development at the inlet of domain (*YZ* plane at $X = 0$), a wall of wind boundary condition is applied, which follows a 1/7 power law model (Mell *et al.* 2007). The velocity profile in a turbulent boundary layer is often approximated by the 1/7th power law equation (normalised wind speed vs fuel height).

$$\frac{U_Z}{U_H} = \left(\frac{z}{Z_H}\right)^{\alpha}, \tag{4.1}$$

where U_Z is the wind speed (in m.s^{-1}) at height Z (in m) and U_H is the known wind speed at a reference height Z_H (reference height is fixed to be equal to 10 m). The exponent α is an empirically derived coefficient that varies depending upon the turbulence. Following Morvan et al. (2013), for neutral stability conditions (corresponding to the situation encountered above bare soil), the power law coefficient is approximately 1/7 or 0.143. This is termed as *PLE*=0.143 in the simulation script, as shown in the input file of one of the simulations presented in Annexure B.

Wind speeds of 12.5, 6 and 3 m.s^{-1} at 10-m height are applied at the inlet (corresponding to 11.9, 5.6 and 2.8 m.s^{-1}, respectively, prior to the ignition line). In this study, we endeavour to obtain an appropriately developed wind field above the grassland within the simulated domain. The geometric centre line axis y = 0 and x = 0 are as shown in Figure 4.1. At the inlet (YZ plane at X = –150 m), a wall of wind boundary condition is applied, which follows a 1/7 power law (velocity vs height) with wind speeds of 12.5, 6 and 3 m.s^{-1} at 10 m height. The 'Open' boundary condition is applied at top (XY plane at Z = 60 m) and outflow (YZ plane at X = +210 m) while symmetry boundary conditions are applied on both the left (ZX plane at Y = –60 m) and right side (ZX plane at Y = +60 m) of the domain. The bottom (XY plane at Z = 0) is considered as the solid ground.

As detailed in methodology Sections 3.2.4 and 3.2.5, a linear pyrolysis sub-model is used with a boundary fuel (BF) vegetation model, where ground vegetation is modelled like a porous solid with thickness equal to the height of the vegetation. In the default LES approach, turbulence is introduced at the domain inlet using the SEM proposed by Jarrin.N *et al.* (2006), as detailed in section 3.2.2.2. Synthetic turbulence is invoked in the simulations by setting up the characteristic eddy length scale (L_EDDY), number of eddies (N_EDDY, obtained by dividing the area of domain inlet (m^2) by square root of L_EDDY) and the root mean square (RMS) velocity fluctuation (VEL_RMS) in the script, as shown in the input file of one of the simulations (Annexure B).

The radiative fraction or radiation loss is described as 35%. Further, a sand-grain roughness, the roughness height that gives the same actual resistance coefficient as that caused by real non-uniform wall roughness, (h_r), of 0.9 m is used for the grass top surface. Stull and Arhens (2000) suggested 0.03 m as the aerodynamic roughness (z_0) for grass prairie and farm fields. The FDS User Guide (McGrattan *et al.* 2013) recommended that:

$$h_r = 30 z_0 \tag{4.2}$$

The size of the mesh cells throughout the grass height is automatically chosen using a rule that makes cell sizes smaller than the square root of the material diffusivity. By default, finer grid cells are selected on the gas and solid phase interface and coarser grid cells are selected at the solid phase.

The fuel considered is grass, which is classified in Australian Standards AS3959 (AS3959 2018) as 'near-surface and surface fuel layers vary from few centimetres up to 0.6 m in height'. The slope is implemented in the simulations by changing the magnitude of components of gravitational force in the *x*- and *z*-directions. FDS/WFDS has a provision to specify the gravitational components in the simulation, which allows a new orientation to the gravity vector in the momentum equation. The gravitational components in the *x* and *z* directions are obtained by multiplying the magnitude of the gravity vector (9.81 $m.s^{-2}$) with the sine and cosine of the slope angle, respectively. The Y direction has been left out because there is no Y variation in the gravity vector. (McGrattan *et al.* 2013).

Once the flow field is fully developed, a prescribed line fire of 1000 $kW.m^{-2}$ is ignited. The ignition fire is 40 m wide and 1 m deep, aligned with the leading edge of the burnable grass width as shown in Figure 4.1. (Sutherland *et al.* 2020) used 4 s of ignition duration and the present study used 10 s to ensure that the line was adequately ignited.

4.2 Parameters and variables

Experimentally measured parameters are used as inputs to the simulations. These [inputs] are the thermo-physical, pyrolysis and combustion parameters, measured from various experimental studies. The details of vegetation, thermo-physical properties of the fuel and other input parameters are shown in Table 4.1.

Fuel considered is kerosene grass (Eriachne burkittii), a type of grass found in the Northern Territory, Australia. In the simulations, this grass is represented by its thermo-physical properties. Moinuddin *et al*. (2018) conducted a validation of a fire propagation experiment involving this type of grass. They used WFDS version compatible with FDS 6.0 (McGrattan *et al. 2015)* on flat terrains, firstly to achieve grid and domain convergences alongwith fully developed wind field, then to validate against Australian grassland experiment C064. They found that at four instances of times, experimental and simulated isochrones matched quite well in terms of location, pattern and head fire widths.

The values of some of these parameters are taken from Mell *et al.* (2007), based on the experimental studies of Cheney *et al*. (1993*),* Cheney and Gould (1995). The thermo-physical properties used here follow Moinuddin *et al*. (2018), which were chosen to match the C064 grassfire experimental studies of Cheney *et al*. (1993). Following Moinuddin *et al.* (2018), char fraction, heat of combustion, heat of pyrolysis and soot yield were selected to match recent measurements of cellulosic fuel. Physical properties of the vegetation layer include the fuel load, fuel density, height of vegetation, surface-to-volume ratio, fuel moisture content and relative humidity**.**

Table 4.1: Thermo-physical, pyrolysis and combustion parameters for grassfire modelling

Input parameters	**Values used**	**Source and reason**
Fuel - grass		Grass type: kerosene (Eriachne burkittii) Cheney *et al.* (1993), Mell *et al.* (2007), Moinuddin *et al*. (2018)
Heat of combustion	16,400 $kJ.kg^{-1}$	Bluestem grass (Overholt *et al.* 2014)
Soot yield	0.008 $g.g^{-1}$	White pine (Australian radiata pine) (Abu Bakar 2015)
Vegetation drag coefficient	0.125	Assuming vegetation elements are spherical (Morvan and Dupuy 2004)
Vegetation load	0.283 $kg.m^{-2}$	Experimental, Cheney *et al.* (1993), Cheney and Gould (1995)
Vegetation height	0.21 m	Experimental, Cheney *et al.* (1993), Cheney and Gould (1995)
Vegetation moisture content	0.065	Experimental, Cheney *et al.* (1993), Cheney and Gould (1995)
Surface-to-volume ratio of vegetation	9770 m^{-1}	Experimental, Cheney *et al.* (1993), Cheney and Gould (1995)

Vegetation char fraction	0.17	Average of Cheney *et al.* (1993), Cheney and Gould (1995) and bluestem grass (Overholt *et al.* 2014)
Vegetation element density	440 kg. m^{-3}	White pine (Australian radiata pine) (Abu Bakar, 2015)
Ambient temperature	32°C	Cheney *et al.* (1993), Cheney and Gould (1995), experimental
Relative humidity	40%	Cheney *et al.* (1993), Cheney and Gould (1995), experimental
Emissivity	0.99	Cheney *et al.* (1993), Cheney and Gould (1995), experimental
Pyrolysis temperature	400–500 K	(Morvan and Dupuy 2004)
Degree of curing	100%	Assuming vegetation 100% cured
Vegetation heat of pyrolysis	200 $kJ.kg^{-1}$	White pine (Australian radiata pine) (Abu Bakar 2015)
Maximum mass loss rate	0.15 ($kg.s^{-1}.m^{-3}$)	Cheney *et al.* (1993), Cheney and Gould (1995), experimental Maximum amount of fuel allowed to be pyrolysed

4.3 Model reliability and accuracy

4.3.1 Model reliability and validation studies

Considering the complexity of physical phenomena occurring in wildfire modelling, including numerous non-linear processes, such as radiation heat transfer, chemical reaction in the gaseous phase and turbulent transfers, it is difficult to envisage that physics-based models can be fully validated (Morvan *et al.* 2007). Despite this, the latest WFDS model has been rigorously validated for surface fires propagating in grassland (Mell *et al.* 2007, Moinuddin *et al.* 2018, Moinuddin *et al.* 2021) and for burning Douglas fir trees (Mell *et al.* 2009, Moinuddin and Sutherland (2020)). Furthermore, the WFDS model has successfully been validated against laboratory-scale experiments (Perez-Ramirez *et al.* 2017, Sánchez-Monroy *et al.* 2019).

As previously discussed in Section 2.2.1, Sánchez-Monroy *et al.* (2019) conducted laboratory-scale experiments, with no wind imposed, for fuel bed slopes ranging from 0° to 45° accompanied by physics-based simulation using WFDS. They conducted this study as a validation study of WFDS through comparison with laboratory-scale experiments to examine the capability of WFDS simulations to reproduce the experimental results for slopes. Three different fuel bed depths (δ)

were used with three different packing ratios (β). The rate of spread and flame geometry were measured for each of the experimental tests. They then conducted WFDS simulations for two of their experimental cases. The experiment and WFDS modelling results of *RoS* are presented in Figure 4.2(a). The simulations reproduced the experimental *RoS* quite well.

Recently, Moinuddin *et al.* (2021) validated WFDS, with SEM and roughness, against field-scale grassfire experiment C064 of Cheney *et al.* (1993) on a flat terrain, as discussed in Section 2.4. The simulations were performed using converged grid resolution. Fire contours at four instances of time were compared with WFDS simulations and good agreement was observed with the experimental results. These fire contour results are reproduced in Figure 4.2(b).

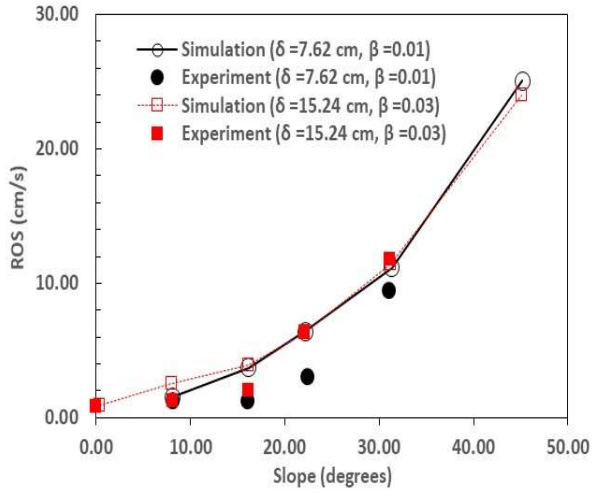

(a) Laboratory-scale sloped case modelling validation results from Sánchez-Monroy *et al.* (2019)

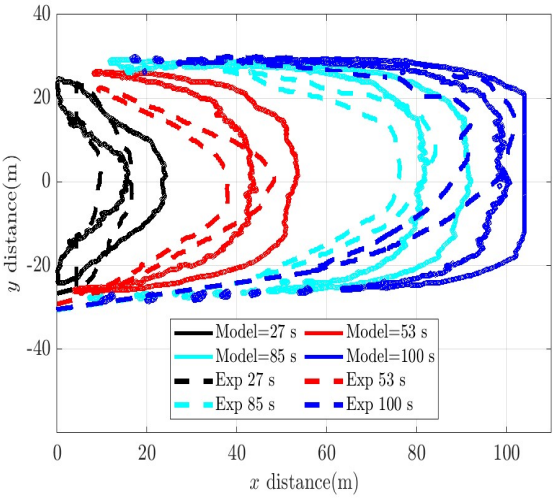

(b) Flat ground case modelling at field scale (Moinuddin *et al*. 2021)

Figure 4.2 – Evidence of model reliability and accuracy

The above validation studies show that the WFDS model is a reliable research tool that can be applied to study the effects of wind and slope interaction on fire propagation in a vegetative fuel bed. The present study follows the same model used for the two validation studies above (Moinuddin *et al.* 2018, Moinuddin *et al.* 2021). Given the scarcity of controlled field-scale grassfire experimental data with slope scenario for a validation study, we have endeavoured to satisfy that the results in this study are accurate in such a novel situation.

4.3.2 Sensitivity analysis

Sensitivity studies are required to be performed for a systematic modelling approach. In this study, sensitivity studies to the gas-phase grid resolution, ignition line intensity and domain size are conducted to ensure that the results are sensitivity-tested.

The grid sensitivity studies were performed for two scenarios: 0° at nominal wind velocity (U_{10}) of 6 m.s^{-1} and –10° at lower wind velocity (U_{10}) of 3 m.s^{-1}, to observe the effect on *RoS* and fire behaviour due to the influence of grid size. For the former, cubic grid sizes of 0.25 × 0.25 × 0.25 m, 0.375 × 0.375 × 0.375 m and 0.5 × 0.5 × 0.5 m are considered for the burnable/simulated grass domain. For the remaining domain, a coarser grid is applied as 0.5 m adjacent to the burnable grass plot and 1 m at the inlet and outlet of the domain. For the latter, simulation with grid size of 0.1875 × 0.1875 × 0.1875 m, was also conducted (albeit for a shorter duration due to significant computational cost) to make certain that converged results were obtained. Figure 4.3(a) and (b) shows that, in terms of fire front location as a function of time, the 0.25 × 0.25 × 0.25 m grid is sufficient to achieve a numerically converged solution for minimal variation of *RoS*, so that the simulation will be grid independent. Figure 4.3(c) and (d) shows the convergence in terms of heat release rate (HRR) vs time as well for both the grid scenarios.

With 0.25 × 0.25 × 0.25 m grid size around the burnable plot, ignition sensitivity study had been conducted with 500,1000 and 1500 kW.m^{-2} ignition intensity, for 0° slope at U_{10} of 6 m.s^{-1}. Minimal variaion found in terms of firefront location and HRR as shown in Figure 4.3(e) and Figure 4.3(f), as function of time, respectivily. Therefore, a prescribed line fire of 1000 kW.m^{-2} was selected.

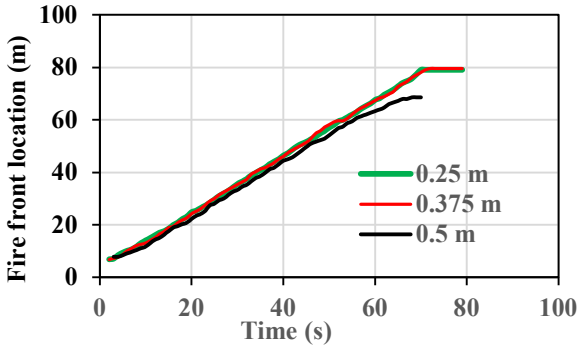

(a) Grid sensitivity in terms of firefront location vs time : 0° at 6 m.s^{-1}

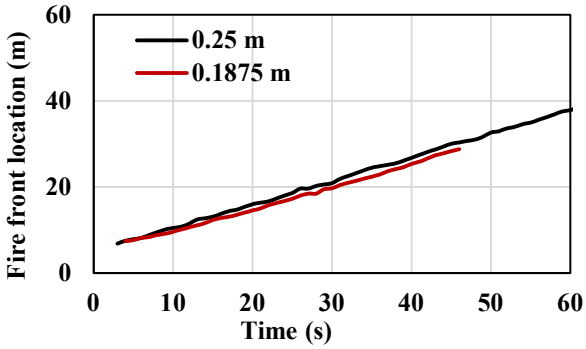

(b) Grid sensitivity in terms of firefront location vs time: –10° slope at 3 m.s^{-1}

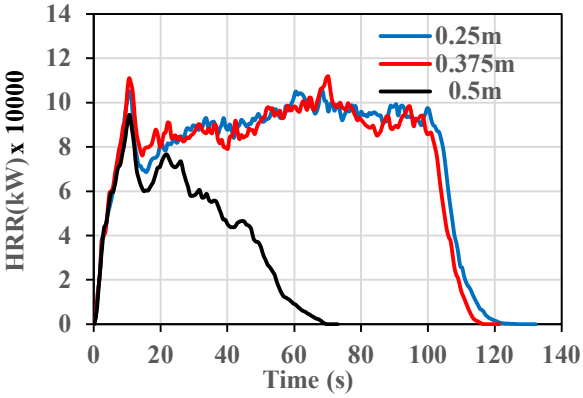

(c) Grid sensitivity in terms of HRR vs time : 0° at 6 m.s^{-1}

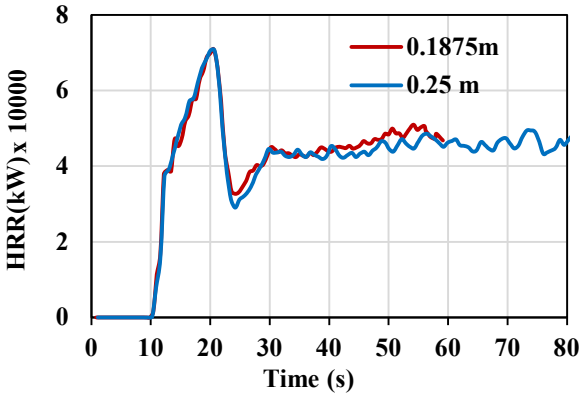

(d) Grid sensitivity in terms of HRR vs time: –10° slope at 3 m.s^{-1}

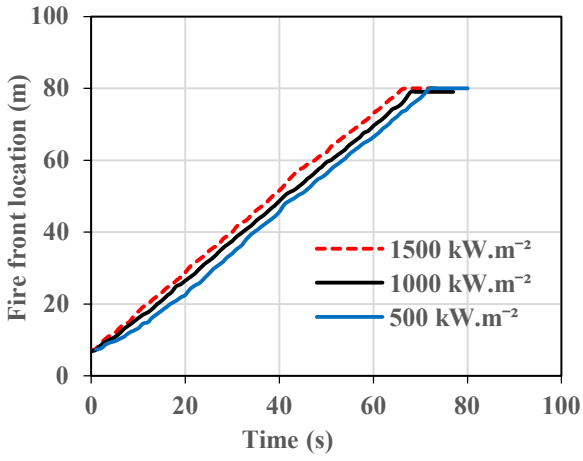

(e) Ignition line intensity (kW.m^{-2}) in terms of firefront location vs time : 0° slope at 6 m.s^{-1}

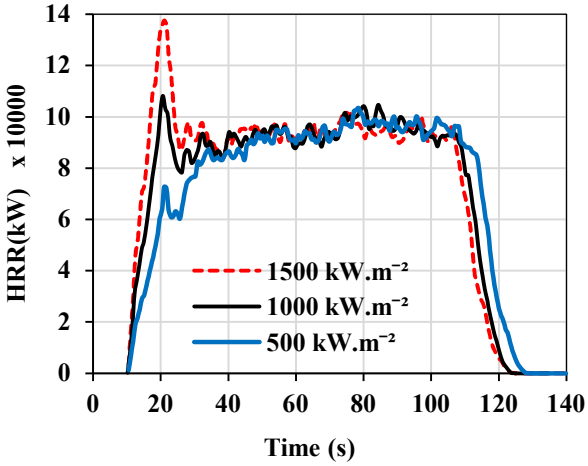

(f) Ignition line intensity (kW.m$^{-2)}$ in terms of HRR vs time: 0° slope at 6 m.s^{-1}

Figure 4.3 – Sensitivity studies in terms of gas-phase grid resolution and ignition fire line intensity: fire front location and HRR plotted against time.

Table 4.2 presents three different domain set-ups considered in the domain sensitivity study, for 0° slope at U_{10} of 6 m.s^{-1}.

Table 4.2: Parameters for domain sensitivity

Simulation	Domain size	Distance of ignition line from inlet	Bordering subdomain (both sides)	Distance from end of burnable plot to outlet
Larger domain	480 m long ×180 m wide 80 m high	220 m	140 m	180 m
Selected domain	360 m long ×120 m wide × 60 m high	160 m	80 m	120 m
Smaller domain	280 m long × 80 m wide × 40 m high	120 m	40 m	80 m

Figures 4.4(a) and (b) show the fire front propagation and HRR results, respectively, confirming that 360 × 120 × 60 m is appropriate for this study. Figure 4.5(d) shows wind velocity profiles for the three domains, at driving wind velocity of 6 m.s^{-1}, taken at streamwise location immediately before the grass plot. The results show minimal differences in the wind profiles among the three domain sizes.

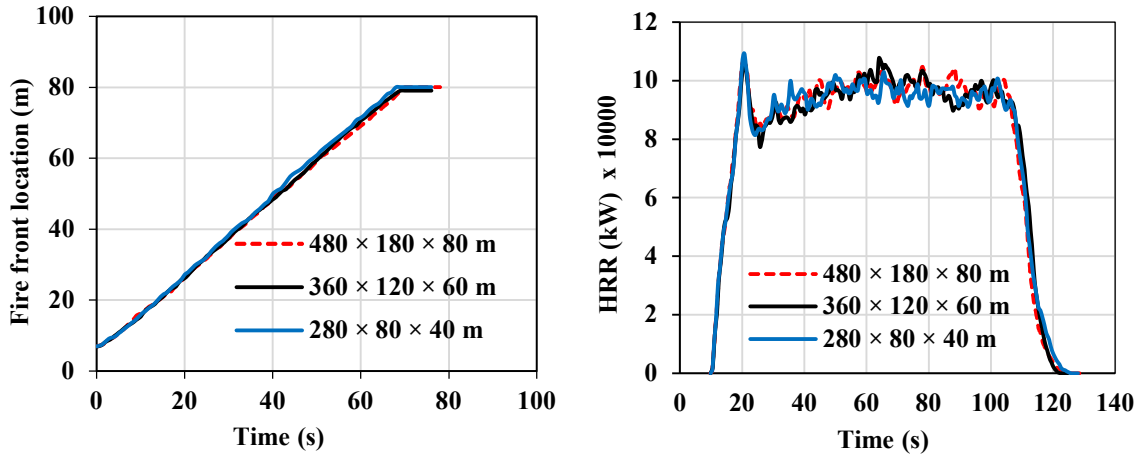

(a) Fire front location vs time **(b)** HRR vs time

Figure 4.4 – Domain sensitivity in terms of (a) fire front location vs time, and (b) HRR vs time

4.3.3 Wind flow development time

The simulations allowed enough time to develop a stable and fully developed wind flow in the domain. The wind velocity profiles for selected domain at different streamwise locations and through the geometric centre line (y = 0) of grass plot are shown in Figure 4.5. Enlarged views of Figures (a) and (b) between 0 to 5 m height are shown in Appendix A, Figure S4.1(a) and (b), respectively, to view the wind profile near the vegetation clearly. Figure S4.1(c) in Appendix A shows the enlarged wind profile view up to 5 m height for the three domains.

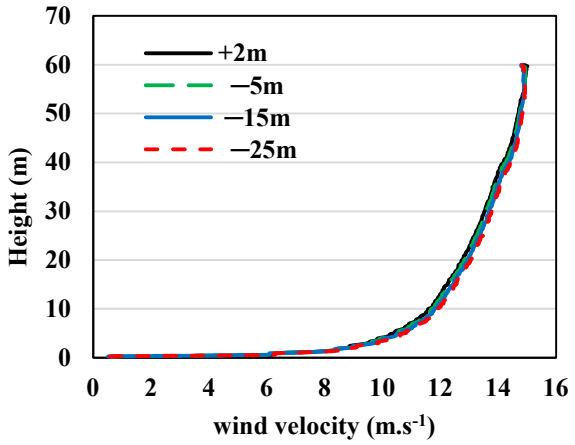

(a) wind profiles taken –25, –15, –5 and +2 m distance from the burnable domain

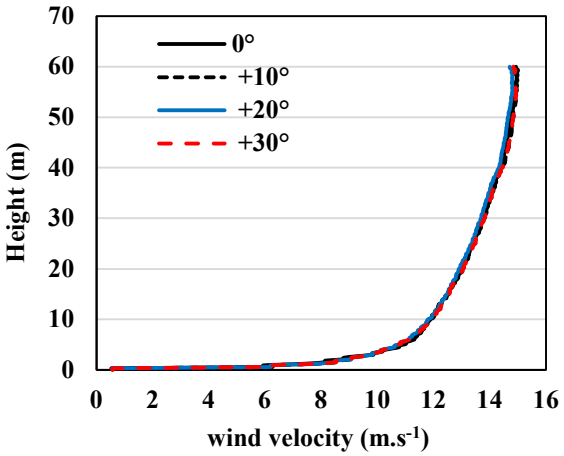

(b) wind profiles taken at –25 m for four cases, 0°, +10°, +20° and +30°

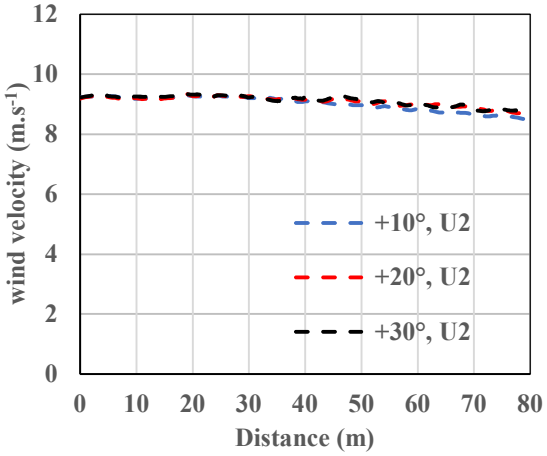

(c) Mean velocity U_2 vs distance profile, through the geometric centreline of the grass plot, for +10°, +20° and +30°

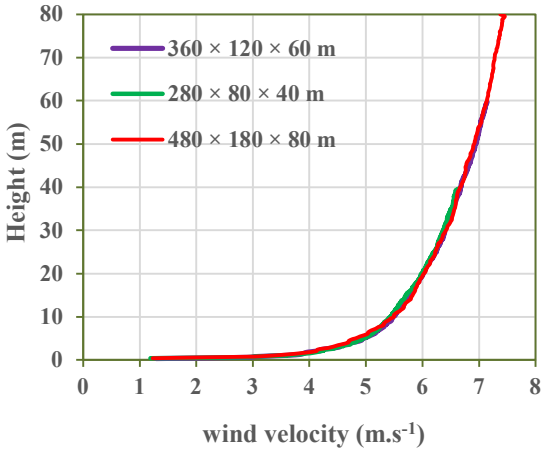

(d) wind profiles vs height for 0° slope at 6 $m.s^{-1}$ for the three domains, taken at the inlet (+2 m) of gras plot.

Figure 4.5 – Wind profiles at driving wind velocity of 12.5 $m.s^{-1}$

The velocities presented are time averaged velocities along the centreline of the domain.These figures show very little variations of velocities and stable wind fields are developed in all simulations.

In this study, a fully developed turbulent wind flow has been used and a grid convergence study has been conducted. Roy *et al*. (2018) conducted a comparative study of wind fields generated by different methods and their effects on fire spread (Roy *et al.* 2018). There were no remarkable differences in terms of flow filed and simulation results although some methods are quicker than the others for the development of fully developed flow fields in the domain. The synthetic eddy simulation method is handy to reduce the spin up time for fully developed flow field generation without compromising the accuracy of the simulation.

Figures 4.3, 4.4 and 4.5 demonstrated that grid- and domain-converged results and fully developed wind field boundary conditions are obtained before the fire is ignited.

4.4 Results and discussion

Table 4.3 lists the simulations conducted at different slope angles for both upslopes and downslopes (–30° to +30°), with higher and medium driving wind velocities (U_{10}) of 12.5, 6 and 3 m.s^{-1} (corresponding to 11.9, 5.6 and 2.8 m.s^{-1}, respectively, prior to the ignition line). Simulations with higher upslope angles, +30°, +25° at 12.5 m.s^{-1} and +30° at 6 m.s^{-1}, are repeated with an extended burnable grass plot (120 m in the *x*-direction), to ensure better quasi-steady state results are attained for a fairly long period of time.

The fire isochrones, head fire width or pyrolysis width, location of the fire front, rate of spread of fire (*RoS*), fire intensity, plume and flame dynamics, mode of fire propagation and heat fluxes (convective and radiative) were analysed, and the results are presented in the following sections in order. The *RoS* is compared with the empirical modelling studies found in the literature: McArthur models MKIII and MKV, the CSIRO model, and the Rothermel ‘Original’ and ‘Modified’ models.

Table 4.3: List of Simulations

Slope angle	Simulation abbreviation	Driving wind velocity		
		12.5 m. s^{-1}	6 m.s^{-1}	3 m.s^{-1}
–30°	downslope 30	√	√	√
–25°	downslope 25	√		
–20°	downslope 20	√	√	√
–15°	downslope 15	√		
–10°	downslope 10	√	√	√
–5°	downslope 5	√		
0°	no-slope	√	√	√
+5°	upslope 5	√		
+10°	upslope 10	√	√	√
+15°	upslope 15	√		
+20°	upslope 20	√	√	√
+25°	upslope 25	√*		
+30°	upslope 30	√*	√*	√

4.4.1 Progression of isochrones and pyrolysis width

This section analyses and discusses the fire isochrones and the pyrolysis width (or head fire width) results for all the slope angles at the three driving wind velocities.

4.4.1.1 Progression of isochrones

The instantaneous contour plot of temperature filtered at pyrolysis temperature of fuel, which represent the fire region is known as isochrones of fires. It represents the development of the fire (the instantaneous leading and trailing boundaries of fire front), as it progresses though the grass plot. The isochrones of fire progression as a function of time are presented in Figures 4.6 and 4.7 for the three wind velocities, for upslopes and downslopes, respectively.

* Simulations repeated with longer burnable grass plot (extended to 120 m in *x*-direction)

In these simulations, the fire contours are defined as the region on the boundary (the fire perimeter representing the contours of the boundary temperature) where the minimum threshold temperature of vegetation is above the pyrolysis temperature of 400 K.

The fire contours are extracted by post-processing the time-averaged boundary temperature outputs, using numeric computing software Matlab, (https://mathworks.com) (Davis and Sigmon 2005). Further details about determining the isochrones can be found in Moinuddin *et al.* (2018) and Sutherland *et al.* (2020).

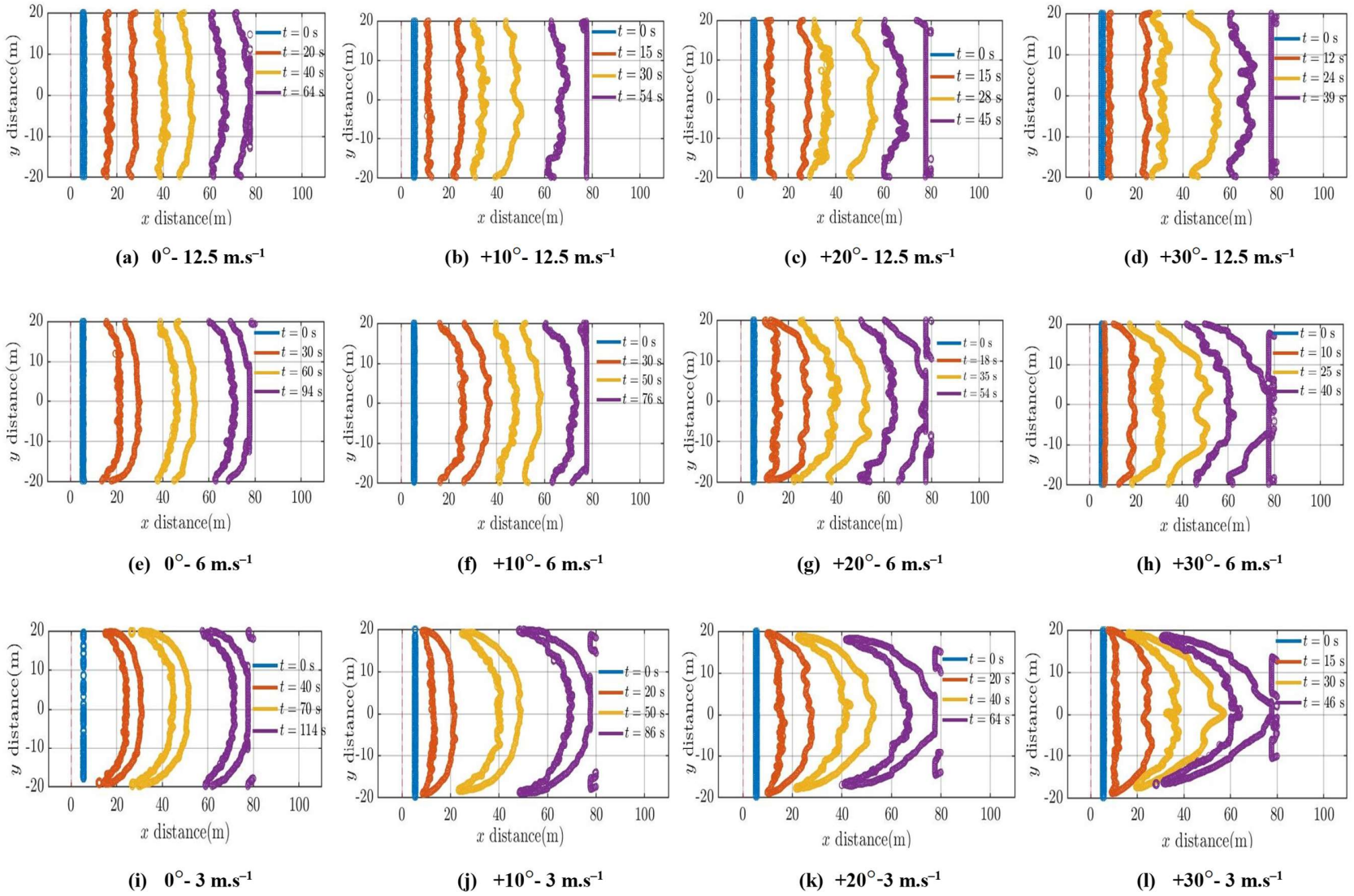

Figure 4.6 – Progression of isochrones, 0° +10°, +20°, +30° at wind velocities: Frames (a–d) 12.5 m.s^{-1}; (e–h) 6 m.s^{-1}; (i–l) 3 m.s^{-1}

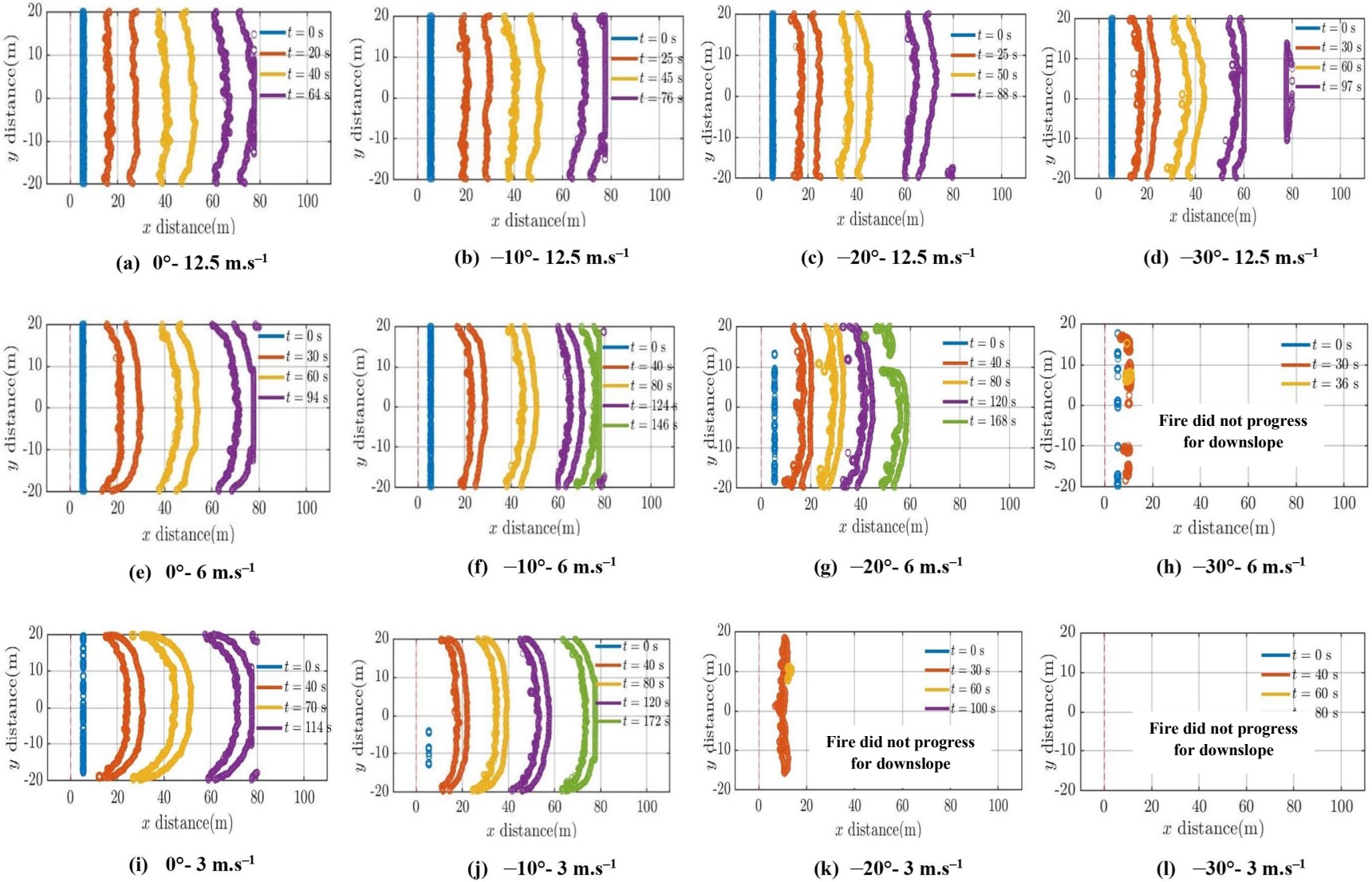

Figure 4.7 – Progression of isochrones: 0°, –10°, –20°, –30° at wind velocities: (a–d) 12.5 m.s^{-1}; (e–h) 6 m.s^{-1}; (i–l) 3 m.s^{-1}

Isochrones are plotted at different times after the ignition starts and when the fire propagates towards the end of burnable grass plot. As the slope angle increases, the isochrone becomes wider (or the separation between isochrone flank at a given time becomes larger) and reaches the end of burnable grass plot much earlier (frames c, f and i). With U_{10} = 12.5 m.s^{-1}, the isochrone travel times obtained are: 64, 60, 54, 48, 45, 42 and 39 s for upslopes 0°, +5°, +10°, +15°, +20°, +25° and +30°, respectively, whereas the isochrone is moving more slowly with the increase in downslope angles. For –5°, –10°, –15°, –20°, –25°and –30° downslopes, the isochrone travel times are 70, 76, 80, 88, 90 and 97 s, respectively. As the downslope angle increases, the isochrone becomes thinner; however, the decrease in pyrolysis width (along y = 0) is significantly lower compared with upslopes, where the isochrone becomes wider with increase in slope angle.

For the same slope angle, with increase in wind velocity the isochrone travels quicker and reaches the end of grass plot earlier (Figures 4.6 and 4.7). For downslopes with lower wind velocities (especially at 3 m.s^{-1}), with increase in downslope angles, the isochrone moves very slowly (Figure 4.7).

4.4.1.2 Pyrolysis width

The pyrolysis width or width of head fire (separation between isochrone flanks, taken through the centre of isochrone) as a function of time is presented in Figure 4.8(a–c) for wind velocities 12.5, 6 and 3 m.s^{-1}, respectively. Results with the extended burnable grass plot (120 m in *x*-direction) for higher upslopes, +30° and +25° at 12.5 m.s^{-1} and +30° at 6 m.s^{-1}, are presented in Figure S4.2 of Appendix A.

For upslope cases, pyrolysis width increases as the fire front progresses from the ignition line, then it plateaus or reaches a quasi-steady state, and finally decreases. Generally, as the upslope angle increases, the width of the plateau decreases, and its magnitude or value increases. The reverse scenario occurs with the downslope cases, where the width of the plateau increases, and its magnitude or value decreases with increase in downslope angle. Pyrolysis width values are much higher for upslopes compared with downslopes.

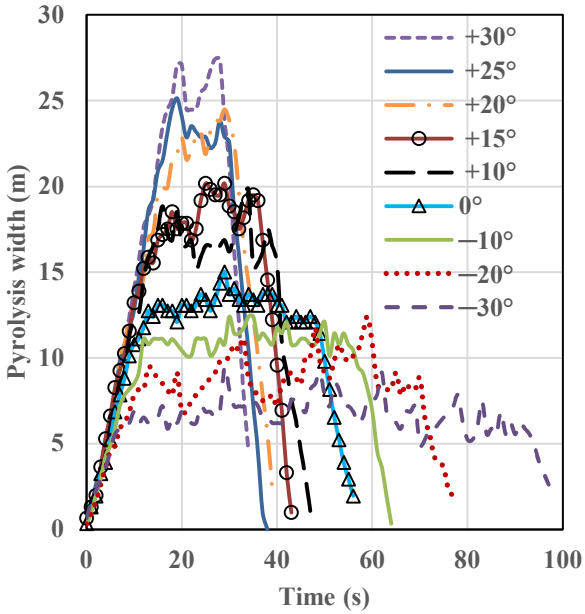

(a) Pyrolysis width vs time –12.5 m.s^{-1}

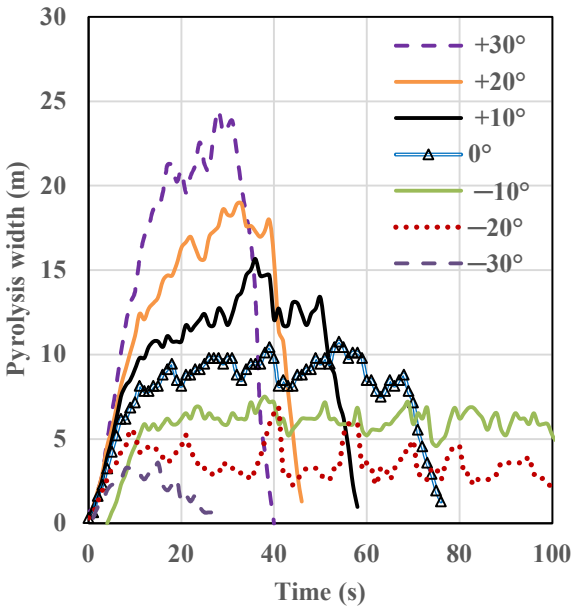

(b) Pyrolysis width vs time– 6 m.s^{-1}

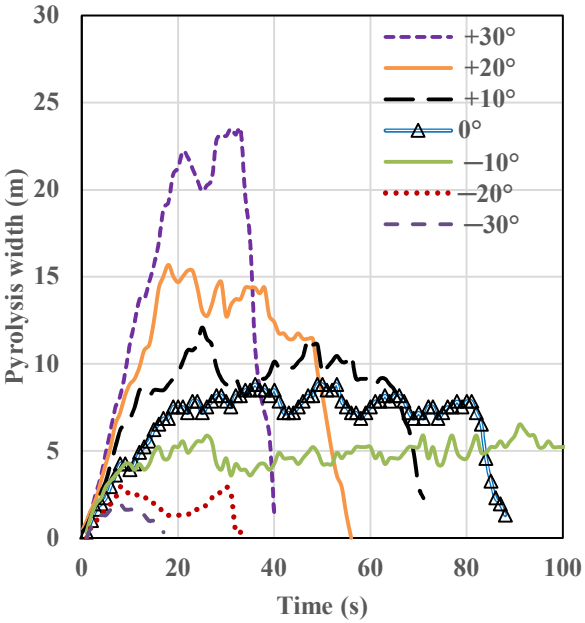

(c) Pyrolysis width vs time – 3 m.s^{-1}

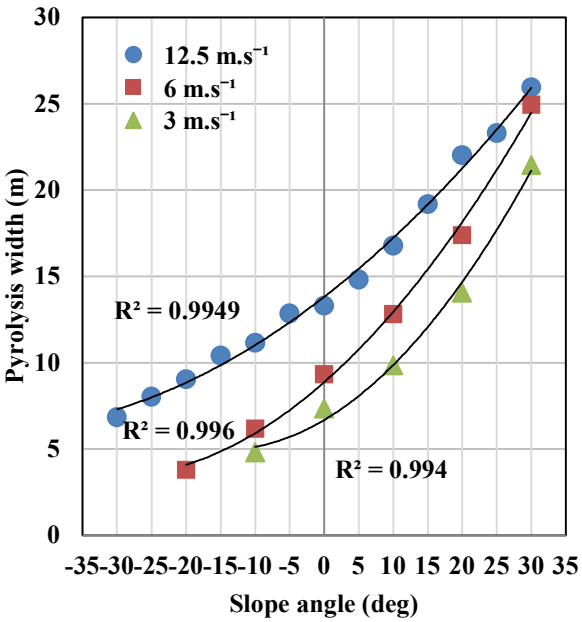

(d) pyrolysis width vs slope angle

Figure 4.8 – Pyrolysis width vs time: upslope and downslopes (a) at 12.5 m.s^{-1}; (b) at 6 m.s^{-1}; (c) at 3 m.s^{-1}; (d) quasi-steady pyrolysis width vs slope angles, at 12.5, 6 and 3 m.s^{-1}

Comparing among the velocities, for a given slope angle, the pyrolysis width values increase with driving wind velocity. At the lower wind velocities 6 and 3 m.s^{-1}, the pyrolysis width values are much lower for steep downslope angles. This is evident in Figures 4.8(b) and (c) where the pyrolysis width values are significantly lower for –30º at 6 m.s^{-1} and –30º and –20º at 3 m.s^{-1}. This is consistent with Figure 4.7, where the isochrones are moving very slowly on steep downslopes at lower wind velocities.

Figure 4.8(d) represents quasi-steady pyrolysis width versus slope angle for all cases at the three driving wind velocities. In almost all scenarios, the pyrolysis width reaches a quasi-steady state, as shown in Figures 4.8 (a–c) and Figure S4.2 of Appendix A. The width values are extracted approximately 15 to 35 s after the start of ignition for upslopes and approximately 12 to 60 s after the start of ignition for downslopes. For upslope cases, for higher wind speed, the head fire width increases by approximately 20–30% at every 10° upslope. The pyrolysis width decreases with increase in downslopes. Fire did not propagate for steep downslope cases and hence –30° at 6 m.s^{-1} and –30° and –20° at 3 m.s^{-1} are not included in the slope angle–pyrolysis width plot (Figure 4.8(d)). A second-order polynomial relationship (R^2 value is shown in the plot) is observed between the pyrolysis width and slope angle for the three driving wind velocities.

Figures 4.9(a), (b) and (c) show the pyrolysis width vs fire front location for the same three wind velocities. The results obtained from the extended grass plot (120 m in the *x*-direction) are used for +30°, +25° at 12.5 m.s^{-1} in Figure 4.9(a) and +30° at 6 m.s^{-1} in Figure 4.9(b). For higher upslopes, the pyrolysis width increases as the fire front moves forward, then it plateaus or reaches a quasi-steady state. Compared with the pyrolysis width vs time plots in Figure 4.8, quasi-steady states are better visible (over the longer distance). Longer quasi-steady states are observed for lower upslopes, no slope and 10° downslope angles. For –30° at 12.5 m.s^{-1} and –20° at 6 m.s^{-1}, pyrolysis width gradually decreases over the distance, leading to extinction consistent with the fire isochrones plots shown in Figure 4.7.

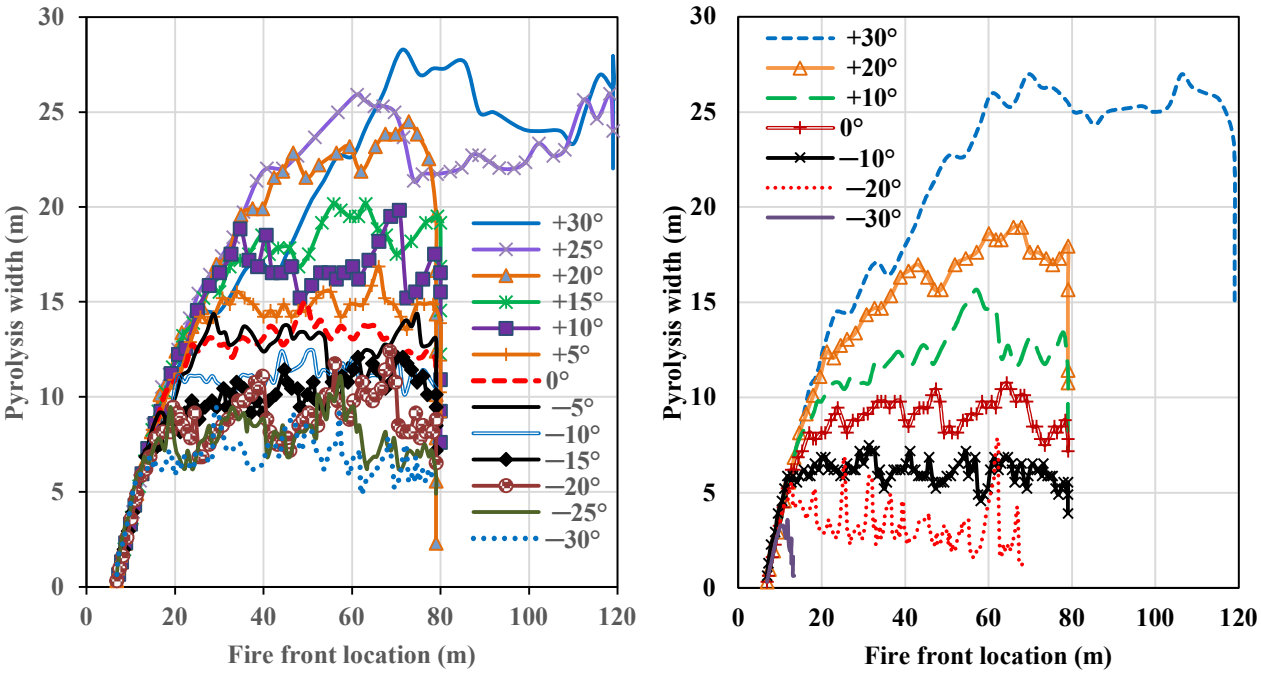

(a) Pyrolysis width vs fire front – 12.5 m.s^{-1}

(b) Pyrolysis width vs fire front – 6 m.s^{-1}

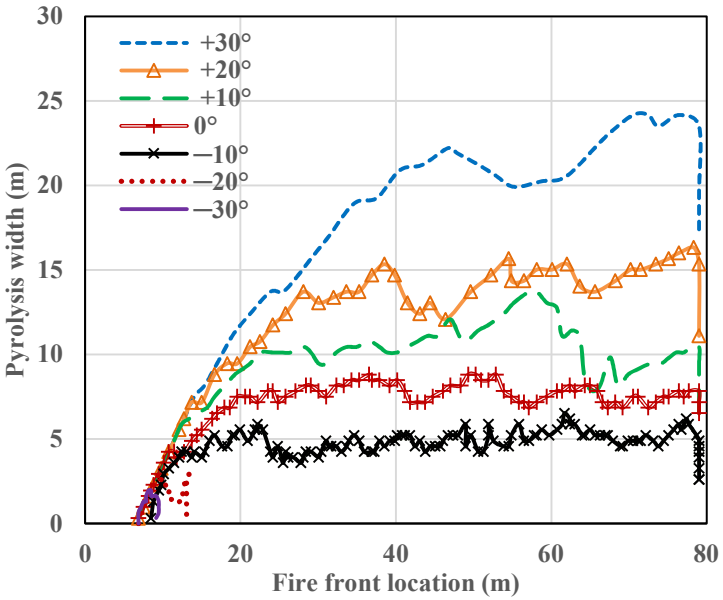

(c) Pyrolysis width vs fire front – 3 m.s^{-1}

Figure 4.9 – Pyrolysis width vs fire front location for upslopes and downslopes at wind velocities of: (a) 12.5 m.s^{-1}; (b) 6 m.s^{-1}; and (c) 3 m.s^{-1}

It is evident from the fire isochrone plot (Figure 4.7) and pyrolysis width results (Figures 4.8 (b), (c) and Figures 4.9(b), (c)) that fire did not propagate for steep downslopes at lower wind velocities. This lower driving wind velocity may not be sufficiently enough to drive the fire front as it moves steep downslopes such as –20° and –30° at 3 $m.s^{-1}$ and –30° at 6 $m.s^{-1}$. In these cases, the fire eventually extinguishes because lower wind enhancement in steep downslope scenarios causes the buoyancy force acts against the wind direction, which tends to decelerate the flow (Eftekharian *et al.* 2019). Another possibility for extinguishment is due to approximations made in the derivation of the boundary fuel model. These approximations make the model more consistent with conditions in which the flame leans over unburned vegetation. Other reasons for extinguishment may be the physical parameters of the fuel such as fuel height, fuel load, the thermo-physical properties. This aspect can be investigated separately in future studies with the fuel element model when computational power increases substantially. It is to be noted that the fuel element model needs very fine grid resolutions (of the order of cm) which implies a very high computational cost and normally used for laboratory-scale simulations, while the boundary fuel model allows to simulate surface fires in field-scale with quite large grid cell resolutions (Sánchez-Monroy *et al.* 2019).

Hence, Simulation results from steep downslopes, –30° at 6 $m.s^{-1}$ and –30° and –20° at 3 $m.s^{-1}$, are not included in further analysis and discussions.

4.4.2 Dynamic *RoS*, fire front locations and *RoS* calculations

This section discusses the *RoS* calculation and correlation of *RoS* with slope angles for the three driving wind velocities. Evidence of dynamic *RoS*, fire front locations and *RoS* calculations are presented. The *RoS* values obtained from WFDS simulations are then compared with the results from the following empirical models: McArthur MKIII and MKV, CSIRO, Rothermel 'Original' and 'Modified' models. Finally, relative *RoS* (*RoS* on any slope divided by *RoS* at no-slope) of WFDS quasi-steady *RoS* values are compared with the Australian slope function (rule of thumb) and the Rothermel model variations.

4.4.2.1 Dynamic *RoS*

Although the focus of this study is to compare quasi-steady fire behaviour with empirical models, an attempt is also made to analyse dynamic fire behaviour. In Section 2.4, evidence of the dynamic

behaviour of fire propagation from the studies found in the literature (both experimental and simulation studies) was discussed. Sutherland *et al.* (2020) presented *RoS* as a function of time by differentiating the fire front location data. They extracted the firefront location (as a threshold surface temperature) along the centreline of the burnable grass plot at each simulation output time. The standard first-order forward finite difference was used to obtain the approximate rate of spread over time. The rate of spread data is obtained as a function of time with frequency at every second. The numeric computing software Matlab (https://mathworks.com) (Davis and Sigmon 2005) was used to extract the data. The same analysis technique (Sutherland *et al.* (2020)) is used in this study to derive dynamic *RoS* for all the slope cases. A temperature threshold of 400 K, the minimum pyrolysis temperature (Table 4.1), is used to define the minimum threshold boundary of the data. We have also analysed the data smoothed using 3 -point moving average to reduce noise caused by turbulent fluctuation and to obtain a clear view. The instantaneous *RoS* values smothered using a 3-point moving average are presented in Appendix A, Figure S4.3, which shows a less noisy plot.

The dynamic *RoS* values as a function of time are plotted in Figures 4.10(a) and (b) at wind velocity of 12.5 m. s^{-1}, Figures 4.10(c) and (d) at wind velocity of 6 $m.s^{-1}$ and Figures 4.10(e) and (f) at wind velocity of 3 $m.s^{-1}$, for upslopes and downslopes, respectively. Dynamic *RoS* results with the extended burnable grass plot (120 m in the *x*-direction) for +30°, +25° at 12.5 $m.s^{-1}$ and +30° at 6 $m.s^{-1}$ are presented in Figure S4.4 of Appendix A.

The plots show numerous spikes or ups and downs (random fluctuation) in *RoS* values as the fire front moves forward, and maximum values of dynamic *RoS* are observed with +30° slope, compared with lower slope angles. The fluctuations in dynamic *RoS* values for the downslope cases are notably lower than that observed in the upslope cases, as demonstrated in Figure 4.10 (b), (d) and (f).

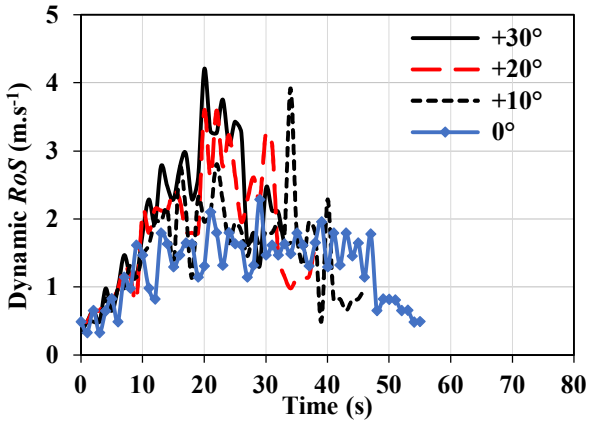

(a) upslopes, 12.5 m.s^{-1}

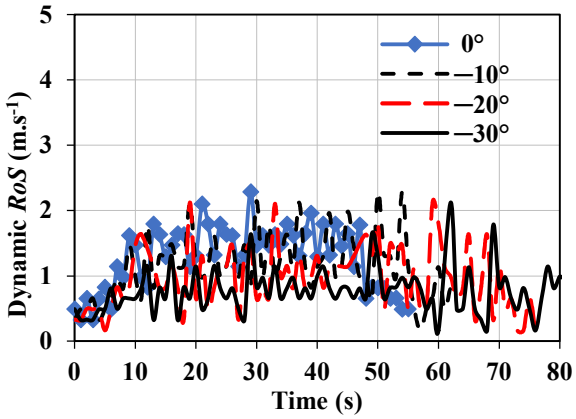

(b) downslopes, 12.5 m.s^{-1}

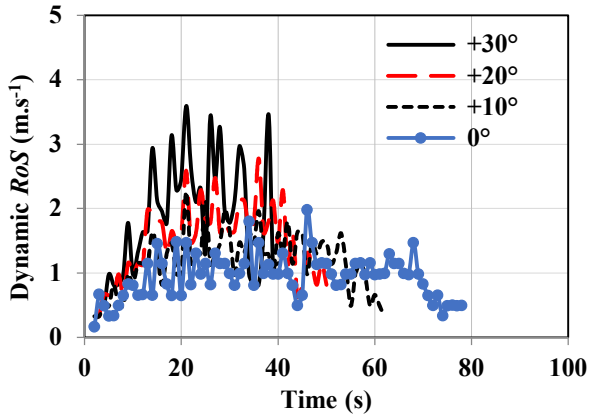

(c) upslopes, 6 m.s^{-1}

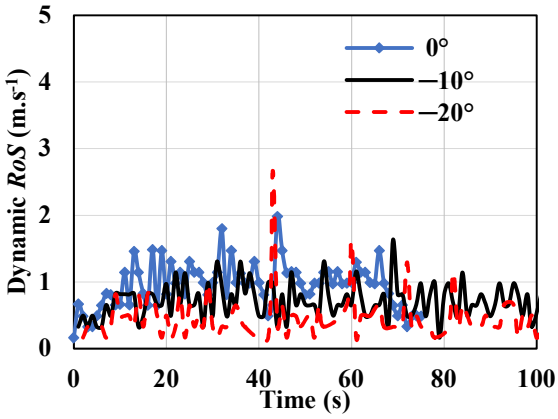

(d) downslopes, 6 m.s^{-1}

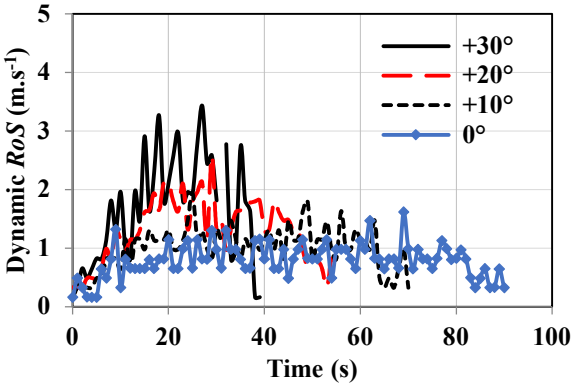

(e) upslopes, 3 m.s^{-1}

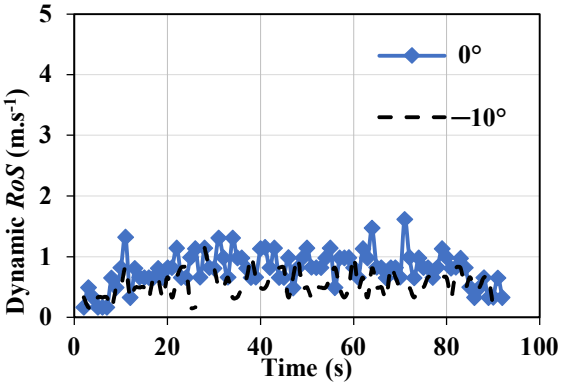

(f) downslopes, 3 m.s^{-1}

Figure 4.10 – Dynamic *RoS* vs time at all three wind velocities: (a) upslopes at 12.5 m.s^{-1}; (b) downslopes at 12.5 m.s^{-1}; (c) upslopes at 6 m.s^{-1}; (d) downslopes at 6 m.s^{-1}; (e) upslopes at 3 m.s^{-1}; and (f) downslopes at 3 m.s^{-1}

The dynamic *RoS* as a function of fire front are plotted in Figures 4.11 for the three wind velocities, for both upslopes and downslopes. The results obtained from the extended burnable grass plot (120 m in the *x*-direction) are used for +30° and +25° at 12.5 m.s^{-1} in Figure 4.11(a) and for +30° at 6 m.s^{-1} in 4.11(b). Like the dynamic *RoS* vs time plot in Figure 4.10, the plots show numerous spikes in *RoS* values as the fire front moves forward and the values are noticeable until the fire front reaches the end of the burnable grass plot. For –20° at 6 m.s^{-1}, the *RoS* gradually decreases over the distance, consistent with the pyrolysis width shown in Figure 4.9.

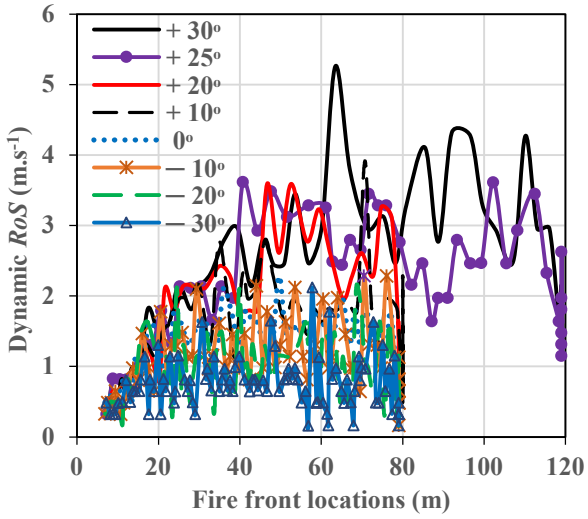

(a) 12.5 m.s^{-1}

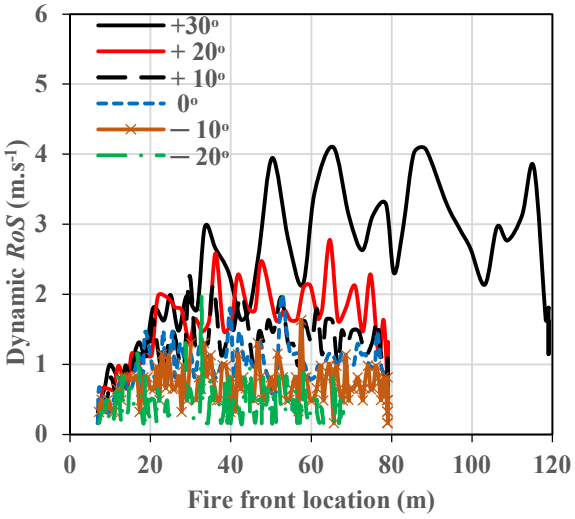

(b) 6 m.s^{-1}

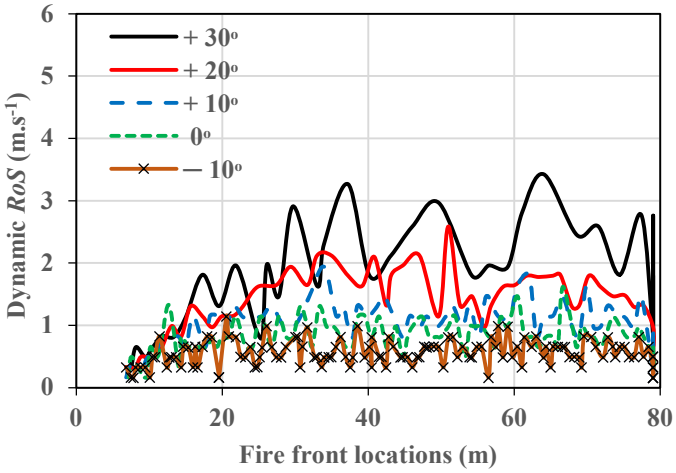

(c) 3 m.s^{-1}

Figure 4.11 – Dynamic *RoS* vs fire font location, at driving wind velocities of: (a) 12.5 m. s^{-1}; (b) 6 m.s^{-1}; and (c) 3 m.s^{-1}

4.4.2.2 Fire front locations

To calculate *RoS*, the firefront location (location of leading edge of the isochrone) is first determined by the boundary centreline temperature as the fire moves through the grass plot at each simulation output time.

The location of the leading edge of the firefront at driving wind velocity of 12.5 m.s^{-1} are shown in Figure 4.12(a) and (b) for upslopes and downslopes, respectively. Fire front locations at 6 and 3 m.s^{-1} are shown in 4.12 (c) and (d), respectively. Fire front locations with extended burnable grass plot for higher upslopes, +30°, +25°at 12.5 m.s^{-1} and +30° at 6 m.s^{-1} are shown in Figure S4.5 of Appendix A.

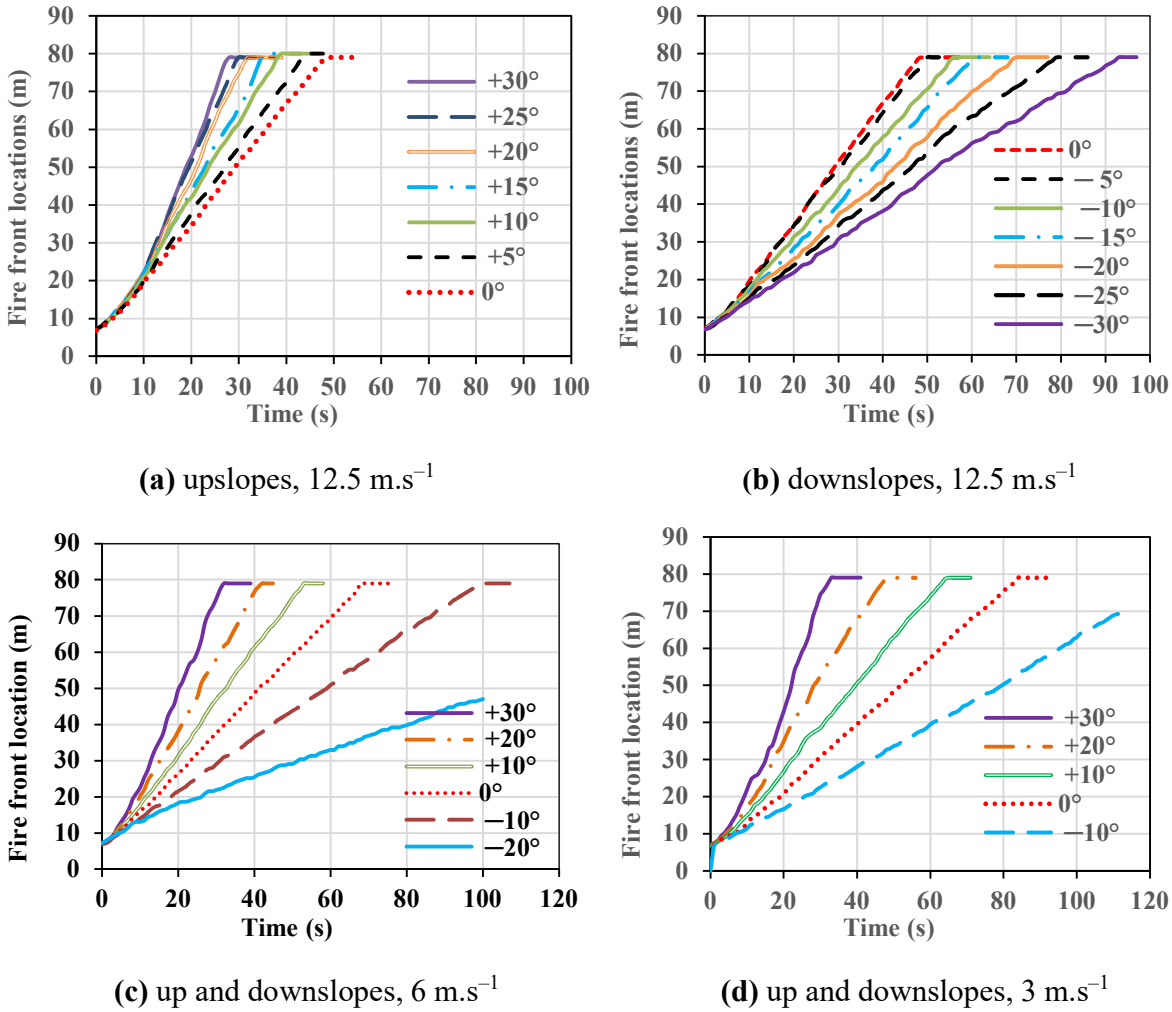

(a) upslopes, 12.5 m.s^{-1}

(b) downslopes, 12.5 m.s^{-1}

(c) up and downslopes, 6 m.s^{-1}

(d) up and downslopes, 3 m.s^{-1}

Figure 4.12 – Fire front location vs time for: (a) upslopes at 12.5 m.s^{-1}; (b) downslopes at 12.5 m.s^{-1}; (c) upslopes and downslopes at 6 m.s^{-1}; (d) upslopes and downslopes at 3 m.s^{-1}.

The fire front is found to be moving faster with an increase in upslope angle, as shown in Figure 4.12(a) and Figure S4.5 in Appendix A. At a given time, the fire front location for +30° slope is farther by approximately 45% than that of no slope. For downslopes, as shown in Figure 4.12(b), the fire front is moving more slowly with increase in downslope angle. The higher the downslope angle, the nearer (to the ignition line) the fire front location is or the shorter the distance travelled by the fire front. At a given time, the fire front location for the 30° downslope is nearer by approximately 55% than that of no slope situation (the fire front has travelled approximately 55% less far than no slope case). A similar trend is observed with 6 and 3 $m.s^{-1}$wind velocity cases (Figures 4.12 (c) and (d)).

Comparing among the wind velocities, for a given slope angle, the fire front is found to be travelling more slowly with lower wind velocities compared with a higher wind velocity, consistent with fire isochrones shown in Figure 4.6.

4.4.2.3 *RoS* calculation

From an operational perspective, *RoS* is one of the most important parameters. The averaged *RoS* is calculated in two ways and between these two values, the difference is found to be very minimal. To the averaged *RoS*, we have included uncertainty in two ways: (1) using the maximum and minimum dynamic values as whiskers (i.e. upper bound and lower bound) and (2) using error bars from *RoS* fluctuations. These are explained in the following paragraphs.

Figure 4.13 represents *RoS* calculations and comparisons for all the slope cases at the three driving wind velocities, along with the whiskers. The quasi-steady state *RoS* values for each of the slope cases are calculated from the fire front location when steady-state conditions (the region in the plot where the fire front appears to be progressing at a constant rate) are reached. The least-squares approximation method is applied to develop the *RoS*–slope angle correlations with a linear fit to the fire front location plots for each of the cases shown in Figures 4.12(a), (b), (c) and (d). For higher upslopes, +30°, +25° at 12.5 $m.s^{-1}$ and +30° at 6 $m.s^{-1}$ cases, the linear fit applied to the fire front location plotted in Figure S4.5 of Appendix A (extended grass plot simulations). As mentioned previously, steady-state conditions are not achieved for steep downslopes at lower wind velocities and hence –30° at 6 $m.s^{-1}$, –30° and –20° at 3 $m.s^{-1}$ are not included in the *RoS*–slope angle correlation plots.

The slope of each linear fit/linear regression formula represents quasi-steady *RoS* for each of the cases. For all the cases, for the quasi-steady region, the R^2 value is found to be ~0.99, indicating that the quasi-steady state *RoS* values are captured accurately from a linear curve. The slope values (quasi-steady *RoS*) obtained from the linear fit equations are plotted against slope angles in Figures 4.13 (b–d), for 12.5, 6 and 3 $m.s^{-1}$ wind velocity.

Along with quasi-steady *RoS* values, the dynamic *RoS* values are also plotted in Figures 4.13 (b–d) with maximum and minimum bounds. For the 12.5 $m.s^{-1}$ cases, the dynamic *RoS* values (maximum, averaged and minimum) for upslopes are extracted from Figures 4.10(a) and Figure S4.4(a) of Appendix A, for downslopes from Figure 4.10(b), and they are presented in Figure 4.13(b). The 'dynamic averaged' values are extracted from approximately 15-50 s from ignition for upslopes, and from 10–70 s for downslopes. The 'dynamic maximum' and 'minimum' values are the peak and trough *RoS* values, respectively, from instantaneous dynamic *RoS*, for a particular case.

Same analysis techniques are used to derive dynamic *RoS* for the 6 $m.s^{-1}$ case (from Figures 4.10 (c), (d) and Figure S4.4(b) in Appendix A), and they are presented in Figure 4.13(c). Dynamic *RoS* for the 3 $m.s^{-1}$ cases are extracted from Figures 4.10(e), (f), and they are presented in Figure 4.13(d).

Figure 4.13(a) represents the quasi-steady *RoS* vs wind velocity results of this study for flat terrain (no slope) for three wind velocities, along with empirically derived *RoS* vs wind velocities.

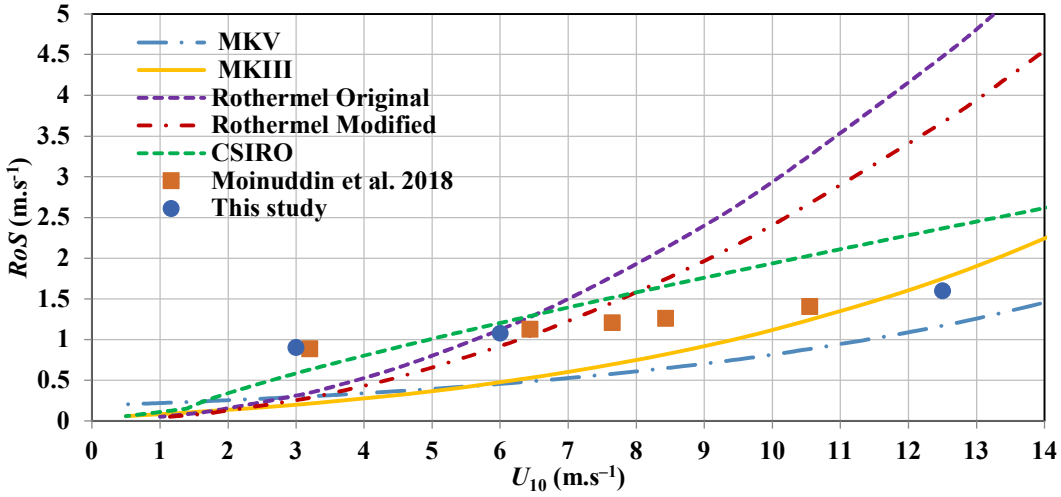

(a) *RoS* – wind velocity, at 0° slope (flat terrain)

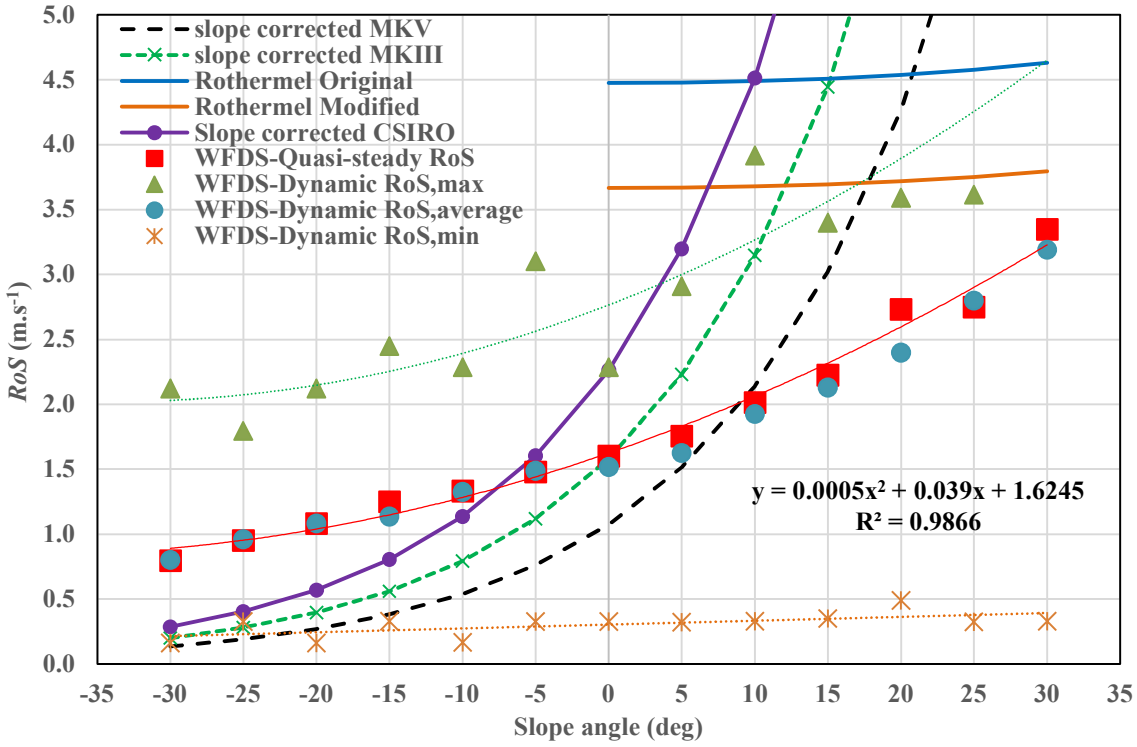

(b) *RoS* – slope angle, 12.5 m.s^{-1}

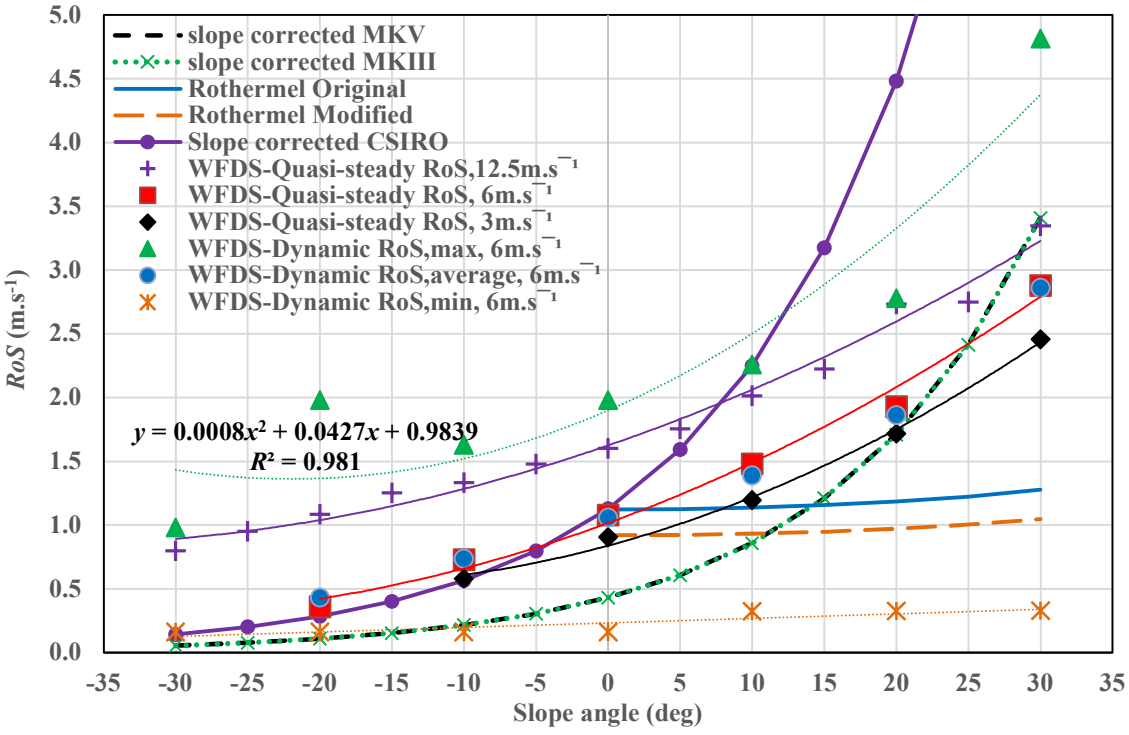

(c) *RoS* – slope angle, 6 m.s^{-1}

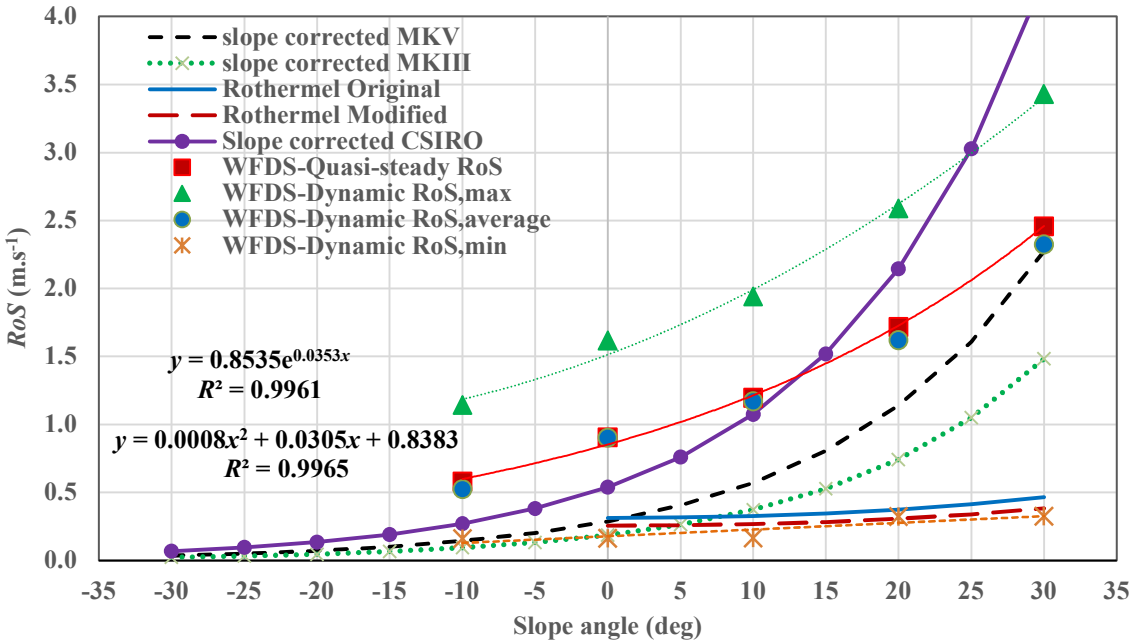

(d) *RoS* – slope angle, 3 m.s^{-1}

Figure 4.13 – Rate of spread (*RoS*) correlations: (a) *RoS* vs wind velocities at 0° slope (flat terrain); (b) *RoS* vs slope angle at 12.5 m.s^{-1}; (c) *RoS* vs slope angle at 6 m.s^{-1} along with quasi-steady *RoS* at 12.5 and 3 m.s^{-1}; (d) *RoS* vs slope angle at 3 m.s^{-1}.

In Figure 4.13(a), the quasi-steady *RoS* values obtained from this study are comparable with the WFDS simulations of Moinuddin *et al.* (2018) for flat terrain. The minor differences (approximately 1- 4%) are due to the use of SEM methodology and a different ignition protocol. Empirically derived *RoS* values for flat terrain, derived from MKIII and MKV, CSIRO, Rothermel Original and Rothermel Modified models are also presented in Figure 4.13. These empirical formulas are derived from experimental observations conducted under a range of fuel parameters and ambient weather conditions. Some were developed from wind tunnel data. Furthermore, fires are fundamentally dynamic, as shown in Figures 4.10 and 4.11. Overall, the geometry, scale of the fire and various boundary conditions were different from the simulations and despite these, the results of the physics-based simulations at different wind velocities with no slope agree within 5–65% with different empirical models. Generally, MKIII and CSIRO model results are found to be the nearest to WFDS results and at lower velocity, higher difference (approximately 65%) is noted for MKIII values, whereas with CSIRO model values higher difference (approximately 27%) is observed at higher wind velocity.

In Figures 4.13 (b–d), the *RoS* values obtained with sloped terrains are presented: the empirically derived *RoS* values from the empirical models mentioned above (Australian models are 'slope-corrected'), along with the *RoS* values (quasi-steady and dynamic) obtained from the WFDS simulations in this study with sloped terrains.

Both Original and Modified Rothermel values do not change much with slope (for all three velocities).When compared with the four sets of WFDS data, it can be observed that, for 6 $m.s^{-1}$ Rothermel values match with quasi-steady *RoS* values for up to +10° and match better with dynamic maximum *RoS* values for 12.5 $m.s^{-1}$, with dynamic averaged *RoS* values up to +10° for 6 $m.s^{-1}$ and dynamic minimum *RoS* values for 3 $m.s^{-1}$. The Rothermel models were developed for upslope fire spread (Weise and Biging 1997) and hence the *RoS* for downslopes are not compared with Rothermel models.

Overall, the slope-corrected CSIRO values match the closest with quasi-steady and dynamic averaged *RoS* values as follows; For 12.5 $m.s^{-1}$, only with –5° and –10° reasonably (+8% and –17% respectively), for 6 $m.s^{-1}$ quite well for downslopes and for 3 $m.s^{-1}$ closest (20% difference) for ≤ +20°. The CSIRO values are quite high for many upslope cases (upslopes for 12.5 and 6 $m.s^{-1}$; ≥ +20° for 3 $m.s^{-1}$), often close to dynamic maximum *RoS* values.

The *RoS* values at no-slope for MKIII and MKV, look identical as shown in Figure 4.13(a) for 6 $m.s^{-1}$ and hence the slope-corrected MKIII and MKV values also look identical for 6 $m.s^{-1}$.This is owing to to the same slope correction factor applied to both the models. Slope- corrected MKIII and MKV values are often close to the dynamic minimum *RoS* values, especially for downslope cases (–15° ≤ for 12.5 $m.s^{-1}$, downslopes for 6 $m.s^{-1}$; +10° < for 3 $m.s^{-1}$). For 12.5 $m.s^{-1}$ cases, these model values are closer to the quasi-steady and dynamic averaged *RoS* values for the range of –10° to +10° and then rises higher than the dynamic maximum for high upslope cases. On the other hand, for >+ 10° at 6 $m.s^{-1}$, the model values are closer to the quasi-steady and dynamic averaged *RoS* values.

Except for higher slope-corrected Australian model values at 12.5 $m.s^{-1}$ for >+ 15°, slope-corrected CSIRO values at 6 $m.s^{-1}$ for > +15° and at 3 $m.s^{-1}$ for ≥ +30°, all empirical values roughly lie between dynamic minimum and dynamic maximum *RoS* values.

The simulations in this study represent idealised slope scenarios with homogenous fuel beds which are different to real fire scenarios with potentially the existence of fuel inhomogeneity, and wind gusts and directional changes. Taking into account of these, measurement of quasi-steady values in outdoor experiments is quite challenging (Mell *et al.* 2018; Sutherland *et al.* 2020). All these factors can be attributed to any observed differences.

The quasi-steady *RoS* value for –20° is found to be around 40% and 60% less than that of the zero-slope condition, for 12.5 and 6 m.s^{-1}, respectively. For 12.5 m.s^{-1} cases, the results are consistent with Sullivan *et al.* (2014), who argued that the value of *RoS* for a negative slope situation should be at most 0.6 of the *RoS* at no-slope condition (or at most 40% lower than the *RoS* of the zero-slope). The different relationships obtained between quasi-setady *RoS* and slope angle are presented in Table 4.4.

Table 4.4: *RoS* vs slope angle relationship

Pattern	**12.5 m.s^{-1}**	**6 m.s^{-1}**	**3 m.s^{-1}**
Exponential	$1.6443e^{0.0223x}$	$0.9487e^{0.0389x}$	$0.8535e^{0.0353x}$
R^2	0.9786	0.9887	0.9961
Polynomial	$0.0005x^2 + 0.039x$ +1.6245	$0.0006x^2 + 0.0415x$ + 1.0158	$0.0008x^2 + 0.0305x$ + 0.8383
R^2	0.9866	0.9894	0.9965
Linear	$0.039x$ + 1.7939	0.0474x + 1.1732	$0.0457x$ + 0.9141
R^2	0.9464	0.9578	0.9596

Genrally, a second-order polynomial relationships are found to be the best fit between quasi-steady *RoS* and slope angles for all three wind velocities. The polynomial trend lines (for visual representation only) with R^2 vlaues are shown in Figure 4.13 (b–d). The exponential relationship for 3 m.s^{-1} is also found to be good (see Figure 4.13(d) and Table 4.4). It is likely that as the driving wind velocity decreases, the relationship becomes exponential. Most researchers report an exponential relationship in low or with no driving wind velocities (Noble *et al.* 1980, Beck 1995, Pimont *et al.* 2012). The slope factors in empirical correlations are exponential (McArthur 1967, Sharples 2017, Sullivan *et al.* 2014) which are likely to be derived from very low wind velocity laboratory slope studies. However, with significant driving wind velocity and the dynamic nature of fire propagation, the trend between quasi-steady *RoS* and slope angles fit on to a second-order

polynomial relationship more, as shown in Figures 4.13 (b–d) for the three wind velocities. A second-order polynomial relationship is also observed between dynamic maximum *RoS* values and slope angles for all three wind velocities. However, for dynamic minimum values, the relationships are linear.

To compare among the three wind velocity cases, for corresponding slopes, the quasi-steady *RoS* values for 12.5 and 3 m.s^{-1} are presented along with 6 m.s^{-1} in Figure 4.13(c). From Figure 4.13(c), it is evident that for a given slope angle, *RoS* values with lower wind velocities are lower, but the difference narrows between 3 and 6 m.s^{-1} as the slope angle decreases.

To provide uncertainty estimates using the second method, we have calcuated error bars from dynamic *RoS* values and and these are fitted on the WFDS quasi-steady *RoS* data, as presented in Figures 4.14 (a–c), for all three wind velocities. This plot shows the confidence bounds around the WFDS *RoS* estimate. The length of the error bar or margin of error is determined for 95% confidence interval using eqn. (4.3–4.4). The full time series *RoS* data (*RoS(t)*) is used to calculate the length of error bar. A 95% confidence interval is a range of values above and below the point estimate within which the true value in the population is likely to lie with 95% confidence. The other 5% is the possibility that the true value is not within the confidence interval.

$$Mean, \mu = \sum \frac{ABS(RoS(t) - qRoS)}{N}, \tag{4.3}$$

$$length\ of\ error\ bar = \mu + \frac{1.96}{\sqrt{N}} \sqrt{\frac{\sum \{\mu - ((RoS(t) - qRoS))\}^2}{N}}, \tag{4.4}$$

Where, N = number of datapoints, *RoS(t)* = time series of *RoS* (*RoS* values at every instant in time) and *qRoS* = quasi-steady *RoS.*

The length of the error bar on each side of the data point represents the confidence bounds around the quasi-steady *RoSs* (WFDS *RoS* and empirically derived slope corrected *RoS* values: MKIII and MKV, CSIRO, Rothermel Original and Rothermel Modified models).

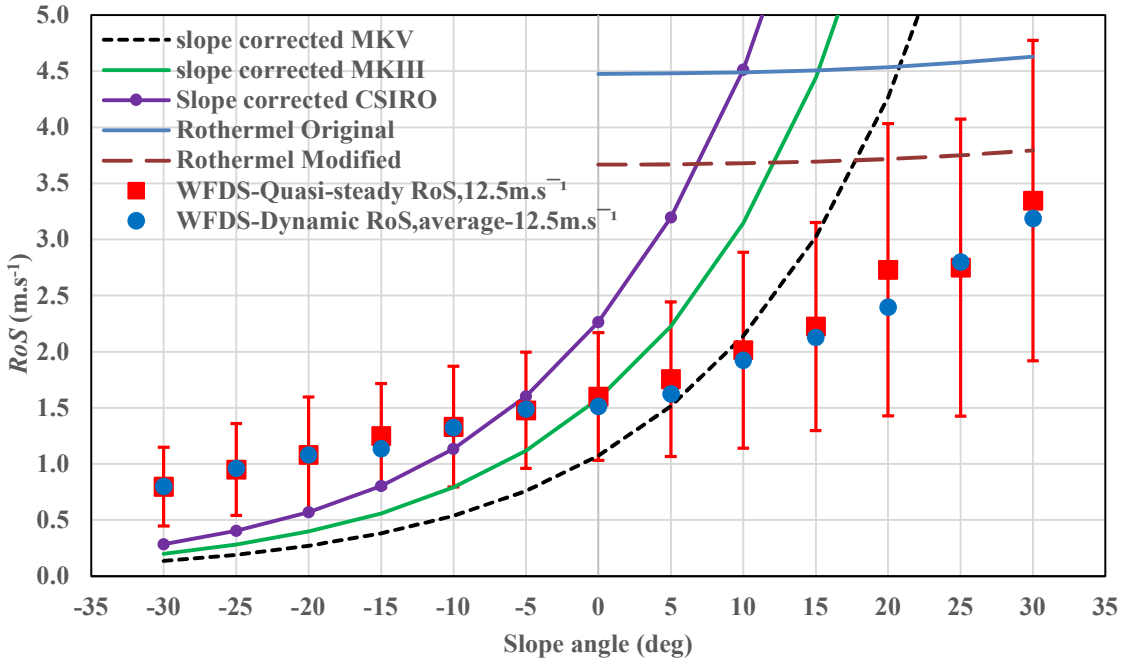

(a) *RoS* – slope angle, with 95% confidence bounds, 12.5 m.s^{-1}

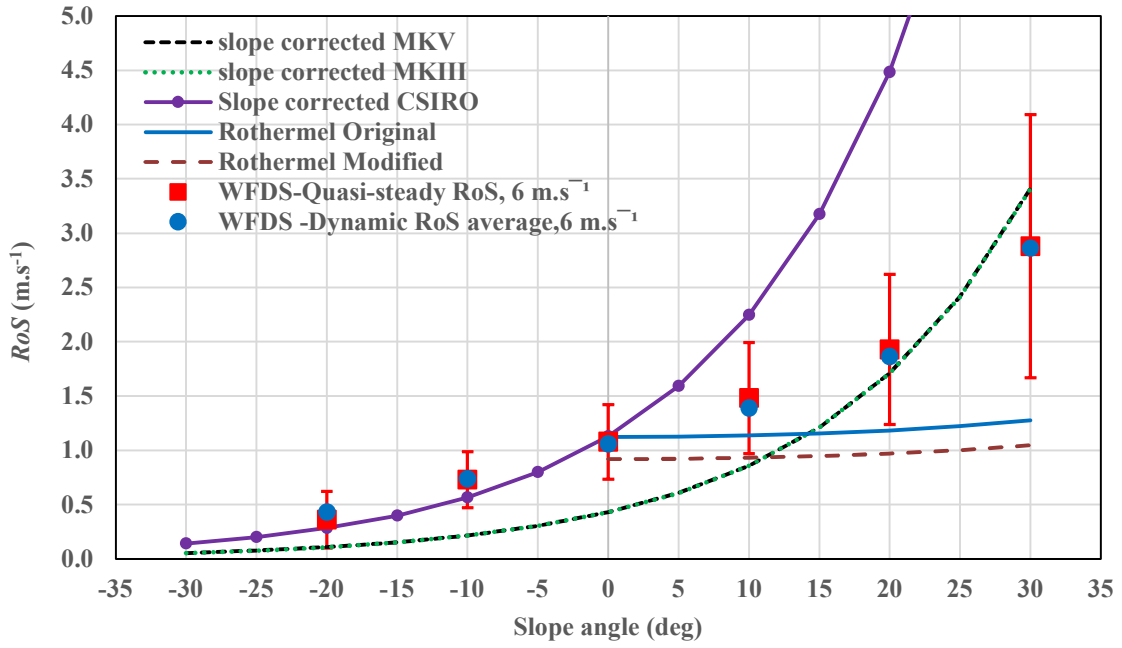

(b) *RoS* – slope angle, with 95% confidence bounds, 6 m.s^{-1}

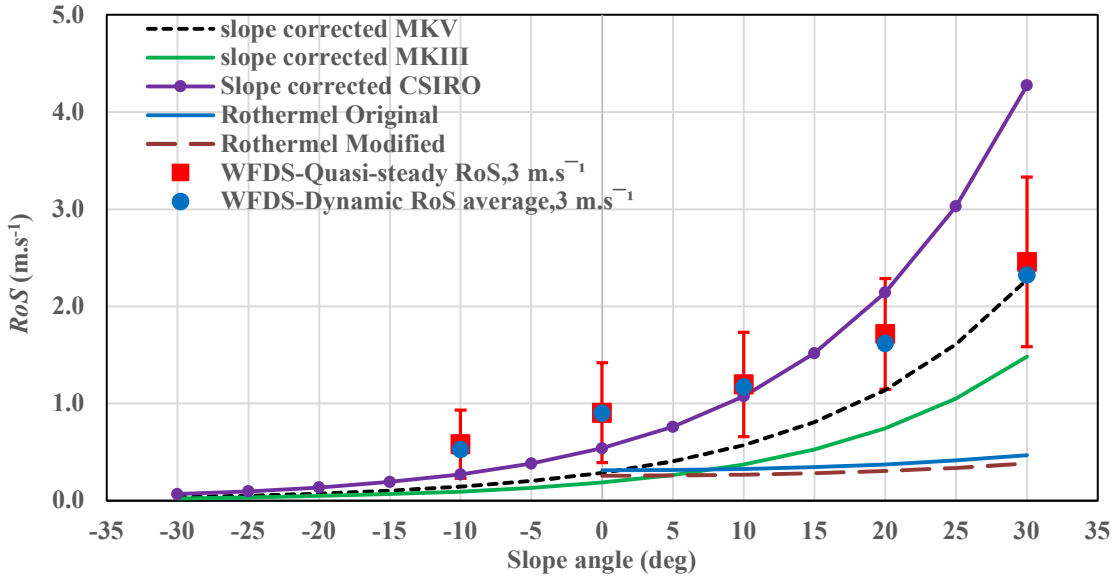

(c) *RoS* – slope angle, with 95% confidence bounds, 3 m.s^{-1}

Figure 4.14 – *RoS* – slope angle: WFDS quasi-steady *RoS* values fitted with margin of error (95% confidence bounds) : (a) at 12.5 m.s^{-1}; (b) at 6 m.s^{-1}; (c) at 3 m.s^{-1}.

Figure 4.14(b) for 12.5 m.s^{-1} cases shows that the error bar encapsulates the slope-corrected MKV *RoS* values for no slope and for upslopes up to +20°. For higher upslopes (+20° to +30°), the error bar encapsulatesthe Rothermel Modified model values and for +30°, the Rothermel Original values as well. However, the MKIII model is confined only for the lower slope angles (–10° to +5°). The CSIRO model *RoS* values are outside the error bar range for all upslope angles; however, the error bar encapsulates the CSIRO model for downslopes (–5° to –20°). For steep downslopes, the empirical models *RoS* values are not encapsulated by the error bar.

The error bar fitted on the WFDS quasi-steady *RoS* for 6 m.s^{-1} (Figure 4.14(b)) shows that, except for 0°, the error bars encapsulate the MKIII, MKV, model *RoS* values for all upslope angles. Rothermel Original and Modified model values are encapsulated for 0° to +10° only. For 0° slope, the error bars encapsulate the CSIRO and both the Rothermel models. Again, the CSIRO model *RoS* values are beyond the bounds of the error bars for all the upslope angles but capture the downslope angles (–5° to –20°).

Figure 4.14(c) for the 3 m.s^{-1} cases shows that the error bar encapsulate the CSIRO model values for 0° to +20° and MKV values for higher upslope angles. However, MKIII values and both the

Rothermel model values are outside the error bar range for all upslope cases, though the noslope values for these cases closer to the lower range of error bar. Similarly, as observed with higher wind velocity cases, the CSIRO model *RoS* value for downslope (–10°) is captured by the error bar range.

Overall, the error bar fitted on the WFDS quasi-steady *RoS* data encapsulated MKV values for most of the upslopes (all upslopes at 6 m.s^{-1}, up to +20° at 12.5 m.s^{-1} and for higher upslopes at 3 m.s^{-1}), whereas MKIII values are confined only for the upslopes at 6 m.s^{-1} . The CSIRO model *RoS* values are outside the error bar range for all upslopes at both 12.5 and 6 m.s^{-1}, which mostly encapsulated the downslope angles (–5° to –20°). Generally, the Rothermel model values are found to be outside the error bar range for most of the slope angles for all three wind velocities.

4.4.2.4 Relative *RoS*

In Figure 4.15, relative *RoS* (*RoS* on any slope divided by *RoS* at no slope) for each of the driving wind velocities of WFDS quasi-steady values are compared with the Australian slope function (rule of thumb) and the Rothermel model variations.

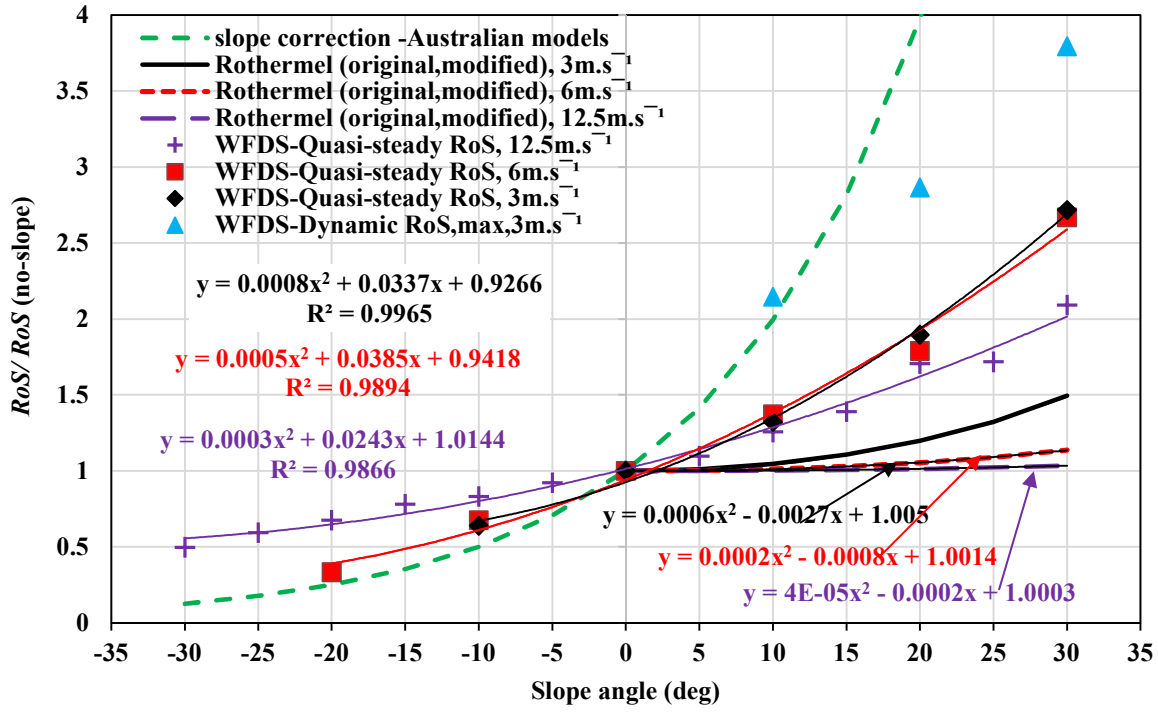

Figure 4.15 – Comparison of the effect of slope at different driving wind velocities*: RoS/RoS (at no-slope)* between WFDS quasi-steady results and empirical models

Owing to the multiplicative nature of the Australian models' slope functions, the relative *RoSs* (*RoS* on slope/*RoS* at no-slope) values unchanged for all wind velocities for MKIII, MKV and CSIRO models. Both Original and Modified Rothermel models give the same values for each wind velocity. WFDS results give different values for different wind velocities. It is observed that the Rothermel models and WFDS functions are best fitted to a second-order polynomial relationship with $R^2 > 0.99$, as shown in Table 4.5.

Table 4.5: Relative *RoS* vs slope angle relationship

	Pattern	**12.5 m.s^{-1}**	**6 m.s^{-1}**	**3 m.s^{-1}**
WFDS Relative *RoS*	Exponential R^2	$1.0268e^{0.0223x}$	$0.8796e^{0.0389x}$	$0.9435e^{0.0353x}$
		0.9786	0.9887	0.9961
	Polynomial R^2	$0.0003x^2 + 0.0243x + 1.0144$	$0.0005x^2 + 0.0385x + 0.9418$	$0.0008x^2 + 0.0337x + 0.9266$
		0.9866	0.9894	0.9965
	Linear R^2	$0.0243x + 1.1202$	$0.044x + 1.0877$	$0.0505x + 1.0104$
		0.9464	0.9578	0.9596
Rothermel model Relative *RoS*	Exponential R^2	$0.995e^{0.0011x}$	$0.9814e^{0.0042x}$	$0.9459e^{0.0134x}$
		0.8999	0.9078	0.9294
	Polynomial R^2	$0.00005x^2 + 0.0002x + 1.0003$	$0.0002x^2 + 0.0008x + 1.0014$	$0.0006x^2 + 0.0027x + 1.005$
		0.9991	0.9991	0.9991
	Linear R^2	$0.0011x + 0.9949$	$0.0045x + 0.9795$	$0.0161x + 0.9264$
		0.897	0.897	0.897

For upslopes, the relative *RoSs* are quite different from the Australian models' slope function. The Rothermel models under the influence of strong wind show minimal slope effects and as the wind velocity decreases, a greater effect is observed. A similar trend is noted for WFDS results, with a stronger slope effect. For downslopes, at 6 and 3 m.s^{-1}, WFDS relative *RoS* are closer to the Australian slope function. When WFDS dynamic maximum *RoS* values for 3 m.s^{-1} are normalised by the quasi-steady value, an even closer relative *RoS*s' is observed. For downslopes, Australian relative *RoS* functions are lower than WFDS relative *RoSs* by 25–75% for 12.5 m.s^{-1} and 10–25% for 6 and 3 m.s^{-1} wind velocites. For upslopes, Australian relative *RoS* functions are higher than

WFDS relative *RoSs* by 29–280% (+5 to +30°) for 12.5 m.s^{-1} and 45–197% (+10° to +30°) for 6 and 3 m.s^{-1} wind velocities. The difference widens as the slope angle increases. Hence, the multiplicative nature of the Australian slope function (especially for upslopes) may need strong scrutiny.

4.4.3 Heat Release Rate (HRR) and Fire Intensity

Time series data of HRR obtained from all simulations for the three wind velcoites are presented in Figure 4.16 (a-c). Results with longer domain (to ensure quasi-steady state) for +30°, +25° at 12.5 m.s^{-1} and +30° at 6 m.s^{-1} are presented in Figure S4.6 of Appendix A.

Byram's fire intensity (Byram 1959) is the HRR per unit length of the fireline measured along the centre of the pyrolysis region at each time step. In this study, we have calculated HRR per unit length differently from the method used in Moinuddin *et al.* (2021) which is one of the basis of validated WFDS model. The reasons are: we used instantaneous ignition line running across the width of the fire isochrone plots as shown in Figure 4.17(a) and (b), fire propagations are mostly on slopes and the driving wind velocity ranges are higher (up to 12.5 m.s^{-1}) compared to Moinuddin *et al.* (2021). As a result, for 6 and 12.5 m.s^{-1} cases, we did not observe trailing edges of isochrones which contributes very little to the total HRR. For these cases, to determine the fireline length, a line is drawn on the fire isochrones along the centre of the curvature and the fireline length is measured physically through this line as demonstrated in Figure 4.17(a). For 3 m.s^{-1} cases, trailing edges of isochrones are visible for slopes => 0°. For these cases, the fireline length is calculated excluding the trailing edges, using the method demonstrated in Figure 4.17(b), where the measured length is represented by the dotted straight line. This method is not fully following Moinuddin *et al.* (2021), but consistent with the method used with 6 and 12.5 m.s^{-1} cases.

The HRR (kW) values obtained from the simulations at various instants in time (at interval of 10 s), are divided with the measured fire front length (m) at the same instants, to obtain the fire intensity Q (kW.m^{-1}). The measured fire front length and corresponding Q values are shown in Table S4.1 of Appendix A. Fire intensity Q vs time are plotted in Figure 4.18 (a–c) for wind velocities of 12.5, 6 and 3 m.s^{-1}, respectively. The quasi-steady Q values derived from these plots are presented in Figure 4.18(d), against slope angles for all three wind velocities. The quasi-steady

Q values are obtained from 20 s from ignition to approximately 60 s for higher upslopes, to 60–80 s for no-slope and to 120–160 s for downslopes.

From Figure 4.16 (a-c) and Figure S4.5, the HRR (and hence *Q*) increases with slope angle and the values are higher for upslopes at any given time, consistent with the *RoS* results. For downslopes, the HRR decreases with increasing downslope angle, stabilizes at peak values with some fluctuations and then decreases as the firefront reaches the end of grass plot. Keeping in mind that for higher slope angles at 12.5 and 6 m.s^{-1} wind velocities the domain size might not be long enough to capture all aspects of fire behaviours (and hence the true behaviour of HRR), we observed a closer to quasi-steady state in almost all scenarios.

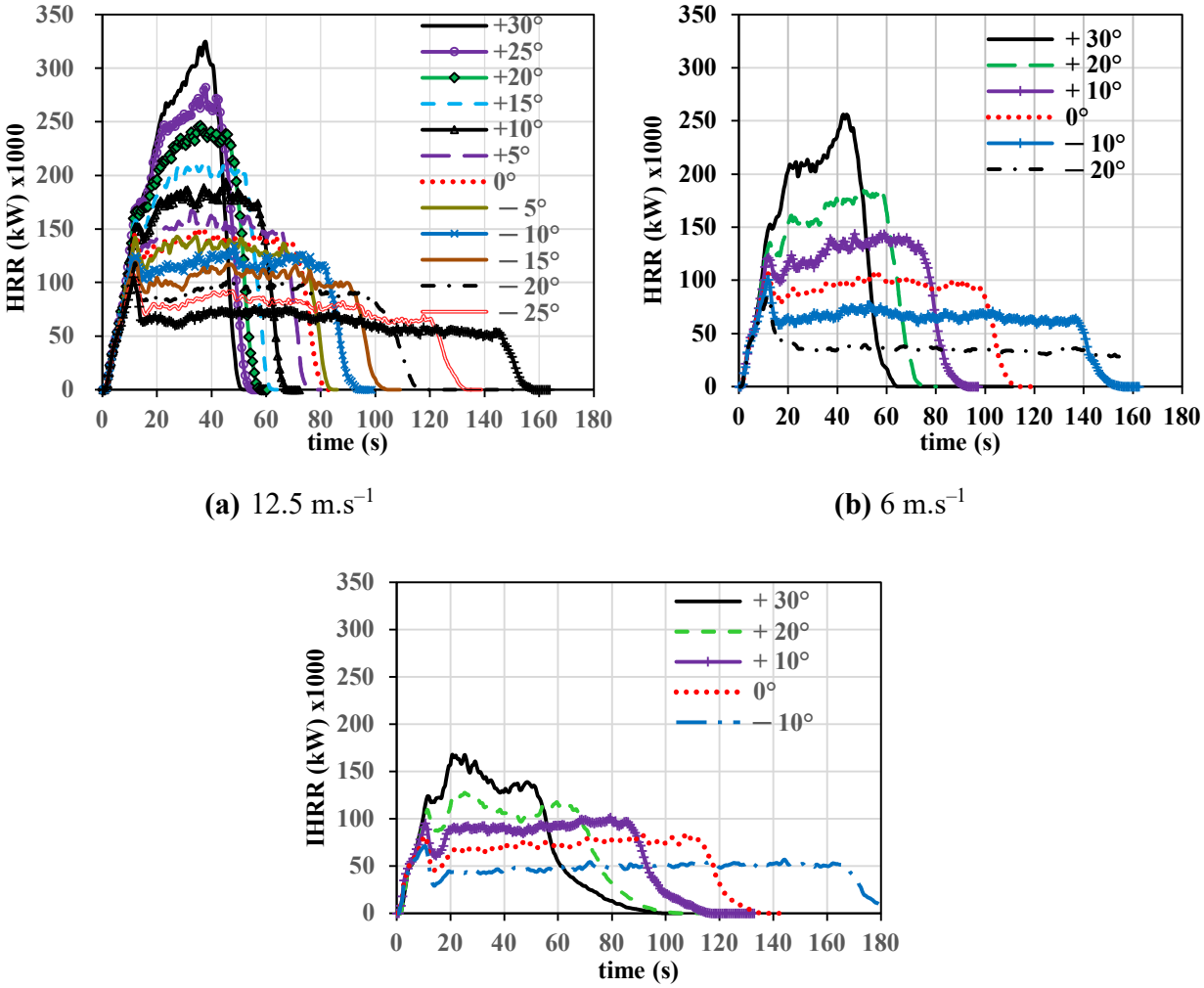

(a) 12.5 m.s^{-1}

(b) 6 m.s^{-1}

(c) 3 m.s^{-1}

Figure 4.16 – HRR vs time at wind velocities: (a) 12.5 m.s^{-1}; (b) 6 m.s^{-1}; (c) 3 m.s^{-1}

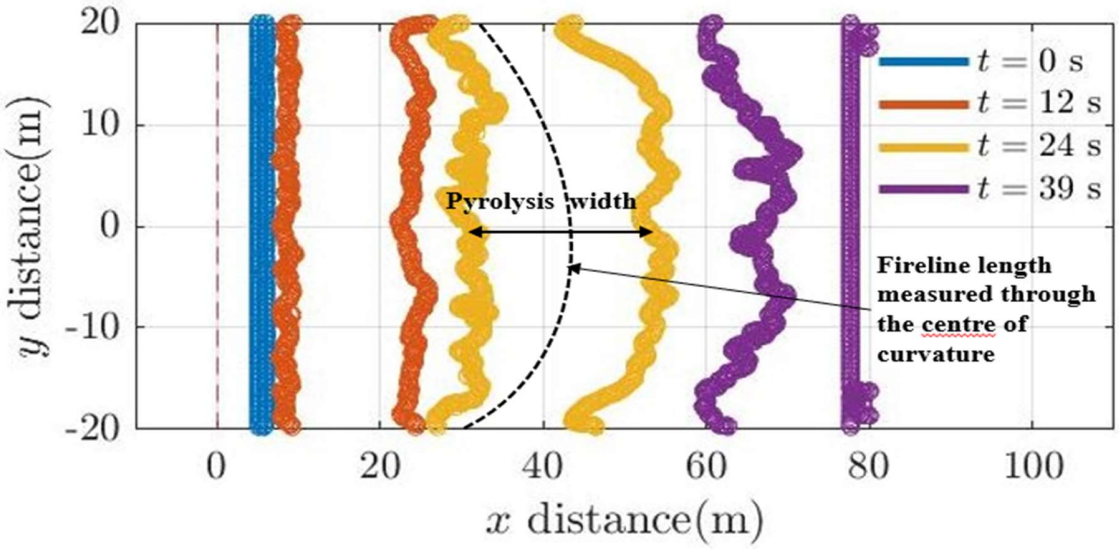

(a) method used for higher wind velocity cases

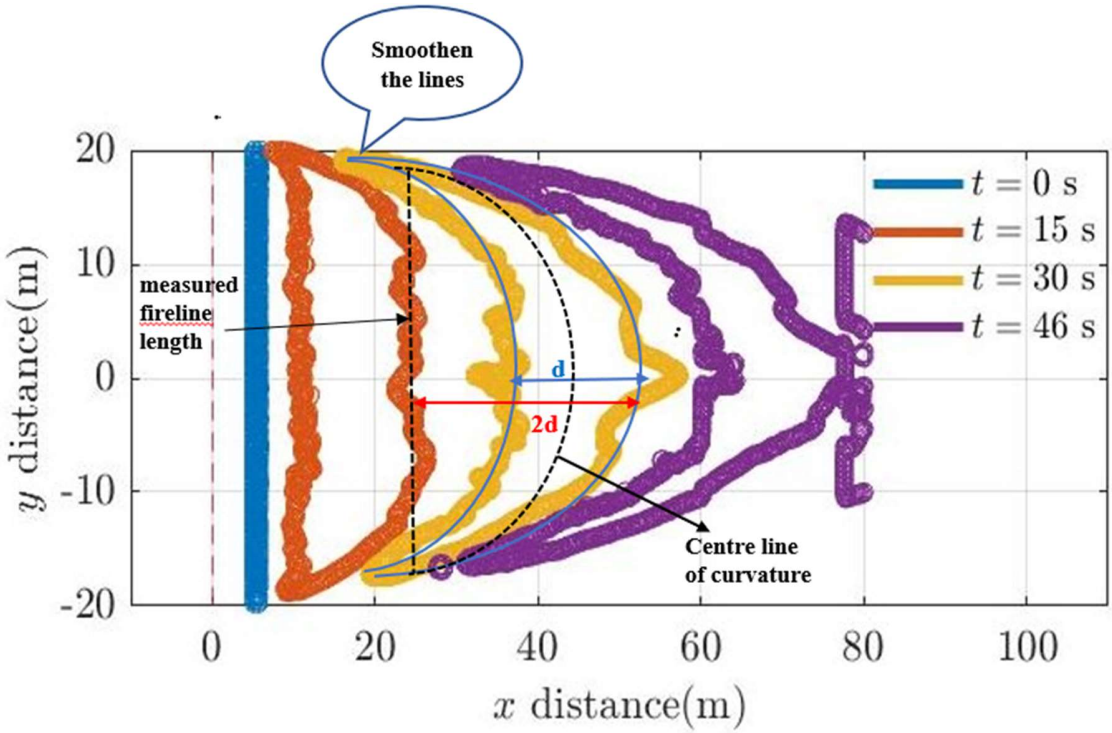

(b) method used for 3m.s^{-1} cases

Figure 4.17 – Methods used to measure firefront length from fire isochrone plots (typical case) for: (a) 12.5 and 6 m.s^{-1} cases; and (b) 3 m.s^{-1} cases. The letter 'd' denotes pyrolysis width. The contour plots are taken from +30° slope case, at 12.5 m.s^{-1} and 3 m.s^{-1}, respectively.

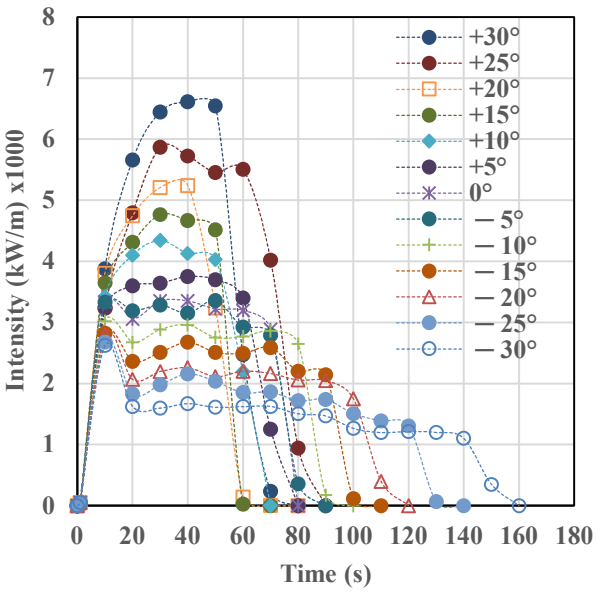

(a) Intensity vs time – 12.5 m.s^{-1}

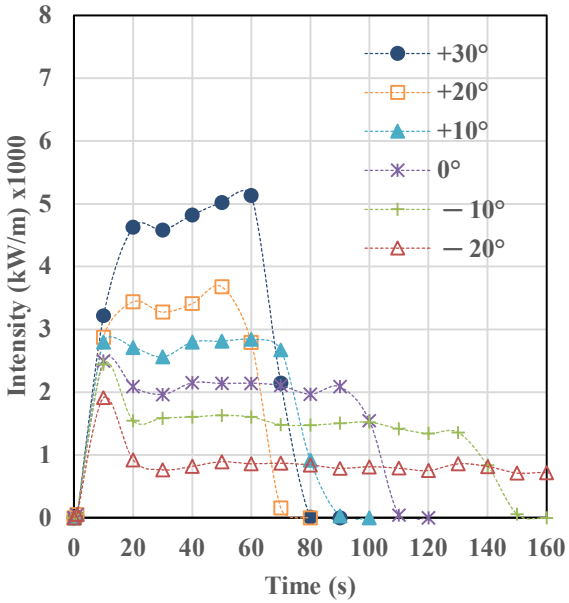

(b) Intensity vs time – 6 m.s^{-1}

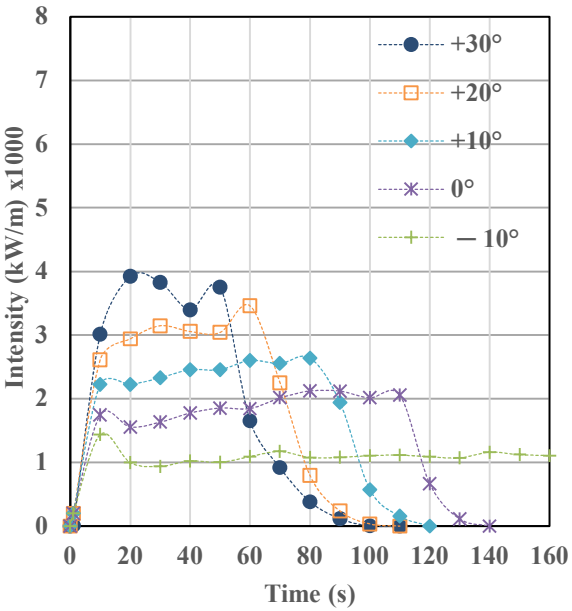

(c) Intensity vs time- 3 m.s^{-1}

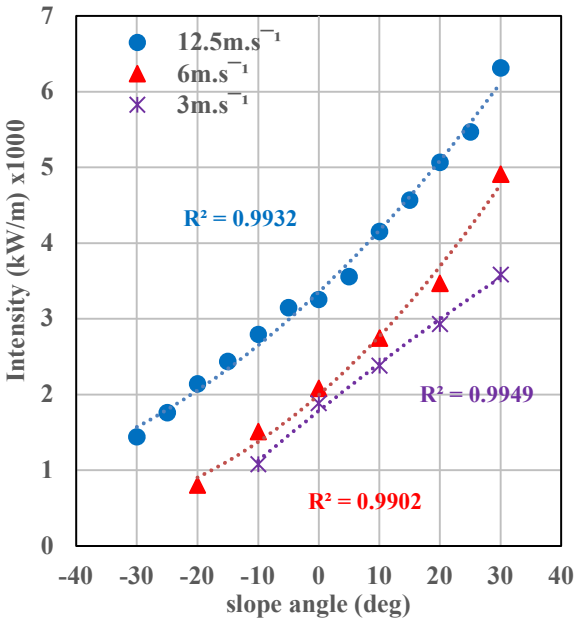

(d) Quasi-steady intensity vs slope angle

Figure 4.18 – Fire Intensity *Q* as a function of time at wind velocities of: (a) 12.5 m.s^{-1}; (b) 6 m.s^{-1}; (c) 3 m.s^{-1}; and (d) quasi-steady intensity vs slope angles, at 12.5, 6 and 3 m.s^{-1}. (for +30° at 12.5 m.s^{-1} and 6 m.s^{-1} cases, the values are derived from longer grass plot simulation results)

On sloped terrain, for a given slope angle, the Q value increases with the driving wind velocity (Figure 4.18d). For all three wind velocities, the quasi-steady Q value for +10° is approximately 26–32% higher than that of 0° slope. At 12.5 and 6 m.s^{-1}, the increase of Q with slope appears to follow a second-order polynomial relationship, whereas for 3 m.s^{-1} the relationship can also be developed as linear. Table 4.6 shows the different relationships obtained between quasi-steady intensity and slope angle and Figure 4.18(d) shows the R^2 value using polynomial fit.

Table 4.6: Intensity vs slope angle relationship

Pattern	**12.5 m.s^{-1}**	**6 m.s^{-1}**	**3 m.s^{-1}**
Exponential	$3246.2e^{0.0228x}$	$1866.9e^{0.0339x}$	$1649.4e^{0.0285x}$
R^2	0.9813	0.9871	0.9574
Polynomial	$0.5471x^2 + 75.852x + 3353.7$	$0.7619x^2 + 69.805x + 1994.2$	$0.1838x^2 + 64.268x + 1783.3$
R^2	0.9932	0.9902	0.9949
Linear	$75.852x + 3545.2$	$77.424x + 2197.4$	$60.592x + 1764.9$
R^2	0.9791	0.9702	0.9936

In Figure 4.19, Q (quasi-steady) is plotted against RoS (quasi-steady RoS obtained from Figure 4.13 (b-d)), for the three wind velocities. The relationship is linear for 12.5 m.s^{-1} wind velocity (R^2 value is shown) and the same linear relationship is observed for other two wind velocities until certain upslope angle. For 6 and 3 m.s^{-1} wind velocities, the data set falls in the linear regression fit up to +10°) and deviation from the linearity occurs after +10°. Beyond +10° slope a quadratic dependence of Q on RoS is noted (polynomial relationship, R^2 values are shown). For these wind velocities, the no-slope cases fall on the linear line (shown with circles). This shows that Q-RoS relationship deviates from linearity as the driving wind velocity decreases, and it occurs at higher upslope angles.

Byram's fire intensity (Byram 1959) model equation is given by,

$$I = H \times w \times RoS \qquad (4.5)$$

where H is the heat of combustion of the fuel (kJ.kg^{-1}), RoS is the rate of fire spread (m.s^{-1}) and I is the intensity (kW.m^{-1}). In some literature w is total fuel load (kg.m^{-2}) and in others, total fuel consumed. There is no empirical value available as to what % or fraction of fuel load can be consumed. By matching with the intensity vs RoS linear line, we have determined that a factor of 0.42 to the total fuel load is suitable to satisfy Byram's intensity equation. Considering all values from all velocities on the linear line, it appears that Byram's intensity (Byram 1959) (Q = fuel load × heat of combustion × RoS) is satisfied with ~42% fuel load, instead of 100% fuel load, for all cases at 12.5 m.s^{-1} and up to (including) +10° for 6 and 3 m.s^{-1} wind velocities.

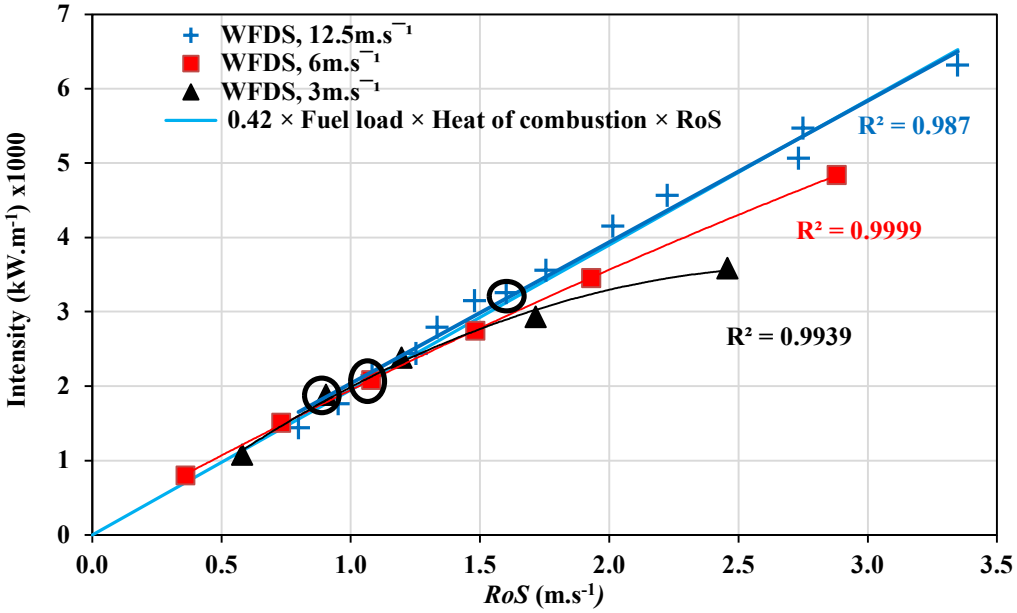

Figure 4.19 – Fire intensity *(Q)* as a function of *RoS* . The black circles represent the values at no-slope case for all three wind velocities.

4.4.4 Plume and flame dynamics

To visualise the plume contours, the instantaneous temperature slice output files obtained from the simulations are analysed using the numeric computing software Matlab (https://mathworks.com), (Davis and Sigmon 2005). The temperature slice data are obtained through the geometric centreline of the burnable grass plot and temperature contours for all cases are extracted at about the same instant of time, 30 s after ignition (± 1 s variation). This study acknowledges that fire behaviour can vary as the fire progresses. Caution needs to be taken in interpreting these plots since they represent indicative plume behaviour of the turbulent flow at the instant. This best

instant in time was selected after cautious examination to be a broadly representative of the fields that reflect the finest graphic representation of plume attachment and up-rising behaviour for the cases presented.

The temperature contours (representing plumes) are plotted in Figure 4.20 for each of the slope cases, at the same instant in time as the fire moves though the burnable grass plot in the *x*-direction, for the three wind velocities. These plots represent indicative behaviour of plume at a particular instant of time (30 s after ignition) which reflect the plume attachment or up-rising behaviour for the cases presented.

To compare fires at a point where they have consumed a similar amount of fuel, we have also presented the fire's plume contour at the same distance from ignition line, for all the cases. The plume contour at the same firefront position (from ignition line) for 0°, +10°, +20° and +30° are shown in Figure S4.7 of Appendix A, for all three wind velocities.

The plume is shown by colour shading that represents air temperature (K), in the same temperature scale (indicated in the colour bar in the frames) for the same wind speed cases. Plumes (instantaneous) emanating from the fire front for 0°, +10°, +20° and +30° upslopes at wind velocity 12.5 $m.s^{-1}$ are shown in frames (a–d); at 6 $m.s^{-1}$ are shown in frames (e–h); and at 3 $m.s^{-1}$ are shown in frames (i–l). Frames (m–o) represent the downslope angles: –10°, –20°, –30° at 12 $m.s^{-1}$; and Frames (p–r) show –10°, –20° at 6 $m.s^{-1}$ and –10° at 3 $m.s^{-1}$.

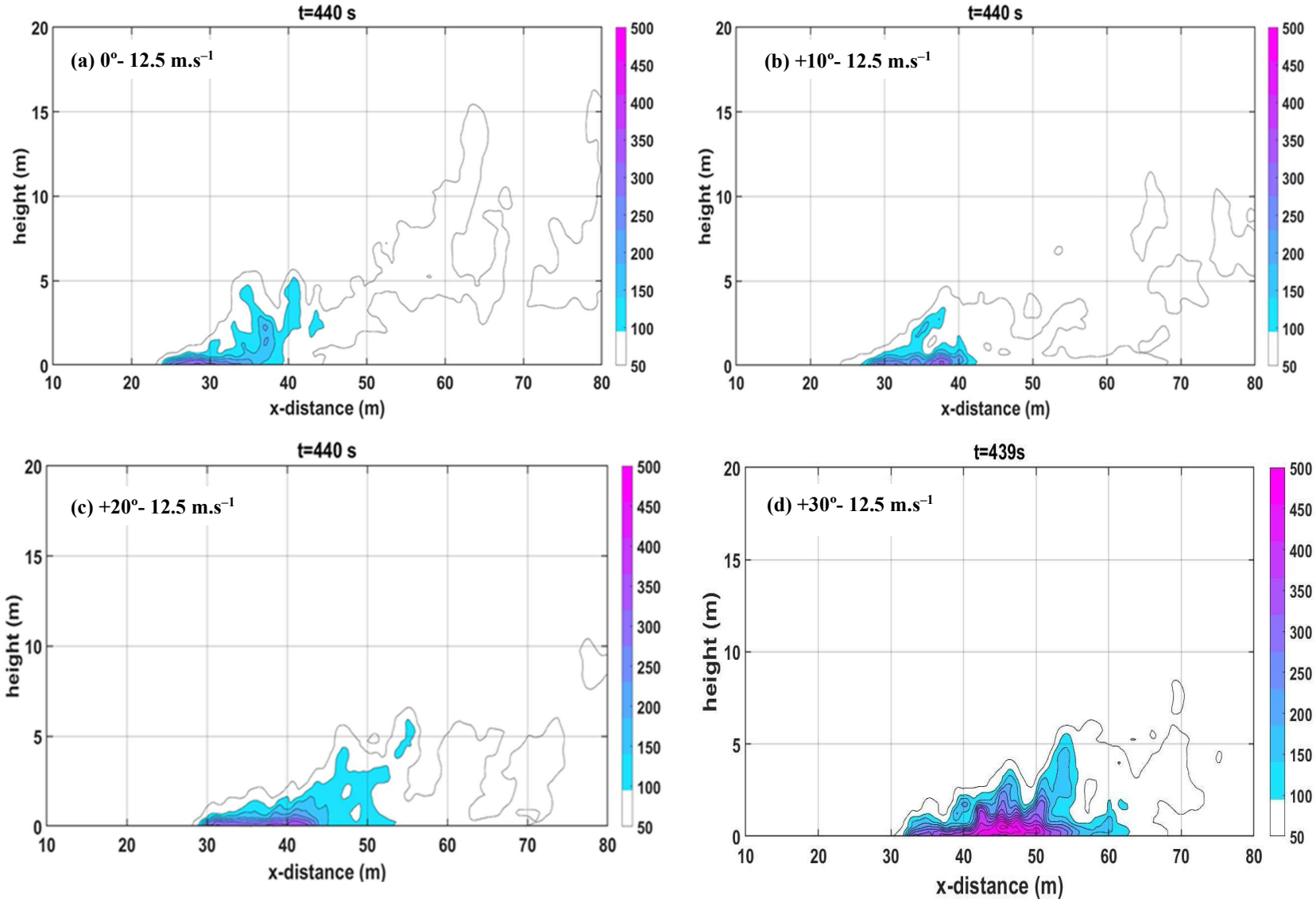

Figure 4.20 (a–d). Plume contour, upslopes at 12.5 m.s^{-1}: 0°, +10°, +20°, +30°

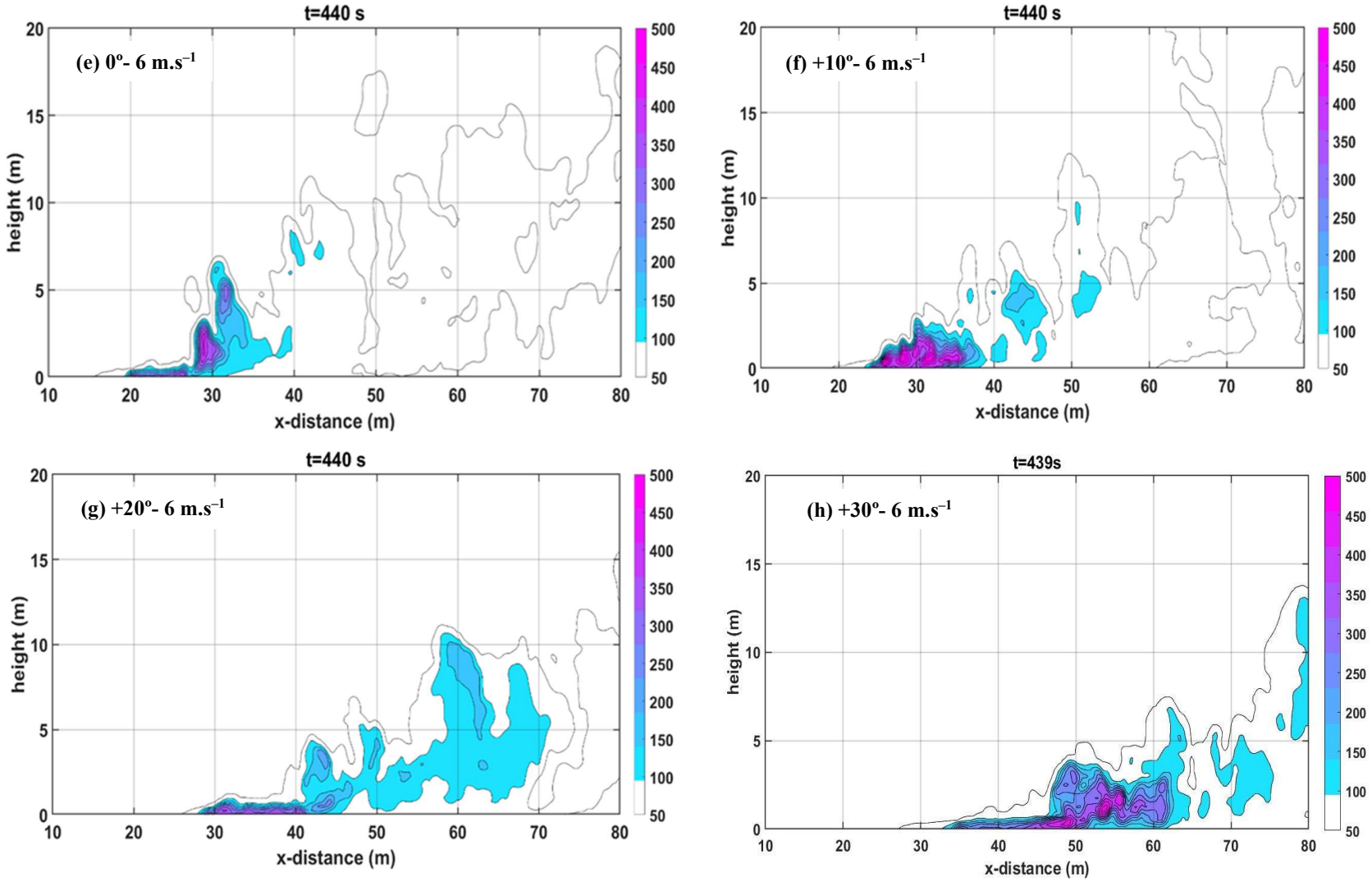

Figure 4.20 (e–h). Plume contour, upslopes at 6 m.s^{-1}: 0°, +10°, +20°, +30°

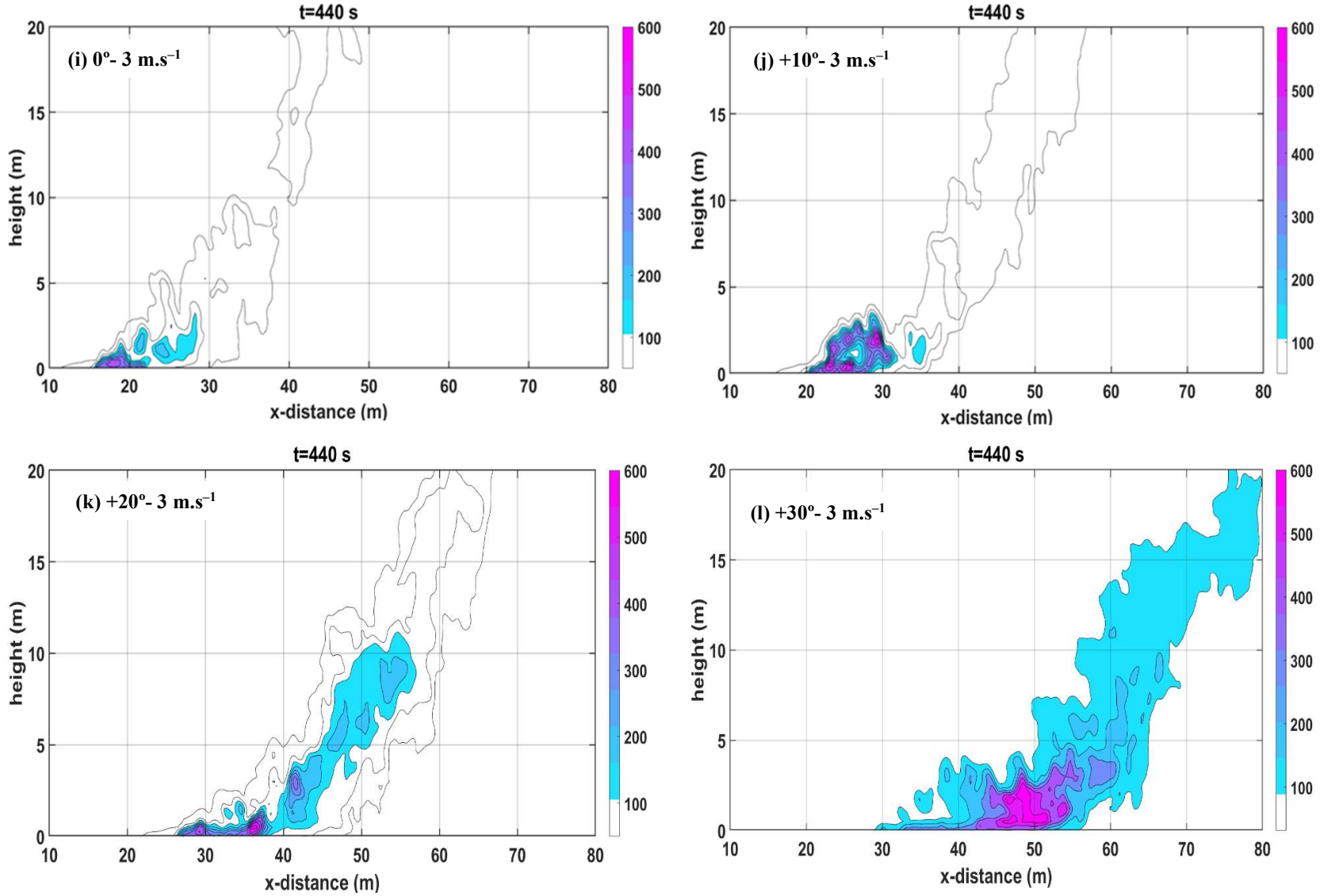

Figure 4.20 (i–l) Plume contour, upslopes at 3 m.s^{-1}: 0°, +10°, +20°, +30°

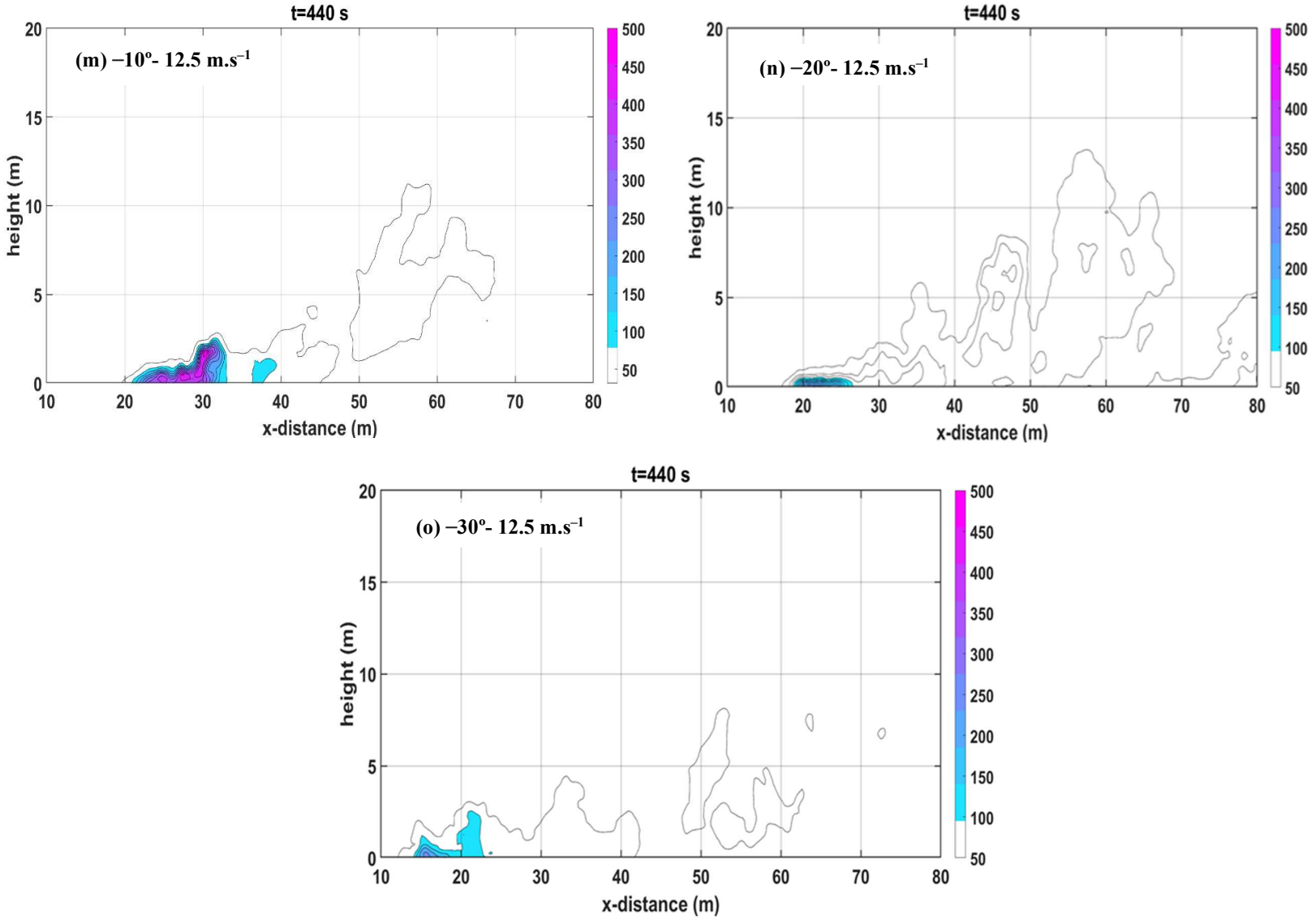

Figure 4.20 (m–o). Plume contour, downslope cases: –10°, –20°, –30° at 12.5 m.s^{-1}

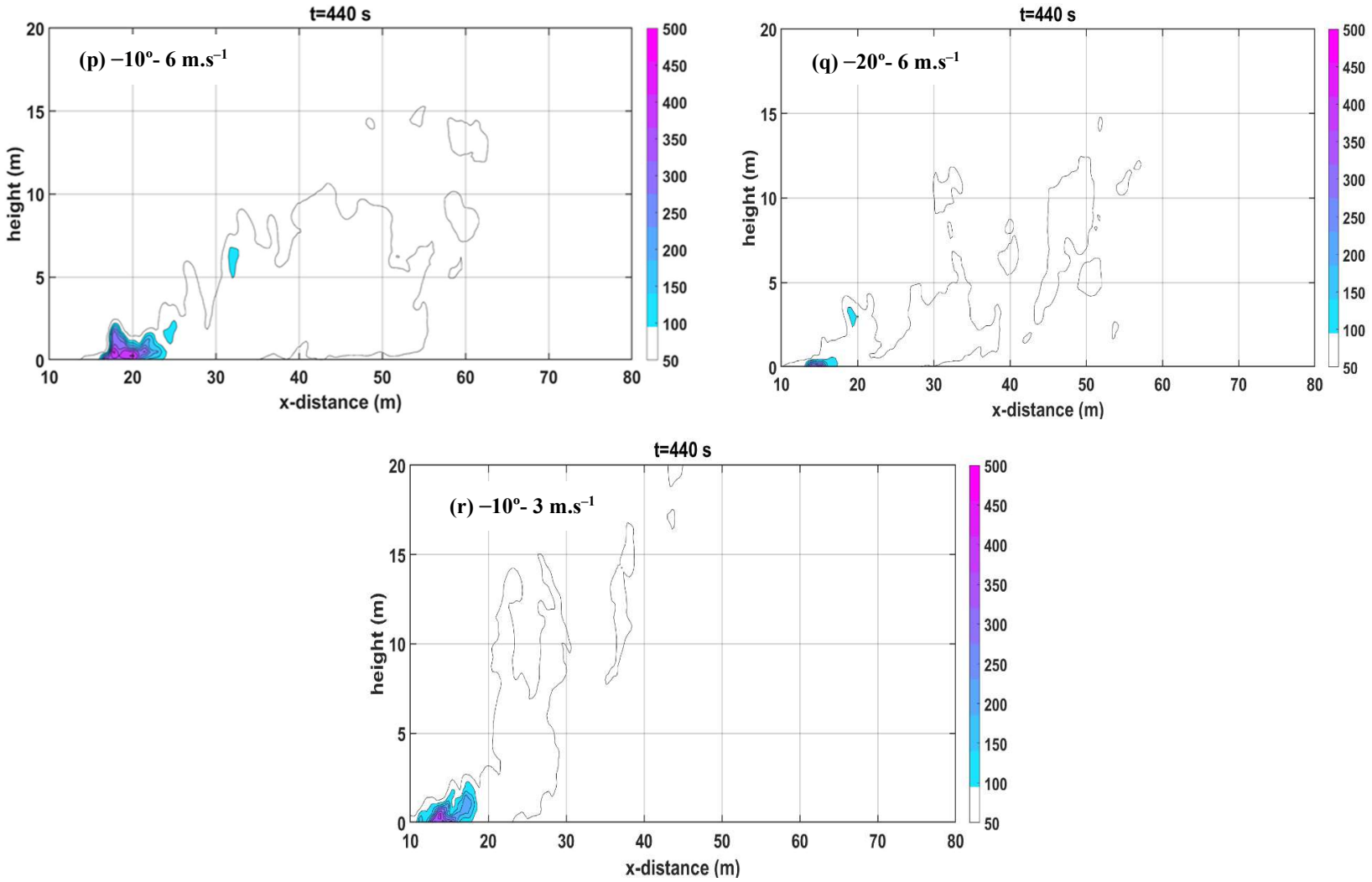

Figure 4.20 (p–r). Plume contour, downslope cases: –20°, –30° at 6 m.s^{-1} and –10° at 3 m.s^{-1}

Figure 4.20 – Temperature contours (representing plumes) at the same instant in time, for upslopes and downslopes.

At 12.5 m.s^{-1} wind velocity, the fire front travels more quickly and the plume is leaned (leads to its attachment) to the ground for all three cases, as shown in frames (a–d). At +20° and +30°slopes, the plume is more inclined towards the ground, as evident for +30° where the plume can be seen attached nearly until the end of the burnable plot. The same trend is generally observed with 6 m.s^{-1} upslope cases as well (fames e–h) where the plume can be seen inclined towards the ground; however, for the instances shown, the inclination distance (the distance covered by the plume when it is attached to the ground) is shorter compared with 12.5 m.s^{-1} cases for the same upslope angle. Inspecting the same data at slightly later or earlier, the observation can be different on higher upslopes. The interaction between the plume and the terrain is captured clearly for +30° slope cases where the plume is attached for nearly half of the burnable grass plot at most instances.

Frames (i–l) show that for 3 m.s^{-1} wind velocity, the plume rises from the ground near the ignition line for 0° and +10° slopes, and for greater upslopes, the buoyant plume inclines towards the ground for a longer distance. However, compared with higher wind velocity cases, for the same slope angle, the plume rises earlier.

For downslopes, frames (m–r), the plume rises from the ground earlier compared with upslope cases. As the downslope angle increases, the plume rises from the ground at shorter distances and fire does not propagate, consistent with the fire isochrones progression shown in Figure 4.7. As stated previously, the fire (and hence plume) extinguishes for steep downslopes at lower wind velocities (–30° at 6 m.s^{-1}, –30° and –20° at 3 m.s^{-1}) and hence these cases are not included in the plot.

The plume contour plotted at the same fire front location (Figure S4.7 of appendix A) shows similar behaviour and interaction pattern as demonstrated with the contours plotted at same instant in time (Figure 4.20), for the respective wind velocity.

As the wind speed increases, the plume attachment occurs at much lower slope angle, as shown in Figures 4.20 (a–d). Overall, these results show similarity to the observations of Dold and Zinoviev (2009) and Sharples (2017) that plume attachment occurs owing to an interaction between the slope of the terrain and the plume itself.

Defining and measuring where the flame is attached to the ground is difficult. Empirical measurements of flame attachment (for example, the experiments of (Tang *et al.* 2017) are based upon visual intensity thresholds in a prescribed region of interest. The detachment location shown in these frames is where the plume lifts off from the ground at that time frame. At detachment, the vertical velocity will be greater than the streamwise velocity (Burridge and Hunt 2017). It is then possible to study the behaviour of

$$\theta(x,z,t) = \operatorname{atan}\left(\frac{W}{U}\right), \tag{4.6}$$

where U and W are the streamwise and vertical components of the wind velocity at the y centreline of burnable grass plot, to estimate the detachment location. Specifically, we consider the mean of θ in the z-direction, denoted

$$\bar{\theta}(x,t) = \langle \theta(x,z,t) \rangle_z, \tag{4.7}$$

in the neighbourhood of the flame. The detachment location, x_d, is then defined as the location of the first zero-crossing of $\bar{\theta}(x)$, that is, the first negative to positive crossing of average θ The neighbourhood of the flame is taken as the rectangle extending from z = 0 to five times the maximum z-value of the flame contour, and from the minimum x-value of the pyrolysis region to x = L_x (the location of the end of the burnable plot). Because we only consider the first (lowest x value) zero crossing the maximum x-point in the neighbourhood is immaterial. The two points either side of the zero crossing are averaged to obtain x_d, Since this process is repeated for all times, we obtain a time series of x_d, Note that each field discussed is at an instant in time and hence every quantity is then a function of time.

To understand the flame behaviour, it is useful to visualise the flame contours, temperature contours, detachment location and wind velocity vectors taken through the centreline of the burnable grass plot at various instants in time.

To visualise the flame contours, the output files obtained from the simulations are analysed using the numerical computing software Matlab (Davis and Sigmon 2005), (https://mathworks.com). Streamwise and vertical components of wind velocity *U* and *W*, HRR and temperature data, taken through the centreline of the burnable grass plot, are analysed to obtain the flame and temperature contours and the velocity quiver plots. The flame envelops are determined from minimum

threshold temperature of 400K to maximum temperature of the flame. Co-incidentally the same 400K threshold is used for flame envelopment as well as the onset of pyrolysis of the surface fuel.

The contours are plotted in Figure 4.21as the fire moves though the grass plot, at five instants in time from start of ignition, for each of the three wind velocities 12.5, 6 and 3 $m.s^{-1}$. The plot shows flame contour (red), with temperature contours shaded in the background (yellow), along with flame detachment or up-rising locations (black dots) and wind vectors (white arrows) at three slope angles (+30°, +10° and 0°).

The wind velocity vectors are presented to visualise the flow pattern and demonstrate the dynamic behaviour as the fire progresses. Such dynamic behaviour is the result of dynamic pressure differences between zones upstream and downstream of the flame, consistent with (Eftekharian *et al.* 2019, Eftekharian *et al.* 2020).The vectors show instantaneous flow direction and thus a picture of the turbulence at a particular instant. In order to understand entrainment trends, one would need to build an ensemble average of the wind as the fire moves. This has been attempted by Sutherland *et al.* (2022). However, this is beyond the scope of the current manuscript. Eftekharian *et al.* (2020), in their simulation study, found that the strongest fire-induced pressure gradient occurs in the low-density region immediately downstream of the fire source, causing maximum wind enhancement, and wind enhancement gradually decays longitudinally along the plume line further downstream of the fire.

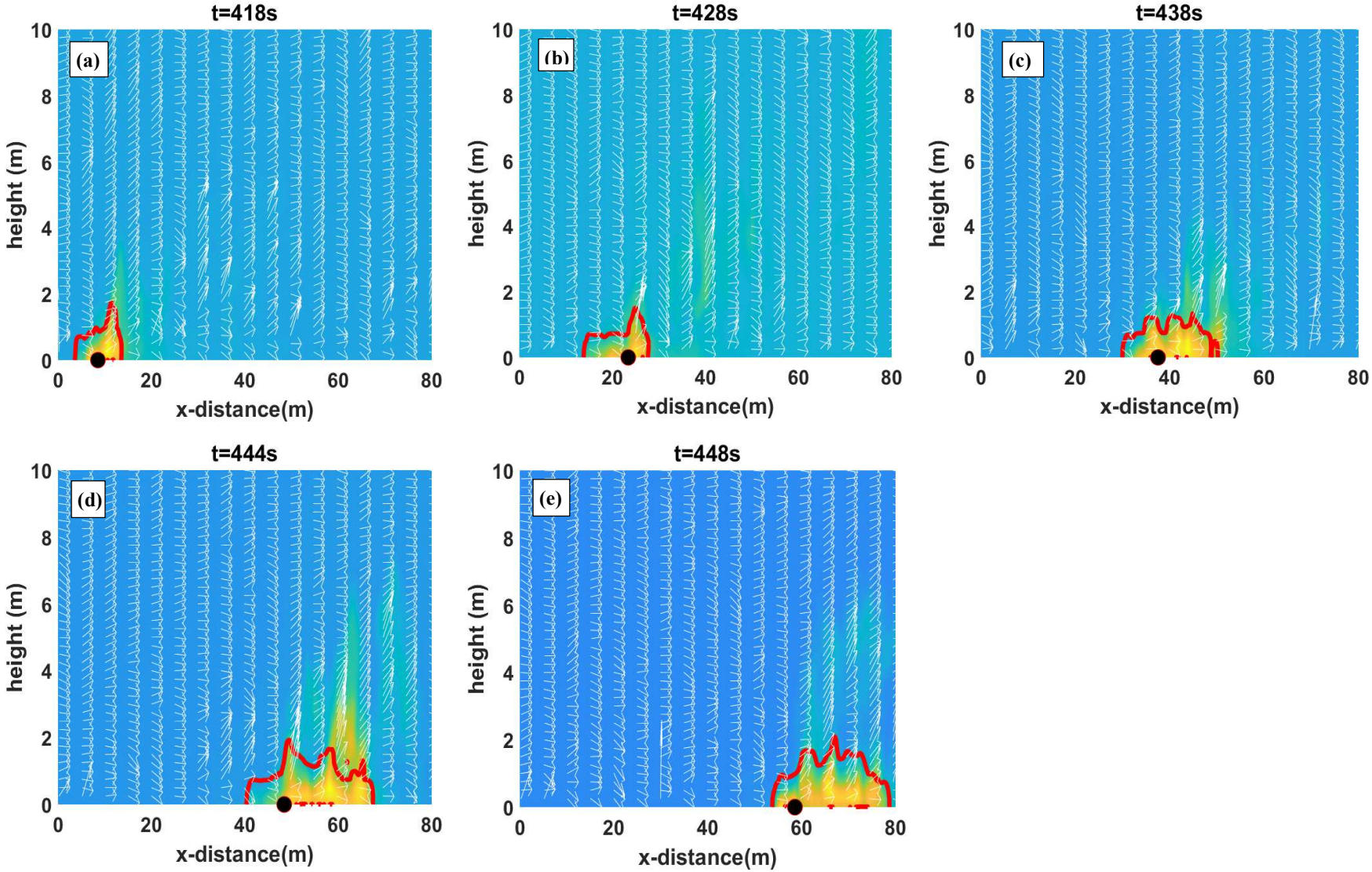

Figure 4.21 (a–e). +30° at 12.5 m.s^{-1}

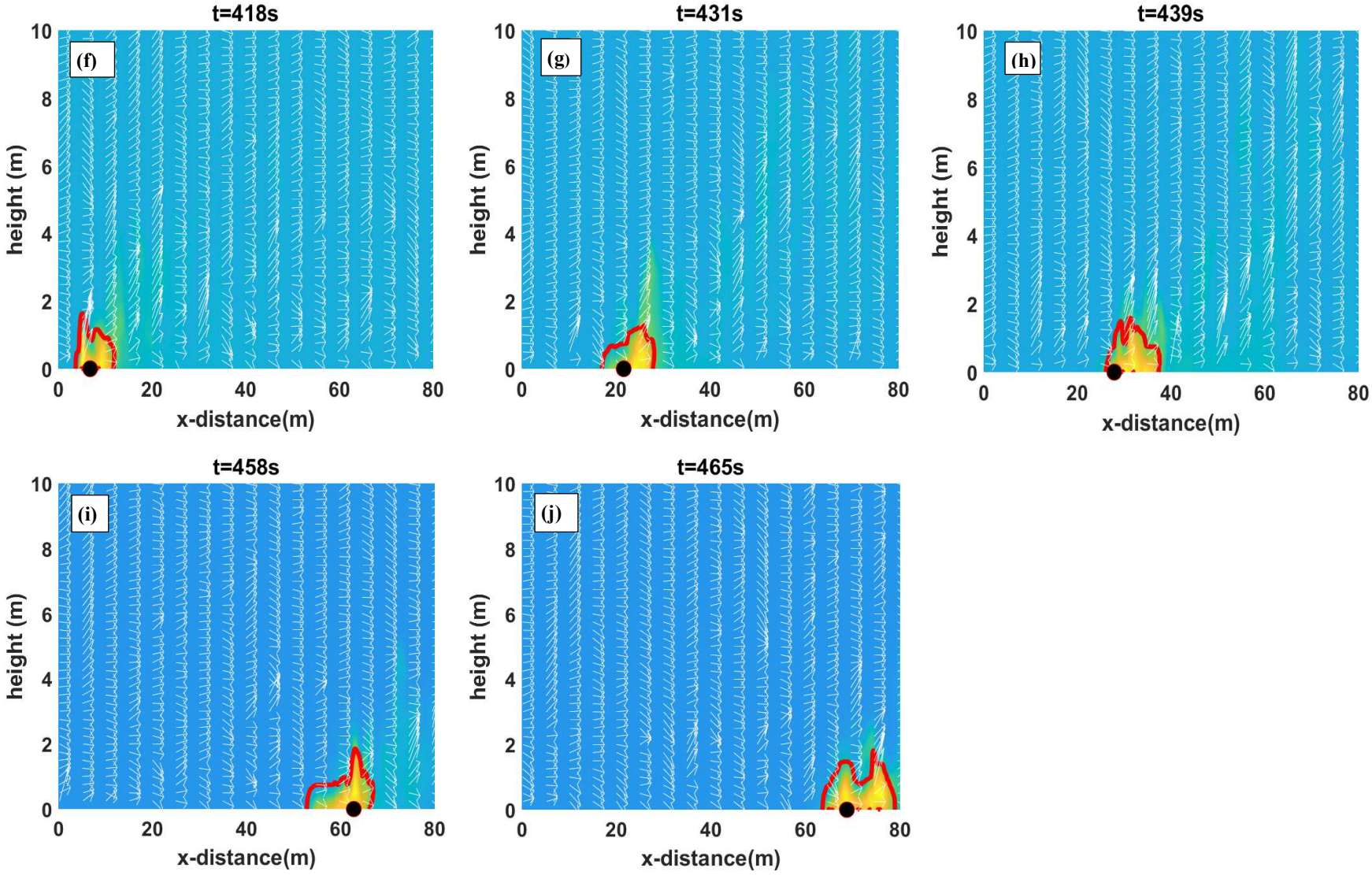

Figure 4.21 (f–j). +10° at 12.5 m.s^{-1}

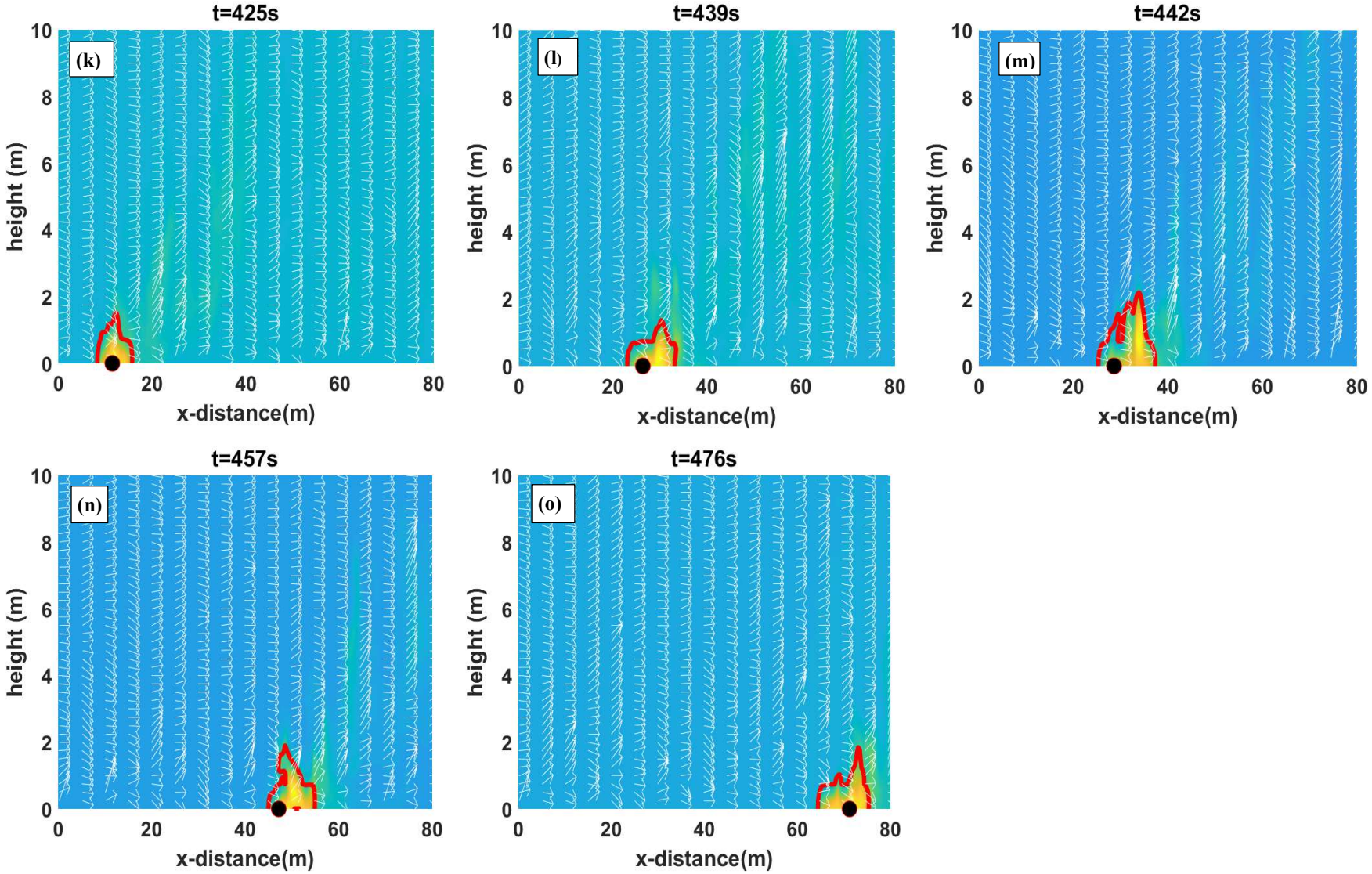

Figure 4.21 (k–o). 0° at 12.5 m.s^{-1}

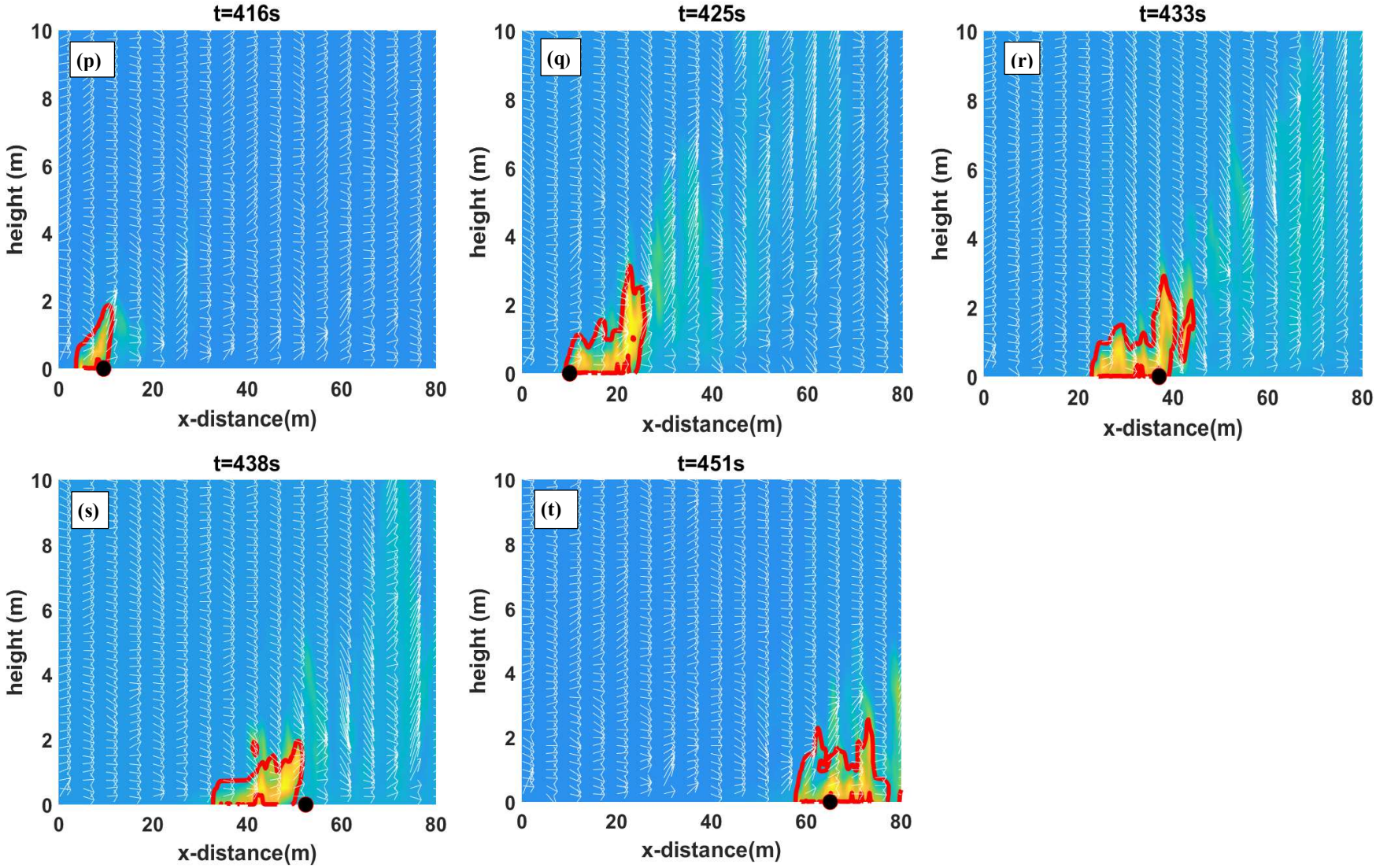

Figure 4.21 (p–t). +30° at 6 m.s^{-1}

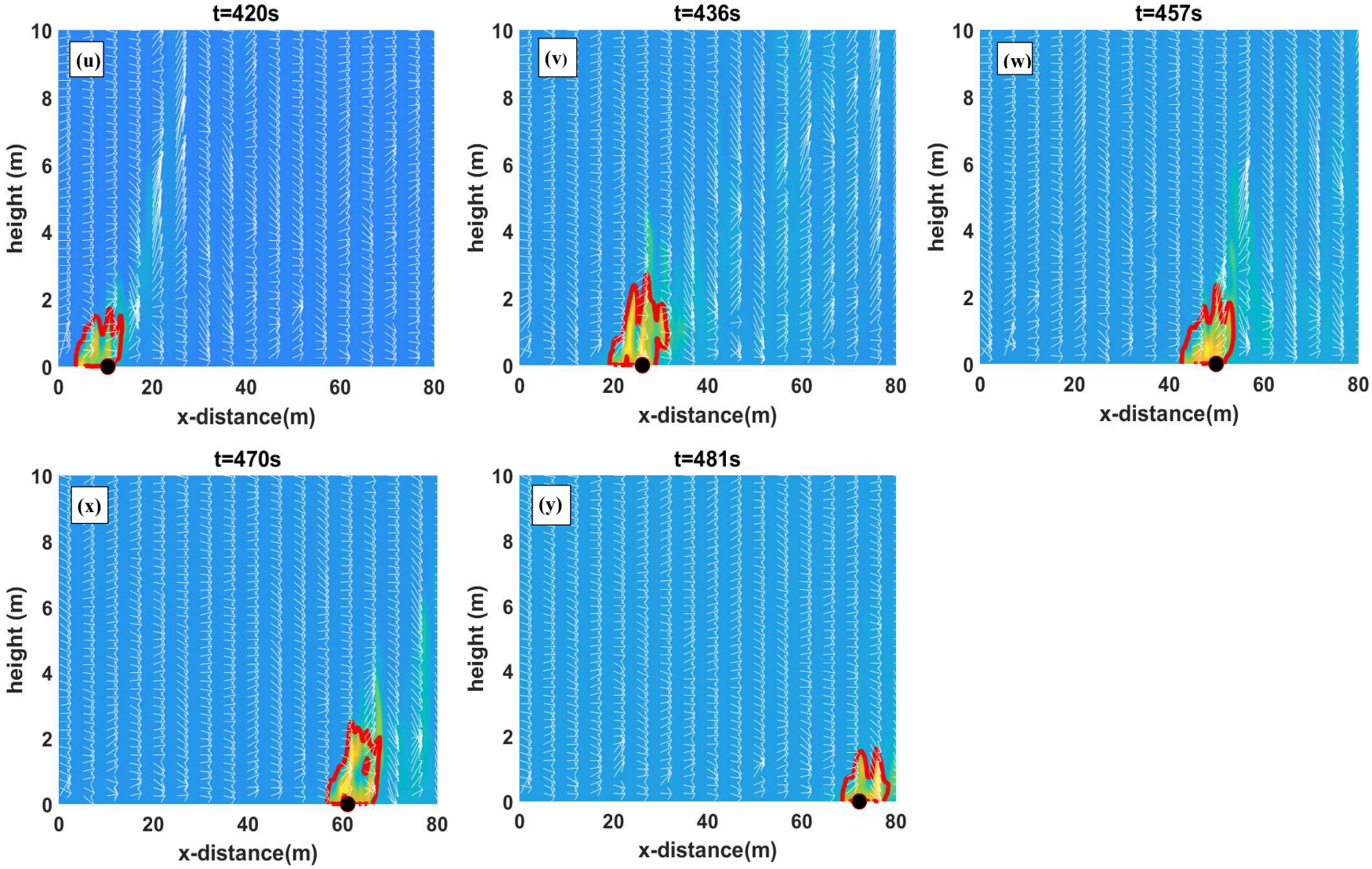

Figure 4.21 (u–y). +10° at 6 m.s^{-1}

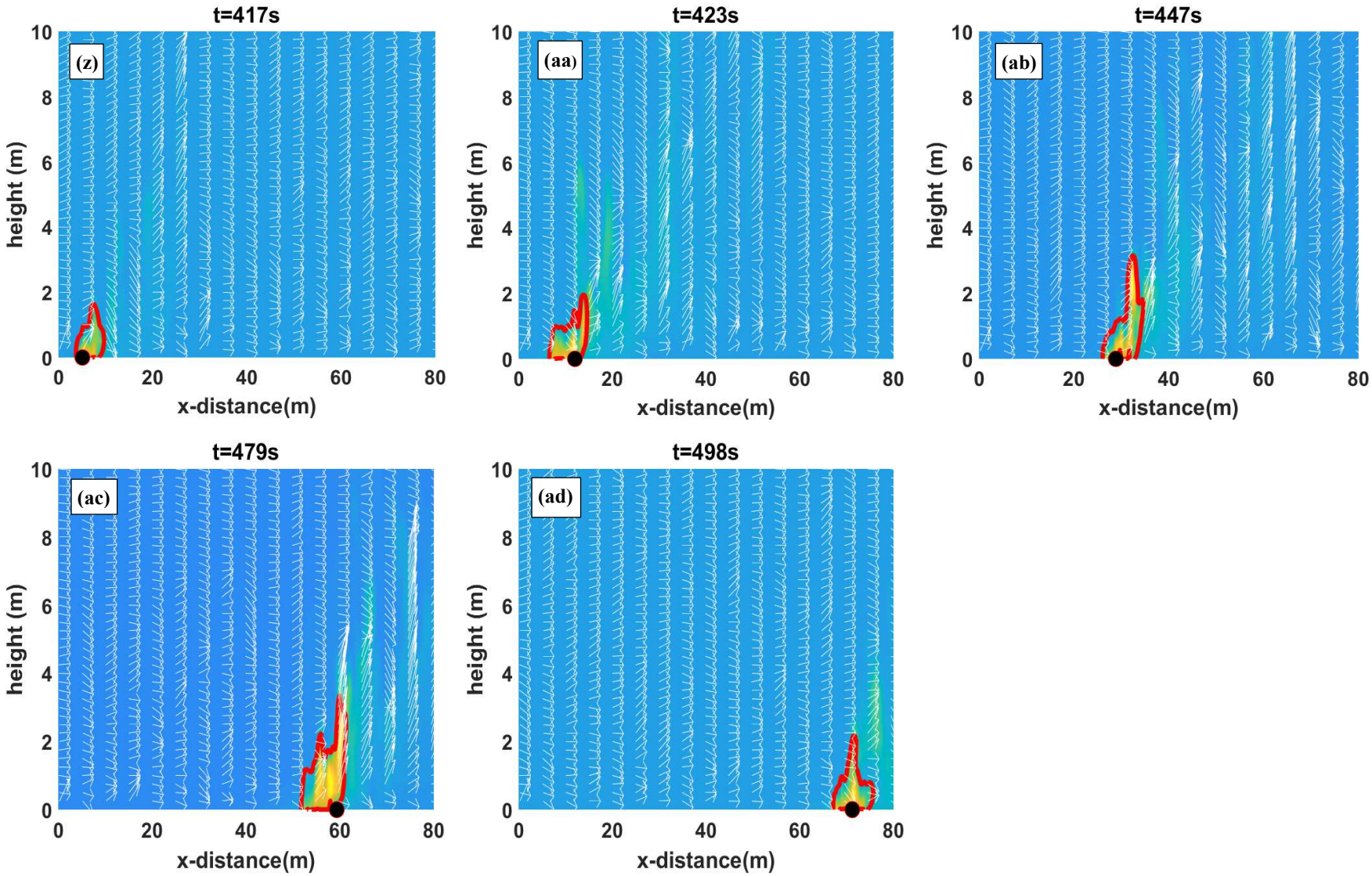

Figure 4.21 (z–ad). 0° at 6 m.s^{-1}

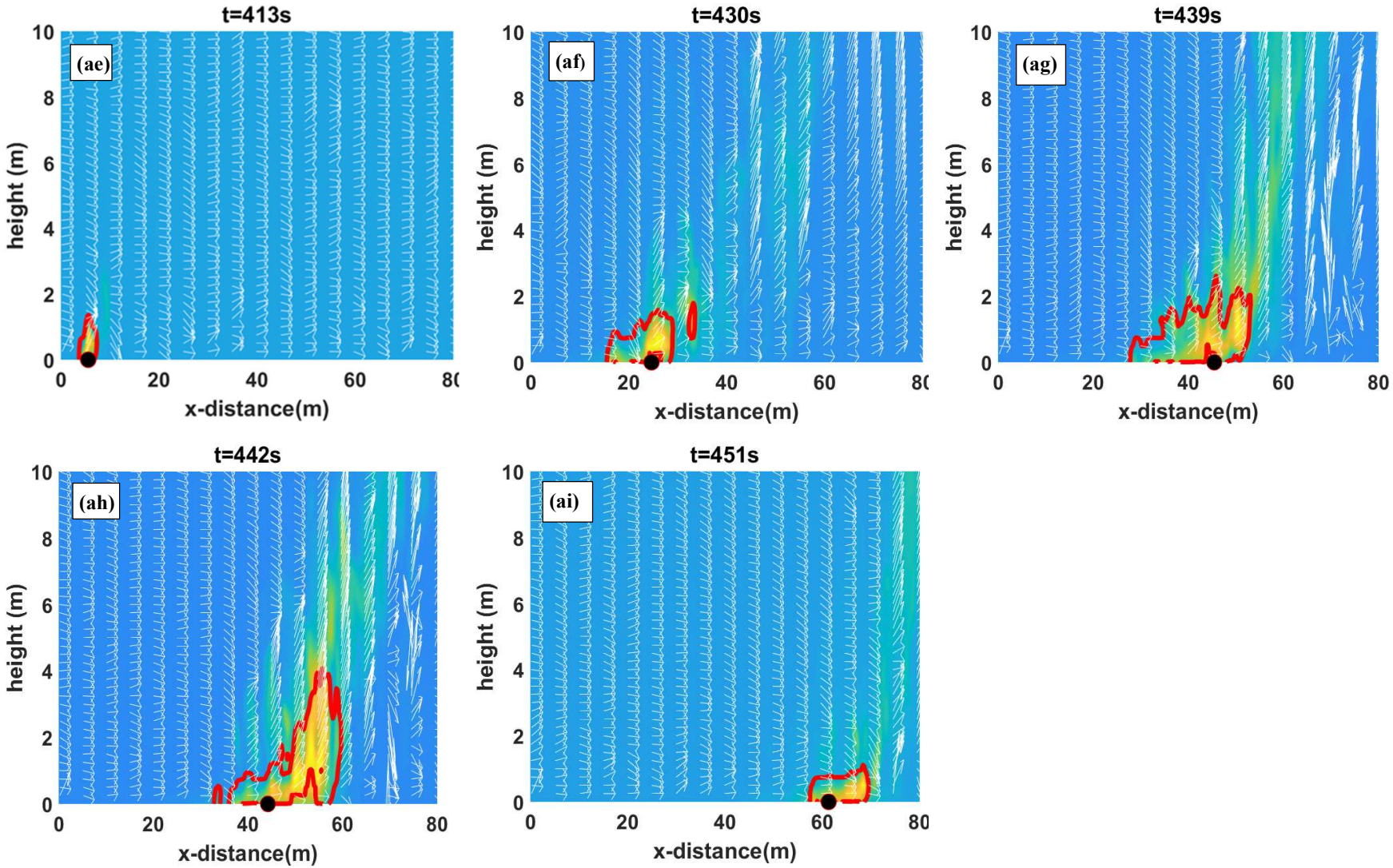

Figure 4.21 (ae–ai). +30° at 3 m.s^{-1}

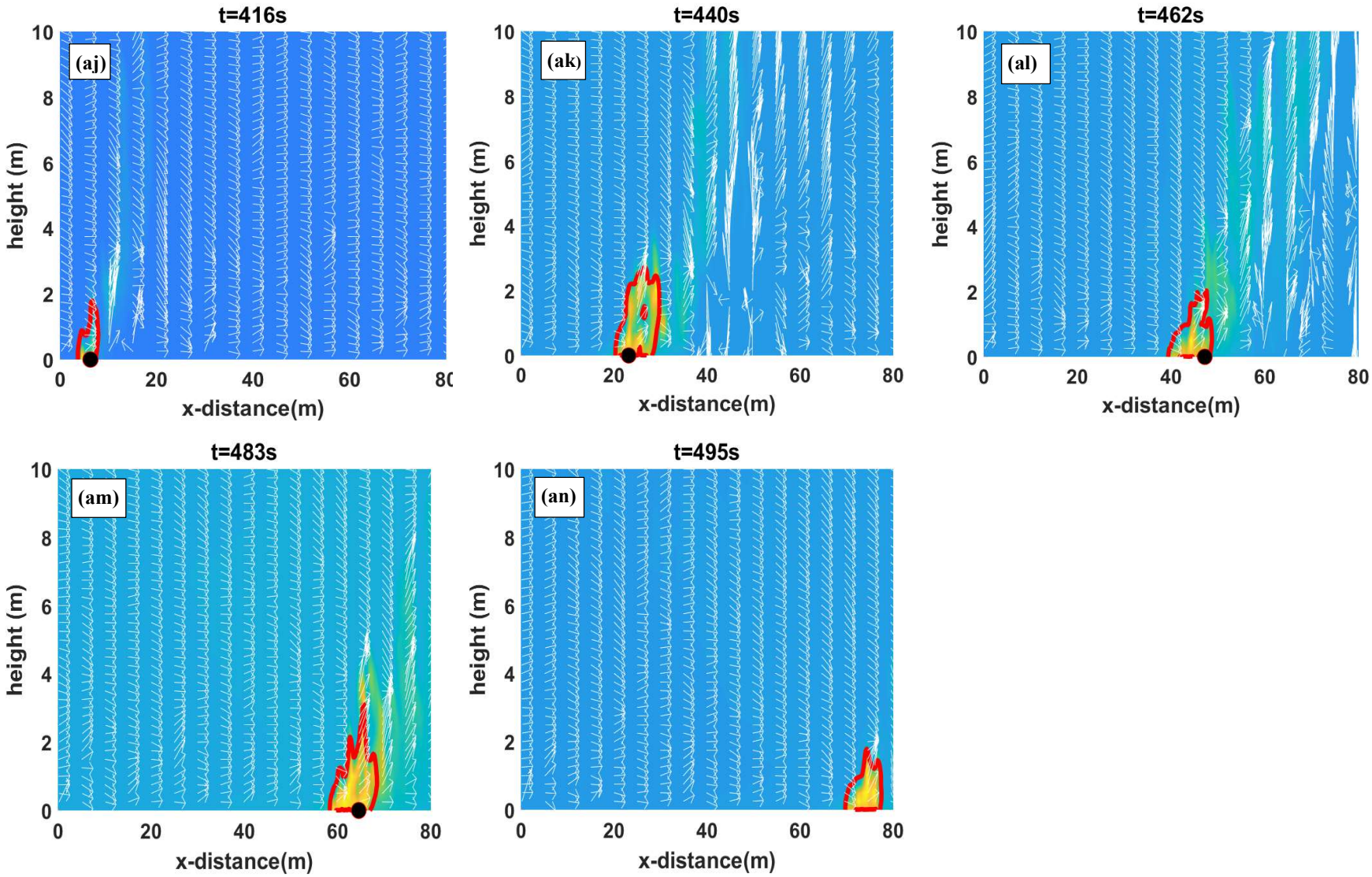

Figure 4.21 (aj–an). +10° at 3 m.s^{-1}

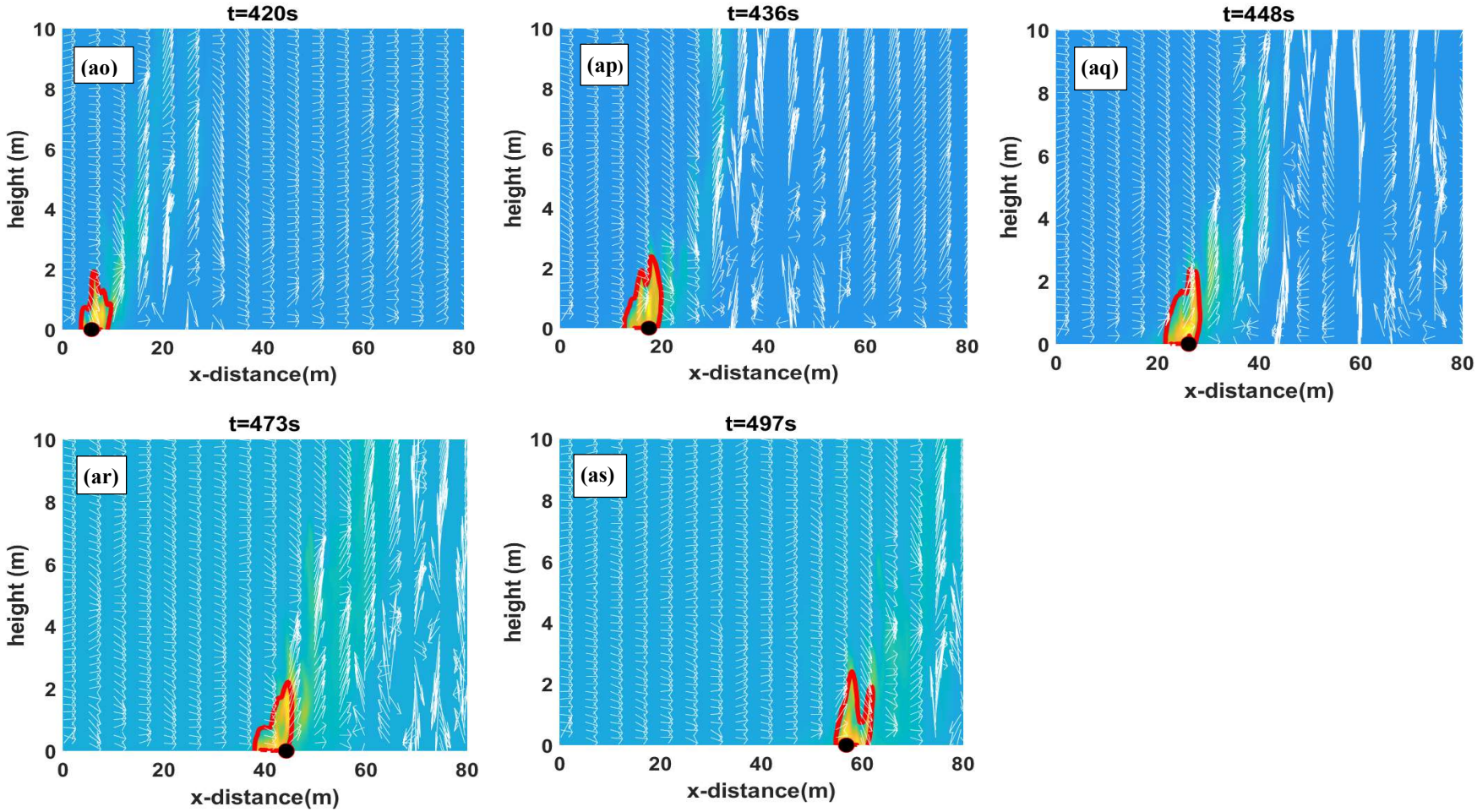

Figure 4.21 (ao–as). 0° at 3 m.s^{-1}

Figure 4.21 – Flame contour (red) with temperature contour shaded in the background (yellow)along with detachment locations (black dot) and wind vector plots (white arrows), at various instants in time for wind velocities 12.5, 6 and 3 m.s^{-1}. Figures (a–o): +30°, +10° and 0° at 12.5 m.s^{-1}; (p–ad): +30°, +10° and 0° at 6 m.s^{-1}; (ae–as): +30°, +10° and 0° at 3 m.s^{-1}

Figures 4.21 (a–o) represent +30°, +10° and 0° at 12.5 m.s^{-1} wind velocity. For the highest slope angle +30°, at the initial time point, the near flame behaviour is vertical, and the flame-perturbed velocity vector is inclined upward. However at (x,z) locations far downstream from the ignition line, the plume (represented by the temperature contour) is horizonal with little vertical perturbation. The flame-perturbed velocity vector inclination is closer to the surface. The flame dynamics indicate that the flame appear to be up-rising; however, the plume is leaned or attached (see Frame 4.21 (c)) as similarly observed in the plume contour Figure 4.20(d), indicating that the flame does not necessarily follow the plume behaviour. At 1 or 2 m above the ground where the wind velocity is lower, the flame behaviour appears to be buoyancy-driven (or closer to buoyancy-driven mode), whereas, at higher z-values, the velocity vector is horizontal, consistent with a wind-driven fire. As the fire moves on, it becomes more buoyancy-dominated and the flame becomes deeper (frames (c) and (d)) and finally the flame shrinks as the fuel is depleted. Slope angles +10° and 0° follow a similar pattern: buoyancy-dominated flame near the ground, tending towards a wind-dominated fire for a very short time, and then transiting to buoyancy-dominated as the fire progresses. The flame becomes deeper as the slope angle increases. For no slope, generally the flame remains vertical and pointed upwards compared with higher slope angles as evident with frames (l–n). When the fire runs uphill, the flame length is higher at the instant the flame attaches to the terrain, which is consistent with the study of Dold and Zinoviev (2009).

The +30°, +10° and 0° cases at 6 m.s^{-1} wind velocity are presented in frames (p–ad) of Figure 4.21. The plots generally reflect the same trend as 12.5 m.s^{-1} cases. For the no-slope cases, up-rising flame is observed throughout (frames aa–ac); however, as the slope angle increases, some intermittent attachment occurs, resulting in subsequent flare up of the flame. The flame is more vertical for 0° compared with +30°. As the slope angle increases, the flame becomes deeper as the fire moves on. For higher slopes, the plumes tend to be rising more compared with the cases at the higher wind velocity 12.5 m.s^{-1}, as similarly observed with Figure 4.20(h), and they appear to be more within the buoyancy-dominated regime.

The +30°, +10° and 0° cases at 3 m.s^{-1} driving wind velocity are presented in frames (ae–as). Compared with 12.5 and 6 m.s^{-1}, the plumes emanating from the grass plot are up-rising (and vertical), as similarly observed in Figure 4.20 (i–l). The fire establishes itself and then becomes inclined to the ground, which leads to rapid intensification and a buoyancy-dominated fire (frames

ag–ah). The rising of flame is more evident in the 0° case (frames ap–ar). For lower slope angles, the flame is more vertical; however, the flame becomes deeper for the highest slope angle, +30°. This agrees with (Mendes-Lopes *et al.* 2003), who in their low-velocity experimental studies observed that the flame tended to be vertical, owing to buoyancy forces.

The Byram number (N_c) is used to quantify the mode of fire propagation into wind-driven or buoyancy-driven fire mode (Mell *et al.* 2018). N_c uses the wind velocity at 10 m (U_{10}) as the relevant velocity scale. However, the results shown in Figure 4.20 demonstrate that the flame behaviour can be different from the overall plume behaviour and that N_c based upon U_{10} may capture the plume behaviour but not the flame behaviour. The mode of fire propagation is analysed in Section 4.4.5.

4.4.5 Mode of fire propagation

For the simulations presented, Byram number, N_c, (eqn 2.48, Section 2.2.2) analysis is performed to quantify the mode of fire propagation. Since N_c is dimensionless, this study exercises the discretion to choose the velocity at any relevant height to analyse the fire behaviour.

For the simulations presented here, the *RoS* is taken from the measurements shown in Figure 4.13 (Section 4.4.2.3) and Q values are taken from Figure 4.18 (Section 4.4.3). Both the *RoS* values; the quasi-steady *RoS* measured from the slope of the fire front location (by applying linear fit to the firefront location in time) and the averaged dynamic *RoS* values (obtained by differentiating the firefront location data) are used to compute different N_c values. While there are differences between the values computed using the two measurements of *RoS*, none of the differences are significant enough to change the classification of the mode of fire propagation. Hence, only the N_c values obtained using quasi-steady *RoS* measurements are show in Figure 4.22. The HRR (kW) values obtained at various instants in time are divided by the measured fire front length (m) to obtain fire intensity at that instant and then determined the quasi-steady Q value (kW.m^{-1}) of the respective simulation (as detailed in Section 4.4.3)

The N_c values derived using eqn (2.48), using the quasi-steady *RoS* values, are shown in Figure 4.22(a). Following Mell *et al.* (2018), the N_c values in Figure 4.22(a) are based on U_{10} wind velocities (inlet wind velocity at 10 m height) of 12.5, 6 and 3 m.s^{-1} and is referred to as Nc_{10} in the discussions.

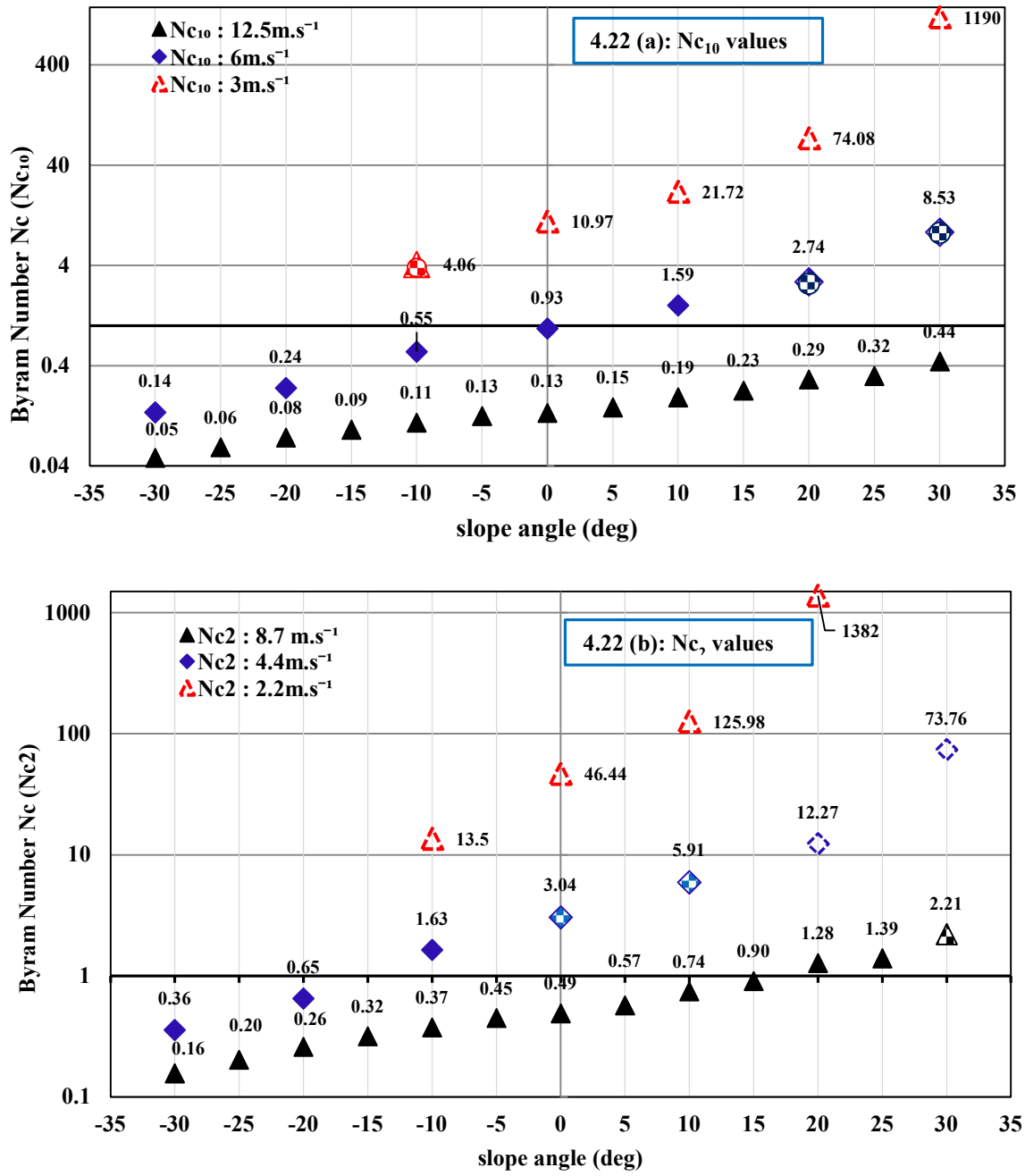

Figure 4.22 – N_c vs slope angle: (a) based on U_{10} values of 12.5, 6 and 3 m.s^{-1}; (b) based on U_2 values of 8.7, 4.4 and 2.2 m.s^{-1}. Plots are in logarithmic scale (y-axis). Wind-driven fire propagation is shown as solid symbols, buoyancy-driven is shown as hollow symbols and the intermediate regime is shown as pattern filled symbols

The plots are in logarithmic scale (y-axis). The calculated N_c data values using the quasi-steady *RoS* are indicated in the plots. Wind-driven fire propagation is shown as solid symbols, buoyancy-driven as hollow symbols and the intermediate regime as pattern filled symbols.

For simulations with 12.5 m.s^{-1} wind speed, N_{c10} is observed to be lower than 2 and hence within the wind-driven regime for all the slope angles. With wind speed 6 m.s^{-1}, $N_{c10} < 2$ for slope angles –30° to +10°, indicating a wind-driven fire. However, for higher upslopes (+20° and +30°), N_{c10} lies between $2 < N_{c10} < 10$, which indicates that these fires are in the intermediate regime. At the lowest wind speed of 3 m.s^{-1}, the upslope cases 0° to +30° can be classified as buoyancy-driven given the large N_{c10} (although for the 0° case, N_{c10} is close to the threshold value of 10). The –10° case is in the intermediate regime. For all no-slope cases, the N_{c10} values are found to be consistent with the observation of Sutherland *et al.* (2020).

Unusually, a very high Byram number value ($N_{c10} > 500$) is observed for wind velocity 3 m.s^{-1} at +30° slope but the instantaneous temperature contours (Figure 4.20(l)) show that the plume is attached locally to the burnable grass plot for a considerable distance; however, the plume eventually detaches at approximately 55 m downstream, and the plume becomes more vertical. In this case, the flame is wind-driven and initially, the flame shape appears similar to the 12.5 m.s^{-1} wind-dominated cases. The flame eventually erupts (transit to an up-rising plume) and becomes more like the buoyancy-dominated flames towards the end of the burnable plot.

Because the Byram number is a comparison of buoyancy forces originating at the surface with the shearing forces driven by the horizontal wind at 10 m, it is possible that the near-surface flame dynamics could be misclassified.

To understand the near-surface flame and wind field behaviour, wind velocity at 2 m (U_2) is used in the N_c calculations in place of U_{10}. Since N_c is dimensionless, this study exercises the discretion to select the velocity at 2 m height (U_2), which is approximately the mid-flame wind velocity. Mean velocity profiles are extracted from the centreline u-velocity slices and U_2 values are found to be 8.7, 4.4 and 2.2 m.s^{-1}, for corresponding U_{10} values of 12.5, 6 and 3 m.s^{-1}.

The N_c values derived using U_2, referred to as Nc_2 in the discussions, are presented in Figure 4.22 (b). For the highest wind velocity, U_2 = 8.7 m.s^{-1}, the fire is within the wind-driven regime with

$N_{c2} < 2$; however, for greater upslope cases, the values are notably closer to the threshold value 2, with +30° slope falling in the intermediate regime. The flame dynamics indicate that the near flame appears to be detached and the fire may not be entirely in wind-driven mode (as observed from N_{c10} values with U_{10} = 12.5 m. s^{-1}, Figure 4.22(a)), though the plume changes to the wind-driven regime. This agrees with flame and near-flame detachment detailed in Section 4.4.4, Figures 4.21(a–o).

With U_2 = 4.4 $m.s^{-1}$, $N_{c2} < 2$ for slope angles –30° to –10°, indicating a wind-driven fire, as observed in Figure 4.22(a). However, for no-slope 0° and upslope +10°, N_{c2} values are higher and lie between $2 < N_{c2} < 10$, indicating an intermediate fire regime, whereas 0° and +10° slopes are in the wind-driven regime with U_{10} = 6 $m.s^{-1}$, as shown in Figure 4.22(a). For higher upslopes (+20° and +30°), $N_{c2} > 10$, classifying these as buoyancy-driven fire regime, a clear shift from the intermediate regime with U_{10} (Figure 4.22(a)) to buoyancy-driven regime with U_2. For greater upslopes, the plumes at lower wind velocities are more likely to be uprising over a longer distance than the higher wind velocity cases and appear to be more in the plume-dominated regime, in line with the flame contour plots (Figures 4.21 (p–f)).

At the lowest wind speed U_2 = 2.2 $m.s^{-1}$, all upslope cases can be clearly classified as buoyancy-driven, given the large N_{c2} values, which agrees with the N_{c10} analysis using U_{10} (Figure 4.22(a)) except for downslope 10°, which is in the intermediate regime using U_{10} but moves into the buoyancy-dominated region using U_2. The eruption in Figures 4.21 (ag–ah) and (ap–ar) could not be explained by using U_2 in place of U_{10} in the Byram number calculation.

Mode of fire propagation for all slope cases at all three wind velocities, based on N_c calculation (N_{c10} and N_{c2}) are summarised in Table 4.4

Table 4.7: Summary- Mode of fire propagation based on N_c calculation

Slope angle	N_{c10} (based on U_{10})			N_{c2} (based on U_2)		
	12.5 m.s^{-1}	6 m.s^{-1}	3 m.s^{-1}	8.7 m.s^{-1}	4.4 m.s^{-1}	2.2 m.s^{-1}
–30°	wind-driven			wind-driven		
–25°	wind-driven			wind-driven		
–20°	wind-driven	wind-driven		wind-driven	wind-driven	
–15°	wind-driven			wind-driven		
–10°	wind-driven	wind-driven	intermediate	wind-driven	wind-driven	buoyancy-driven
–5°	wind-driven			wind-driven		
0°	wind-driven	wind-driven	buoyancy-driven	wind-driven	intermediate	buoyancy-driven
+5°	wind-driven			wind-driven		
+10°	wind-driven	wind-driven	buoyancy-driven	wind-driven	intermediate	buoyancy-driven
+15°	wind-driven			wind-driven		
+20°	wind-driven	intermediate	buoyancy-driven	wind-driven	buoyancy-driven	buoyancy-driven
+25°	wind-driven			wind-driven		
+30°	wind-driven	intermediate	buoyancy-driven	intermediate	buoyancy-driven	buoyancy-driven

4.4.6 Flame length

The flame length is computed from instantaneous centreline HRR data. The geometric centreline HRR data is analysed at every time step and 99% of the maximum observed HRR value is used as the threshold value to create a binary image. The data inside the threshold contour takes the value one and the data outside the threshold contour takes the value zero. Following Cobian-Iñiguez *et al.* (2019), an ellipse is fitted to the binary image at every time level using the Matlab function *regionprops* (https://mathworks.com). The ellipse is constrained so that the second moment of the ellipse is equal to the second moment of the nonzero region of the image. The flame length is computed from the major axis of the fitted ellipse, that represent the distance between the centre of the flame base to the tip of the flame.

Figures 4.23 (a), (b) and (c) show the flame length vs time plotted for all slope angles at wind velocities 12.5, 6 and 3 m.s^{-1}, respectively. In Appendix A, Figures S4.8(a) and (b), the results from the longer (120 × 40 m) burnable grass plot simulations (repeated to ensure quasi-steady state) for higher upslopes at wind velocities 12.5 and 6 m.s^{-1} are presented. The flame length values fluctuate and show irregularity due to the dynamic nature of fire propagation.

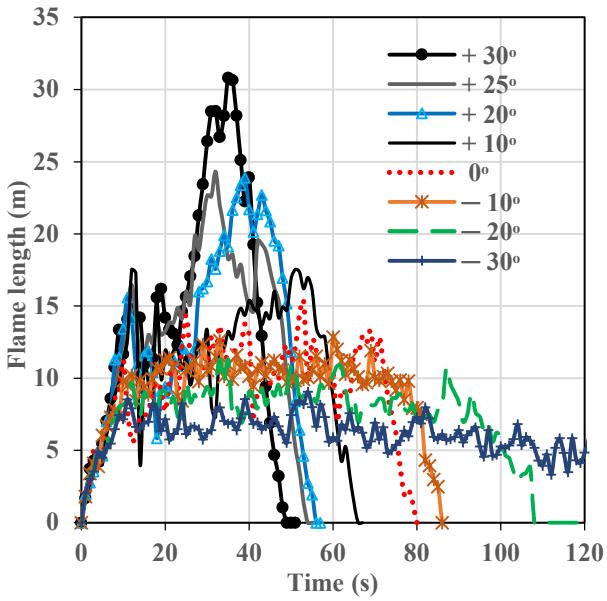

(a) Flame length vs time, 12.5 m.s^{-1}

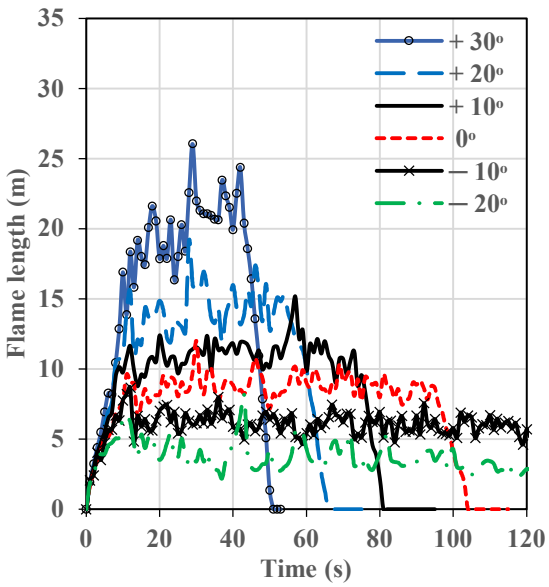

(b) Flame length vs time, 6 m.s^{-1}

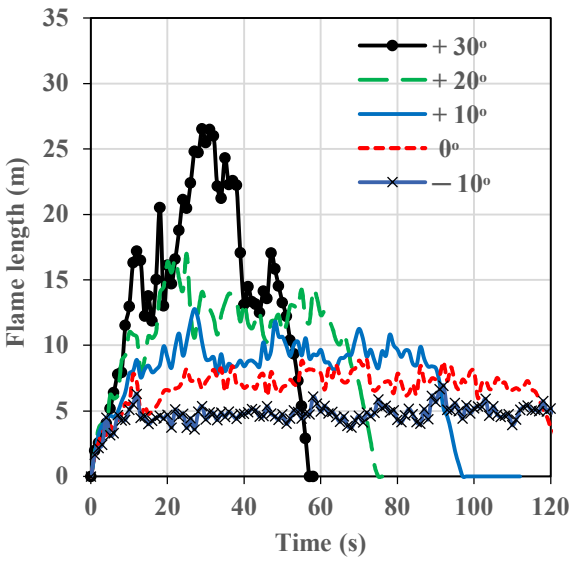

(c) Flame length vs time, 3 m.s^{-1}

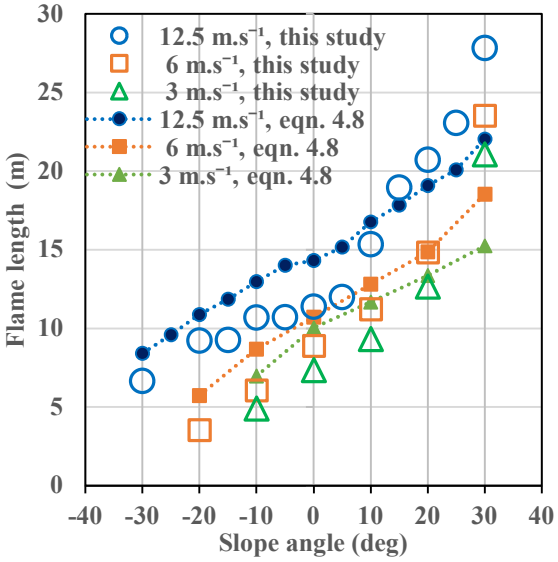

(d) Quasi-steady flame length vs slope

Figure 4.23 – Flame length vs time at wind velocities of (a) 12.5 m.s^{-1}; (b) 6 m.s^{-1}; (c) 3 m.s^{-1}; (d) quasi-steady flame length vs slope angles from this study along with empirically derived flame length values.

In Figure 4.23(a), upslope cases show the highest flame length at +30° slope, and the flame length decreases as the slope angle decreases. The peak flame length value of an upslope angle is found to be approximately 30% higher than the flame length of next lowest (by 10°) angle. This observation is consistent with the plume contour views of Figures 4.20 (a–l): when the upslope angle increases, the plume inclines towards the ground and is more prone to plume attachment. The flame lengths are much higher for upslopes than downslopes. For downslopes, the flame length is highest at downslope 10° and the length decreases with increase in downslope angle. The difference in flame lengths is lower than that observed in upslopes. Comparing the three velocity cases, for corresponding slopes (Figures 4.23 (a), (b) and (c)), the flame length is generally lower for the lower velocity cases. This indicates that with the higher wind velocity, convection plays an increased role in fire propagation.

The flame length values extracted from the quasi-steady region (from Figures 4.23 (a–c) and Figure S4.7 in Appendix A) are plotted in Figure 4.23(d) for all three wind velocities. At lower wind velocities and steep downslopes, the fire front does not propagate down the slope. Therefore, –30° at 6 m.s^{-1}, –30° and –20° at 3 m.s^{-1} are not included in the flame length plots.

Figures 4.24 (a), (b) and (c) show the flame length plotted against fire front location. The results from the extended burnable grass plot simulations (120 m in the *x*-direction) are used in Figure 4.24 (a) and (b) for +30°, +25° at 12.5 m.s^{-1} and +30° at 6 m.s^{-1}. As with other parameters (pyrolysis width, fire intensity, etc.), we observe more visible quasi-steady states. Like with pyrolysis width (in Figure 4.9), longer quasi-steady states are observed for lower upslope, no slope and 10° downslope angles. For –20° at 6 m.s^{-1}, flame length gradually decreases over the distance, leading to extinction.

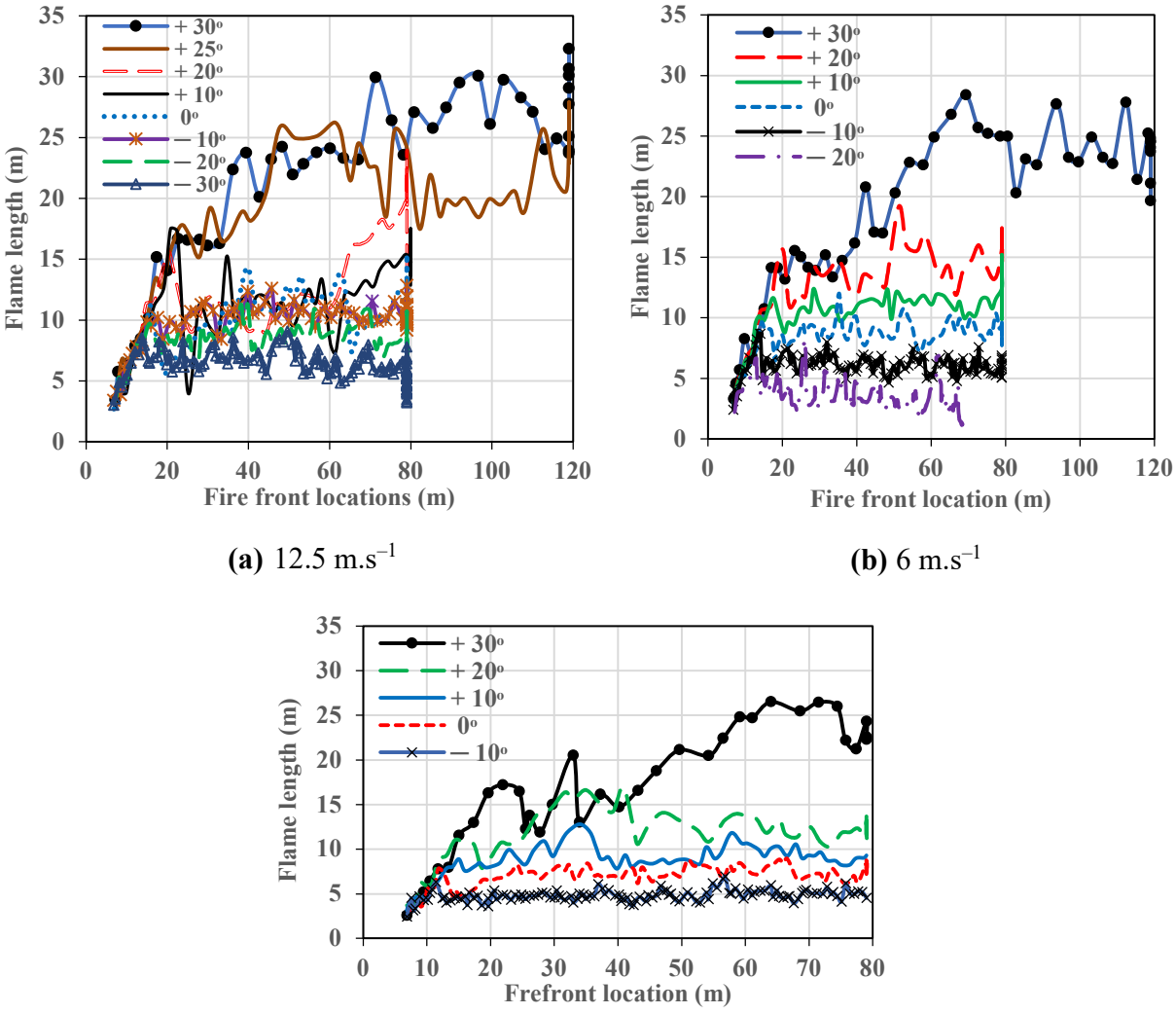

(a) 12.5 m.s^{-1}

(b) 6 m.s^{-1}

(c) 3 m.s^{-1}

Figure 4.24 – Flame length vs fire front location for upslopes and downslopes at wind velocities (a) 12.5 m.s^{-1}; (b) 6 m.s^{-1}; (c) 3 m.s^{-1}

Alexander and Cruz (2012, 2021) examined the underlying assumptions and limitations associated with various empirical correlations between fire line intensity and flame length. They found that fire behaviour characteristics are strongly influenced by the fuel structure and environmental conditions, and there are bounds or limits associated with these empirical relationships. Alexander and Cruz (2012, 2021) presented a list of power-law correlations to facilitate the estimation of flame length as a function of the fire line intensity. Similarly, Barboni *et al.* (2012) presented another list of correlations. The present study attempted to find which of these correlations best fit our numerical data and found that the best results are observed with the correlations derived by Anderson *et al.* (1966), which is listed among the list of correlations presented in Alexander and Cruz (2012, 2021). They proposed flame length as a function of fire line intensity, shown in eqn. (4.6), derived from field experiments conducted using surface fuel of lodgepole pine slash:

$$L = 0.074Q^{0.651}, \qquad (4.8)$$

where L is the flame length in metres. For the simulations presented here, the Q values (quasi-steady fire line intensity) are obtained as described in Section 4.4.3. Q values corresponding to the respective slope angles and wind velocities are used in eqn (4.5) to derive L values. The values of L calculated using eqn (4.8) are also presented in Figure 4.23(d), along with the quasi-steady L values obtained from this study. The L values predicted by eqn (4.8) are nominally higher than the values obtained from this study for slope angles up to +10°. For higher upslopes, eqn (4.8) predicts lower values than the simulation results (especially for 12.5 m.s^{-1} cases).

Presenting all the simulated L values against the simulated Q values in Figure 4.25, a power-law relationship, eqn (4.9), is found to exist between the flame length and intensity. This is in broad agreement with the correlations in the list of empirical models presented in Alexander and Cruz (2012, 2021) and Barboni *et al.* (2012). The +30° cases with 6 and 3 m.s^{-1} wind velocities appeared to be outliers (falls outside the linear fit line), however, relatively minor increase is noted in the R^2 value without these outliers (R^2 values with and without these outliers are indicated in Figure 4.25). Therefore, the power- law relationship shown in eqn. (4.9) includes all simulated L values.

$$L = 0.0047Q^{0.9835} \qquad (4.9)$$

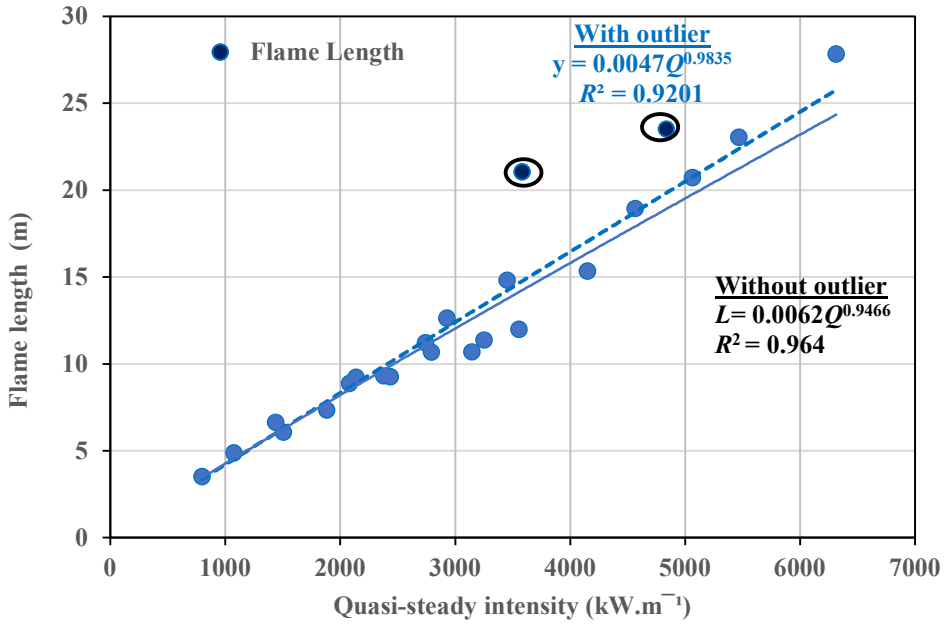

Figure 4.25 – Simulated flame length vs intensity for all the cases. Circles represents +30° cases with 6 and 3 m.s^{-1} wind velocities, which appear to be outliers

Flame height (defined as the vertical distance from the base of the leading edge of the flame to the flame tip) could not be reliably determined from the simulation data. An attempt was made using a method similar to the one used to compute flame length (Cobian-Iñiguez *et al.* 2019), and the flame height was computed analogously from the maximum height of the fitted ellipse. Using this method, it was found that the flame height does not generally vary with the slope and flame height is within the range of 1 to 1.8 m. However, there may be limitations in the ellipse-fitting approach used here.

4.4.7 The Heat fluxes

To understand the role of radiative and convective heat transfer on sloped terrains, contour plots of heat fluxes are analysed and presented in Figure 4.26. The convective and radiative heat flux boundary data obtained from the simulation are analysed using Matlab software (https://mathworks.com) to extract the contours. The averaged heat flux data, at every cell, in time, impinging over the unburnt fuel is analysed. The heat flux data is derived based on the trailing edge (or pyrolysis rear) of the pyrolysis region, as the fire front moves from left to right through the burnable grass plot. Since there is no physically meaningful threshold for the heat fluxes, the

data is normalised to lie in the range from 0 to 1 and the 0.5 value contour is plotted. That is, 50% of the heat transfer occurs inside the contour. The heat flux contour plots shown in Figure 4.25 are taken at different times as the fire front moves through the grass plot for +30°, +10° and –10° slopes, at all three wind velocities.

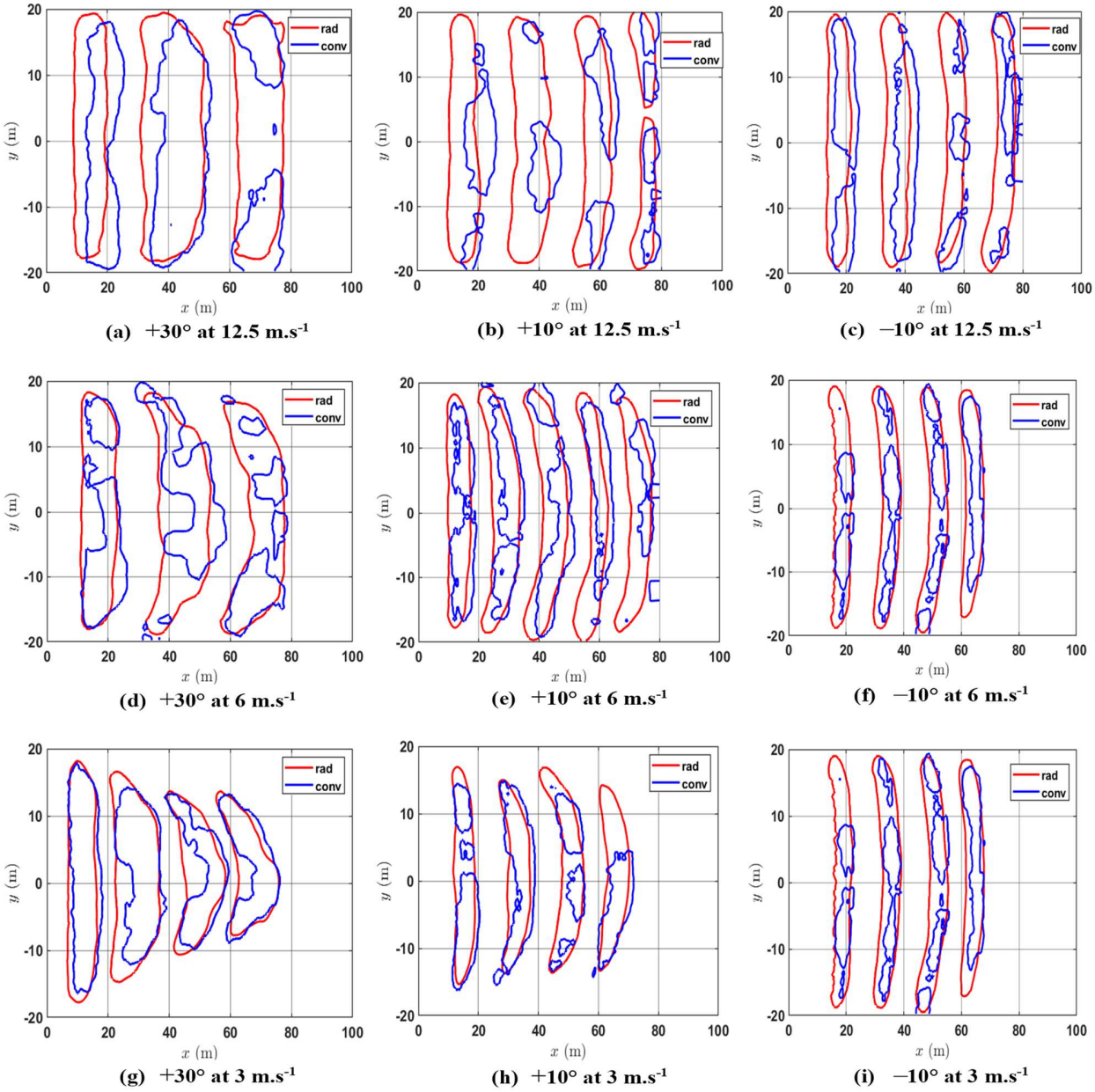

Figure 4.26 – Instantaneous heat flux contours taken at different times as the fire front moves through the grass plot, for slope angles +30°, +10° and –10°, at: (a–c) 12.5 m.s^{-1}; (d–f) 6 m.s^{-1}; and (g–i) 3 m.s^{-1}; 'rad' and 'conv' represent radiative and convective heat fluxes, respectively.

At 12.5 m.s^{-1}, the convective heat flux (blue lines) tends to lie ahead of the radiative heat flux (red lines) for all three slopes. The convective heat flux is the leading heat transfer mechanism for 12.5 m.s^{-1} cases, which are predominantly wind-driven fire propagation as demonstrated in the Byram number analysis (Section 4.4.5). The trend of convective heat flux leading over radiative heat flux also occurs at 6 m.s^{-1} for +30° and +10° slopes, while it remains spatially overlapping or lagging at some instances in the –10° slope. However, at lower wind velocity of 3 m.s^{-1}, the radiative heat flux contours mostly overlap the convective heat flux contours. The leading or lagging of the fire front by the convective heat flux does not necessarily mean that the total heat flux is dominated by the convective heat flux. Rather, these contours provide information about where the heat transfer occurs.

The results presented show that the convective heat fluxes are more relevant in wind-driven fires and at higher slopes compared with buoyancy-driven fires and for lower slopes; these results are consistent with the studies of Sánchez-Monroy *et al.* (2019) and Dupuy *et al.* (2011).

The total radiative and convective heat fluxes on the ground ahead of the fire front are presented in Figures 4.27 (a–f) for wind velocities 12.5, 6 and 3 m.s^{-1}. The results from repeated simulations with the longer 120-m grass plot (to ensure quasi-steady state) for higher upslopes +30°, +25° at 12.5 m.s^{-1} and +30° at 6 m.s^{-1} are presented in Appendix A, Figures S4.8 (a–d). To obtain this data, the boundary heat flux data at every time step is multiplied by a filter that discriminates burnt and unburnt fuel. The heat flux to the unburnt surface is summed to get the total boundary heat flux (both radiative and convective) value at that instant of time.

For all three wind velocities, with increased slope angle, the heat fluxes reach their maximum values earlier, as the fire front travels much more quickly on upslopes. The heat flux increases as the fire front progresses from the ignition line, then reaches a quasi-steady state and finally decreases. The total heat fluxes increase with slope angle and wind velocity. However, the opposite scenario is found with downslopes.

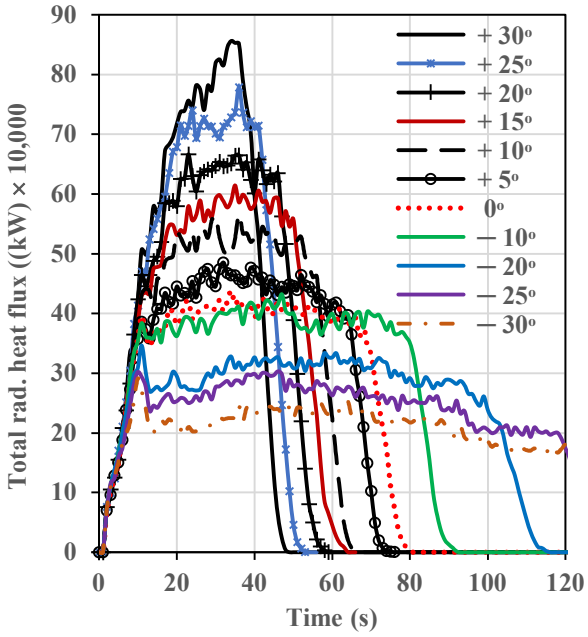

(a) Radiative flux vs time – 12.5 m.s^{-1}

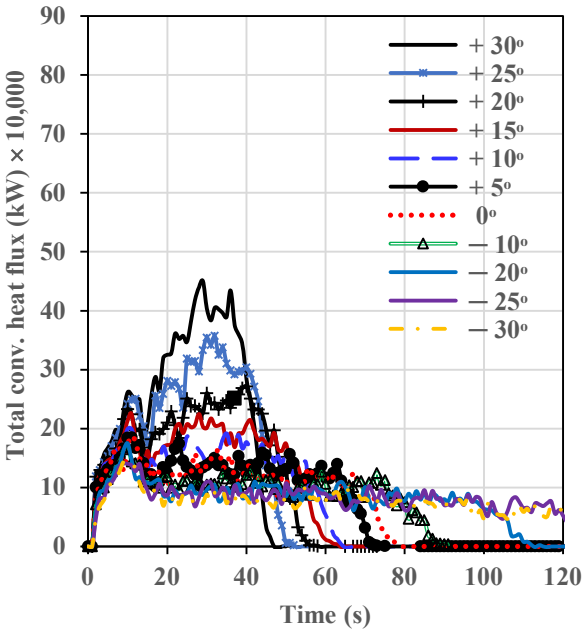

(b) Convective flux vs time – 12.5 m.s^{-1}

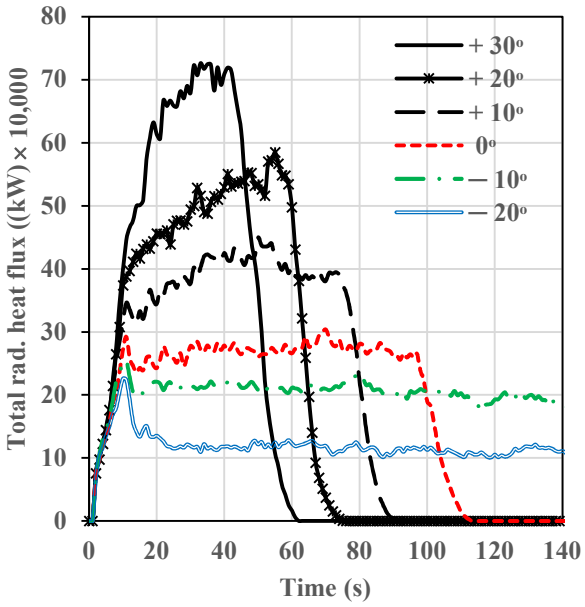

(c) Radiative heat flux vs time – 6 m.s^{-1}

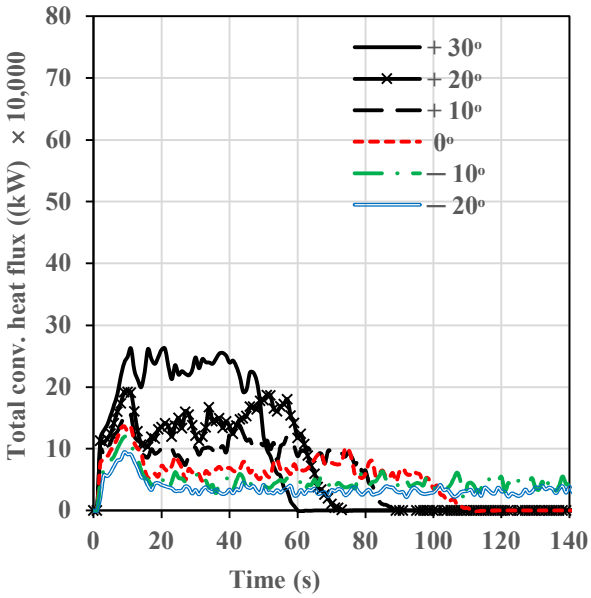

(d) Convective heat flux vs time – 6 m.s^{-1}

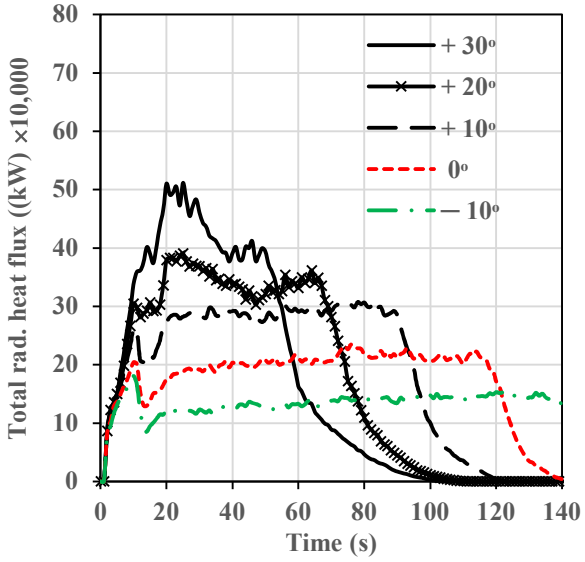

(e) Radiative heat flux vs time – 3 m.s^{-1}

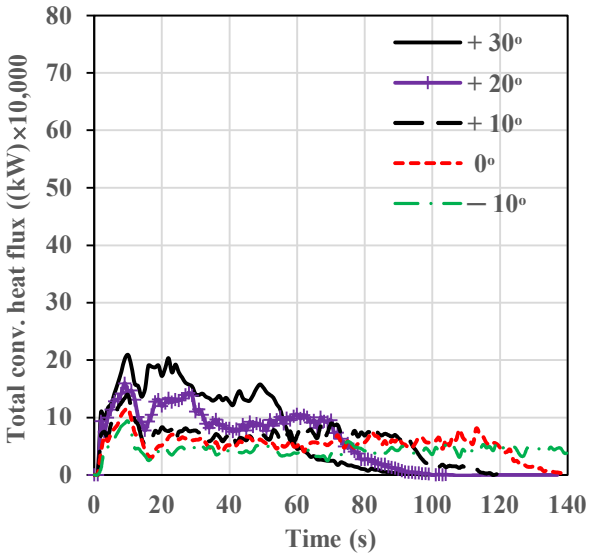

(f) Convective heat flux vs time – 3 m.s^{-1}

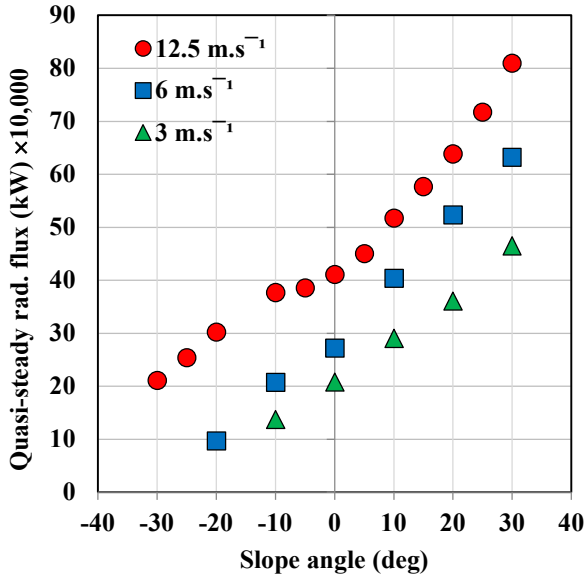

(g) Quasi-steady rad. flux vs slope angle

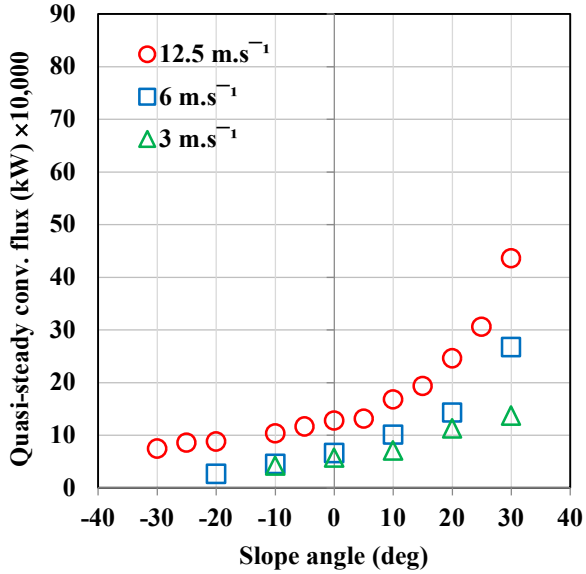

(h) Quasi-steady conv. flux vs slope angle

Figure 4.27 – Heat fluxes as a function of time: (a) radiative heat flux at 12.5 m.s^{-1}; (b) convective heat flux at 12.5 m.s^{-1}; (c) radiative heat flux at 6 m.s^{1}; (d) convective heat flux at 6 m.s^{1}; (e) radiative heat flux at 3m.s^{1}; (f) convective heat flux at 3 m.s^{1}; (g) quasi-steady radiative heat flux vs slope angles at 12.5, 6 and 3 m.s^{-1}; (h) quasi-steady convective heat flux vs slope angles at 12.5, 6 and 3 m.s^{-1}.

The radiative and convective heat flux values extracted from the quasi-steady region (from Figures 4.27 (a–f) and Figure S4.9 in Appendix A) are plotted against slope angles in Figure 4.27(g) and (h) for the three wind velocities. For a given slope angle, the radiative heat flux is higher than convective heat flux for all three wind velocities.

Comparing among the velocities, as the driving wind velocity increases, both radiative and convective heat flux values increases. For 12.5 m.s^{-1}, the radiative heat flux value for higher upslope (+30°) is approximately 95% higher than that for no-slope, and that for higher downslope (–30°) is approximately 94% lower than no-slope. The convective heat flux value for higher upslope is approximately 200% higher than no-slope and that for higher downslope (–30°) is approximately 72% lower than no-slope. For lower wind velocities of 6 and 3 m.s^{-1}, the convective heat flux values are closer for slope angles –30° to +10°, indicating that the wind velocity has less effect on the convective heat flux on downslopes compared with its effect on radiative heat flux.

Figures 4.28 (a–f) show the radiative and convective heat fluxes vs fire front location for the same three wind velocities. The results from the extended burnable grass plot simulations (120 m in the *x*-direction) are used in Figures 4.27 (a–d) for +30°, +25° at 12.5 m.s^{-1} and +30° at 6 m.s^{-1}.

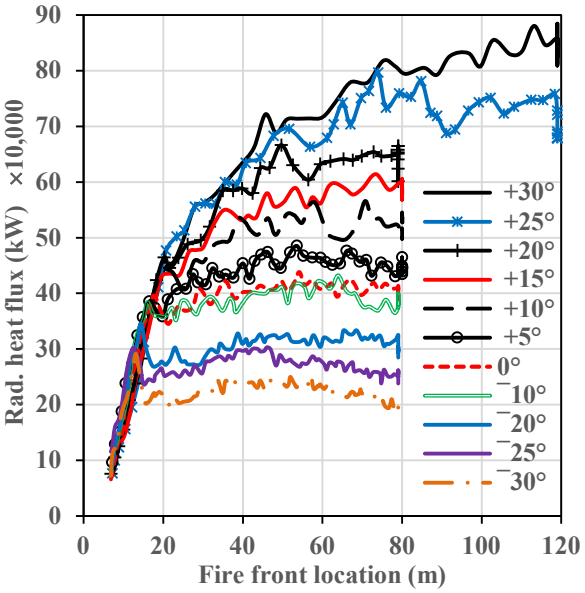

(a) Radiative flux vs fire front – 12.5 m.s^{-1}

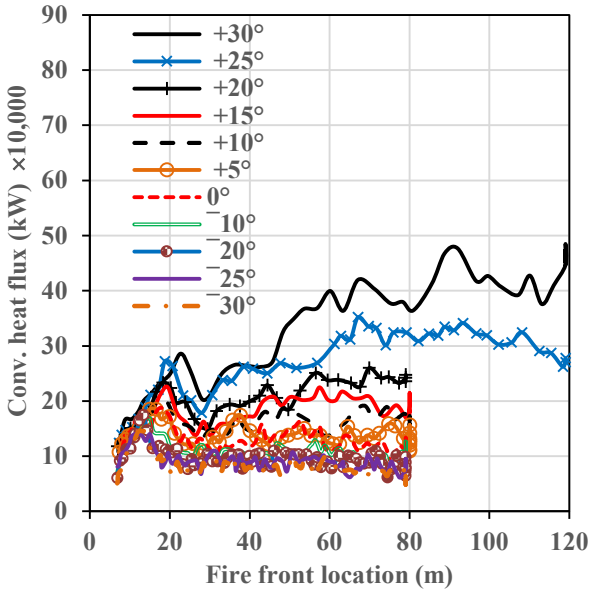

(b) Convective flux vs fire front – 12.5 m.s^{-1}

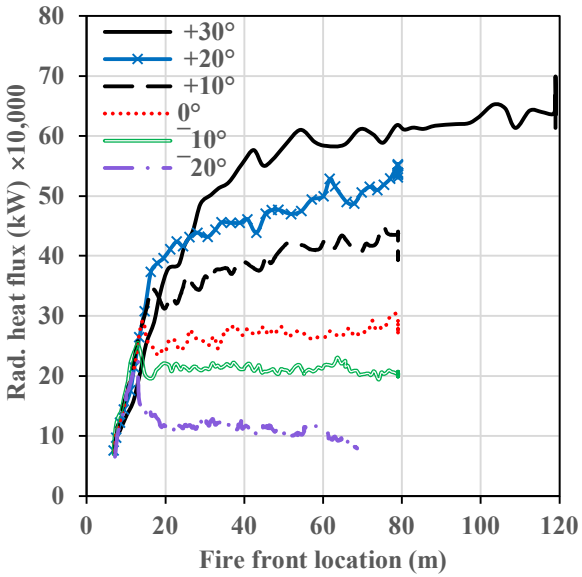

(c) Radiative flux vs fire front – 6 m.s^{-1}

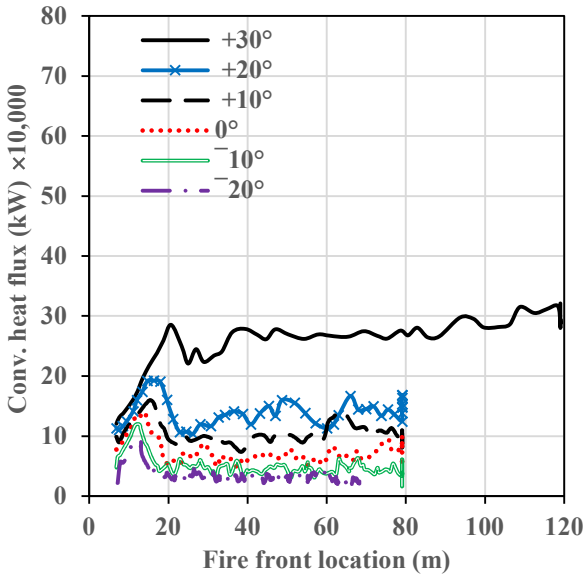

(d) Convective flux vs fire front – 6 m.s^{-1}

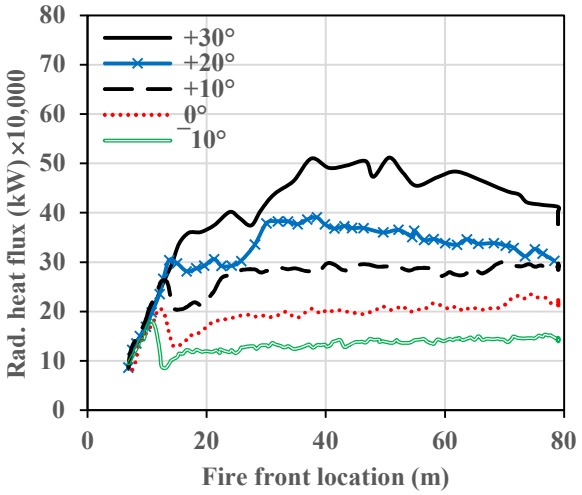

(e) Radiative flux vs fire front – 3 m.s^{-1}

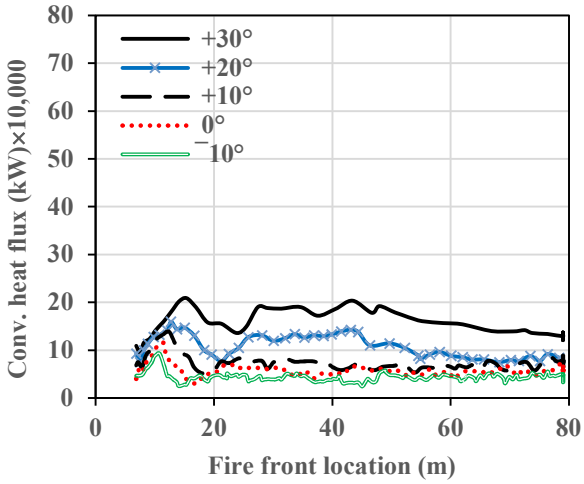

(f) Convective flux vs fire front – 3 m.s^{-1}

Figure 4.28 – Heat fluxes vs fire front location: (a) radiative heat flux at 12.5 m.s^{-1}; (b) convective heat flux at 12.5 m.s^{-1}; (c) radiative heat flux at 6 m.s^{-1}; (d) convective heat flux at 6 m.s^{-1}; (e) radiative heat flux at 3 m.s^{-1}; (f) convective heat flux at 3 m.s^{-1}.

As noted with fire intensity, beyond 20 m, in most cases, both radiative and convective heat fluxes plateau or reach a quasi-steady state. For higher upslopes and higher wind speed cases, a quasi-steady state is reached after the fire front has travelled a longer distance. Compared with the heat flux vs time plots in Figure 4.27, quasi-steady states are more clearly visible (over a longer

distance). Longer quasi-steady states are observed for lower upslope, no-slope and downslope angles. Like intensity, for downslope –20° at 6 m.s^{-1}, heat fluxes maintain a quasi-steady state until the fire is extinguished at approximately 65 m.

4.5 Summary

In this study, a set of simulations on both the upslopes and the downslopes were conducted at field-scale with varying slope angles and driving wind velocities. It is to be noted that the input values used in these simulations, as presented in Table 4.1, represent one particular grass type. The next chapter, which discusses the grass fire propagation at lower wind velocities, analyse a set of simulation where some of the fuel characteristics are changed (increased ambient temperature along with reduced fuel moisture content, relative humidity and fuel load) from that presented in Table 4.1. Caution needs to be taken in interpreting the results for wider range of grass species. Furthermore, the velocity range can also alter the physical behaviour of fire.

Within the simulations conducted in this study, *RoS* and intensity (*Q*) of fire increased with both driving wind velocity and slope angle. Comparing among the wind velocities, for a given slope angle, *RoS* and *Q* values with lower wind velocity are lower, however, the difference narrowed between 3 and 6 m.s^{-1} cases as the slope angle increases.

Evidence of dynamic fire behaviour was observed when time series of *RoSs* were plotted. For convenience to compare with empirical model values, quasi-steady *RoS* were plotted together with dynamic maximum, minimum and averaged *RoS*. The dynamic maximum and minimum (upper and lower bounds of instantaneous *RoS* values) were provided as whiskers. The main findings and *RoS* comparison with the empirical models are briefed below.

For all three wind velocites, the Original and Modified Rothermel values did not change much with slope. For 6 m.s^{-1}, Rothermel values matched with quasi-steady *RoS* values for up to +10° and, found to match better with dynamic maximum *RoS* values for 12.5 m.s^{-1} and dynamic minimum *RoS* values for 3 m.s^{-1}.

Overall, the CSIRO model's predicted empirical values roughly lied between the simulated minimum and maximum values of *RoS*. However, the increasing trend of *RoS* with slope angle is greater in the CSIRO model than observed in the simulations.

Slope- corrected MKIII and MKV values for 12.5 $m.s^{-1}$ cases were found to be closer to the WFDS quasi-steady *RoS* values for slope angles –10° to +10° and then rises higher than the dynamic maximum for high upslope cases. At 6 $m.s^{-1}$, only for >+ 10°, these model values were closer to the WFDS quasi-steady *RoS* values and at 3 $m.s^{-1}$, these values were often found to be closer to dynamic minimum *RoS* values.

It appeared that ideal nature of grassfire propagation simulation and challenges related to measure quasi-steady values in experimental studies are likely reasons for the observed differences.

The results showed that, within the slope angles and driving wind velocities considered in this physics based modelling study using WFDS, a second-order polynomial relationship exists between the quasi-steady *RoS* and slope angle, which was also the case for Rothermel models. The slope factor in *RoS* in Australian empirical correlations, which are likely to be derived from very low wind velocity laboratory slope studies, is exponential. We found that, for upslopes, the relative *RoS* values from WFDS are closer to Rothermel models than the Australian correlations. It is due to multiplicative nature of Australian correlations compared to Rothermel models' additive nature.

Between the *Q* and slope angle at 12.5 and 6 $m.s^{-1}$ driving wind velocity, a second-order polynomial relationship exists, however the relationship was linear for lower wind velocity. The relationship between *Q* and *RoS* was linear (expected from Byram's relationship for the identical fuel characteristics) for all 12.5 $m.s^{-1}$ cases as well as until +10° slope for 6 and 3 $m.s^{-1}$ cases, *Q*-*RoS* relationship deviated from linearity as the driving wind velocity reduced and it occured at higher upslopes.

Within these simulations, it was found that with the increase of upslope angle and wind velocities, the plume inclined more towards the ground whereas on downslopes, the plume rose from the ground earlier. Bearing in mind that our simulations are at a much smaller scale compared to a real wildfire scenario, we found that with higher upslopes the eruptive growth of fires may lead to flame attachment, which can result in firefighters' causalities (Lahaye *et al.* 2018). Our results indicated that such attachment can occur in higher upslope cases (>+ 20° slopes). However, our highly idealised simulations are at a much smaller scale and caution must be applied in extrapolating these results. As wind speed increased, the plume attachment occursed at a much lower slope angle due to an interaction between the slope of the terrain and the plume itself. For

higher wind velocities, the flame and near flame appeared to be up-rising, even though the plume was attached. Overall we found similarities with the results of Dold and Zinoviev (2009) and Sharples (2017).

Considering the behaviour of the plume at higher altitudes, at z = 10 m, the plume appeared to be wind-driven in agreement with Byram number analysis. For higher wind velocities (12.5 and 6 $m.s^{-1}$), the flame was buoyancy dominated near the ground, tended towards wind dominated for a very intermittent time and then transitioned to buoyancy dominated regime as the fire progressed. At lower wind velocity (3 $m.s^{-1}$), the plume risen up, the fire established and then became attached which lead to rapid intensification and a buoyancy dominated fire. The flame was more vertical at lower slope angles and became deeper with increased slope angle. To understand the near flame wind field behaviour, we have used wind velocity at 2 m (U_2) in the Byram number calculation in place of U_{10}. Within the simulations conducted in this study, we fodunt that, the flame behaviour could be different from the overall plume behaviour and the Byram number based upon U_{10} captures the plume behaviour, not the flame behaviour.

When the fire run uphill, the flame length was found to be higher with the flame attached to the ground. Flame length at a given slope angle increases with the driving wind velocity. For all three wind velocities, the flame lengths obtained from this study were found to reasonably in agrement with the values predicted by the empirical model proposed by Anderson *et al.* (1966). Additionally, within the simulated flame lengths and intensity, a power-law correlation was found to exists between the flame length and fireline intensity.

The contours of heat fluxes showed that the convective heat fluxes are more relevant at wind-driven fire propagation and on higher upslopes. Both the total radiative and the total convective heat flux values increased with wind velocity. Similar observations were reported by Mendes-Lopes *et al.* (2003), Dold and Zinoviev (2009), Dupuy and Maréchal (2011), Sharples (2017) and Sánchez-Monroy *et al.* (2019). For a given slope angle, the total radiative heat flux values were higher than convective heat flux values for all three driving wind velocities. However, the difference between the fluxes decreased as the wind velocity reduced and both fluxes were equally significant at lower driving wind velocity compared with higher wind velocities. Sánchez-Monroy *et al.* (2019) reported that for no-wind conditions on slopes above 30°, convective heat flux is larger and a tendency towards that was observed in our study.

In Chapter 5, we investigate the combined effect of slope and wind on grassfire behaviour at lower driving wind velocities of 0.1 and 1 $m.s^{-1}$. Four different sets of simulations are performed for 1 $m.s^{-1}$ cases, with varying fuel parameters and domain sizes. The results – fire isochrones, head fire width, fire front locations, *RoS*, fire intensity, plume and flame dynamics, mode of fire propagation and heat fluxes – with different scenarios are analysed and compared with empirical studies.

Chapter 5. Grassfire propagation on sloped terrains at lower wind velocities

This chapter analyses and discusses the simulations conducted at different slope angles with lower driving wind velocities (U_{10}) of 1 and 0.1 m.s^{-1}. Section 5.1 presents the summary of simulations and simulation set-up, Section 5.2 presents the parameters and variables used in the simulations and Section 5.3 presents the results, detailed analysis and discussions.

5.1 Simulation set-up

Four sets of simulations were conducted with lower driving wind velocities of 0.1 and 1 m.s^{-1}, as listed in Table 5.1.

Table 5.1: List of Simulations

Slope angle (degree)		**Domain Size : 360 × 120 × 60 m**		**Domain Size : 480 ×180 × 80 m**	
		Burnable grass plot 80 × 40 m			
	Wind velocity	0.1 m.s^{-1}, Set 1	1 m.s^{-1}, Set 2	1 m.s^{-1}, Set 3	1 m.s^{-1}, Set 4
	Fuel parameters	original	original	original	changed
–10°		√	√		
0°		√	√	√	√
+5°		√	√	√	√
+10°		√	√	√	√
+15°		√	√	√	√
+20°		√	√	√	√
+25°		√	√	√	√
+30°		√	√	√	√

One set of simulations (set 1) is conducted at a wind velocity of 0.1 m.s^{-1} (nearly no wind) and three sets (sets 2, 3 and 4) at 1 m.s^{-1} (corresponding to 0.95 m.s^{-1} prior to the ignition line). Simulation sets 3 and 4 are performed with varied domain sizes and 'changed' fuel parameters, respectively, to analyse fire isochrones progression with these two different scenarios and to further investigate the effect (if any) of these distinction on the *RoS.* The simulations are performed with two domain sizes, termed 'original': 360 × 120 × 60 m and 'larger': 480 × 180 × 80 m. Sets

1 and 2 simulations use the domain size 360 × 120 × 60 m, the same model set-up used with the higher wind velocity cases detailed in Section 4.1 (Figure 4.1).

Sets 3 and 4 simulations use the larger domain size of 480 ×180 × 80 m, one of the domain sizes considered for the domain sensitivity study (Section 4.3.2), as shown in Figure 5.1. Comparing between the original domain size and this larger domain size, converged results were obtained in the sensitivity studies in terms of fire front location and HRR. Hence, 480 × 180 × 80 m domain size is chosen along with the original domain size in the analysis to compare fire isochrone progression for the low velocity cases. Further, isochrone progression is better observed with the larger domain in lower slope angle cases. For the larger domain, the distance of the ignition line from the inlet is 220 m, the bordering subdomains (both sides) are 140 m wide (70 m on each side) and the distance from the burnable grass plot to the outlet is 180 m. A burnable grass plot section of 80 × 40 m, the same as used with higher wind velocity cases, is chosen for the four sets of simulations, with a line fire set up at the beginning of this section. The simulation methodology, inlet boundary conditions, grid size and ignition fire used with higher wind velocity cases detailed in Section 4.1 are retained for the lower wind velocity cases.

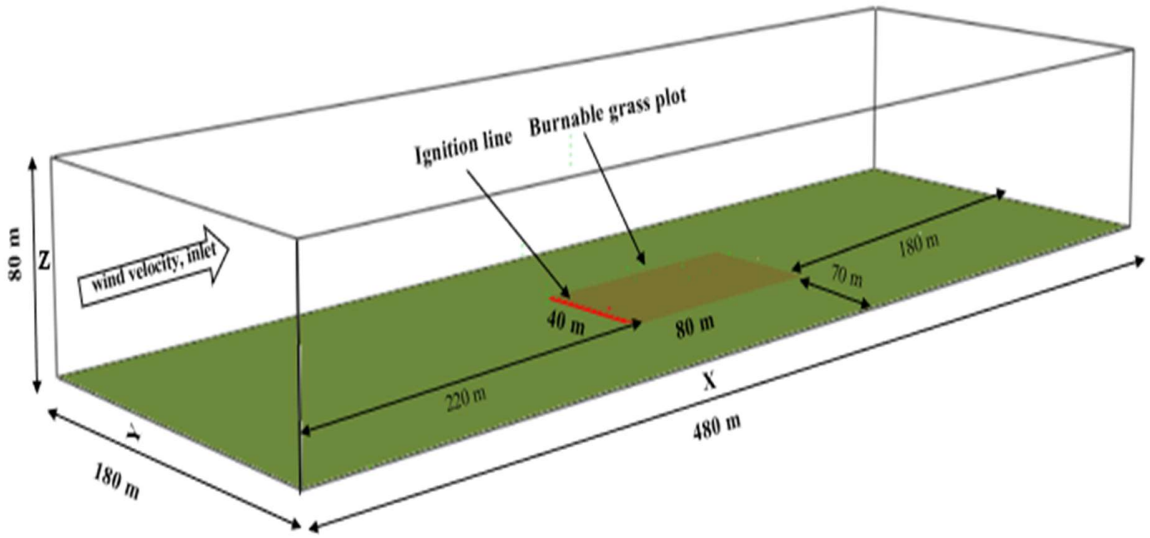

Figure 5.1 – Geometry of the domain used with simulation Sets 3 and 4: Size 480 ×180 × 80 m with burnable grass plot 80 × 40 m (dark green shaded region).

5.2 Parameters and variables

When simulations were conducted using the same physical parameters of the fuel (fuel height and load) used with higher wind velocity cases, the fire front was found to be not progressing for the lower wind velocities of 0.1(nearly 'no wind') and 1 $m.s^{-1}$. Hence, the fuel height and fuel load are increased for the lower wind velocity simulations. A grass height of 0.6 m (the maximum height of 'Near-surface and Surface fuel layers' as classified in AS3959) and grass load of 0.85 $kg.m^{-2}$ (triple the fuel load, in line with the increase in fuel height) are considered in these simulations. The simulations presented in this chapter refer to these fuel parameters as 'original' and 'changed'. The original fuel parameters are those used with higher wind velocity cases (Table 4.1, Section 4.2), other than for fuel height and fuel load (fuel load increased to 0. 85 $kg.m^{-2}$ and fuel height to 0.6 m).

With the larger domain, a set of simulations (Set 4) are performed with changed fuel parameters to observe the difference in fire front progression from the 'original' fuel parameters. The ambient temperature is increased to 50 °C and relative humidity is reduced to 10% along with a reduced fuel moisture content, fuel density and fuel load, as highlighted in Table 5.2. The fuel bulk density is maintained the same as that used in the other three sets of simulations. Arguably, increased temperature along with reduced fuel moisture content, relative humidity and fuel load are important parameters that influence the rate of fire spread and heat release rate (HRR).

The thermo-physical, pyrolysis and combustion parameters used for the four sets of simulations are shown in Table 5.2; the changed parameters used for Set 4 are highlighted with an asterisk.

Table 5.2: Thermo-physical, pyrolysis and combustion parameters for grassfire modelling

Input parameters	Values used	Source and reason
Fuel - grass		Grass type: kerosene (Eriachne burkittii) Cheney *et al.* (1993), Mell *et al.* (2007), Moinuddin *et al*. (2018)
Heat of combustion	16400 $kJ.kg^{-1}$	Bluestem grass (Overholt *et al.* 2014)
Soot yield	0.008 $g.g^{-1}$	White pine (Australian Radiata pine) (Abu Bakar 2015)
Vegetation drag coefficient	0.125	assuming vegetation elements are spherical (Morvan *et al.* 2004)

Vegetation load	0.85 kg.m^{-2} 0.31 kg.m^{-2}*	
Vegetation height	0.6 m	
Vegetation moisture content	0.065 0.024*	Experimental (Cheney *et al.* (1993), Cheney and Gould (1995))
Surface area-to-volume ratio of vegetation	9770 m^{-1}	Experimental (Cheney *et al.* (1993), Cheney and Gould (1995)
Vegetation char fraction	0.17	Average of Cheney *et al.* (1993), Cheney and Gould (1995) and Bluestem grass (Overholt *et al.* 2014)
Vegetation element density	440 kg. m^{-3} 160 kg. m^{-3}*	White pine (Australian Radiata pine) (Abu Bakar 2015) hay or straw density
Ambient temperature	32 °C 50 °C*	Experimental (Cheney *et al.* (1993), Cheney and Gould (1995)
Relative humidity	40 % 10 %*	(Cheney *et al.* (1993), Cheney and Gould (1995)
Emissivity	0.99	Cheney *et al.* (1993), Cheney and Gould (1995)
Pyrolysis Temperature	400–500 K	(Morvan *et al.* 2004)
Degree of curing	100%	Assuming vegetation100% cured
Vegetation heat of pyrolysis	200 kJ.kg^{-1}	White pine (Australian Radiata pine) (Abu Bakar 2015)

* Fuel parameters used with simulation Set 4.

5.3 Results and discussions

The fire isochrones, head fire width, fire line intensity, location of fire front, *RoS*, flame dynamics, mode of fire propagation and heat fluxes (convective and radiative) are analysed and the results are presented in the following sections. The *RoS* values are then compared with the empirical modelling studies found in the literature: McArthur models MKIII and MKV, CSIRO model, and Rothermel Original and Modified models. Further, the quasi-steady *RoS* results are compared for different domain sizes and fuel parameters.

5.3.1 Progression of isochrones and pyrolysis width

This section analyses and discusses the fire isochrones and the pyrolysis width (or head fire width) results from the four sets of simulations.

5.3.1.1 Progression of isochrones

As for the higher wind velocity cases (Section 4.4.1.1), the pyrolysis fronts are extracted from the boundary temperature and plotted at different times after ignition and when the fire progress towards the end of the burnable grass plot. The fire progression isochrones as a function of time for the four sets of simulations at wind velocities of 0.1 and 1 $m.s^{-1}$ are presented in Figure 5.2.

Slope	360 × 120 × 60 m – 0.1 m.s^{-1} (Set 1)	360 × 120 × 60 m – 1 m.s^{-1} (Set 2)	480 × 180 × 80 m – 1 m.s^{-1} (Set 3)	480 × 180 × 80 m – 1 m.s^{-1} (Set 4)
–10°	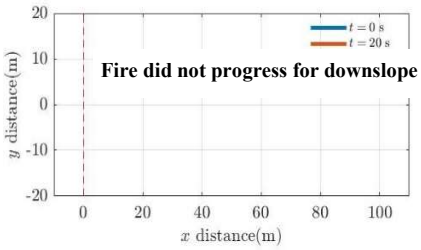 Fire did not progress for downslope **(a)**	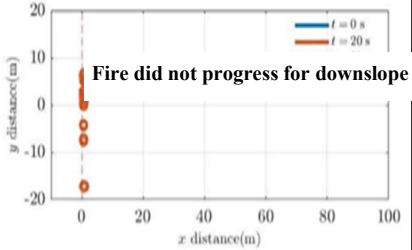 Fire did not progress for downslope **(i)**	Fire did not progress for downslope	Fire did not progress for downslope
0°	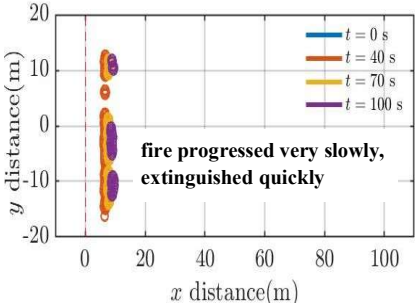 fire progressed very slowly, extinguished quickly **(b)**	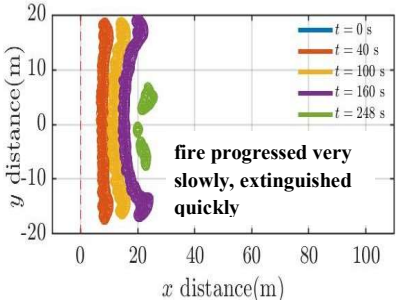 fire progressed very slowly, extinguished quickly **(j)**	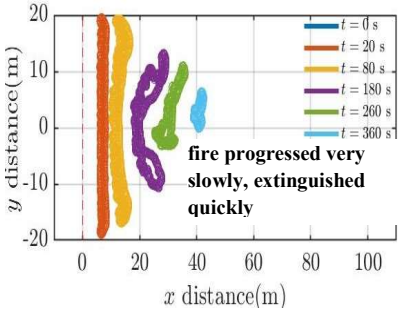 fire progressed very slowly, extinguished quickly **(q)**	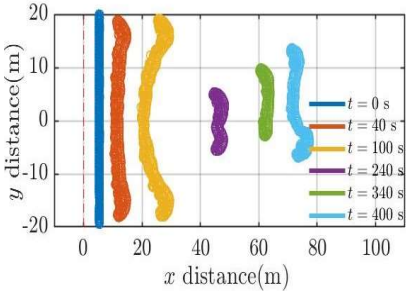 **(x)**
+5°	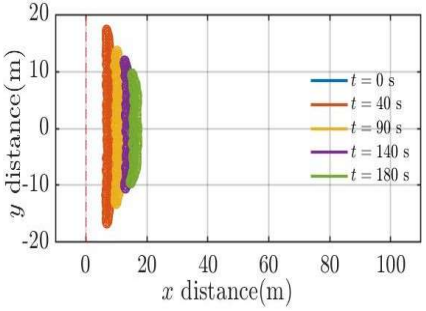 **(c)**	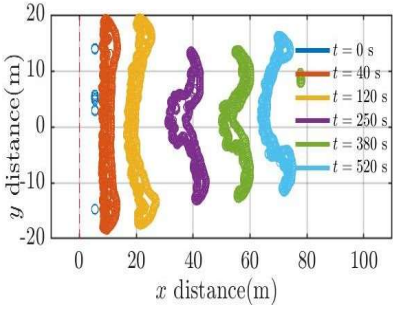 **(k)**	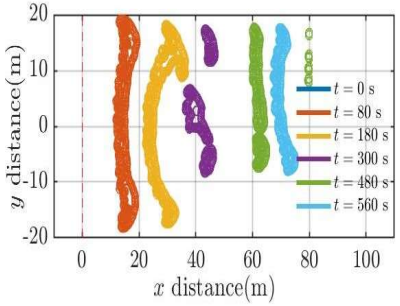 **(r)**	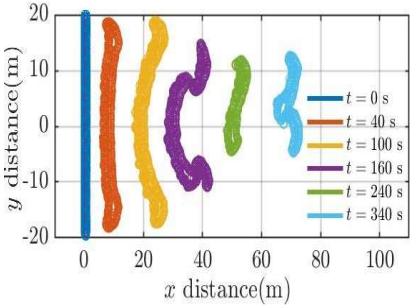 **(y)**

Slope	360 × 120 × 60 m – 0.1 m.s^{-1} (Set 1)	360 × 120 × 60 m – 1 m.s^{-1} (Set 2)	480 × 180 × 80 m – 1 m.s^{-1} (Set 3)	480 × 180 × 80 m – 1 m.s^{-1} (Set 4)
+10°	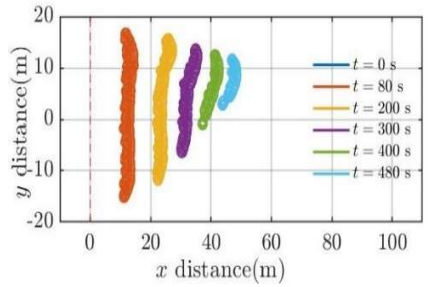 (d)	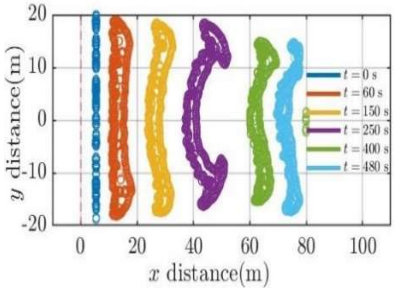 (l)	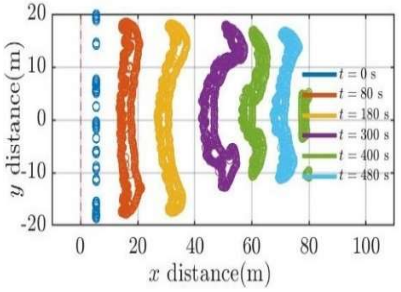 (s)	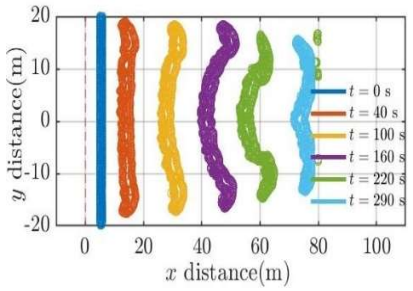 (z)
+15°	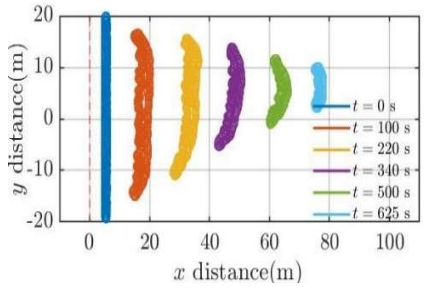 (e)	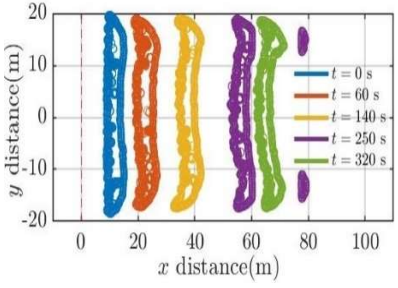 (m)	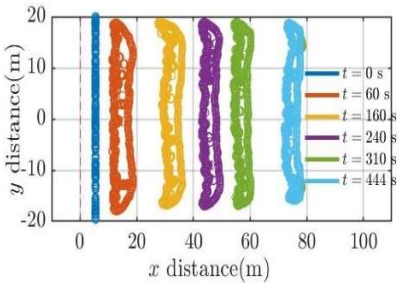 (t)	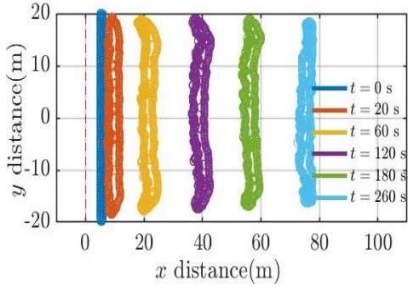 (aa)
+20°	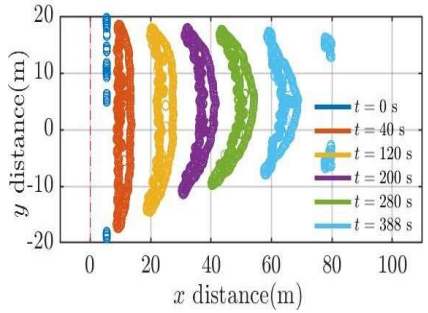 (f)	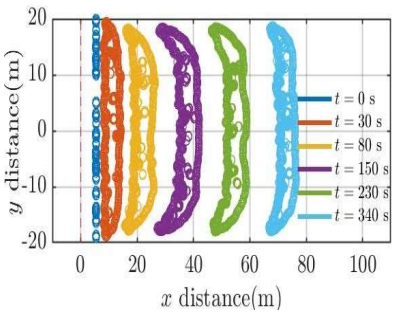 (n)	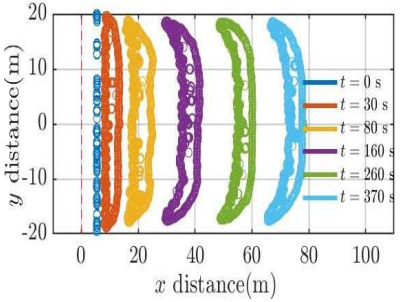 (u)	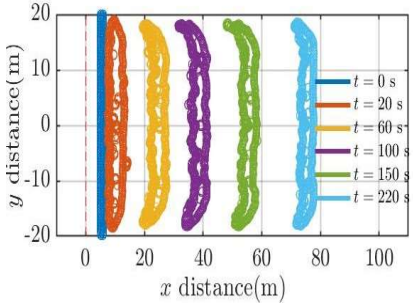 (ab)

Slope	360 × 120 × 60 m – 0.1 m.s^{-1} (Set 1)	360 × 120 × 60 m – 1 m.s^{-1} (Set 2)	480 × 180 × 80 m – 1 m.s^{-1} (Set 3)	480 × 180 × 80 m – 1 m.s^{-1} (Set 4)
+25°	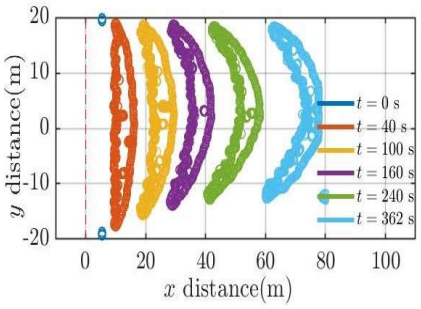 **(g)**	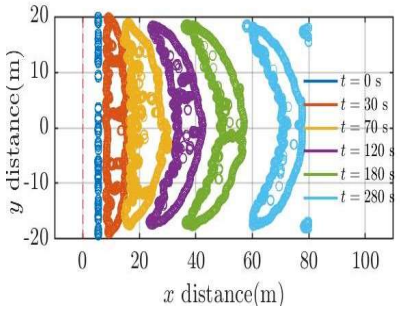 **(o)**	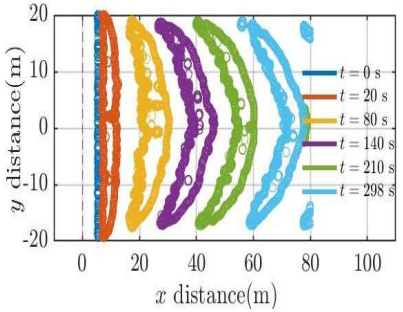 **(v)**	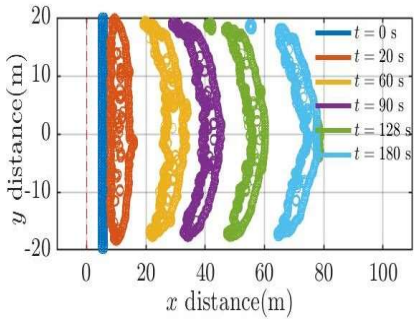 **(ac)**
+30°	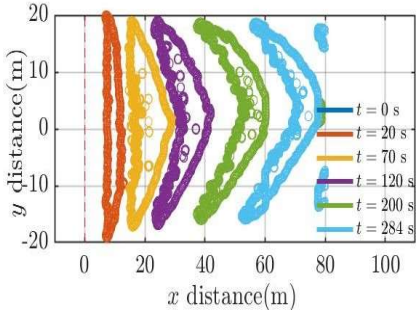 **(h)**	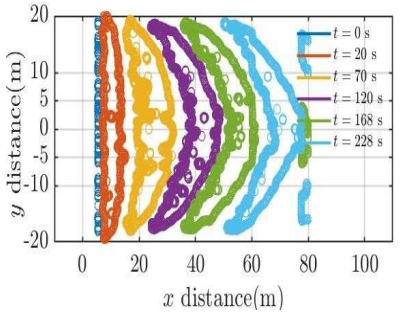 **(p)**	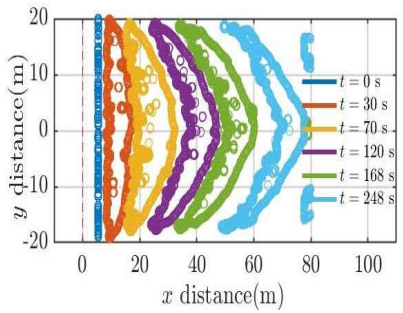 **(w)**	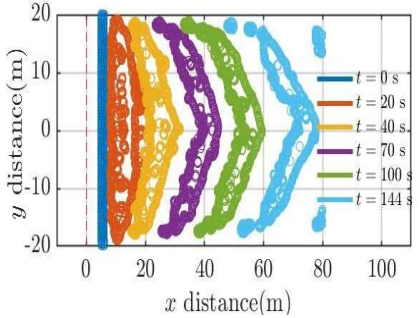 **(ad)**

Figure 5.2 – Progression of isochrones : Frames (a–h) original domain at 0.1 m.s^{-1} (Set 1) ; Frames (i–p) original domain at 1 m.s^{-1} (Set 2) ; Frames (q–w) large domain, original fuel parameters at 1 m.s^{-1} (Set 3); and Frames (x–ad) large domain, changed fuel parameters at 1 m.s^{-1} (Set 4).

For lower wind velocities of 0.1 and 1 m.s^{-1}, the fire isochrones did not progress for downslope –10° as shown in Frames (a) and (i) of Figure 5.2. As observed with downslopes at 3 m.s^{-1} (Section 4.4.1, Figure 4.7), this lower wind velocity may not be sufficient to drive the fire front as it moves downslope and the fire extinguished instantly. Hence, steeper downslopes are not simulated, and downslope cases are not discussed further in this chapter. Again, for no slope and lower upslope angles (0°, +5° at 0.1 m.s^{-1} and 0° at 1 m.s^{-1},) the fire isochrones progressed very slowly and extinguished much earlier as evident in Frames (b), (c) and (j), (q) of Figure 5.2.

As the slope angle increases, the pyrolysis front becomes wider (pyrolysis width is presented in the following section) and reaches the end of burnable grass plot earlier. With 0.1 m.s^{-1}, the isochrone travel times obtained are: 625, 388, 362 and 284 s for +15°, +20°, +25° and +30°, respectively and with 1 m.s^{-1} (Set 3) , the isochrone travel times obtained are: 444, 370, 298 and 248 s for +15°, +20°, +25° and +30°, respectively. For the same slope angle, with increase in wind velocity, the pyrolysis front travels more quickly and reaches the end of grass plot earlier. This is in line with the observations from the higher velocity cases presented in Figure 4.6, that the pyrolysis front travels more quickly with increase in wind velocity and slope angle.

To investigate the effect of domain size and fuel characteristics on fire isochrone progression, further simulations are performed with a larger domain (Set 3), and with changed fuel properties (Set 4). Both these simulations are conducted for slope angles +0° to +30°, at the same driving wind velocity of 1 m.s^{-1}. The resultant fire isochrones are also presented in Figure 5.2. Frames (q–w) show the fire isochrones for Set 3 and Frames (x–ad) show that for Set 4 simulations.

The fire isochrones at lower slope angles show an inward shape pattern (up to +10° for 0.1 m.s^{-1} and up to +15° for 1 m.s^{-1} cases) and do not attain a convex shape. As the slope angle increases (in some cases as the isochrones travel downstream), the contours evolve into a more pointed convex curve that is sharper at higher upslopes. This agrees with the experimental studies conducted by Dupuy *et al.* (2011) with no wind as detailed in Chapter 2 (Section 2.2.2). They observed that on +20° and +30° upslope fires, the fire isochrones changed to a pointed V-shape, whereas no-slope fires adopted a smooth curved shape. Overall, although the geometry, boundary conditions, length of fuel bed and fuel type were different from the simulations presented by Dupuy *et al.* (2011), Figure 5.2 demonstrates that the fire contours become more pointed for higher

upslopes. Also, the fire isochrone patterns generally shows agreement with the experimental observation of Tihay *et al.* (2014) (Chapter 2, Section 2.2.2), at no-wind, who noted that for a +20º slope fuel bed, the fire contour turned out into a V-shape pattern as the fire progressed though the fuel bed.

The fire isochrones with Set 3 (Frames q–w) show a similar pattern to Set 2 (Frames i–p). Comparing the domain sizes (set 2 and set 3), we did not observe any notable variations in fire isochrone patterns. Again, comparing Set 3 and 4 simulations with different fuel parameters, generally, the fire isochrones demonstrated similar progression patterns. However, Set 4 shows slightly more convex curvatures and a thinner pyrolysis width (or head fire width).

5.3.1.2 Pyrolysis width

The pyrolysis width as a function of time is presented in Figure 5.3 for all the four sets of simulations. Pyrolysis width for Sets 1 and 2 (original domain at 0.1 and 1 m.s^{-1}) are shown Figure 5.3(a) and (b) and those of Sets 3 and 4 (larger domain with original and changed fuel parameters, at 1 m.s^{-1}) are shown in Figures 5.3(c) and (d), respectively.

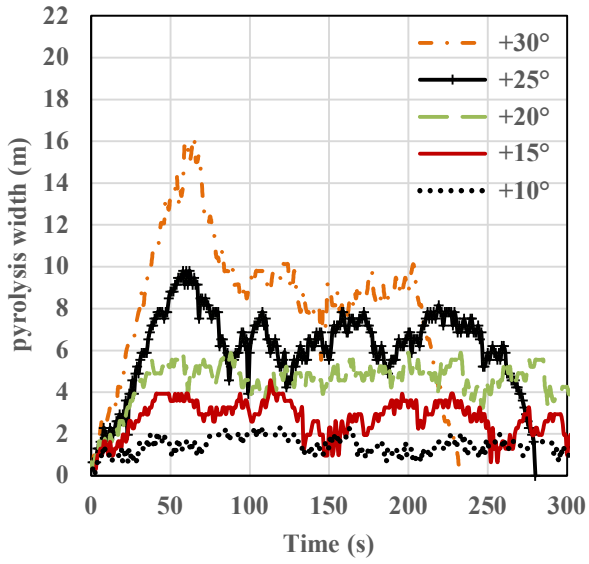

(a) Set 1, 0.1 m.s^{-1}

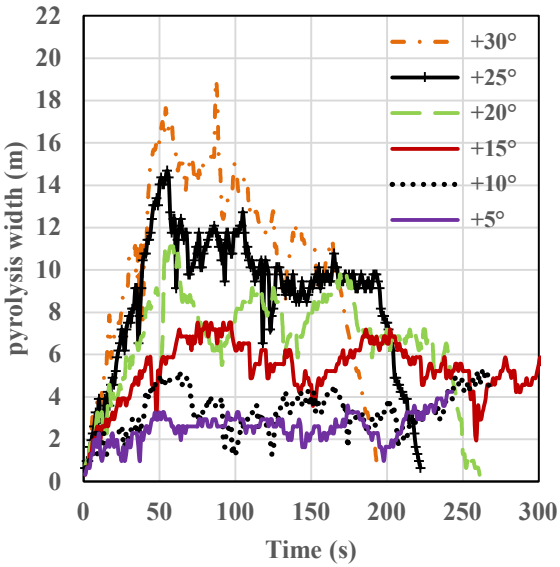

(b) Set 2, 1 m.s^{-1}

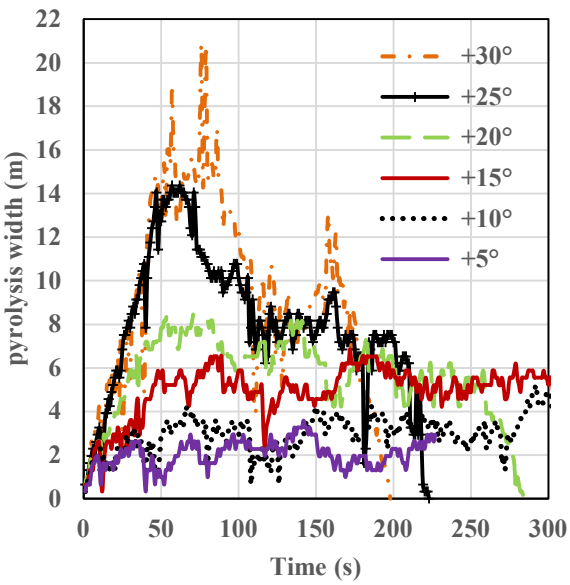

(c) Set 3, 1 m.s^{-1}

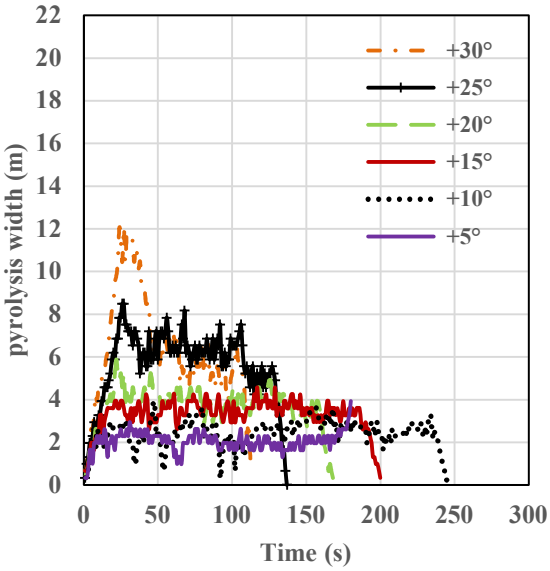

(d) Set 4, 1 m.s^{-1}

Figure 5.3 – Pyrolysis width vs time: (a) Set 1, original domain at 0.1 m.s^{-1}; (b) Set 2, original domain at 1 m.s^{-1}; (c) Set 3, larger domain with original fuel, at 1 m.s^{-1}; and (d) Set 4, larger domain with changed fuel, at 1 m.s^{-1}.

For all four sets, the pyrolysis width increases as the fire front progresses from the ignition line, then plateaus or reaches a quasi-steady state and finally decreases. However, for high upslopes (+25° and +30°), the values fluctuate, and the plateau is observed only for a shorter period of time. Generally, as the upslope angle increases, the width of the plateau decreases, and its magnitude or value increases. At lower slope angles, the pyrolysis width values are lower. The pyrolysis widths for +5° and +10° are lower, consistent with Figure 5.2, where the isochrones are moving very slowly at lower slope angles and the fire extinguishes relatively quickly.

Figure 5.4(a) shows the quasi-steady pyrolysis width vs slope angle for all four sets of simulations and 5.4(b) the relative pyrolysis width (normalised by pyrolysis width at +10°) vs slope angle.

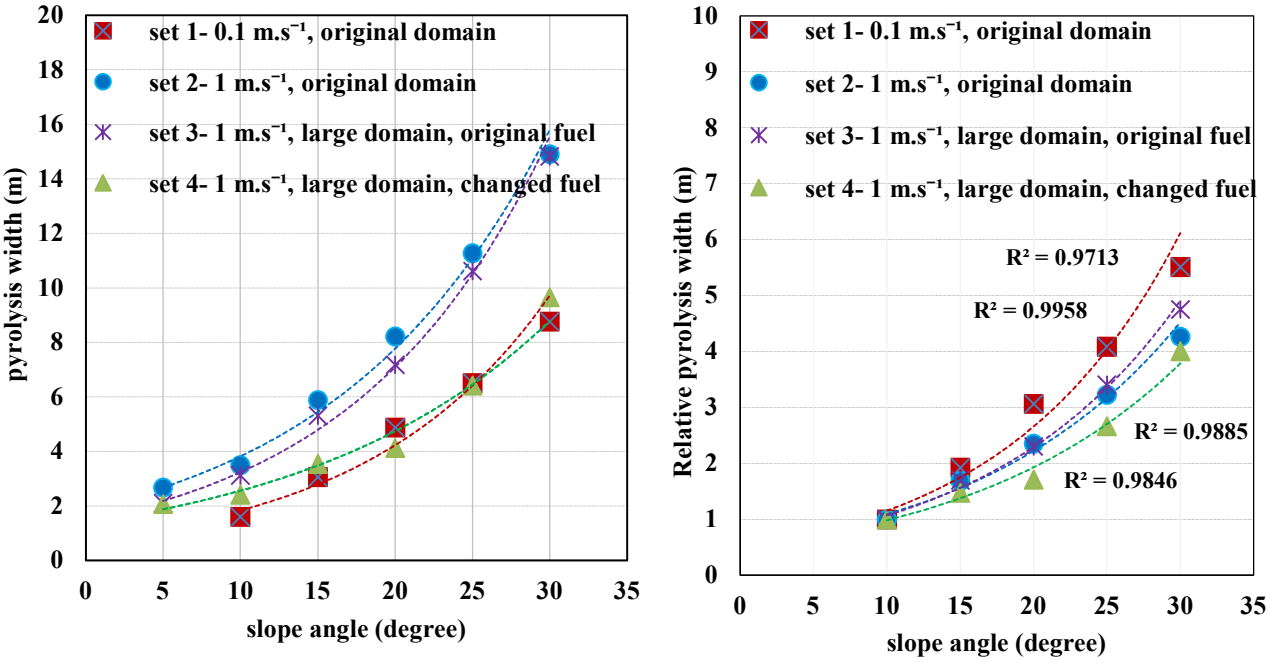

(a) Quasi-steady pyrolysis width vs slope angle

(b) Relative pyrolysis width vs slope angle

Figure 5.4 – (a) Quasi-steady pyrolysis width vs slope angles for all four sets; (b) relative pyrolysis width (normalised by pyrolysis width at +10°) vs slope angle for all sets

In Figure 5.4(a), the width values are extracted approximately 40 to 200 s from the start of ignition for Sets 1, 2 and 3 and from 20 to 120 s for Set 4. These values are approximate for +25° and +30° slopes as the fire front reaches the end of the burnable grass plot more quickly, attaining peak values much earlier. Hence, for higher upslopes (+25° and +30° with Sets 2, 3 and +30° with Sets 1 and 4), a perfect steady-state width condition is not attained at any given time. For these upslopes, the pyrolysis width is averaged over a very short period at the peak of the width (from approximately 60 to 100 s for +25° and +30° for Set 2 and 3 simulations, from 100 to 200 s for +30° for Set 1 and from 30 to 50 s for +30° for Set 4). Pyrolysis width values are found to be lower for lower slope angles (for Set 2, the pyrolysis width at +10° is approximalety 75% lower from that at +30° slope). The fire did not propagate for lower slopes and hence 0° and +5° at 0.1 $m.s^{-1}$ and 0° at 1 $m.s^{-1}$ are not included in the slope angle–pyrolysis width plot in Figure 5.4.

The relationship between pyrolysis width and slope angle can be constructed as a linear, exponential or second-order polynomial for all four sets of simulations. Relationships and R^2 values are presented in Table 5.3. For all three types of relationships, $R^2 > 0.95$, except for the Set

4 linear relationship, where R^2 = 0.88. For the four sets, the pyrolysis width was found to approximately double at every +10° increase in upslope, which is indicative of an exponential relationship. It is to be noted that doubling of *RoS* at every +10° increase and decrease in slope is considered as a rule of thumb for Australian empirical models. Therefore, in Figure 5.4(a), trend lines are shown only for exponential fits.

Table 5.3: Pyrolysis width vs slope angle relationship

Pattern	0.1 m.s^{-1}, Set 1	1 m.s^{-1}, Set 2	1 m.s^{-1}, Set 3	1 m.s^{-1}, Set 4
Exponential	$0.7985e^{0.0833x}$	$1.877e^{0.071x}$	$1.4748e^{0.0785x}$	$1.3801e^{0.0617x}$
R^2	0.9713	0.9909	0.9953	0.9788
Polynomial	$0.0004x^2 + 0.1954x + 0.7546$	$0.0119x^2 + 0.0783x + 1.8466$	$0.015x^2 + 0.021x + 1.8847$	$0.0136x^2 + 0.021x + 2.8312$
R^2	0.9989	0.9985	0.9979	0.9879
Linear	$0.3558x - 2.158$	$0.4958x - 0.9368$	$0.5027x - 1.6066$	$0.2888x - 0.3524$
R^2	0.9945	0.9686	0.9529	0.8828

Comparing the wind velocities (Sets 1 and Set 2), for a given slope angle, the pyrolysis width increases with wind velocity, as for the results with higher wind velocity cases discussed in Section 4.4.1.2. Comparing the pyrolysis width among the two domain sizes (Sets 2 and 3) – with the same driving wind velocity and fuel characteristics – the values are generally closer for all slopes. The increased domain size has no insignificant effect on pyrolysis width, as for the similar fire isochrone pattern shown in Figure 5.2 for Sets 2 and 3. The pyrolysis width with changed fuel (comparing Sets 3 and 4) – with the same driving wind velocity and domain size – shows that the fuel characteristics influence pyrolysis width. Pyrolysis width is lower with changed fuel parameters for all slope angles. As expected, increased ambient temperature along with reduced fuel moisture content, relative humidity and fuel load decrease the pyrolysis width.

In Figure 5.4(b), relative pyrolysis widths (pyrolysis width on any slope divided by pyrolysis width for +10° slope) are presented for the four sets. Since fire did not progress for lower slope angles (0° and +5° at 0.1 m.s^{-1} and 0° at 1 m.s^{-1}), +10° slope is chosen as the base to determine the relative pyrolysis width instead of 0° slope. Like quasi-steady pyrolysis width vs slope angle, an

exponential relationship (R^2 value shown in the figure) can be constructed between relative pyrolysis width and slope angle. A stronger pyrolysis width effect is observed for 0.1 m.s^{-1} wind velocity cases (Set 1) compared with 1 m.s^{-1} cases (Sets 2, 3 and 4) and the difference widens as the slope angle increases. This may be associated with longer residence times. Generally, the pyrolysis width effect is found to be identical for 1 m.s^{-1} wind velocity cases (Sets 2 and 3).

Figure 5.5 (a–d) shows the pyrolysis width vs fire front location for the four sets of simulations

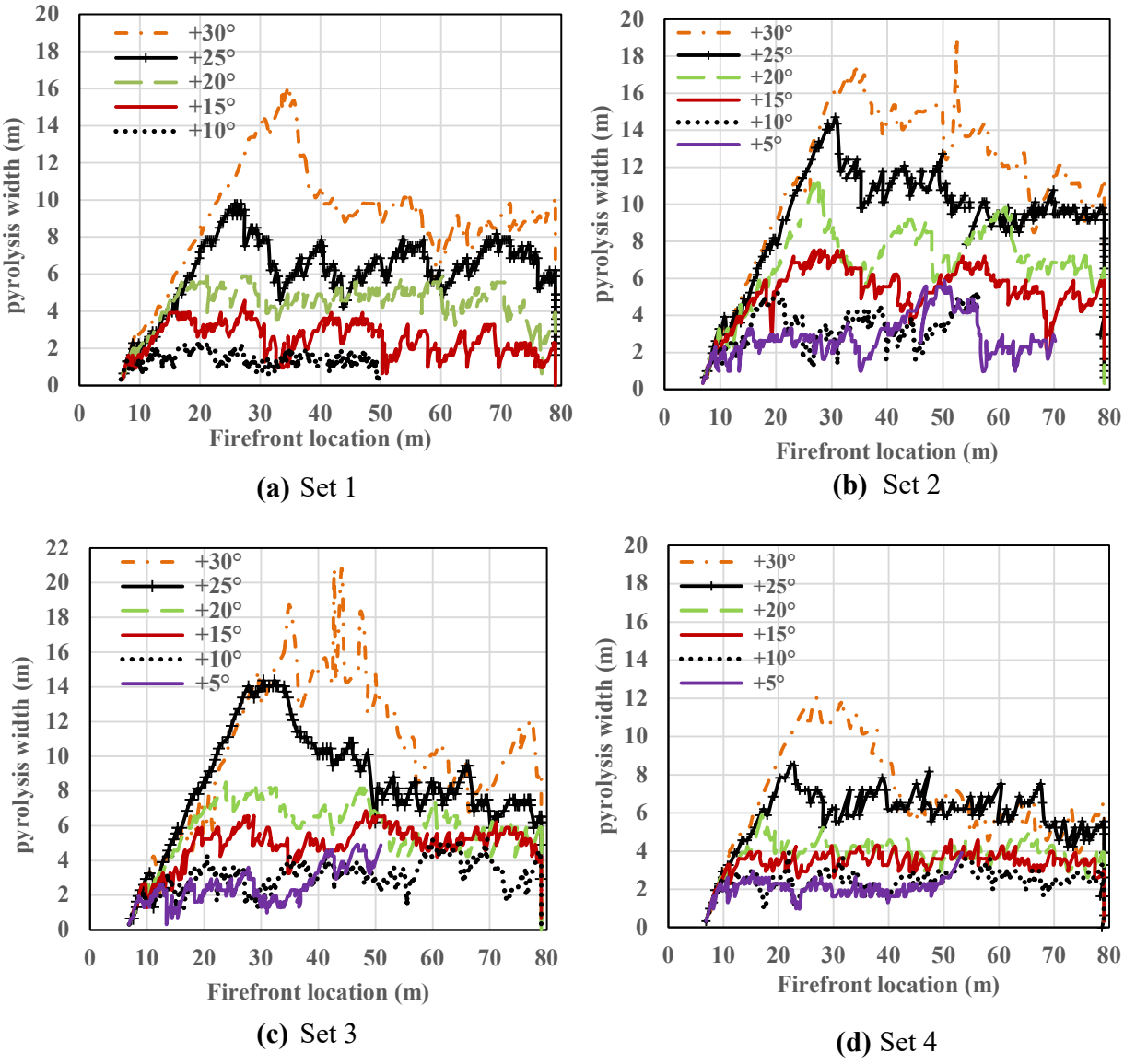

Figure 5.5 – Pyrolysis width vs fire front location: (a) Set 1, original domain at 0.1 m.s^{-1}; (b) Set 2, original domain at 1 m.s^{-1}; (c) Set 3, larger domain, original fuel, at 1 m.s^{-1}; (d) Set 4, larger domain, changed fuel at 1 m.s^{-1}.

As in Figure 5.3, the pyrolysis width increases as the fire front moves forward, then typically plateaus or reaches a quasi-steady state in all four sets. However, upslopes +25° and +30° reach a sharp peak first (between 25 and 30 m from the ignition line) and then gradually decrease to a quasi-steady state that begins after ~40 m in Sets 1 and 4 (for +25º) and after ~60 m in Sets 2 and 3. Compared with the pyrolysis width vs time plots in Figure 5.3, quasi-steady states are more clearly visible over longer distances (though the values fluctuate for higher upslopes +25° and +30°). For the lower slope angle +10° at 0.1 m.s^{-1}, pyrolysis width gradually decreases over the distance, leading to extinction, consistent with the fire isochrone plots shown in Figure 5.2.

5.3.2 Heat Release Rate (HRR) and Fire Intensity

Time series of HRR obtained from all four sets of simulations for both 0.1 and 1 m.s^{-1} wind velocities are presented in Figure 5.6. HRR for Sets 1 and 2 (original domain at 0.1 and 1 m.s^{-1}) are shown Figures 5.6 (a) and (b) and for Sets 3 and 4 (larger domain with original and changed fuel parameters at 1 m.s^{-1}) in Figure 5.6 (c) and (d), respectively.

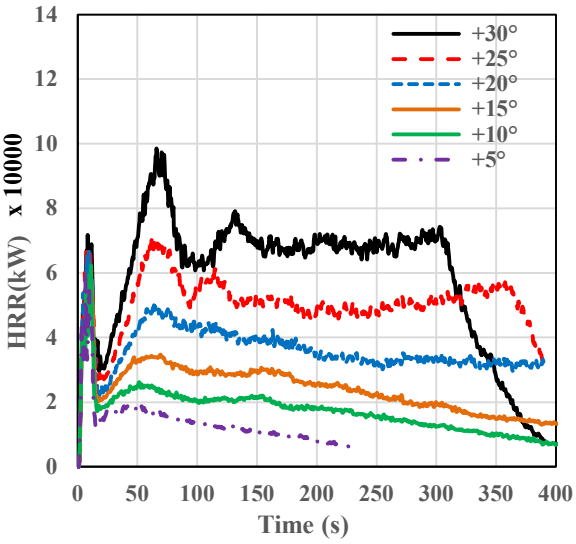

(a) Set 1, 0.1 m.s^{-1}

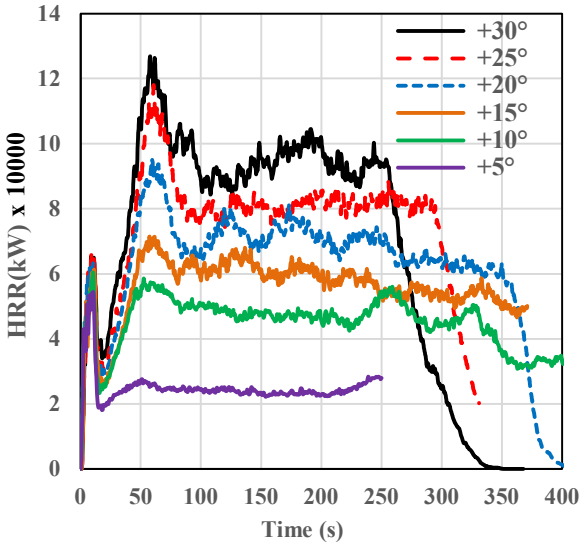

(b) Set 2, 1 m.s^{-1}

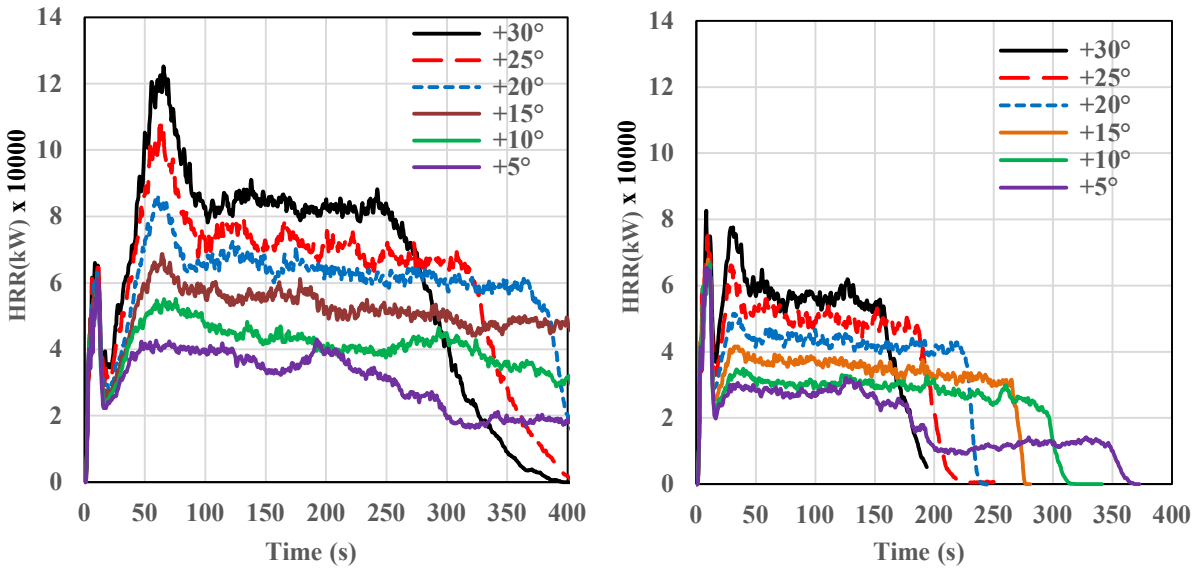

(c) Set 3, 1 m.s^{-1} **(d)** Set 4, 1 m.s^{-1}

Figure 5.6 – HRR vs time: (a) Set 1, original domain at 0.1m.s^{-1}; (b) Set 2, original domain at 1m.s^{-1}; (c) Set 3, larger domain with original fuel, at 1m.s^{-1}; (d) Set 4, larger domain with changed fuel parameters at 1m.s^{-1}.

Following the method detailed in Section 4.4.3, Byram's fire intensity Q (kW.m^{-1}) is calculated by dividing the HRR values (kW) at various instants in time (at intervals of 20 s) by the fireline length (m) measured along the centre of pyrolysis region of fire ischrones at the same instants in time. The instantaneous ignition line running across the width of the fire isochrone plots (shown in Figure 5.2) is measured every 20 s following the method demonstrated in Figure 4.16(a) in Section 4.4.3. A line is drawn on the fire isochrones along the centre of the curvature and the fireline length is measured physically through this line. At the lower wind velocities of 0.1 and 1 m.s^{-1}, as the fire eventually extinguished, it was not possible to measure meaningful fire front lengths for no slope and lower upslope angles (as shown in Fig 5.2). Hence, 0°, +5° and +10° at 0.1 m.s^{-1} and 0°, +5° at 1 m.s^{-1} are not included in the fire intensity plots. Again, at the lower upslope angle +10°, the fire isochrones did not attain a curvature, and hence, the measured fire front lengths for +10° for the four sets are approximate.

Q values as a function of time are presented in Figure 5.7 for the four sets of simulations. The intensities for Sets 1 and 2 (original domain at 0.1 and 1 m.s^{-1}) are shown Figures 5.7(a) and (b) and that of Sets 3 and 4 (larger domain with original and changed fuel parameters, at 1 m.s^{-1}) are

shown in Figures 5.7(c) and (d), respectively. Figure 5.7(e) shows the quasi-steady Q vs slope angle for all four sets of simulations.

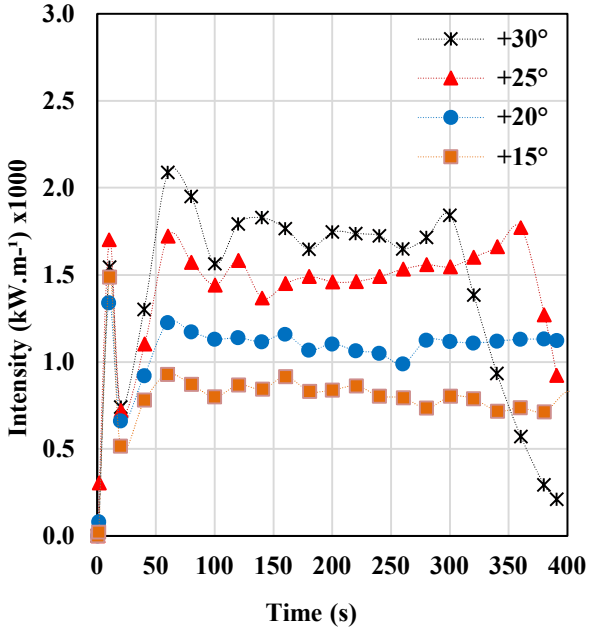

(a) Intensity vs time – Set 1, 0.1 m.s^{-1}

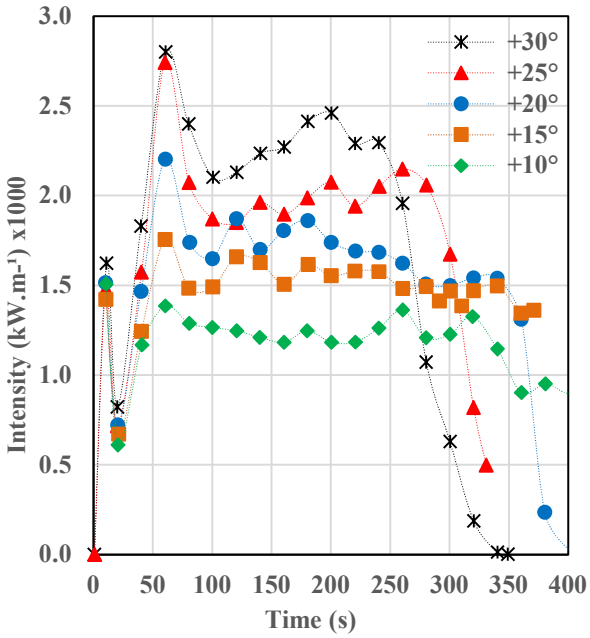

(b) Intensity vs time – Set 2, 1 m.s^{-1}

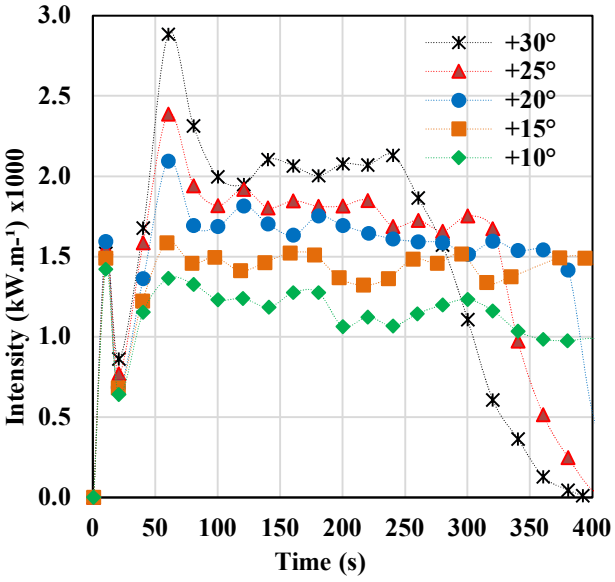

(c) Intensity vs time – Set 3, 1 m.s^{-1}

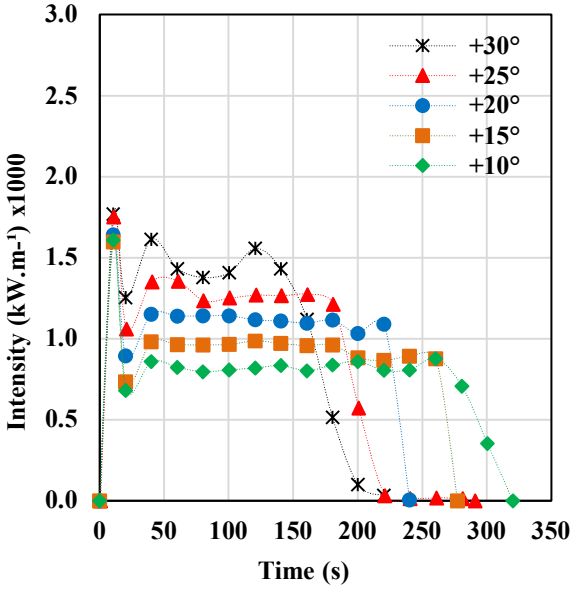

(d) Intensity vs time – Set 4, 1 m.s^{-1}

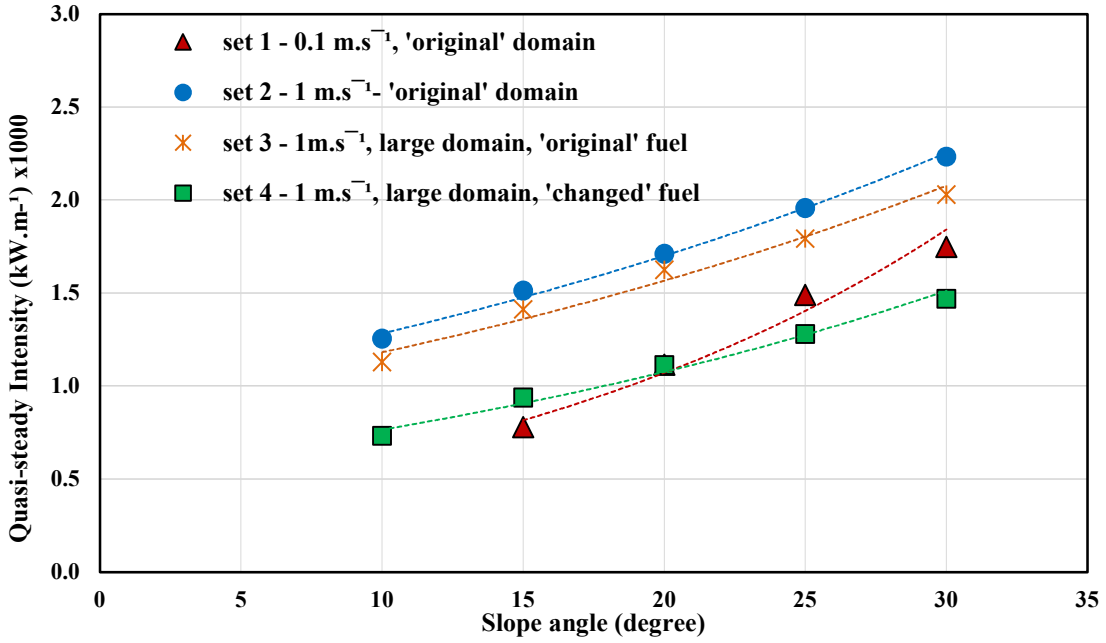

(e *)* Quasi-steady intensity Q vs slope angles for all sets

Figure 5.7 – Fireline intensity vs time: (a) Set 1, original domain at 0.1 m.s^{-1}; (b) Set 2, original domain at 1 m.s^{-1}; (c) Set 3, larger domain with original fuel parameters, at 1 m.s^{-1}; (d) Set 4, larger domain with changed fuel parameters at 1 m.s^{-1}; (e) quasi-steady intensity vs slope angle for all four sets.

The HRR generally increases upon ignition, then decreases for a while and surges again. The first peak occurs at ~10 s for all sets and the second peak occurs at ~65 s for Sets 1, 2 and 3 and about 35 s for Set 4. Note that ignition lasts for 10 s. Once the ignition source is removed, the fire intensity starts decreasing. However, with increased pyrolysis, the intensity starts to surge again. For all four sets, the HRR (and hence Q) increases with slope angle, attains a peak value, and then reaches a quasi-steady state.

The Q values extracted from the quasi-steady region are plotted in Figure 5.7(e) for all four sets. On sloped terrain, for a given slope angle, the Q value increases with the driving wind velocity and slope angle when the fuel characteristics are the same. For 1 m.s^{-1} cases (Sets 2, 3 and 4), the quasi-steady Q values increase by approximately 30–50% at every +10° increase in slope, whereas the increase is approximately 60–90% for 0. 1 m.s^{-1} cases.

Comparing the Q values among the two domain sizes (Sets 2 and 3), the values are generally closer for all slope angles, as observed with the pyrolysis width (Figure 5.4). Comparing Set 3 and Set 4, the Q values decrease with the changed fuel characteristics as noted with pyrolysis width (Figure 5.4(a)). The relationship between fire intensity Q and slope angle can be constructed as a linear, exponential or second-order polynomial (relationship and R^2 values are given in Table 5.4) for all four sets of simulations. For all three types of relationships, the R^2 value is > 0.97. Since a minimal difference is observed in the R^2 values among the three types of relationships, an exponential relationship is considered between the intensity and slope angle, as reasoned in Section 5.3.1.2. The exponential trend lines (for visual representation only) are shown in Figure 5.7(e).

Table 5.4: Intensity vs slope angle relationship

Pattern	**0.1 m.s^{-1}, Set 1**	**1 m.s^{-1}, Set 2**	**1 m.s^{-1}, Set 3**	**1 m.s^{-1}, Set 4**
Exponential	$362.13e^{0.0542x}$	$967.92e^{0.0282x}$	$891.13e^{0.0282x}$	$544.67e^{0.034x}$
R^2	0.9677	0.9957	0.9777	0.9855
Polynomial	$0.7752x^2 + 100.43x$ –560.22	$0.2425x^2 +$ $38.278x + 859.49$	$0.3961x^2 + 59.444x$ + 587.25	$0.1145x^2 + 40.9x$ + 340.78
R^2	0.9978	0.9982	0.9957	0.9991
Linear	$65.546x - 192.01$	$47.979x + 774.6$	$43.601x + 725.87$	$36.321x + 380.84$
R^2	0.995	0.9973	0.9928	0.9988

5.3.3 Dynamic *RoS*, Fire front locations and *RoS* calculations

This section discusses the dynamic *RoS*, fire front locations, *RoS* calculation and correlation of *RoS* with slope angles for the four sets of simulations. The *RoS* values obtained from WFDS simulations are then compared with the results from empirical models: McArthur models MKIII and MKV, CSIRO model, Rothermel Original and Modified models. Then, the relative *RoS* of WFDS 'quasi-steady' values are compared with Australian slope–function (rule of thumb) and the Rothermel model variations. The quasi-steady *RoS* are then compared among different sets of simulations, and finally fire intensity is plotted as a function of *RoS.*

It was demonstrated in previous sections that the fire did not propagate for lower slope angles, therefore, 0° and +5° at 0.1 m.s^{-1} (Set 1) and 0° at 1 m.s^{-1} (Sets 2, 3 and 4) are not included in the *RoS* calculations and further analysis in the following sections.

5.3.3.1 Dynamic *RoS*

Following the method discussed in Section 4.4.2.1 for higher wind velocity cases, an attempt is made to analyse the dynamic *RoS* for simulations conducted with lower wind velocities of 0.1 and 1 m.s^{-1}. These dynamic *RoS* values as a function of time are plotted in Figure 5.8 (a–d) for all four sets of simulations, at 0.1 and 1 m.s^{-1} wind velocities.

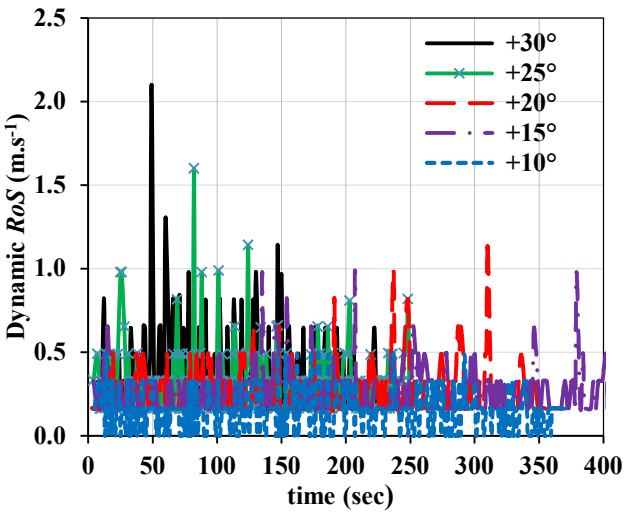

(a) Set 1, 0.1 m.s^{-1}

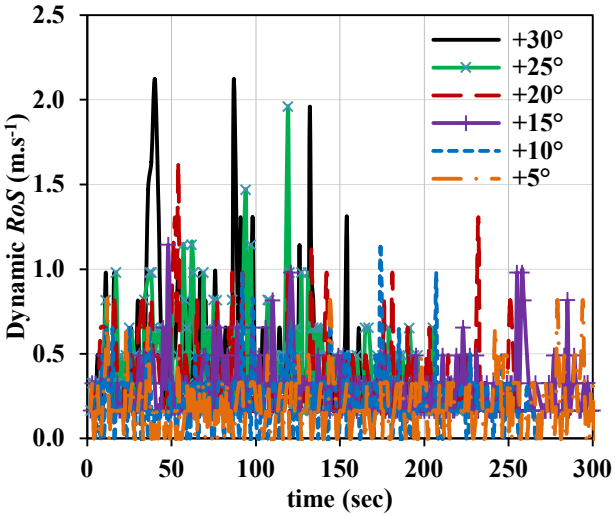

(b) Set 2, 1 m.s^{-1}

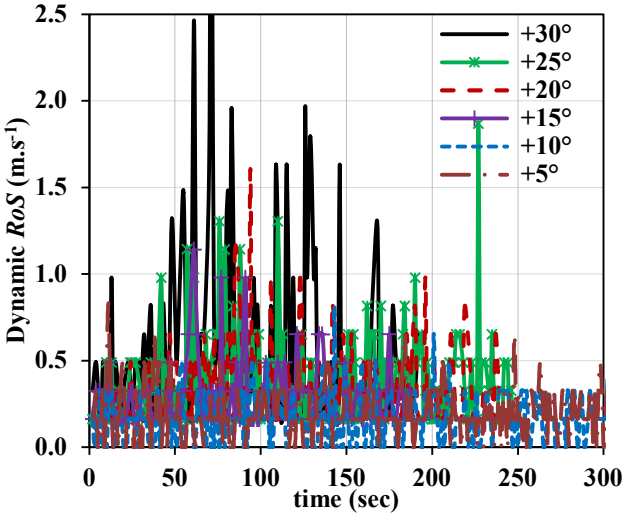

(c) Set 3, 1 m.s^{-1}

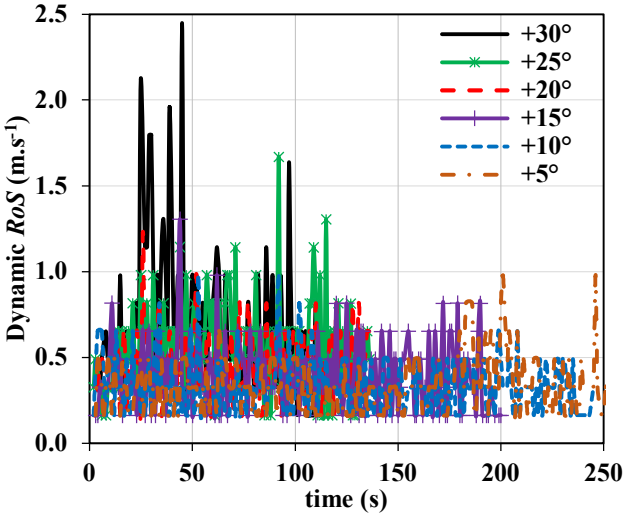

(d) Set 4, 1 m.s^{-1}

Figure 5.8 – Dynamic *RoS* : (a) Set 1, original domain at 0.1 m.s^{-1}; (b) Set 2, original domain at 1 m.s^{-1}; (c) Set 3, large domain with original fuel, at 1 m.s^{-1}; (d) Set 4, large domain with changed fuel at 1 m.s^{-1}

The plots show spikes (random fluctuations) in *RoS* values as the fire front moves on, and the maximum values are observed with +30° slope. The fluctuations in dynamic *RoS* values for lower slope angles are lower compared with that of steep upslopes. Comparing among the wind velocities, for a given slope angle, the dynamic *RoS* values are higher for 1 m.s^{-1} cases compared with 0.1 m.s^{-1}.

5.3.3.2 Fire front locations

The temporal fire front locations, determined from the boundary centreline temperature as the fire moves through the grass plot, are shown in Figure 5.9. Fire front location for sets 1 and 2 simulations are shown in Figure 5.9(a) and (b), respectively.

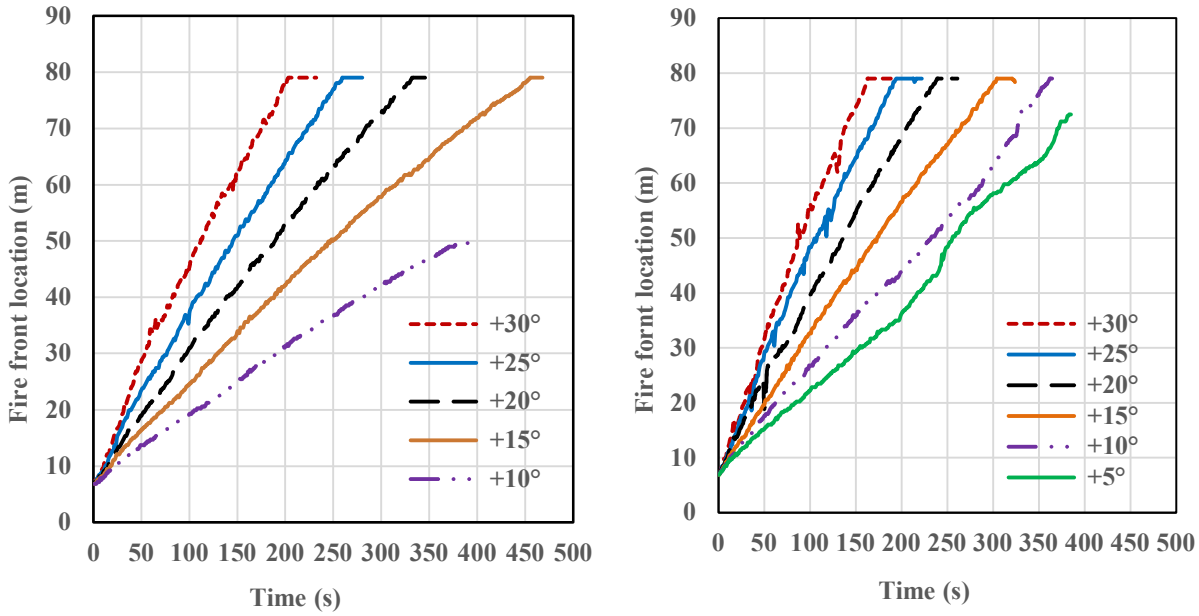

(a) Set 1, 0.1 m.s^{-1} **(b)** Set 2, 1 m.s^{-1}

Figure 5.9 – Fire front location vs time: (a) Set 1, original domain at 0.1 m.s^{-1}, (b) Set 2, original domain at 1 m.s^{-1}.

As expected, the fire front is found to be moving faster with increased slope angle. As the wind velocity decreases, the fire front travels more slowly, consistent with the higher wind velocity cases presented in Section 4.4.2.2. This is in line with the fire isochrones for these cases shown in Figure 5.2.

Figure 5.10(a) shows fire front locations for Set 2 and 3 simulations in a single plot, comparing the original and large domain sizes while conserving the same driving wind velocity (1 $m.s^{-1}$) and fuel characteristics. In Figure 5.10(b), the fire front locations for Set 3 and 4 simulations – original and changed fuel characteristics, conserving the same driving wind velocity (1 $m.s^{-1}$) and domain size – are presented, to demonstrate the effect of fuel characteristics on fire front propagation.

The continuous lines represent the fire front locations with the original domain size and original fuel parameters and the dashed lines represent that of the larger domain and changed fuel parameters.

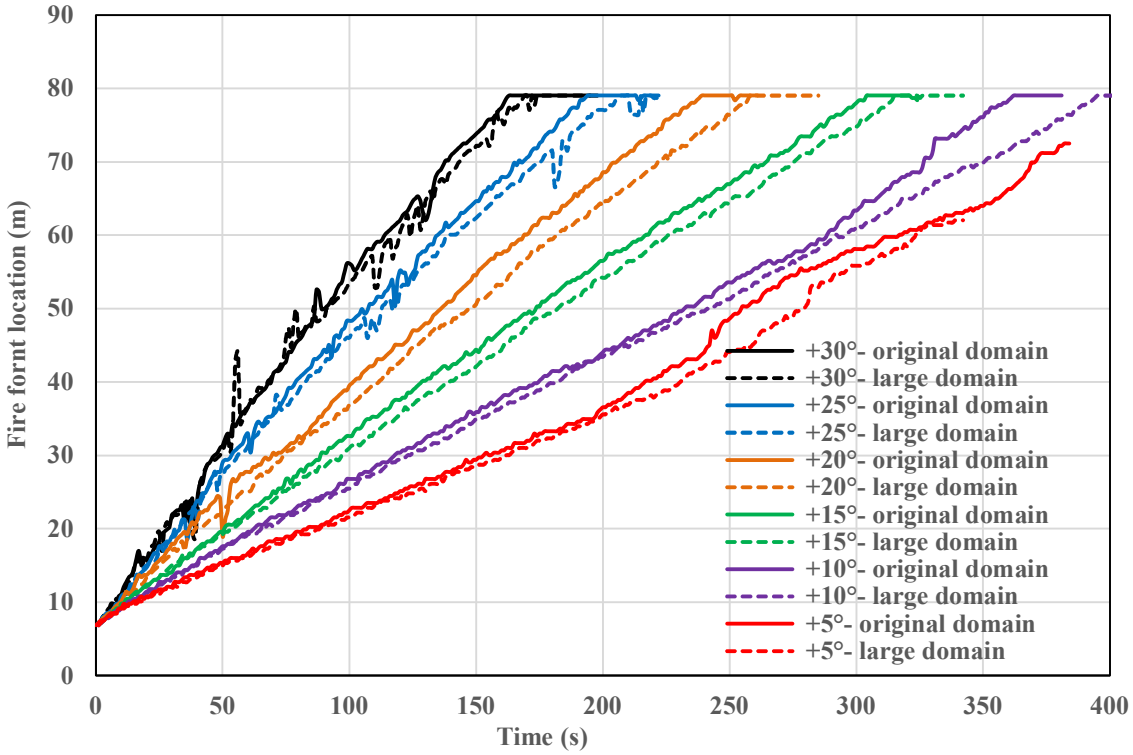

(a) Sets 2 and 3

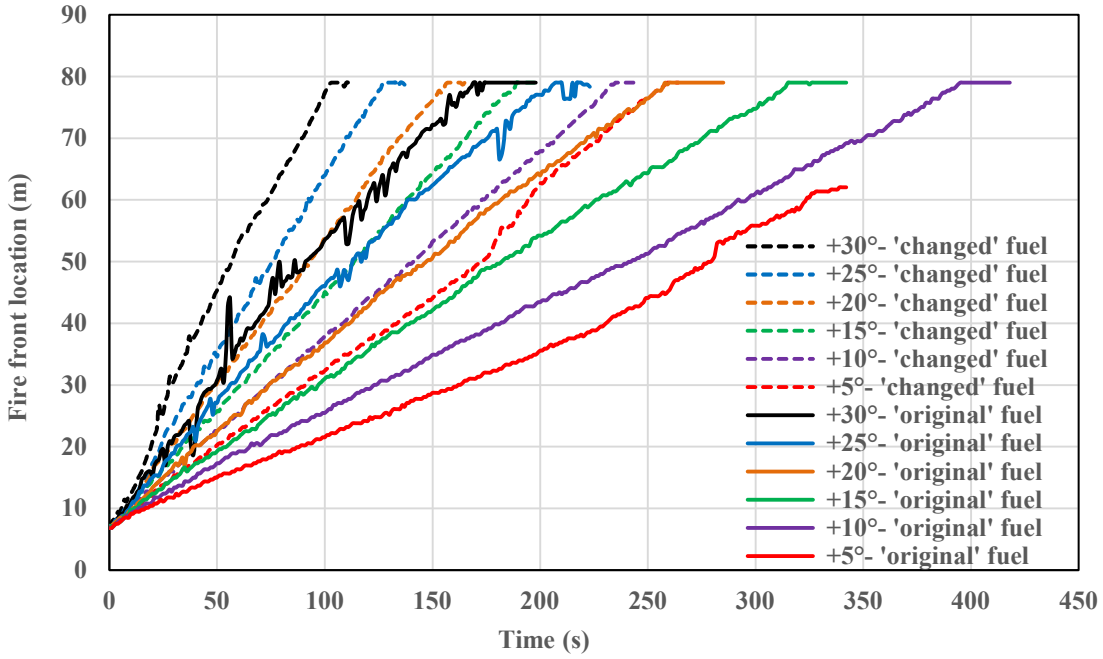

(b) Sets 3 and 4

Figure 5.10 – Fire front location vs time: (a) Sets 2 and 3, original and larger domain, at 1 m.s^{-1}; (b) Sets 3 and 4, original and changed fuel parameters, at 1 m.s^{-1}.

Comparing the different domain sizes (Figure 5.10(a)), for +15° and +20°, the fire front location with the original domain is found be slightly ahead (about 2–4 m) of the larger domain approximately 100 s from ignition. Generally, for a given slope angle, the fire front location at any given time is nearly the same for both the original and large domain cases. As similarly observed with pyrolysis width (Figure 5.4 (a)), increased domain sizes do not have a significant effect on the fire front locations.

Comparing the fuel characteristics (Figure 5.10 (b)), at any given time, the fire front is found to be moving faster with the changed fuel (lower density, fuel moisture content and fuel load) and the difference widens as the fire front progresses through the grass plot. Noticeably, increased ambient temperature along with reduced fuel moisture content, relative humidity and fuel load have impacted the fire front movement. At any given time immediately after ignition (after around 50–100 s), the fire front location with changed fuel parameters is farther by approximately 30–45% than that with original fuel parameters. Like pyrolysis width, the fuel characteristics influence the fire front movement, and hence the fire spread rate, which is investigated in the following section.

For both these scenarios (Figure 5.10 (a) and (b)), for the low slope angle +5°, the fire front location fluctuates as the fire moves towards the end of the grass plot.

5.3.3.3 *RoS* calculations

This section discusses the *RoS* calculation for all slope cases at both driving wind velocities of 0.1 and 1 m.s^{-1}, compares the WFDS *RoS* values with the empirical models, and finally compares the WFDS quasi-steady *RoS* among different scenarios: varied wind velocities, domain sizes and fuel parameters.

Following the same analysis technique used with higher wind velocity cases (Section 4.4.2.3), the quasi-steady *RoS* values for each slope case are calculated from the fire front location when steady-state conditions are reached. The least-square approximation method is applied to develop the *RoS*–slope angle correlations with a linear fit (the slope of each linear fit represents quasi-steady *RoS*) to the fire front location plots for each of the cases shown in Figures 5.9 and 5.10. As stated previously, steady-state conditions were not achieved for lower slope angles and hence 0° slope at 1 m.s^{-1} and 0° and +5° at 0.1 m.s^{-1} are not included in the *RoS*–slope angle correlation plots shown in this section.

The slope values obtained from the linear fit equations to the fire front plots in Figure 5.9(a) for each case are plotted against slope angles in Figure 5.11(a) and (b) for 0.1 m.s^{-1} wind velocity. From the fire front location, the fire front were found to be moving at the same pace for both the original (Set 2) and larger (Set 3) domain cases, with the same fuel parameters and driving wind velocity of 1 m.s^{-1}, as shown in Figure 5.10(a). Since we did not observe any notable variations in the fire isochrones pattern and fire front locations between these two sets, only Set 3 simulation results are presented in the *RoS* calculations. *RoS* results for 1 m.s^{-1} cases are shown in Figure 5.11(c) and (d) , obtained from linear fit equations to the fire front locations plotted for Set 3 in Figure 5.10(a). In Figure 5.11(e), the *RoS* results of changed fuel parameter cases are presented, obtained from the fire front locations plotted in Figure 5.10(b) for changed fuel (Set 4) simulations.

The dynamic *RoS* values are also plotted along with the quasi-steady *RoS* values in Figures 5.11(a) – (e). The dynamic *RoS* values (with maximum and minimum bounds and average values) are extracted from Figure 5.8(a), (c) and (d). Averaged dynamic *RoS* values are extracted from approximately 40–250 s from ignition for all cases. The upper and lower bounds of

instantaneous/dynamic *RoS* values are provided as whiskers, as one of the methods to present uncertainty to the averaged *RoS* values.

The empirically derived *RoS* values from different operational models are also presented in Figures 5.11(a)–(e) along with *RoS* values obtained from the WFDS simulations from this study with sloped terrain. The *RoS* values of slope-corrected MKIII and MKV and CSIRO models are derived from the set of equations presented in Section 2.1.1 and 2.1.2. Empirically derived *RoS* values of Rothermel Original and Modified models (derived from the set of equations presented in Section 2.1.3), are also shown in Figure 5.11.

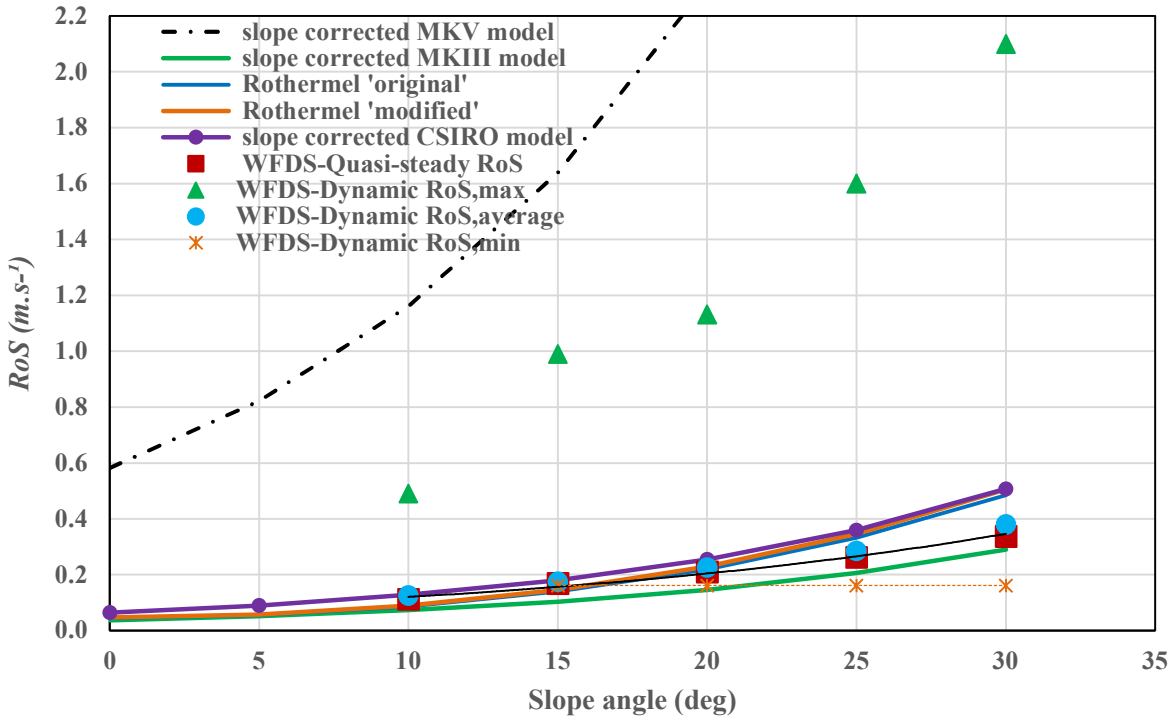

5.11 (a) *RoS* vs slope angle, 0.1 m.s^{-1} (Set 1)

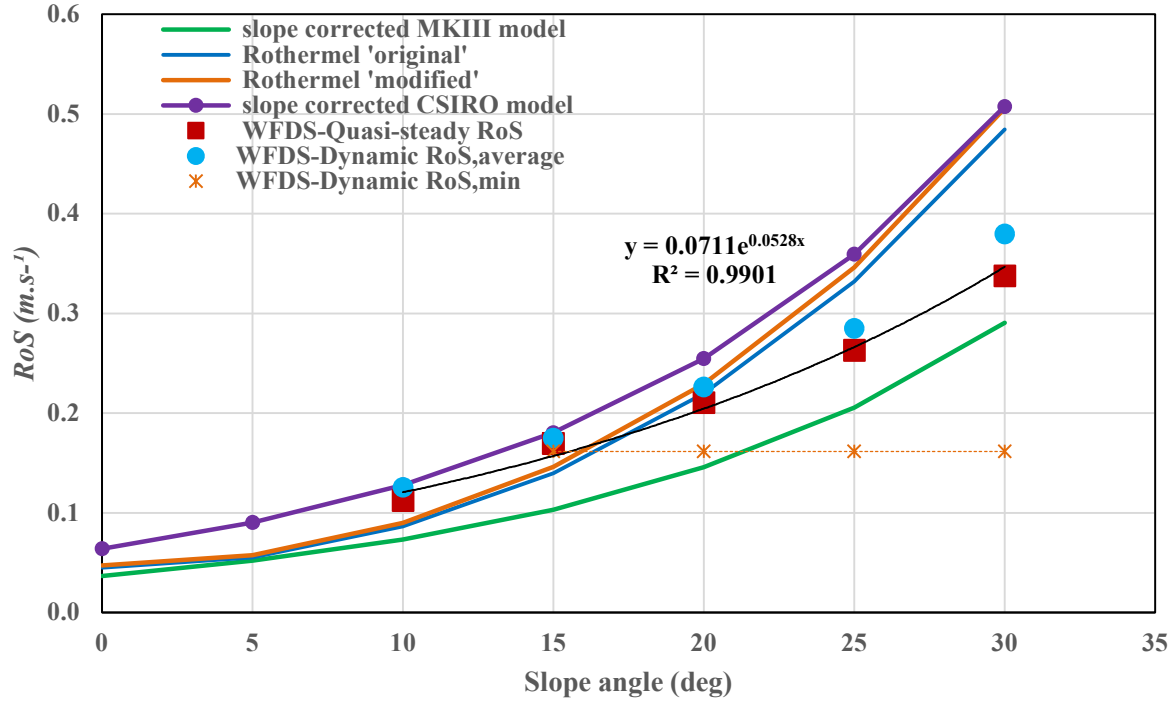

5.11 (b): *RoS* vs slope angle, 0.1 m.s^{-1} (Set 1), enlarged view without MKV and WFDS 'dynamic max' values values

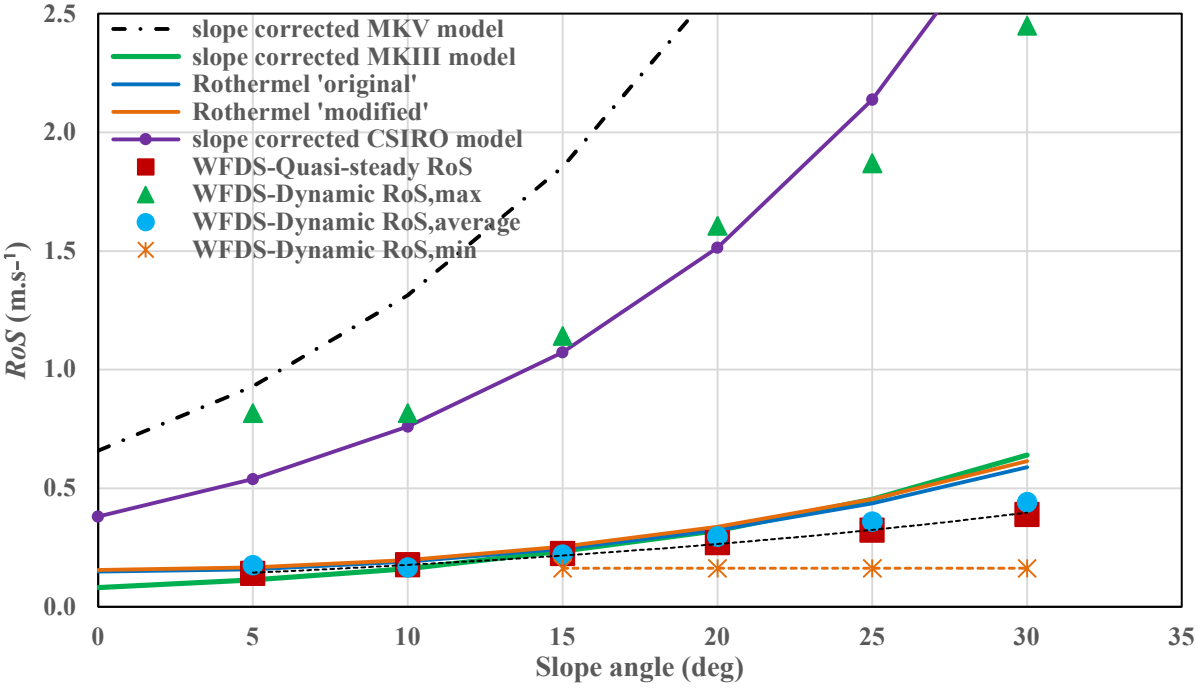

5.11 (c) *: RoS* vs slope angle, 1 m.s^{-1} (Set 3)

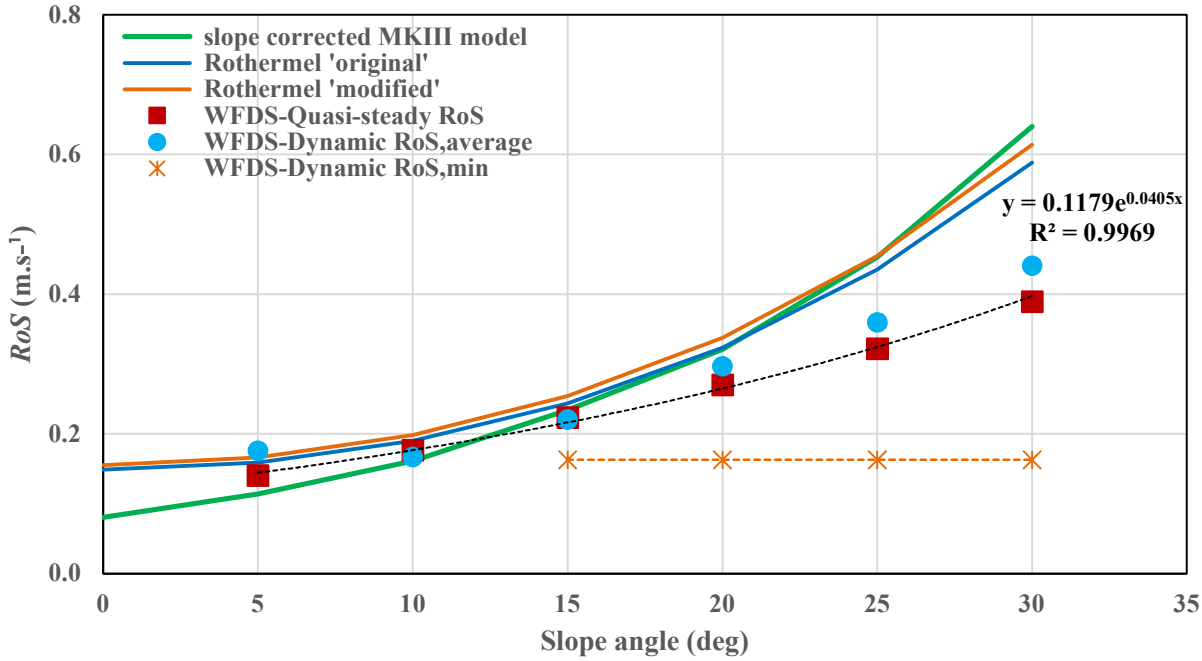

5.11 (d) : *RoS* vs slope angle, 1 m.s^{-1} (Set 3), enlarged view without MKV, 'dynamic max' and 'slope-corrected' CSIRO values

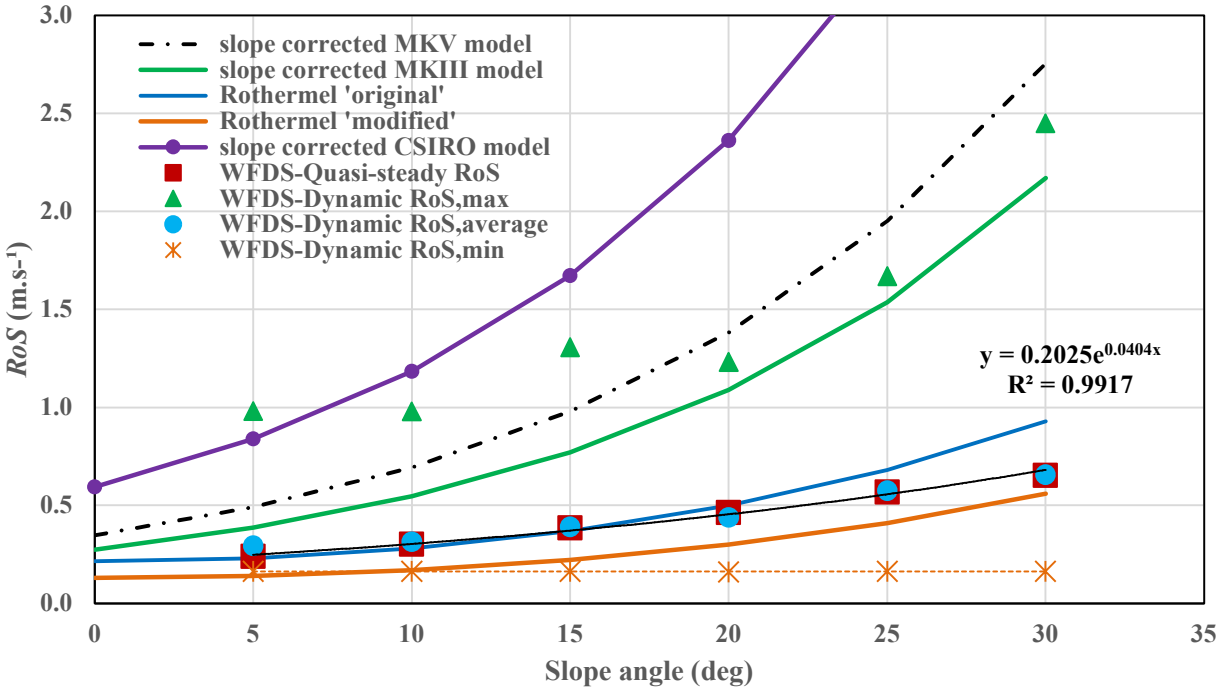

5.11 (e): RoS vs slope angle, 1 m.s^{-1} (Set 4)

Figure 5.11 – *RoS* correlations, *RoS* vs slope angle : (a) and (b) at 0.1 m.s^{-1} (Set 1); (c) and (d) at 1 m.s^{-1} (Set 3), original fuel ; and (e) at 1 m.s^{-1} (Set 4), changed fuel parameters,

Figure 5.11(a) and (b) shows that the quasi-steady and dynamic averaged *RoS* values obtained from this study are close (with some differences) to slope-corrected MKIII and CSIRO model values as well as both Rothermel (Original and Modified) values. The difference ranges from ± 0.04 $m.s^{-1}$ (at +10°) to ± 0.17 $m.s^{-1}$ (at +30°). Slope-corrected MKV values are even higher than dynamic maximum values. It should be noted with no slope, the MKV value is significantly higher than other empirical values, which leads to much higher values when the slope correction is applied. Dynamic minimum values are roughly constant for all slope cases and close to empirical values (except for MKV) other than for higher upslopes of +25° and +30° where dynamic minimum values are lower. Note that for +10° slope at 0.1 $m.s^{-1}$ (Set 1) and +5° and +10° slopes at 1 $m.s^{-1}$ (Set 3), there were many instants in time with zero dynamic values and therefore dynamic minimum *RoS* value are not presented for these cases. Note that dynamic *RoS* values are instantaneous values obtained by differentiating the fire front location data along the centreline of the burnable grass plot at each simulation output time, whereas the quasi-steady value is obtained from a linear fit to the fire front location. The two methodologies used to determine *RoS* may not be consistent in some scenerios, especially for lower slope angles at such a low wind velocity (nearly zero), where the fire front moves very slowly.

Figure 5.11(c) and (d) for 1 $m.s^{-1}$ shows that the quasi-steady and dynamic averaged *RoS* values obtained from this study are very close to slope-corrected MKIII values, Rothermel Original and Modified values, for slope angles up to +25° and slightly lower for +30°. However, the CSIRO model values were found to be higher for all the slope angles and quite close to dynamic maximum values (slightly higher (by 20%) than dynamic maximum at +30°, lower at +5° (by 34%) and +10° (by 7%) than dynamic maximum). As observed in Figure 5.11(a) for 0.1 $m.s^{-1}$ cases, slope-corrected MKV values are even higher than dynamic maximum values. Again, dynamic minimum values are roughly constant for all slope cases and lower than empirical values for all slopes.

Figure 5.11(e) for 1 $m.s^{-1}$ with changed fuel parameters shows that the quasi-steady and dynamic averaged *RoS* values obtained from this study are closer to the Rothermel Original values for all slope angles up to +25° (slightly lower for +30°) and slightly higher than Rothermel Modified values for all slope angles. However, the CSIRO model values were found to be even higher than 'dynamic maximum' values (except for +5°). Both slope-corrected MKIII and MKV values are closer to dynamic maximum values. Again, dynamic minimum values are roughly constant for all

slope cases, close to Rothermel Modified for values up to +10° and lower than empirical values for other slope cases.

Both Original and Modified Rothermel model values were found to be closer to the quasi-steady and dynamic average *RoS* values for both lower driving wind velocities (Figure 5.11). As noted in Section 4.4.2.4, this reinforces that Rothermel models under the influence of strong wind show minimal slope effect and as the wind velocity decreases, a greater effect is observed.

For the original fuel parameters, overall, the quasi-steady and dynamic averaged *RoS* values obtained from this study were found to be closer to slope-corrected MKIII, and Rothermel Original and Modified model values for both the lower wind velocities (Sets 1 and 3), and again, for 0.1 $m.s^{-1}$ cases, these were found to be closer to CSIRO model values as well.

The dynamic averaged *RoS* values are found to be closer to quasi-steady *RoS* values, for both the wind velocities, as for the findings with higher wind velocity cases (Section 4.4.2.3). Other than for the MKV and CSIRO model values for higher upslopes at 1 $m.s^{-1}$, all empirical values roughly lie between dynamic minimum and dynamic maximum *RoS* values for Set 1 and 3. An exponential relationship can be developed between dynamic maximum and dynamic average *RoS* values and slope angles for both the lower wind velocities; however, for dynamic minimum, the values are roughly constant for all slope cases.

Following the method detailed in section 4.4.2.3, error bars are fitted on the WFDS quasi-steady *RoS* data, as shown in Figures 5.12 (a), (b) and (c), as a method to demonstrate confidence bounds around the WFDS *RoS* estimate.

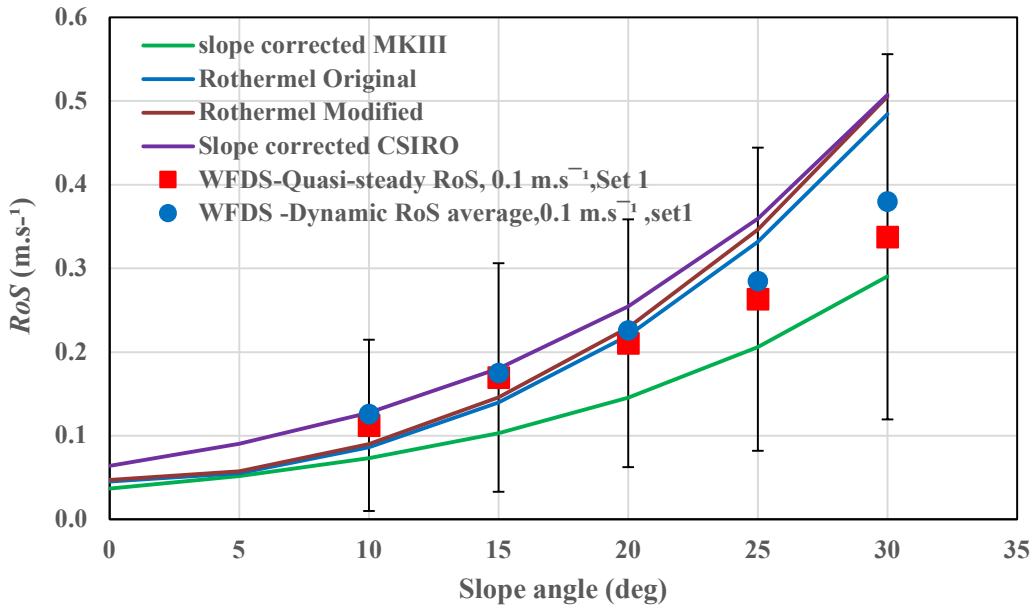

(a) *RoS* – slope angle, with 95% confidence bounds, 0.1 m.s^{-1} (Set 1)

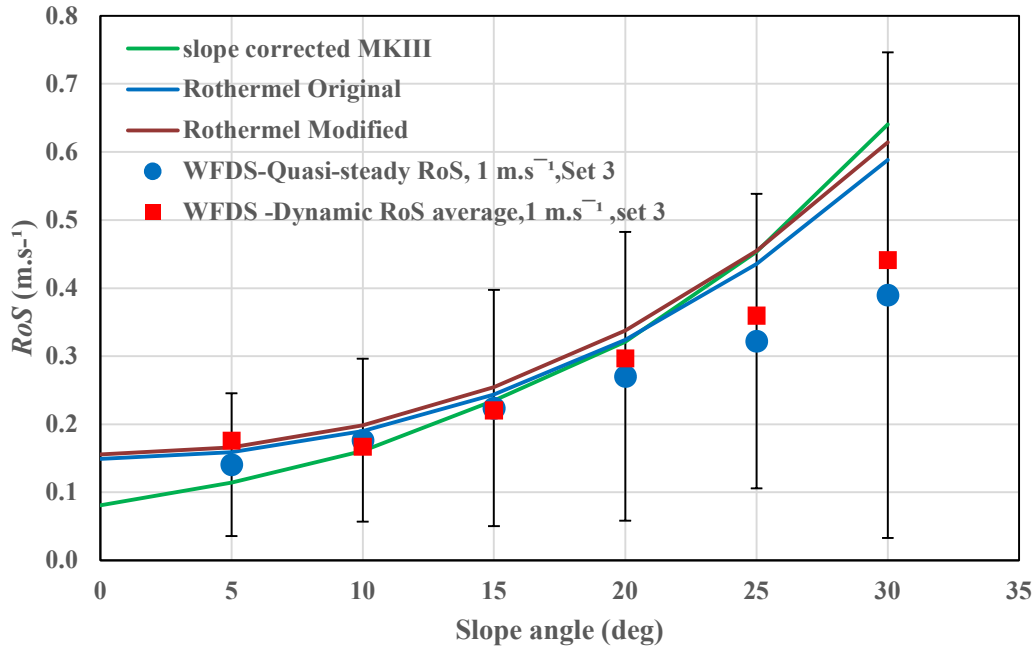

(b) *RoS* – slope angle, with 95% confidence bounds, 1 m.s^{-1} (Set 3)

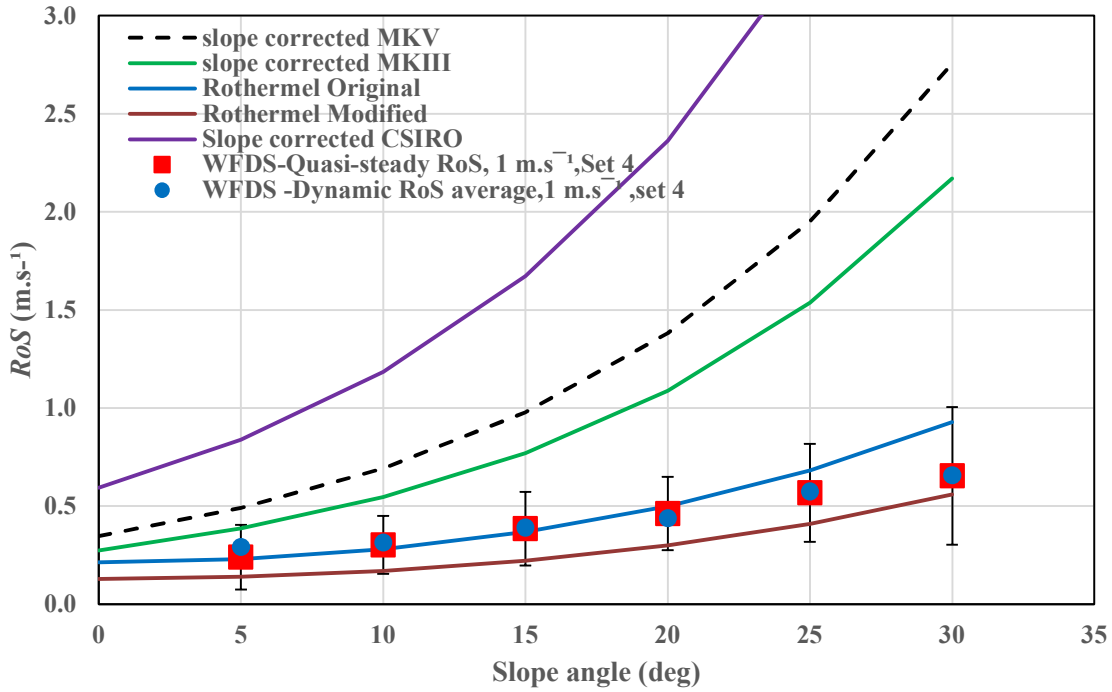

(c) *RoS* – slope angle, with 95% confidence bounds, 1 m.s^{-1}, (Set 4)

Figure 5.12 - *RoS* – slope angle: WFDS quasi-steady *RoS* values fitted with margin of error (95% confidence bounds) : (a) at 0.1 m.s^{-1} (Set 1) ; (b) at 1 m.s^{-1}, original fuel parameters (Set 3) ; (c) at 1 m.s^{-1}, changed fuel parameters (Set 4).

Following Figures 5.11 (b) and (d), the significantly higher MKV values are not shown in Figure 5.12 (a) and both the MKV and CSIRO values are not shown in Figure 5.12 (b). Like higher wind velocity cases (eqn. (4.3 –(4.4)), the length of the error bar or margin of error is determined for 95% confidence interval. Figures 5.12 (a) and (b) for the 0.1 m.s^{-1} and 1 m.s^{-1} cases with original fuel parameters, shows that the error bar encapsulate all the presented emprical model values for all slope angles: CSIRO, MKIII and both the Rothermel model values for 0.1 m.s^{-1} and MKIII and both the Rothermel model values for 1 m.s^{-1}. Figure 5.12(c) for 1 m.s^{-1} cases, with changed fuel parameters, shows that both the Rothermel model values are encapsulated by the error bar for all slope angles. MKV and CSIRO model values are outside the error bar range for all slope cases and MKIII model values are captured only for +5°.

MKV values are found to be outside the error bar range for all the cases. Generally, for original fuel parameters, the error bar fitted on the WFDS quasi-steady *RoS* data encapsulated most of the

presented slope-correct empirical model values. For changed fuel parameters, only the Rothermel model values are found to be within the error bar range.

For both the lower wind velocities, the relationship between quasi-steady *RoS* and slope angles is closer to an exponential relationship (R^2 values are shown in the plots). This is in agreement with the exponential relationship noted for 3 m.s^{-1} cases in Section 4.4.2.3. This implies that the *RoS*-slope angle relationship transition to an exponential fit at lower wind velocites.It is likely that as the driving wind velocity decreases, the relationship becomes exponential, in line with the exponential relationship reported with most of the experimental studies conducted with no or very low wind speeds (Noble *et al.* 1980, Beck 1995, Pimont *et al.* 2012). The exponential relationship between *RoS* and slope angle for lower driving wind velocities of 1 and 0.1 m.s^{-1} are summarised in Table 5.5. In Figure 5.11, trend lines only for the WFDS quasi-steady *RoS* relationship are shown.

Table 5.5: *RoS* vs slope angle relationship

RoS	**Pattern**	**0.1 m.s^{-1}, Set 1**		**1 m.s^{-1}, Set 3, original fuel**		**1 m.s^{-1}, Set 4, changed fuel**	
		Equation	R^2	Equation	R^2	Equation	R^2
Dynamic *RoS,* Maximum	Exponential	$0.2911e^{0.0678x}$	0.969	$0.58e^{0.0475x}$	0.984	$0.7371e^{0.035x}$	0.879
Dynamic *RoS,* average	Exponential	$0.0752e^{0.054x}$	0.998	$0.1263e^{0.0411x}$	0.978	$0.235e^{0.034x}$	0.984
Quasi-steady *RoS*	Exponential	$0.0711e^{0.0528x}$	0.990	$0.1179e^{0.0405x}$	0.997	$0.2025e^{0.0404x}$	0.992

Australian practitioners currently use a 'rule-of-thumb' stating that the *RoS* of fire doubles for every 10° upslope increase or halves with every 10° increase of negative slope (Sharples (2017), Sullivan *et al.* (2014)). Table 5.6 shows the *RoS* (WFDS quasi-steady) % changes at every +10° slope (calculated from Figure 5.11) for the simulations conducted in this study at lower wind velocities.

Table 5.6: *RoS* percentage change at every +10° slope

Slope angle	Driving wind velocity		
	0.1 m.s^{-1}	**1 m.s^{-1}**	
	Set 1	Set 3	Set 4
+5° to +15°	87%	60%	60%
+10° to +20°	87%	55%	53%
+15° to +25°	55%	45%	50%
+20° to +30°	59%	45%	44%

Within the simulations conducted in this study, for the driving wind velocity of 0.1 m.s^{-1}, the quasi-steady *RoS* values increase by 55% to 87% for every 10° increase upslope. For 1 m.s^{-1} (both Sets 3 and 4), the range is ~45–60%. Generally, it is observed that the difference in *RoS* values for every 10° increase upslope narrows as the slope angle increases. The fire isochrones did not progress for downslopes at the lower wind velocities, and therefore it is not possible to comment on the negative slope scenario at very low wind speeds

5.3.3.4 Relative *RoS*

In Figure 5.13, relative *RoS* (*RoS* on any slope divided by *RoS* at +10°) of WFDS quasi-steady values (from Figure 5.11) are compared with the Australian slope–function (rule of thumb) and Rothermel model variations for both lower driving wind velocities. For lower slope angles 0° and +5°, the fire front did not progress for all sets, and steady state conditions were not achieved and, therefore, the relative *RoS* are derived by dividing the *RoS* on any slope by the *RoS* at +10° slope (instead of 0° slope).

As for the higher wind velocity cases (Figure 4.15, Section 4.4.2.4), the relative *RoS* were unchanged for the Australian model slope function – Australian models MKIII, MKV and CSIRO models produce the same relative *RoS* values for all sets, owing to their multiplicative nature –. The Original and Modified Rothermel models give the same values for each of the wind velocities. WFDS quasi-steady *RoS* results gives separate values for each of the wind velocities.

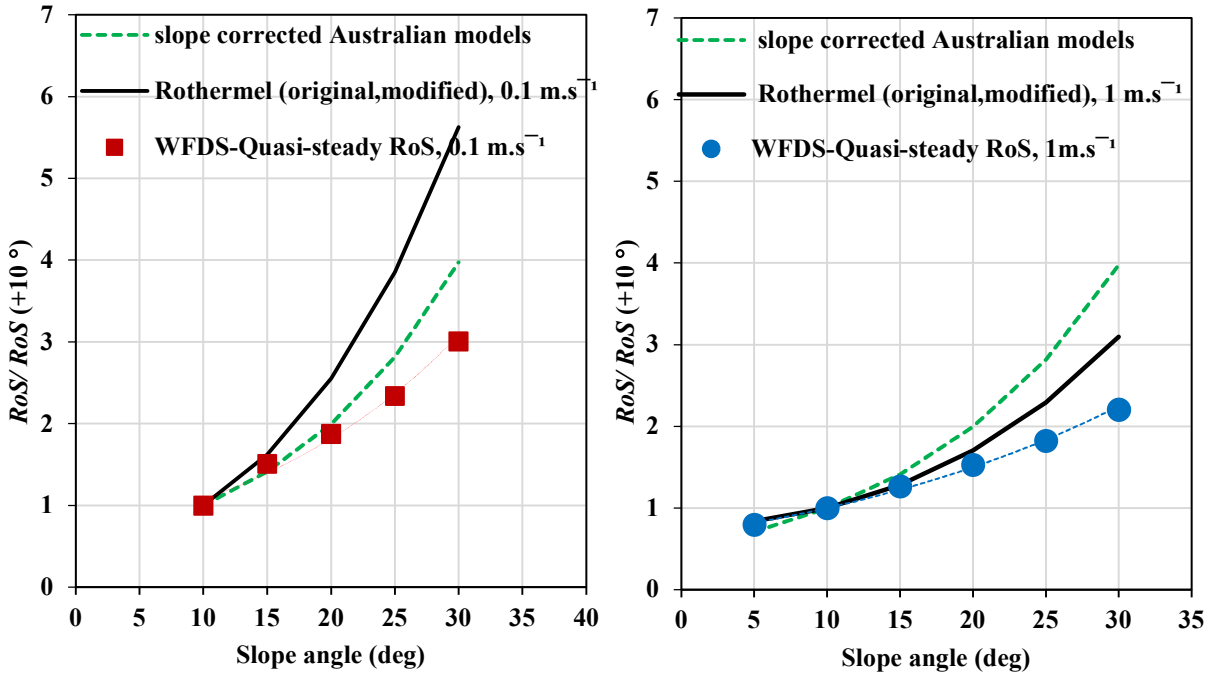

(a) 0.1 m.s^{-1} (Set 1) **(b)** 1 m.s^{-1} (Set 3)

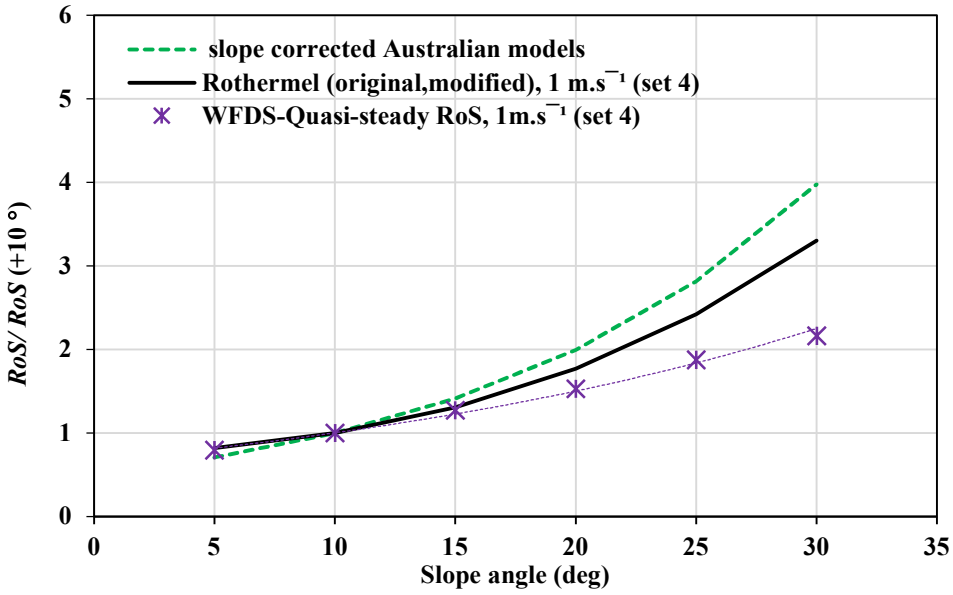

(c) 1 m.s^{-1} (Set 4)

Figure 5.13 – Comparison of slope effect at lower wind velocities: *RoS/RoS* (+10°) between WFDS quasi-steady results and empirical model values, (a) at 0.1 m.s^{-1} (Set 1); (b) at 1 m.s^{-1} (Set 3, larger domain, original fuel); (c) at 1 m.s^{-1}, (Set 4, larger domain, changed fuel characteristics).

For the Rothermel model, a stronger slope effect is observed at 0.1 m.s^{-1} compared with 1 m.s^{-1}. The strong slope effect for both lower wind velocities is in contrast with the results obtained for higher wind velocity cases (Figure 4.15 Section 4.4.2.4), where the Rothermel model was found to have a minimal slope effect. The Australian models slope function under low or near-zero wind velocities (Figure 5.13(a)) was found to be closer to the WFDS quasi-steady results. For higher wind velocities, this was not the case. For the 1 m.s^{-1} wind velocity (Figure 5.13(b) and (c)), the Rothermel model slope is closer to WFDS quasi-steady results than the Australian models's. The relative *RoS* follow the same trend for both the original and changed fuel characteristics (Sets 3 and 4).

Mendes-Lopes *et al.* (2003) in their experimental studies (Section 2.2.1) observed that the strongest influence on *RoS* is by far wind velocity, followed by fuel moisture content, then slope. The Rothermel model results reflect the fact that wind has a stronger influence on *RoS* compared with slope. In general, the WFDS relative *RoS* results from the simulations conducted in this study, with lower driving wind velocities of 0.1 and 1 m.s^{-1}, are found to be nearer to the relative *RoS* functionspredicted by the empirical slope corrections of Australian and Rothermel models

The relationship between WFDS relative *RoS* and slope angle can be construed as second-order polynomial as well as exponential, as shown in Table 5.7, and $R^2 > 0.99$ is observed for all functions at both wind velocities. The trend lines for the exponential relationship (as the Australian slope correction is exponential) between relative *RoS* and slope angle are shown in Figure 5.13.

Table 5.7: WFDS Relative *RoS* vs slope angle relationship

Pattern	**0.1 m.s^{-1}, Set 1**		**1 m.s^{-1}, Set 3**		**1 m.s^{-1}, Set 4**	
	Equation	R^2	Equation	R^2	Equation	R^2
Exponential	$0.6326e^{0.0528x}$	0.990	$0.6675e^{0.0405x}$	0.997	$0.6693e^{0.0404x}$	0.992
Polynomial	$0.0012x^2 + 0.0496x + 0.4224$	0.995	$0.0007x^2 + 0.0309x + 0.6253$	0.999	$0.0005x^2 + 0.0383x + 0.582$	0.998

5.3.3.5 Quasi-steady *RoS* comparison among varied domain and fuel parameters

In Figure 5.14, the quasi-steady *RoS* values of sets 2, 3 and 4 simulations are presented to compare the *RoS* among varied domain sizes and varied fuel characteristics. These three sets of simulations are conducted at the same driving wind velocity of 1 $m.s^{-1}$.

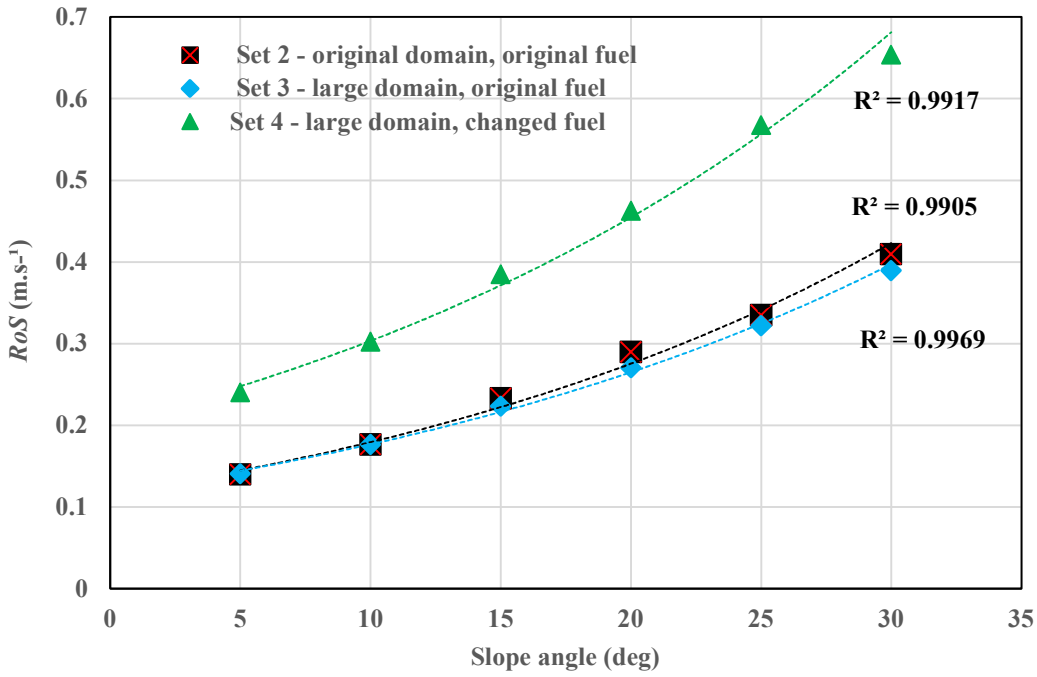

Figure 5.14 – Quasi-steady *RoS* vs slope: varied domain sizes and changed fuel parameters (Sets 2, 3 and 4)

Comparing the quasi-steady *RoS* values among different domain sizes (Sets 2 and 3), as expected, the *RoS* values are found to be nearly the same for all slope angles (a minimal difference is observed with the higher slope angle +30°). This is consistent with the fire front location plotted in Figure 5.10(a), where the fire front is found to be moving at the same pace for both the original and large domains. The quasi-steady *RoS* values of Sets 3 and 4 show that the *RoS* values for changed fuel parameters are higher by approximately 57–60% than with the original fuel parameters. Like pyrolysis width and fire intensity, increased temperature along with reduced fuel moisture content, relative humidity and fuel load impacted the fire front movement and *RoS*. For all three sets of simulations, an exponential relationship is observed between the quasi-steady *RoS* and slope angle (R^2 values shown in the plot), like the relationship obtained for lower wind velocities shown in Figure 5.11.

5.3.3.6 Fire Intensity *Q* as function of *RoS*

In Figure 5.15, *Q* (the quasi-steady intensity from Section 5.3.2) is plotted against *RoS* (quasi-steady *RoS* obtained from Figure 5.11(a, c)) for the lower wind velocities of 0.1 and 1 m.s^{-1} (Set 1 and 3 simulations). As stated in Section 5.3.2, the fire front did not progress for 0º, +5° and +10° at 0.1 m.s^{-1} and 0º, +5° at 1 m.s^{-1} and hence these slope angles were not included in the intensity calculations. Therefore, the *Q* vs *RoS* plot includes only slope angles from +15° to +30° for 0.1 m.s^{-1} and from +10° to +30° for 1 m.s^{-1}.

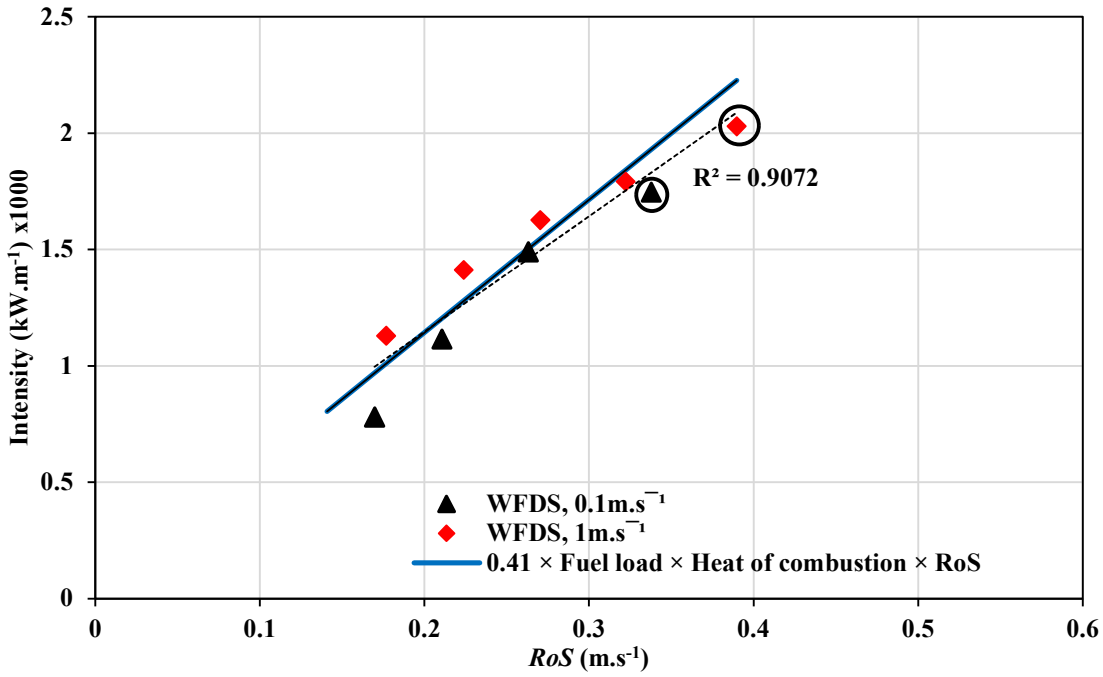

Figure 5.15 – Quasi-steady fire intensity (*Q*) as a function of *RoS*

The *Q*- *RoS* relationship fits a linear regression up to a certain upslope angle (*RoS* ~0.322 m.s^{-1}) with R^2 value as shown in Figure 5.15. Here the intention is to see whether with a particular % fuel load consumption can satisfy Byram's intensity model (which is linear). Figure 5.15 shows that the *Q*-*RoS* relationship deviates from linearity for +30° slope at 0.1 and 1 m.s^{-1} (shown with black circles, these data set falls outside the linear regression fit). Following the details mentioned in section 4.4.3, considering all values from all velocities on the linear line, it appears that Byram's intensity (Byram 1959) (*Q* = fuel load × heat of combustion × *RoS*) is satisfied with ~41% fuel

load, instead of 100%. In Figure 4.19 for higher wind velocities, Byram's intensity was satisfied with ~42% fuel load for higher wind velocity cases.

5.3.4 Plume and flame dynamics at lower wind velocities

In this section, the effect of slope on the plume and flame behaviour at the lower driving wind velocities of 0.1 and 1 m.s^{-1} (sets 1 and 3) is presented. The fire isochrones presented in Section 5.3.1 demonstrated that these lower wind velocities may not be sufficient to drive the fire front at 0° slope and further downslope angles as the fire extinguished instantly. Therefore, noslope and downslopes cases are not included in the plume and flame dynamics discussions.

The analysis technique used with higher wind velocity cases (Section 4.4.4) is followed to extract plume and flame contour plots, using the numeric computing software Matlab (https://mathworks.com). The temperature contours (representing plumes) are plotted in Figure 5.15 for each of the slope cases at the same time (40 s after ignition) as the fire moves though the burnable grass plot in the *x*-direction for both wind velocities. The plume is shown by colour shading representing air temperature (in K, indicated in the colour bar). These plots represent indicative behaviour of plume at a particular instant intime which reflect the plume attachment or up-rising behaviour for the case presented. The temperature represents the air temperature at that instant in time and we have chosen same temperature scale for the similar wind speed cases. Plumes (instantaneous) emanating from the fire front for +10°, +20° and +30° at wind velocity 0.1 m.s^{-1} are shown in Frames (a–c) and at 1 m.s^{-1} are shown in Frames (d–f).

Figure 5.16 shows that for both the lower wind velocities, the plume rises from the ground near the ignition line for +10° slope, and for higher upslopes, the buoyant plume inclines or leans towards the ground for a longer distance. As the slope angle decreases, the plume detaches or rises from the ground closer to the ignition line. The plume is inclined more towards the ground at +30° (Figures 5.16(c) and (f)) compared with lower slope angles. For a given slope angle, the plume rises from the ground earlier at 0.1 m.s^{-1} than at 1 m.s^{-1}, though a minimal difference is observed. Generally, a clearly detached or rising plume is observed for upslopes at both these wind velocities.

Compared with the higher wind velocity cases presented in Section 4.4.4, for any given slope angle at lower wind velocities, the plume is found to rise at a much shorter distance from the igntion line .

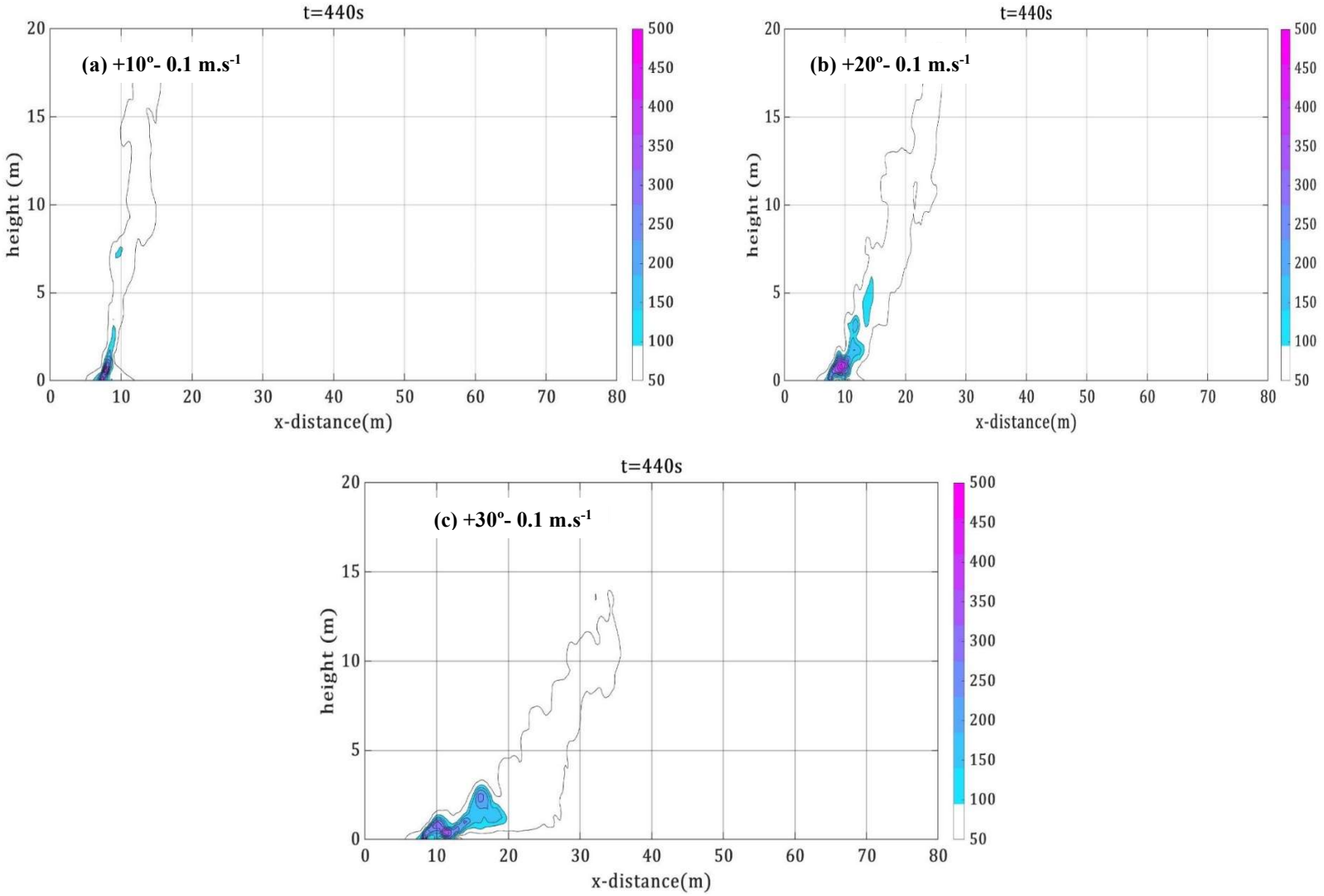

***Figure 5.16 (*a–c)** plume contour, upslopes at 0.1 m.s^{-1} (Set 1): +10°, +20°, +30°

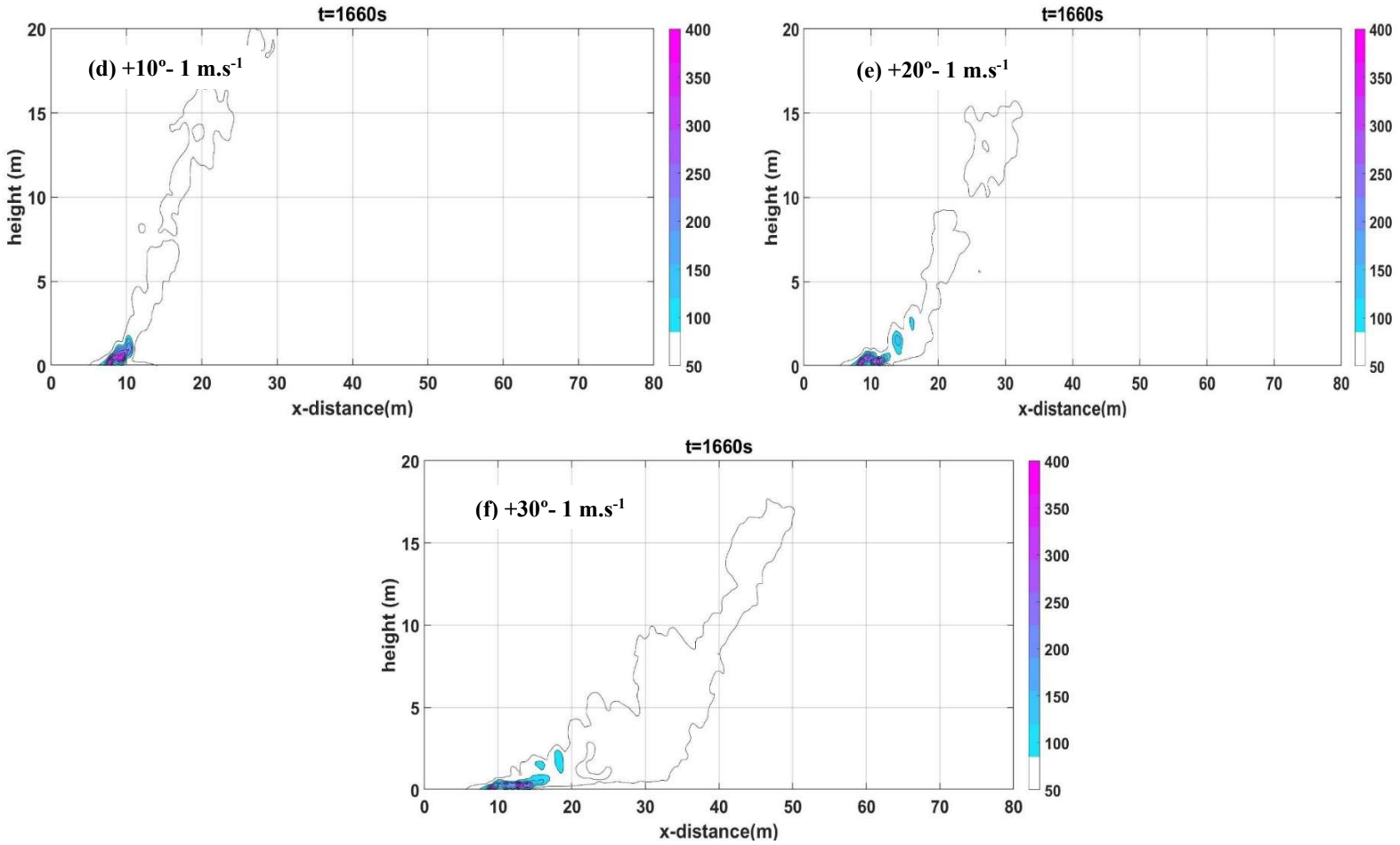

***Figure 5.16* (d–f)** plume contour, upslopes at 1 m.s^{-1} (Set 3): +10°, +20°, +30°

Figure 5.16 – Plumes emanating from grass plot at +10°, +20º and +30° upslopes, at wind velocities 1 and 0.1 m.s^{-1} (Sets 1 and 3). The contours are the temperature (in K, indiated in the colour bar) along the geometric centreline, taken at the same time from the start of ignition.

In the following sections, the flame contours, temperature contours, detachment location and wind velocity vectors are visualised to understand flame behaviour at driving wind velocities of 0.1 and 1 m.s^{-1}.

Streamwise and vertical components of wind velocity U and W, HRR and temperature data taken through the centreline of the burnable grass plot, are used to obtain the velocity quiver plots along with flame and temperature contours. As for higher wind velocity cases, the flame envelopes are determined from the minimum threshold temperature of 400 K to the maximum temperature of the flame. Figure 5.17 shows flame contours (red) with temperature contours shaded in the background (yellow) along with detachment locations (black dots) and wind vectors (white arrows) for both wind velocities, at slope angles +30°, +20° and +10°.

Figure 5.17 Frames (a–o) represent +30°, +20° and +10°at a wind velocity of 1 m.s^{-1}. For the highest slope angle, +30° (Frames (a–e)), the near-flame is vertical, and the flame-perturbed velocity vector is inclined upward. A buoyancy-dominated flame is observed as the fire progresses. The fire establishes itself and then becomes attached for a very short time, which leads to rapid intensification and a buoyancy-dominated fire. The plumes (represented by temperature contours) emanating from the grass plot are also rising (and vertical). This is consistent with the graphic representation of the plume plotted in Figure 5.16(d–f). Slope angles +20° and +10° follow a similar pattern, a rising flame and plume. As the slope angle increases, the flame becomes wider. With lower slope angles, the flame points more direclty upwards (is more veritical) and is taller compared with the higher slope angles, as evident in Frames (k–o). The flame is more vertical at +10° compared with that for higher upslopes. For +30°, the flame appears to be attached for a very short period early in the fire progression (two-sided wind entertainment can be seen into the plume, but not into the flaming zone), prior to rising upwards.

Figure 5.17 Frames (p–ad) represent +30°, +20° and +10° at wind velocity 0.1 m.s^{-1}. The plots generally reflect the same trend as for 1 m.s^{-1} cases. The flame is clearly vertical and rising. The plume emanating from the grass plot also rises vertically, consistent the graphic representation of the plume plotted in Figure 5.16(a–c). Flame detachment is more evident in the +20° and +10° cases (Frames (u–ad)). For lower slope angles, the flame is more vertical; however, the flame

becomes wider at the highest slope angle +30°, and a similar trend is observed with the 1 $m.s^{-1}$ cases.

Comparing among the wind velocities, for a given slope angle, the flame is wider for 1 $m.s^{-1}$ cases compared with 0.1 $m.s^{-1}$. The fire progresses slowly with lower slope angles (e.g. +10°). Hence, for +10°, the contour data is available only approximately up to halfway through the grass plot as the fire did not propagate further at 0.1 $m.s^{-1}$ (Frames ad). This agrees with the fire isochrones for +10° slope plotted in Figure 5.2(d).

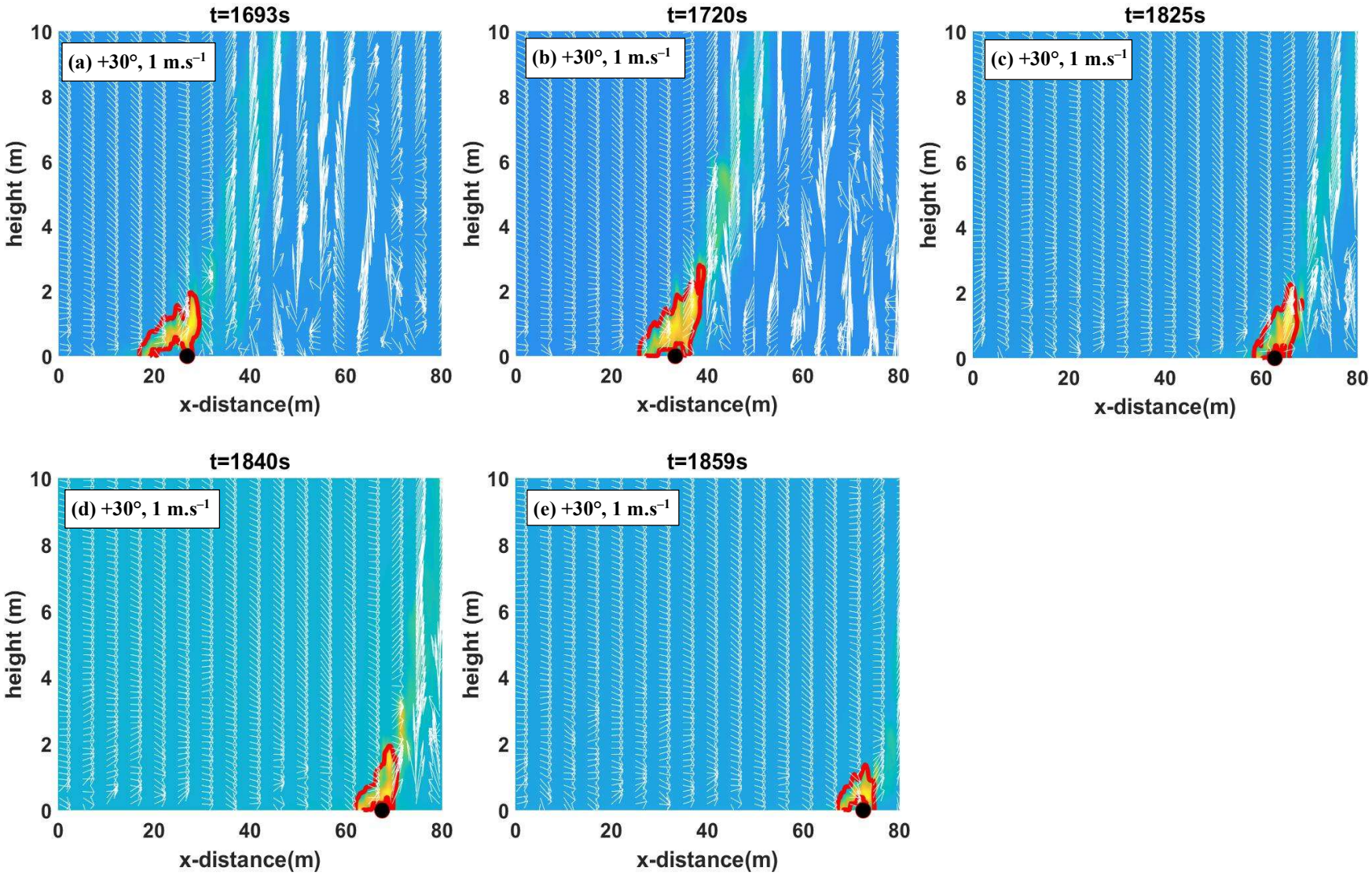

Figure 5.17 (a–e): **+30° at 1 m.s^{-1} (Set 3)**

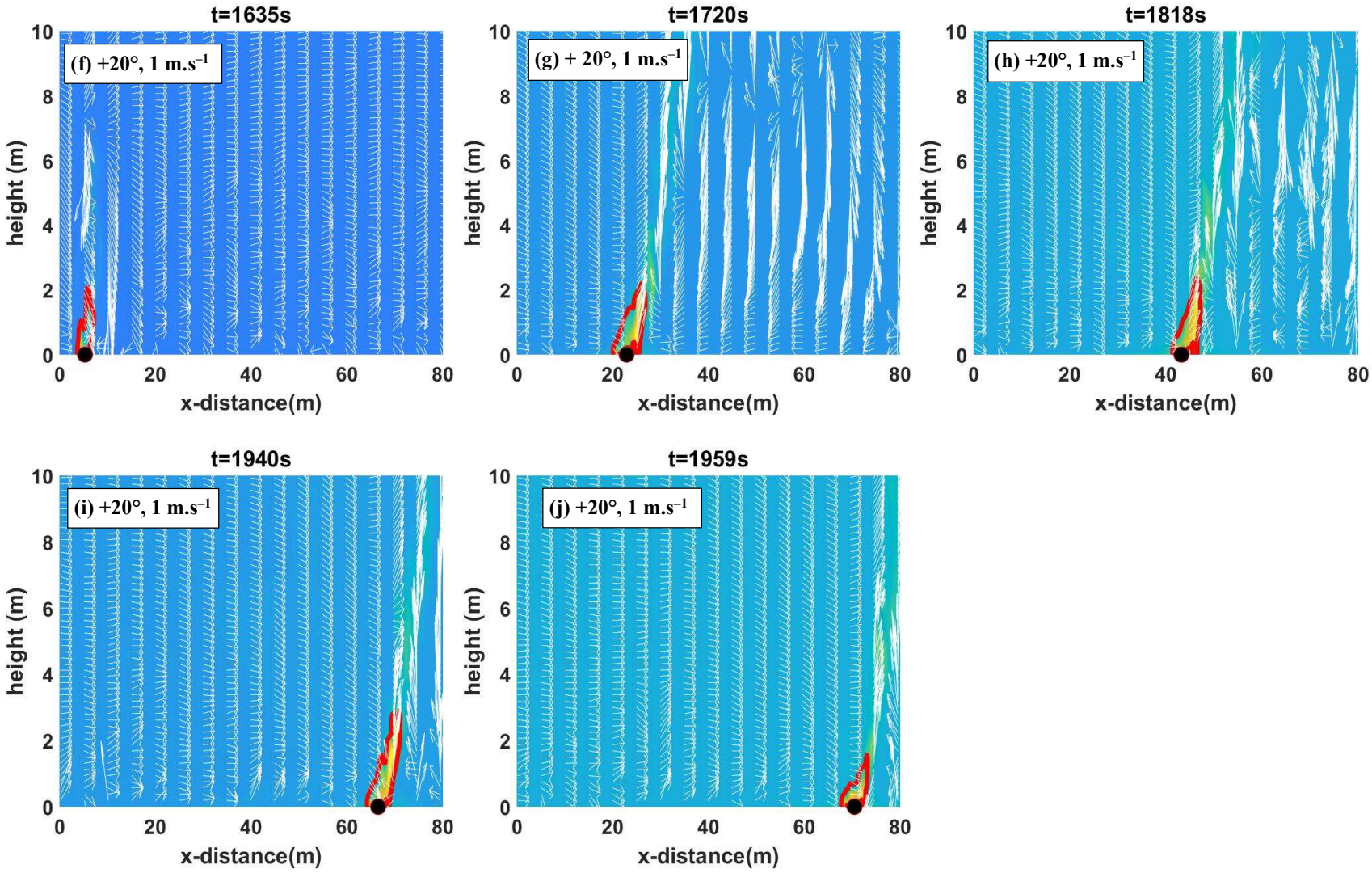

Figure 5.17 (f–j): **+20° at 1 m.s^{-1} (Set 3)**

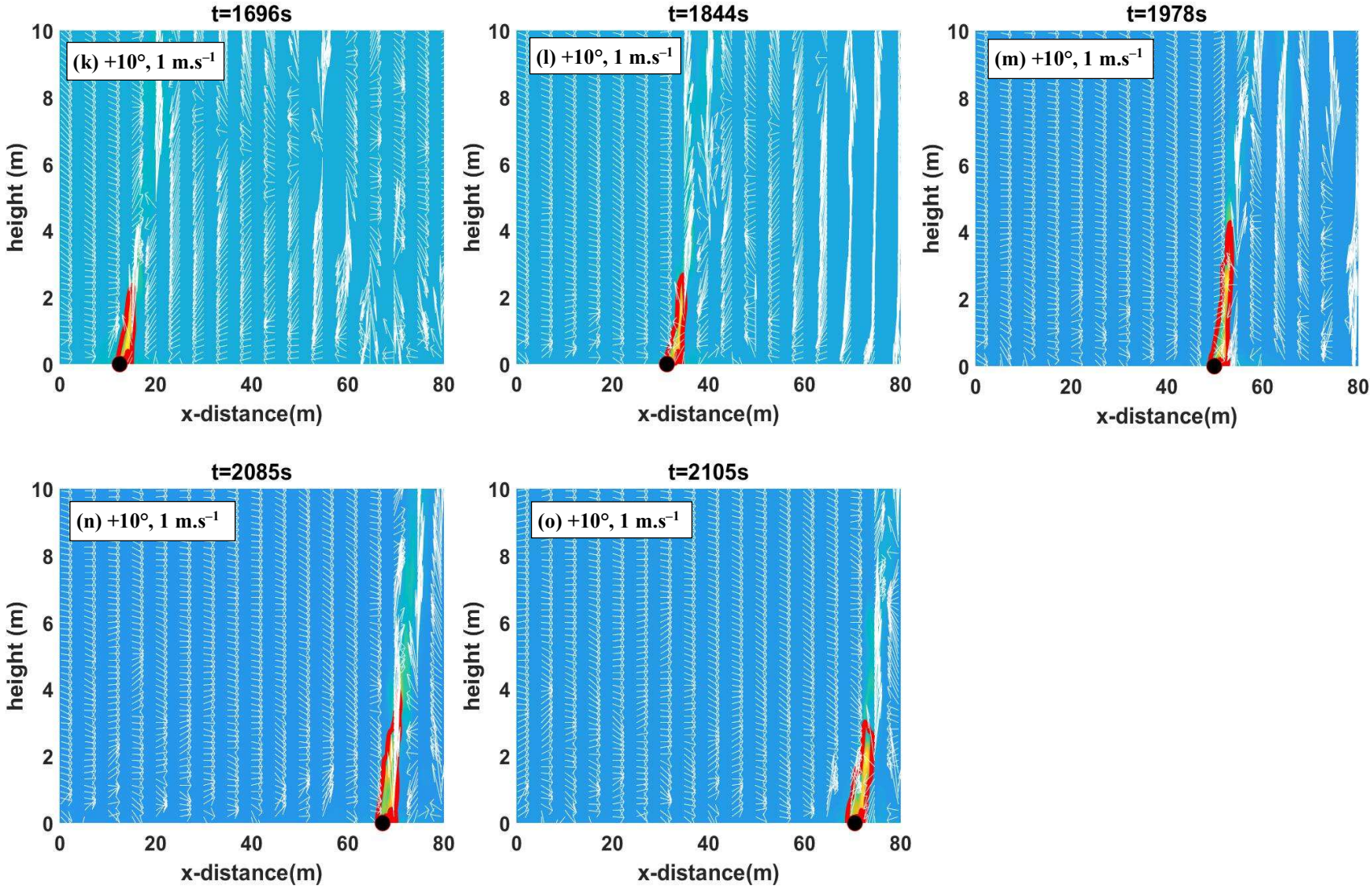

Figure 5.17 (k–0): **+10° at 1 m.s^{-1} (Set 3)**

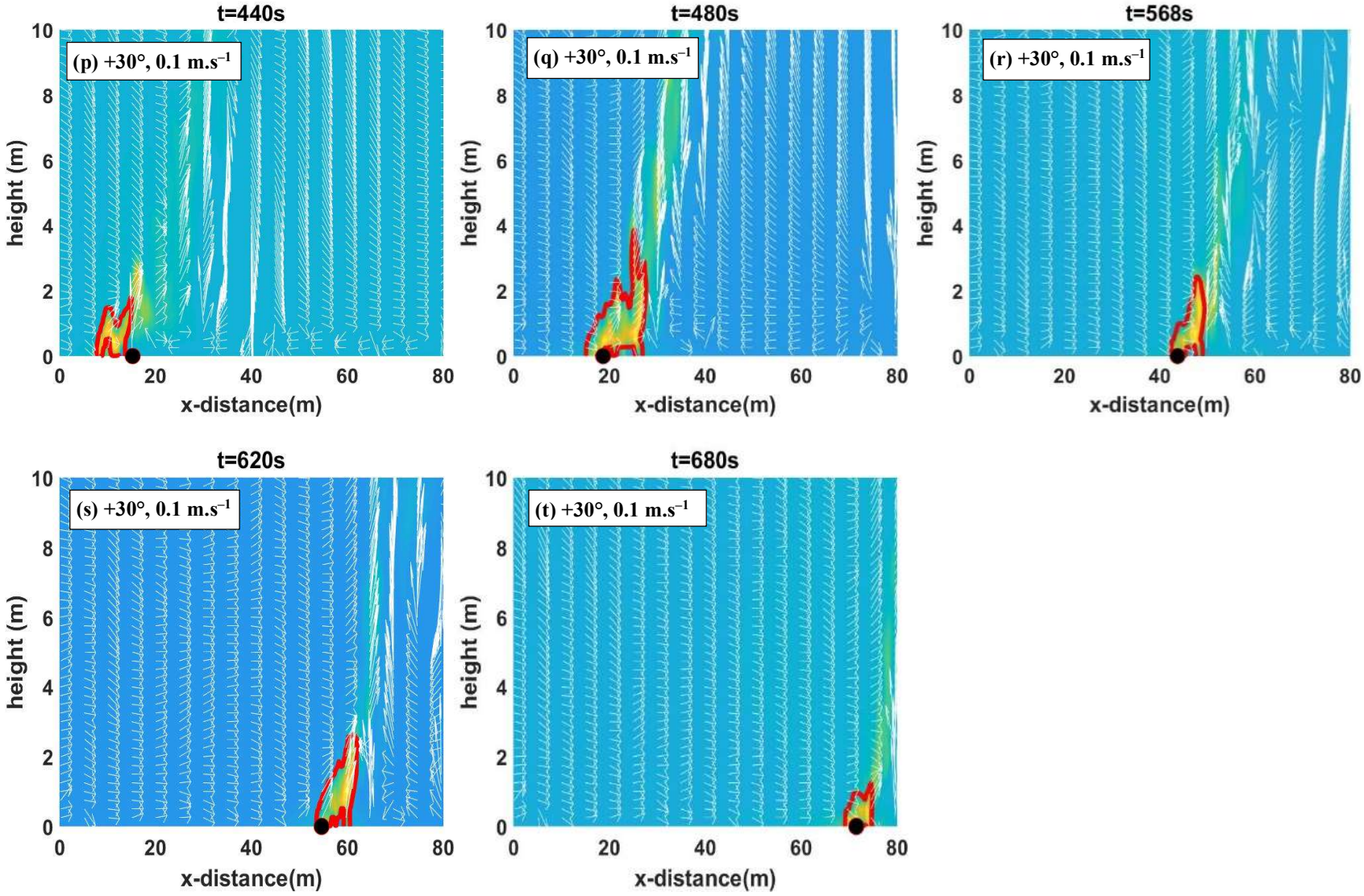

Figure 5.17 (p–t): **+30° at 0.1 m.s^{-1} (Set 1)**

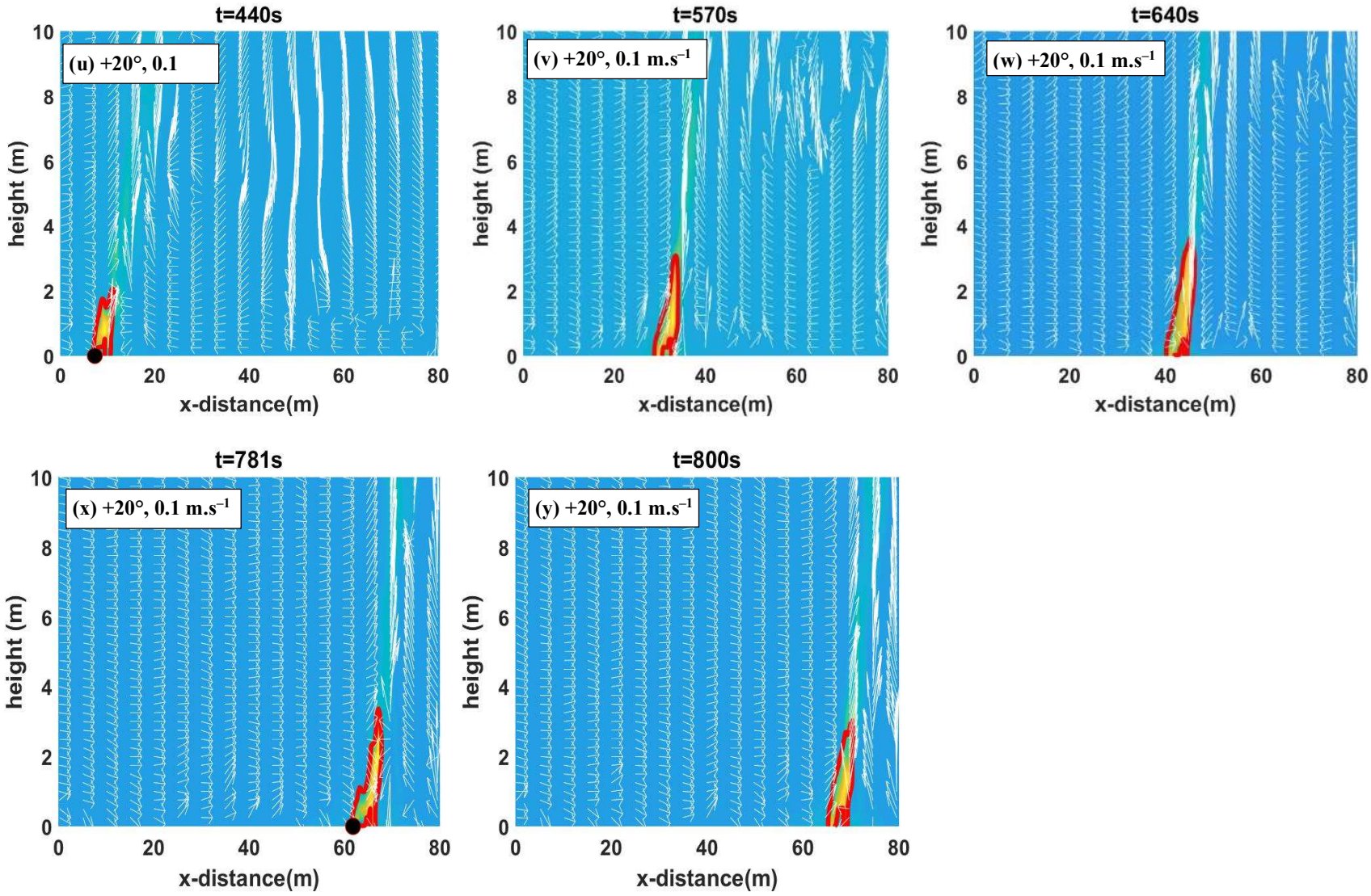

Figure 5.17 (u–y): **+20° at 0.1 m.s^{-1} (Set 1)**

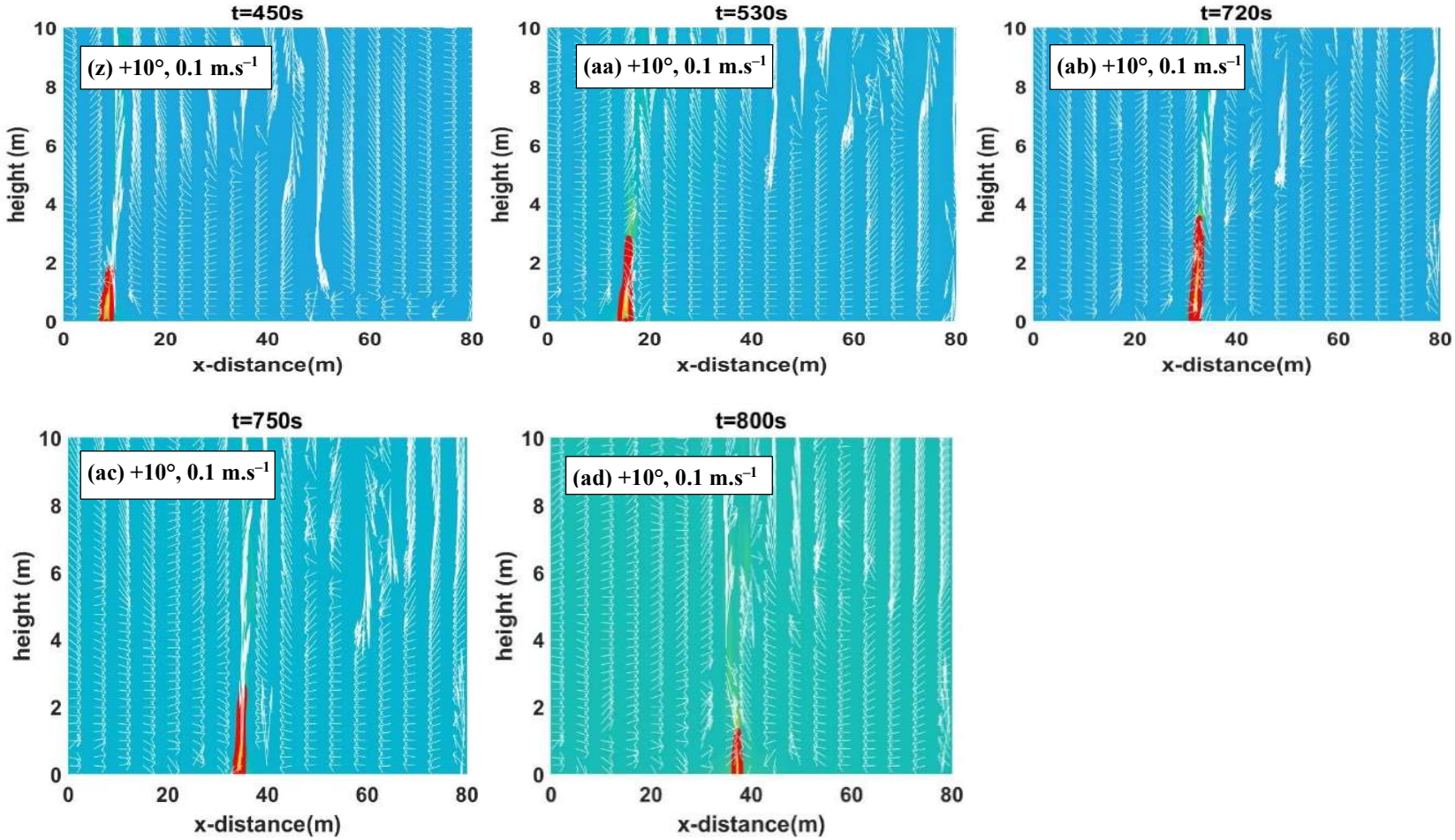

Figure 5.17 (z–ad): **+10° at 0.1 m.s^{-1} (Set 1)**

Figure 5. 17 – Flame contour (red) with temperature contour shaded (in yellow) in the background along with detachment location (black dot) and wind vector plots (white arrows), at various times for wind velocities 1 and 0.1 m.s^{-1}: Frames (a–o): +30°, +20° and +10° at 1 m.s^{-1} (Set 3); Frames (p–ad): +30°, +10° and +10° at 0.1 m.s^{-1} (Set 1).

It is evident from the flame and plume contours presented in Figures 5.17 that, for lower driving wind velocities of 1 and 0.1 m.s^{-1}, the flame dynamics as well as the plume appears to be detached or up-rising. Fire propagation is clearly within the plume or buoyancy-dominated regime. In the following section, Byram number (N_c) analysis is performed with lower driving wind velocities to quantify the fire propagation regime.

5.3.5 Mode of fire propagation

Byram number (N_c) analysis is performed to quantify the mode of fire propagation as wind-driven or buoyancy-driven. N_c is calculated from eqn (2.48) (Chapter 2, Section 2.2.2) for all slope angles, at 1 m.s^{-1} wind velocity (from simulation Set 3). Since meaningful values could not be obtained with 0.1 m.s^{-1} wind velocity cases (with *RoS* values higher than U_{10}, the denominator term $(U_{10} - RoS)^3$ in eqn (2.48) gives negative values, resulting in negative N_c values), only the results with 1 m.s^{-1} cases are presented in Figure 5.18. Following the N_c calculation for higher wind velocity cases detailed in Section 4.4.5, N_c values at U_{10} and U_2 (0.95 and 0.6 m.s^{-1} before the ignition line, respectively) are calculated to analyse the near-surface flame and wind field behaviour. In this study, the N_c values at U_{10} and U_2 are referred to as N_{c10} and N_{c2}, respectively.

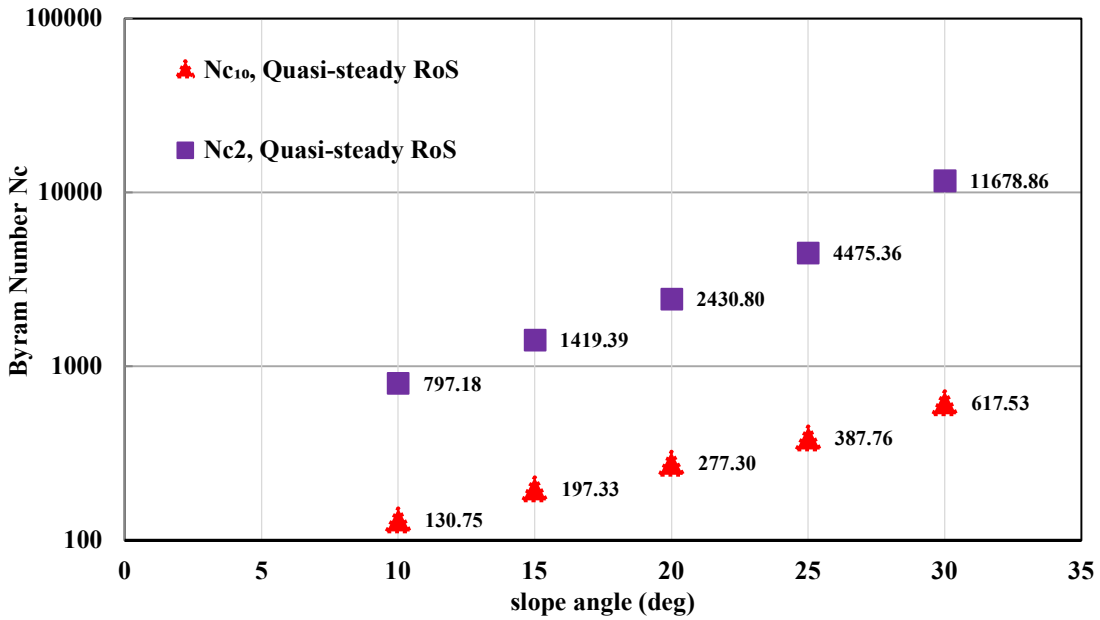

Figure 5. 18 – Byram convective number (N_c) vs slope angle, derived using quasi-steady *RoS,* based on U_{10} and U_2 at wind velocities of 1 m.s^{-1}.

For the simulations presented, the *RoS* is taken from Section 5.3.3.3; both the *RoS* values measured from the slope of the fire front location (quasi-steady *RoS*) and the average dynamic *RoS* are used to compute N_c values. While there are differences between the values computed using the two measurements of *RoS*, none are significant enough to change the classification of the mode of fire propagation. Hence, only the N_c values obtained using quasi-steady *RoS* measurements are shown in Figure 5.18. The N_c values derived from eqn (2.48) using both the quasi-steady and dynamic average *RoS* are plotted in Figure 5.18 for 1 $m.s^{-1}$ wind velocity.

From this figure, all cases can be clearly classified as plume- or buoyancy-driven, given the large N_c values. This agrees with flame and plume temperature contours presented in Figure 5.17 that the flame dynamics are buoyancy- or plume-driven.

In contrast, the higher wind velocity cases presented in Section 4.4.5 demonstrated that, for the highest wind velocity of 12.5 $m.s^{-1}$, the flame and near-flame appeared to be up-rising even though the plume was attached. For wind velocities of 12.5 and 6 $m.s^{-1}$, the flame was found to be buoyancy-dominated near the ground, tended towards wind-dominated for a very short time and then transited to a buoyancy-dominated regime as the fire progressed. However, at a wind velocity of 3 $m.s^{-1}$, the upslope cases 0° to +30° were classified as buoyancy-driven given the large N_c values.

Overall, the flame and temperature contours plotted in Section 4.4.4 for higher wind velocities demonstrated that the near-surface flame dynamics with higher wind velocities were difficult to characterise using Byram's number, whereas at lower wind velocities, fire propagation is found to be clearly buoyancy-driven as captured by the Byram number analysis shown in Figure 5.18.

5.3.6 Flame length

Following the methodology detailed in section 4.4.6 for the higher wind velocity, the flame length is computed from instantaneous centreline HRR data using Matlab software function *regionprops.* (https://mathworks.com).

Figure 5.19(a) and (b) shows flame length vs time plotted for wind velocities of 0.1 (Set 1) and 1 $m.s^{-1}$ (Set 3), respectively. Figure 5.19(c) and (d) shows the quasi-steady flame length vs slope angles plot for the four sets of simulations, along with empirically derived flame length values.

The flame length values do fluctuate and show irregular patterns due to the dynamic nature of the fire propagation. As observed for higher wind velocities, the highest flame length is at +30° slope and the flame length decreases as the slope angle decreases. For 1 $m.s^{-1}$ wind velocity, the flame length for every +10° increase in slope increases by approximately 40–70%, and for 0.1 $m.s^{-1}$, it increases by approximately 64–90%. This observation is consistent with the plume contour view in Figure 5.16; when the upslope angle increases, the plume inclines towards the ground and would be more prone to plume attachment. Like pyrolysis width (in Figure 5.3), longer quasi-steady states are observed for lower slope angles.

The flame lengths extracted from the quasi-steady region are plotted in Figure 5.19(c) and (d) for the four sets of simulations. Quasi-steady flame length vs slope angle for Sets 1 and Set 3 are shown in Figure 5.19(c) and for Sets 2, 3 and 4 are presented in Figure 5.19(d). For higher upslopes, where no clear quasi-steady state exists, the flame length is averaged over a short period at the peak of the length. Comparing among the wind velocities (Sets 1 and 3), for a given slope angle, the flame length is generally lower for lowest wind velocity, 0.1 $m.s^{-1}$, cases. This is in line with higher wind velocity cases (Section 4.4.6, Figure 4.23), which showed the flame length decreases with wind velocity.

Comparing the flame length among the two domain sizes (Sets 2 and 3) – with the same driving wind velocity and fuel characteristics – the flame lengths are nearly the same for all slopes, as observed with pyrolysis width, fire front and HRR.

The flame length with changed fuel characteristics (comparing Sets 3 and 4) – with the same driving wind velocity and domain size – shows that the fuel characteristics influence the flame length. Flame length is lower with changed fuel parameters for all the slope angles. As observed in Figure 5.7, Set 4 simulations produced lower intensity, which resulted in lower flame length. The decreased fuel load is the likely the reason for this result.

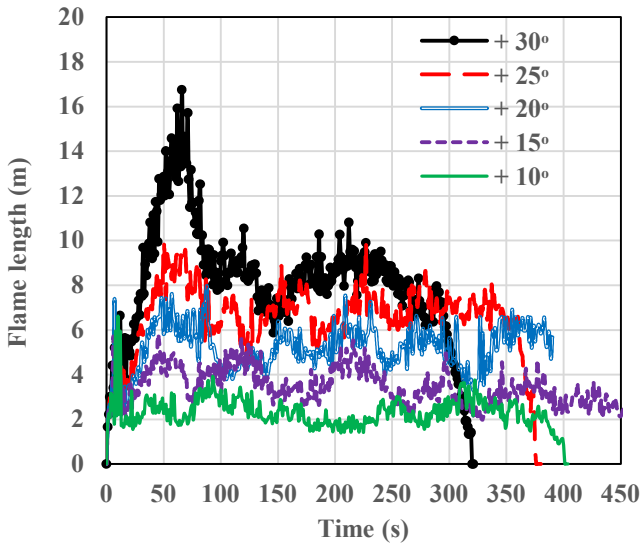

(a) Flame length vs time – Set 1, 0.1 m.s^{-1}

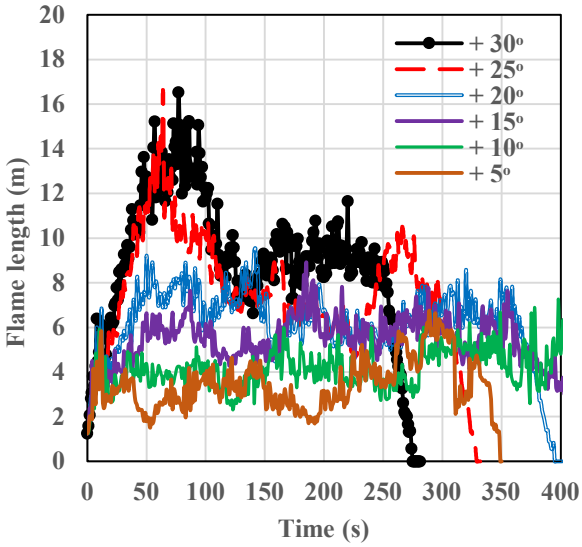

(b) Flame length vs time – Set 3, 1 m.s^{-1}

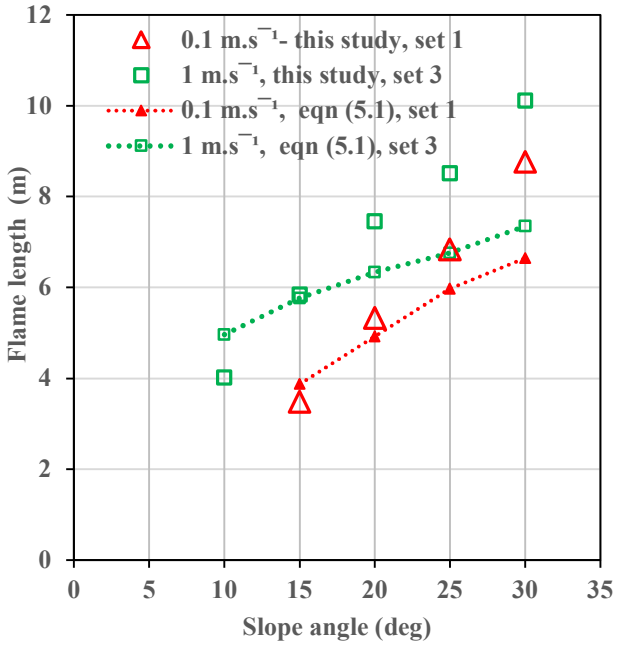

(c) Flame length vs slope – Sets 1 and 3

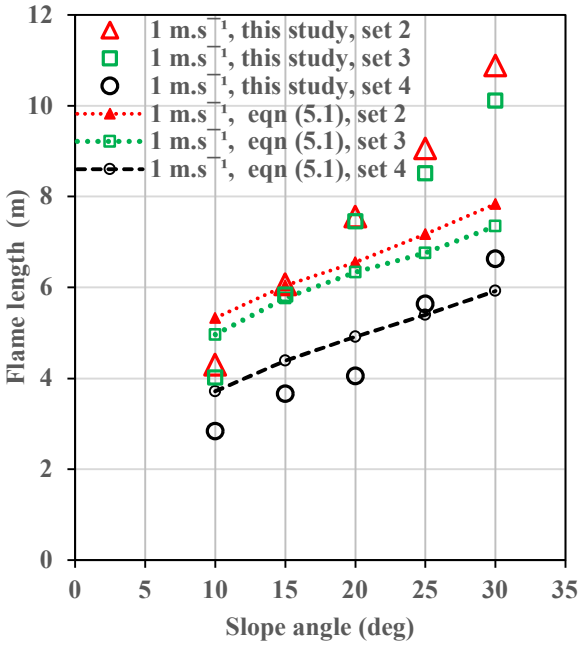

(d) Flame length vs slope – Sets 2, 3, 4 at 1 m.s^{-1}

Figure 5. 19 – Flame length vs time: (a) at 0.1 m.s^{-1} (Set 1); (b) at 1 m.s^{-1} (Set 3); (c) Quasi-steady flame length L vs slope angles with empirically derived values for at 0.1 m.s^{-1} (Set 1) and at 1 m.s^{-1} (Set 3); (d) Quasi-steady L vs slope angles with empirically derived values for Sets 2, 3 and 4 at 1 m.s^{-1}

Figures 5.20(a) and (b) show the flame length plotted against fire front location for both wind velocities.

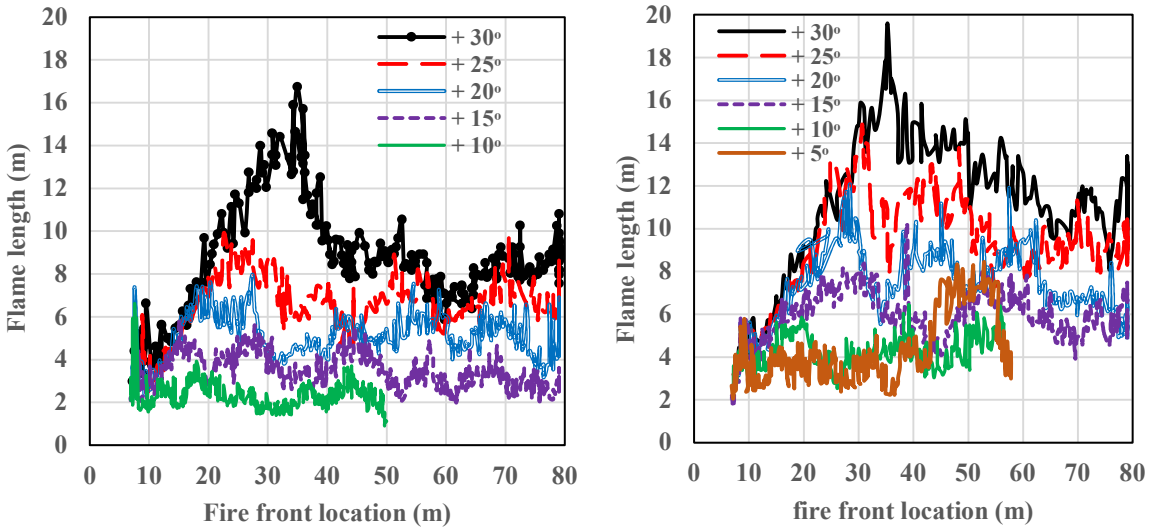

(a) 0.1 m.s^{-1}, Set 1 **(b)** 1 m.s^{-1}, Set 3

Figure 5. 20 – Flame length vs fire front location at wind velocities (a) 0.1 m.s^{-1} (Set 1); (b) 1 m.s^{-1} (Set 3)

As with pyrolysis width, longer quasi-steady states are observed for lower upslopes and flame length gradually decreases over the distance, leading to extinction.

In Section 4.4.6, we examined various empirical correlations between fire line intensity and flame length for high wind velocity cases. Similarly, we now examine empirical correlations for low wind velocity cases. Following the process described in Section 4.4.6, we have examined the list of correlations presented in Alexander and Cruz (2012, 2021) and assessed each of their listed empirical correlations. The flame lengths (L) are calculated from the Q values (quasi-steady fireline intensity) obtained from Section 5.3.2 for the four sets of simulations and found that the correlation of Anderson *et al.* (1966) for Douglas-fir slash (given as eqn (5.1)) fits best with our low wind velocity flame length data.

$$L = 0.0447Q^{0.67}, \tag{5.1}$$

Q values corresponding to the respective slope angles and wind velocities are used in eqn. (5.1) to derive L.

The flame lengths L calculated using Eqn (5.1) are presented in Figure 5.19(c), along with the quasi-steady flame length values obtained from this study for 0.1 and 1 m.s^{-1} cases (Sets 1 and 3) and in Figure 5.19(d) for the 1 m.s^{-1} cases (Sets 2, 3 and 4).

The slope angles 0°, +5° and +10° at 0.1 m.s^{-1} and 0°, +5° at 1 m.s^{-1} were not included in the fire intensity (Q) calculation and therefore, Figure 5.19(c) and (d) does not include these slopes for both the WFDS quasi-steady and empirical L calculations. Again, the Q values (and hence L) are approximate for lower slope angles +10° at 1 m.s^{-1} as the fire isochrones did not progress for these lower slope angles.

For both the lower wind velocities (Figure 5.19 c), the L values predicted by eqn. (5.1) are higher than the values obtained in this study for slope angles > +20°. For <+ 20° with sets 1 and 3, as well as for all slopes with set 4 (different fuel and weather characteristics), eqn. (5.1) predicts nearly the same flame length results as obtained from this study. If we increase the exponent from 0.67 to 0.7 in eqn (5.1), better agreement is found for simulations with the original fuel and slopes ≥ +20°.

In Figure 5.21, all the simulated L values are presented against the simulated Q values for 0.1 and 1 m.s^{-1} wind velocities.

Like the empirical correlations found in Alexander and Cruz (2012, 2021), we tested whether a power-law relationship exist between the flame length and intensity. By linear regression fit, we observed that a relationship does exist (given as eqn 5.2), as shown in Figure 5.21 (a)

$$L = A\,Q^{B}\text{ , where } A = 0.0014 \text{ and } B = 1.1664 \qquad (5.2)$$

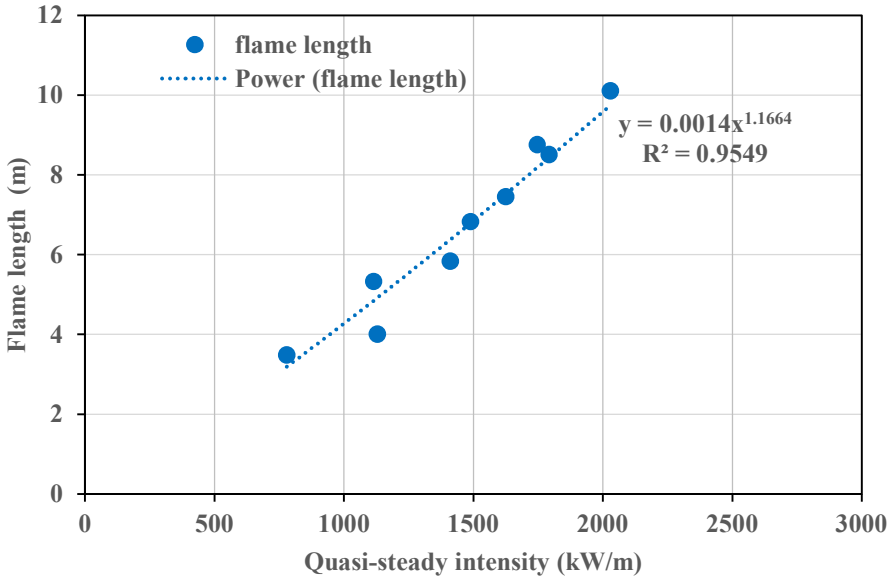

5.21 (a) Flame length vs fire intensity for 0.1 (Set 1) and 1 m.s^{-1} (Set 3)

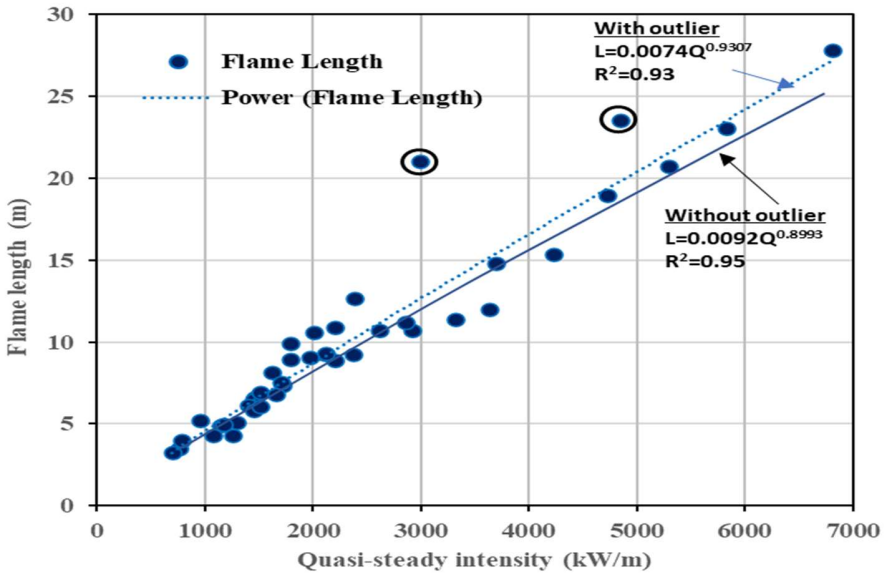

5.21 (b) Flame length vs fire intensity for all five velocites: 12.5,6 and 3, 1 and 0.1 m.s^{-1}

Figure 5.21 – *(a)* Simulated flame length vs fire intensity at 0.1 (Set 1) and 1 m.s^{-1} (Set 3) and (b) all simulated *L* values against *Q* values for all five velocities, including the values from 12.5,6 and 3 m.s^{-1} cases.

The power-law relationship is in broad agreement with the correlations in the list of empirical models presented in Alexander and Cruz (2012, 2021) and Barboni *et al.* (2012), as noted with higher wind velocity cases (Section 4.4.6). However, with higher driving wind velocity, we observed A and B values as 0.0047 and 0.9835, respectively.

In Figure 5.21 (b), all simulated L values against Q values for all five velocities, including the values from 12.5,6 and 3 m.s^{-1} cases (from Section 4.4.6) are presented, to investigate the correlation for a larger set of wind conditions. A power-law relationship is found to exist when the simulated L and Q from all wind velocites are merged in the data, in broad agreement with the correlations reported by various experimentalists.

5.3.7 Heat fluxes

Following the analysis technique detailed in Section 4.4.7 for higher wind velocity cases, contour plots of heat fluxes are extracted from the convective and radiative heat flux boundary data using Matlab software (https://mathworks.com) and are presented in Figure 5.22.. The heat flux contour plots are derived based on the trailing edge of the pyrolysis region, taken at different times as the fire front moves though the burnable grass plot. Slope angles +30°, +20 and +10° at driving wind velocities of 0.1 m.s^{-1} (Set 1) and 1 m.s^{-1} (Set 3) are presented in Figure 5.22 (a–c) and (d–f), respectively.

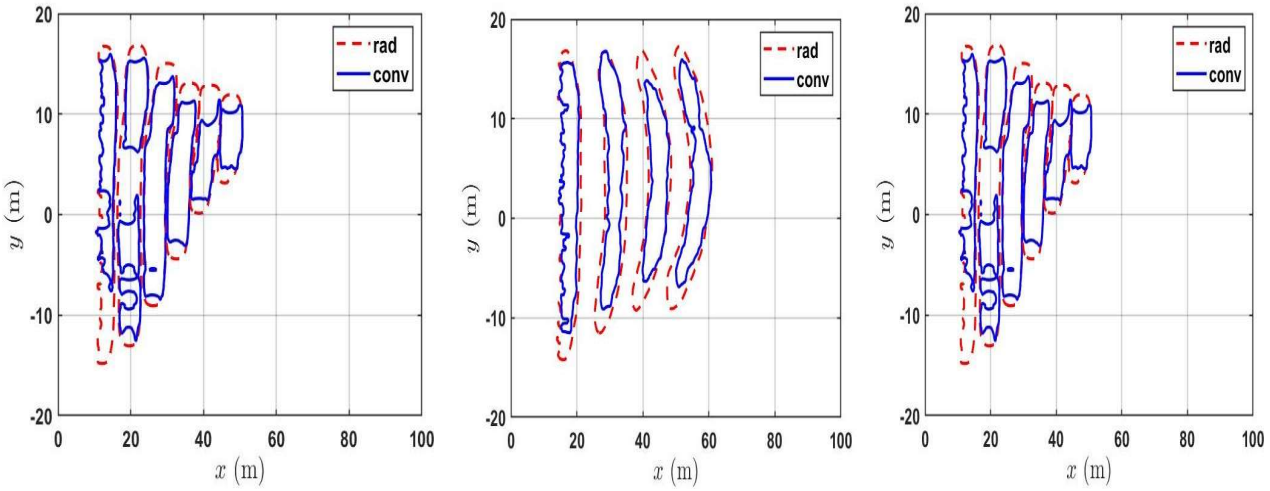

(a) +10° at 0.1 m.s^{-1} **(b)** +20° at 0.1 m.s^{-1} **(c)** +30° at 0.1 m.s^{-1}

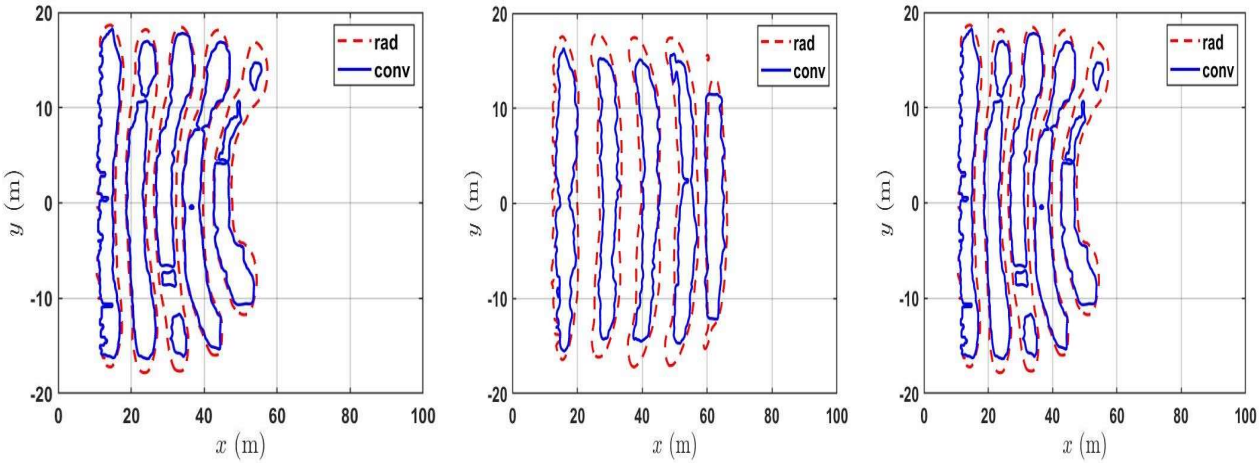

(d) +10° at 1 m.s^{-1} **(e)** +20° at 1 m.s^{-1} **(f)** +10° at 1 m.s^{-1}

Figure 5.22 – Instantaneous heat flux contours taken at different times as the fire front moves through the grass plot, for slope angles +10°, +20° and +30°, at: (a–c) 0.1 m.s^{-1} (Set 1) ; (d–f) 1 m.s^{-1} (Set 3); 'rad' and 'conv' represent radiative and convective heat fluxes, respectively.

For both lower wind velocities, the radiative heat flux contours (red lines) overlap the convective heat flux contours (blue lines) for all slope angles. For higher upslopes, +30° and +20°, the radiative heat fluxes are found to lie ahead of the convective heat fluxes for both lower wind velocities where largely buoyancy–driven fire propagation occurs as demonstrated in the Byram number analysis in Section 5.3.5. The same trend is noted for +10° slope as well, though not as predominantly as observed with higher slope angles. The leading or lagging of the fire front by radiative heat flux provides information about where heat transfer occurs as the fire front moves and does not necessarily mean that the total heat flux is dominated by the radiative heat flux. The total heat fluxes are analysed in the following segment.

The total radiative and convective heat fluxes ahead of fire front are presented in Figure 5.23(a–d) for 0.1 (Set 1) and 1 m.s^{-1} (Set 3) wind velocity. The heat flux analysis technique is detailed in Section 4.4.7. The heat flux to the unburnt surface is summed to get the total boundary heat flux (both radiative and convective) at that instant in time. For both wind velocities, the heat fluxes follow the trend of HRR presented in Figure 5.6, with double peaks. After a sustained fire front is established, the heat fluxes increase as the fire front progresses from the ignition line, then reach

a quasi-steady state and finally decrease. Both the convective and radiative heat fluxes increases with slope angle. Comparing between the velocities, as the driving wind velocity increases, both radiative and convective heat flux values increase. This is consistent with observations for the higher wind velocities presented Section 4.4.7.

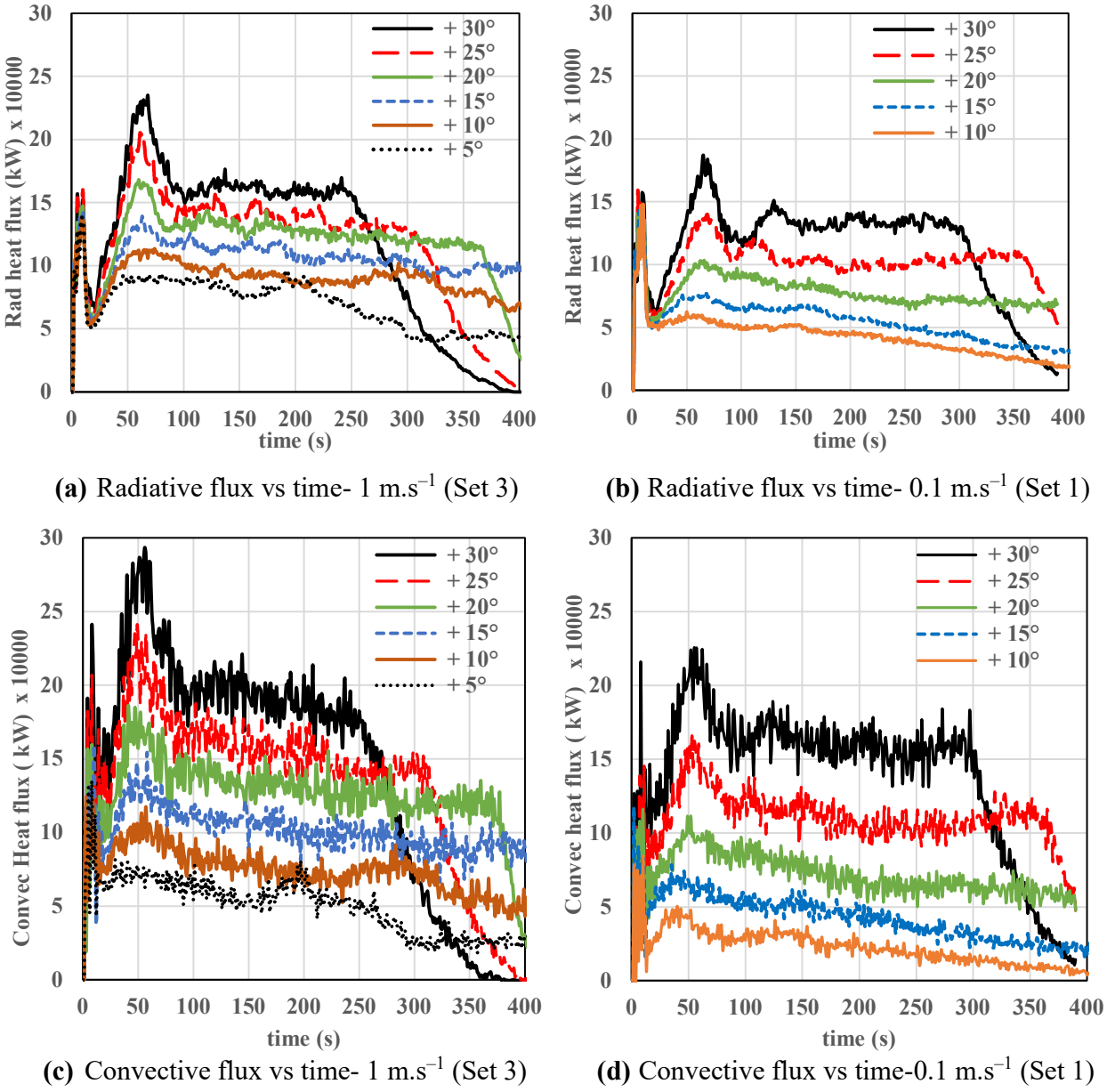

(a) Radiative flux vs time- 1 m.s^{-1} (Set 3)

(b) Radiative flux vs time- 0.1 m.s^{-1} (Set 1)

(c) Convective flux vs time- 1 m.s^{-1} (Set 3)

(d) Convective flux vs time-0.1 m.s^{-1} (Set 1)

Figure 5. 23 – Total Heat fluxes as a function of time: (a) Radiative heat flux vs time at velocity 1 m.s^{-1}; (b) Radiative heat flux vs time at velocity 0.1 m.s^{-1}; (c) Convective heat flux vs time at 1 m.s^{-1}; (d) Convective heat flux vs time at 0.1 m.s^{-1}.

The radiative and convective heat flux values extracted from the quasi-steady region are plotted against slope angles in Figure 5.24. Heat flux values at wind velocities 0.1 (Set 1) and 1 m.s^{-1} (Set 3) are presented in Figure 5.24 (a), extracted from about 60-300 s for slope angles up to +20° and from about 120–250 s for higher slope angles +25° and +30°. The heat flux values with Set 2 simulations are nearly the same as those with Set 3 (same fuel parameters and wind velocity, different domain size) and therefore Set 2 results are not presented.

In Figure 5.24 (b) the heat flux values from Set 3 and 4 simulations (original and changed fuel characteristics – conserving the same domain sizes and driving wind velocity of 1 m.s^{-1}) are presented. These values are extracted from about 50–200 s for slope angles up to +20° and from about 50–150 sec for higher slope angles +25° and +30°.

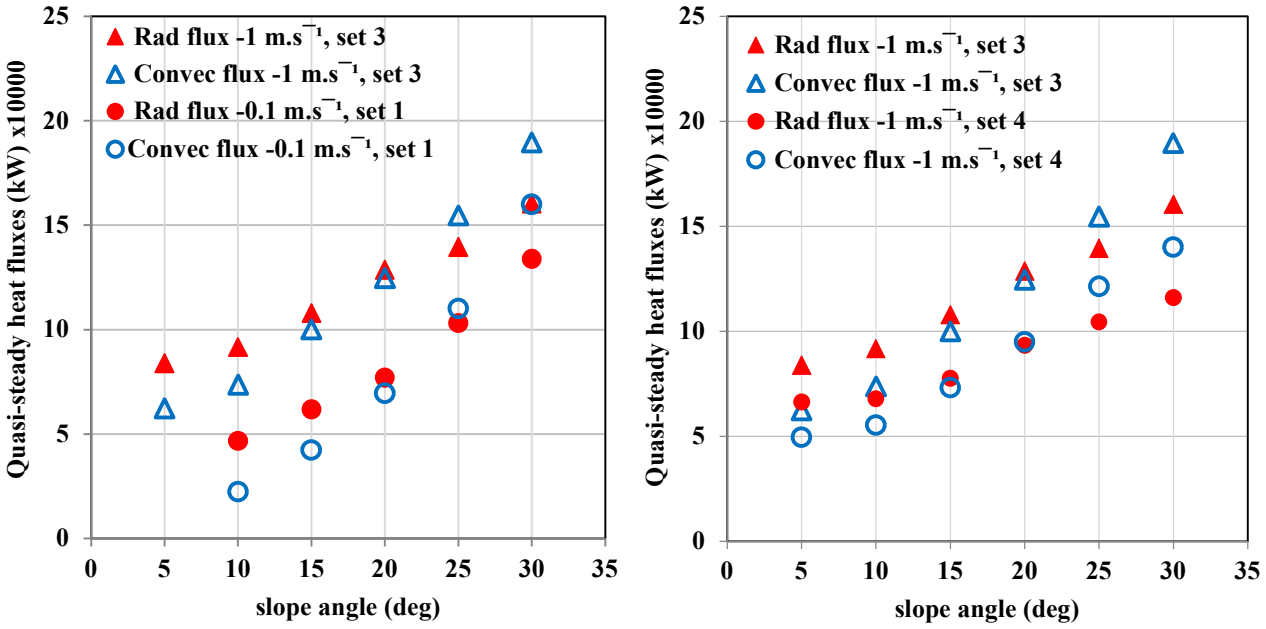

(a) Quasi-steady heat fluxes vs slope angles at wind velocities 0.1 (Set1) and 1 m.s^{-1} (Set 3)

(b) Quasi-steady heat fluxes vs slope angles at wind velocity 1 m.s^{-1}, Sets 3 and 4 simulations

Figure 5. 24 – Quasi-steady heat fluxes vs slope angles: (a) at wind velocities 0.1 (Set 1) and 1 m.s^{-1} (Set 3), and (b) at wind velocity of 1 m.s^{-1}, (Sets 3 and 4 simulations) original and changed fuel characteristics with same domain sizes and driving wind velocity.

From Figure 5.24(a), for both wind velocities, the total radiative heat flux is higher than convective heat flux for up to +20° slope. The difference between the fluxes narrows as the slope angle increases, and for higher slopes +25° and +30°, the total convective heat flux is higher than the radiative heat flux. The same trend is noted in Figure 5.24(b), which compares the heat fluxes for different fuel characteristics, where the total convective heat flux is found to be higher for higher slopes +25° and +30°. For the +30° slope, the convective heat flux is approximately 20% higher than the radiative heat flux, for all sets of simulations for both wind velocities as well as with the changed fuel parameters. For higher upslopes, the plume attaches to the ground over a longer distance, resulting in increased convective heat transfer despite the N_c suggesting that all these fires are buoyancy-dominated. Although the boundary conditions, scale of fuel bed and fuel type were different, results from this study generally agrees with the heat flux results observed by Tihay *et al.* (2014) in their experimental study, at no-wind condition at a higher slope angle (+20° slope for their study). Similary, Sánchez-Monroy *et al.* (2019) from their laboratory scale simulation reported that for no-wind conditions on slopes above +30°, convective heat flux is larger.

For higher wind velocities (Section 4.4.7), the difference between the fluxes decreases as the wind velocity decreases and both fluxes were equally significant at lower driving wind velocity compared with higher wind velocities. Again, the contour plot of heat fluxes showed that the convective heat fluxes are more relevant at higher upslopes. The results presented in Figure 5.23 reinforce that at lower wind velocities, the convective heat flux is more relevant at higher slope angles. These results are consistent with the studies of Sánchez-Monroy *et al.* (2019) and Dupuy *et al*. (2011).

5.4 *Summary*

This chapter discusses the combined effect of slope and wind on grassfire behaviour through a set of simulations performed with varied slope angles at driving wind velocities of 0.1 and 1 $m.s^{-1}$. Furthermore, two additional sets of simulations are conducted with varied domain size and changed fuel characteristics, respectively, to investigate the implication, if any, of domain size and fuel characteristics on fire propagation. The fire isochrone progression, *RoS*, fire intensity, flame parameters and mode of fire propagation are analysed and compared among different scenarios.

Generally, the fire isochrones demonstrated similar progression patterns; however, slightly more convex curvatures and thinner pyrolysis widths (or head fire width) were noted for the isochrones obtained from changed fuel parameters. We did not observe any notable variations in fire isochrone pattern among the two domain sizes.

As for the higher wind velocity cases, on sloped terrain, for a given slope angle, the intensity (Q) increased with driving wind velocity when the fuel characteristics were the same. However, with the changed fuel characteristics, the Q values decreased as similarly noted for pyrolysis width.

For a given slope angle, the fire front location at any given time was nearly the same for both the original and large domain cases. Comparing the cases with changed fuel characteristics, at any given time, the fire front was found to be moving faster with changed fuel parameters (by approximately 30–45% than for the original fuel parameters). The difference widened as the fire front progressed through the grass plot. Noticeably, increased ambient temperature along with reduced fuel moisture content, relative humidity and fuel load impacted the fire front movement and therefore the *RoS*.

The quasi-steady *RoS* results demonstrated that the *RoS* of 'changed' fuel parameters are higher by approximately 57–60% than for the original fuel parameters. For all four sets of simulations, for both 0.1 and 1 $m.s^{-1}$ wind velocities, an exponential relationship was noted between the quasi-steady *RoS* and slope angle, in agreement with the exponential relationship reported in most of the experimental studies conducted with no or very low wind speeds. For both the lower wind velocities, the relationship between Q and *RoS* was found to be linear up to a slope angle of +25°. Byram intensity was satisfied with approximately 41% of the fuel load consumed, close to the value observed for higher wind velocities, where the fuel load consumption was ~42%.

For 0.1 $m.s^{-1}$ wind velocity, the quasi-steady and dynamic average *RoS* values obtained from this study were found to be closer to slope-corrected MKIII and CSIRO model as well as both Rothermel model values. For 1 $m.s^{-1}$, the WFDS *RoS* values were closer to slope-corrected MKIII, Rothermel Original and Modified models (for slope angle up to +25° and slightly lower for +30°). Generally, for both the lower wind velocities, WFDS relative *RoS* results were found to be closer to the *RoS* predicted by the empirical slope corrections. As noted in Chapter 4 (Section 4.4.2.4),

the Rothermel models under the influence of strong wind showed very small slope effect and a greater slope effect was observed with lower wind velocities.

The plume behaviour analyses exhibited a clearly detached or rising plume for upslopes at both these lower wind velocities. Compared with higher wind velocity cases (Section 4.4.4), for any given slope angle, the plume was found to rise at a much shorter distance from the ignition line. The Byram number analysis demonstrated that fire propagation was clearly within the plume- or buoyancy-dominated regime for these lower wind velocities, whereas near-surface flame dynamics with higher wind velocities were difficult to characterise using the Byram number.

Comparing the two domain sizes, for both scenarios, flame length values were found to be nearly the same for all slopes. However, changed fuel characteristic influenced the flame length as flame lengths were lower in simulations conducted with changed fuel parameters. These simulations produced lower intensity, which resulted in lower flame length. For both wind velocities, the flame lengths obtained from this study for < +20° were in reasonably good agreement with the values predicted by the empirical model of Anderson *et al.* (1966). As noted with higher wind velocity cases (Section 4.4.6), a power-law correlation was found to exist between the flame length and fire line intensity.

As observed with higher wind velocities, both the total convective and total radiative heat fluxes increased with slope angle as well as with driving wind velocity. The contours of the heat fluxes demonstrated that at lower wind velocities, convective heat fluxes are more significant at higher upslope angles.

In the following chapter, we discuss the simulations performed with varied ignition line widths at different upslope angles, at a driving wind velocity (U_{10}) of 1 m.s^{-1}. Two different scenarios with varied ignition fire line widths are analysed – burnable grass plot width reduced to align with the width of ignition fire line and preserving, however, the same burnable grass plot size – to investigate the outcome of varying ignition fire line widths on grassfire propagation.

Chapter 6. Grassfire propagation on sloped terrains at lower wind velocity, with varied ignition fire line widths

This chapter analyses and discusses simulations conducted with varied ignition lines at different slope angles under a driving wind velocity (U_{10}) of 1 m.s^{-1}. These simulations are performed to investigate the ramifications of varying ignition fire line widths on fire isochrone progression, rate of fire spread, fire intensity and flame length. Simulations are performed with varied ignition line widths of 40, 30, 20 and 10 m, at different upslope angles, at a driving wind velocity (U10) of 1 m.s^{-1}. Two different scenarios with varied ignition fire lines are analysed. First, we discuss fire propagation with varied ignition fire line widths where the burnable grass plot width is also reduced to align with the width of the ignition fire line. This is followed by simulations conducted with varied ignition fire line widths, however, preserving the same burnable grass plot size. The results – fire isochrones, fire front locations, *RoS*, fire intensity and flame length – with different scenarios are analysed to comprehend the outcome of varying ignition fire lines on fire propagation.

Section 6.1 discusses grassfire propagation with varied ignition fire line widths where the burnable grass plot width is reduced to align with the width of the ignition fire line.

Section 6.2 investigates grassfire propagation on sloped terrain with varied ignition line widths preserving, however, the same burnable grass plot size.

The simulation methodology, inlet boundary conditions, grid size, and ignition fire size used with higher wind velocity cases (detailed in Section 4.1) are retained for the sets of simulations discussed in this chapter.

6.1 Sloped terrain with varied ignition fire line and grass plot width

The motivation to perform these simulations stemmed from the experimental study of Dupuy *et al.* (2011), who conducted a set of laboratory fire experiments to test the effect of slope and fuel bed width on fire behaviour. They conducted the study with varied fuel bed widths and fires were ignited along the entire width of the fuel bed (aligned with the fuel bed width). Dupuy *et al.* (2011)

analysed the fire isochrone geometry, rate of fire spread, flame geometry, temperature and residence time, with upslope angles of 0°, 10°, 20° and 30° and fuel bed widths of 1, 2 and 3 m. Their laboratory-scale experimental study is detailed in Chapter 2, Section 2.2.1. The set of simulations discussed in this section follows the same framework and an attempt is made to analyse the fire behaviour and correlate it with the results of the experimental study of Dupuy *et al.* (2011). It should be noted that the scale of the experimental study was much smaller compared with this simulation study, and the boundary conditions, ignition fire and fuel characteristics were also different.

Section 6.1.1 presents the simulation set-up, Section 6.1.2 the parameters and variables used in the simulations and Section 6.1.3 the results, detailed analysis, and discussions.

6.1.1 Simulation Methodology

Four sets of simulations are conducted with varied ignition fire lines, wherein the burnable grass plot width is reduced to match with the width of the ignition fire line. The grass plot length (80 m) remains the same for all four sets. The four sets of simulations are performed with a domain size of 360 × 120 × 60 m and at a driving wind velocity (U_{10}) of 1 m.s^{-1}. The ignition fire line is 1 m deep, aligned with the width of the leading edge of an 80-m long burnable grass plot. The four simulated ignition fire line widths are 40, 30, 20 and 10 m, represented as L1, L2, L3 and L4 in the discussion, respectively. The simulations are performed at upslope angles of +10°, +15°, +20°, +25° and +30°, as listed in Table 6.1.

For the higher upslope angle of +30°, the simulation is repeated with a wider ignition fine line of 50 m to investigate the effect (if any) of further increasing fire line width on fire propagation behaviour. This simulation is referred to as L0 in the discussion.

Table 6.1: List of Simulations

Slope angle	Simulations				
		L1	**L2**	**L3**	**L4**
	Burnable grass plot	80 × 40 m	80 × 30 m	80 × 20 m	80 × 10 m
	Ignition fire line width	40 m	30 m	20 m	10 m
+10°		√	√	√	√
+15°		√	√	√	√
+20°		√	√	√	√
+25°		√	√	√	√
+30° ∗		√	√	√	√

∗ conducted an additional simulation (L0) with 50 m ignition fire line width on an 80 × 50 m burnable grass plot.

L1 is the 'original' set of simulations with a 40-m wide ignition fire line discussed in Chapter 5, and the same model set-up is used with a burnable grass plot section of 80 × 40 m. Figure 6.1(a–d) represents the model set-up for L1, L2, L3 and L4, where the ignition line width (and width of burnable grass plot) is varied.

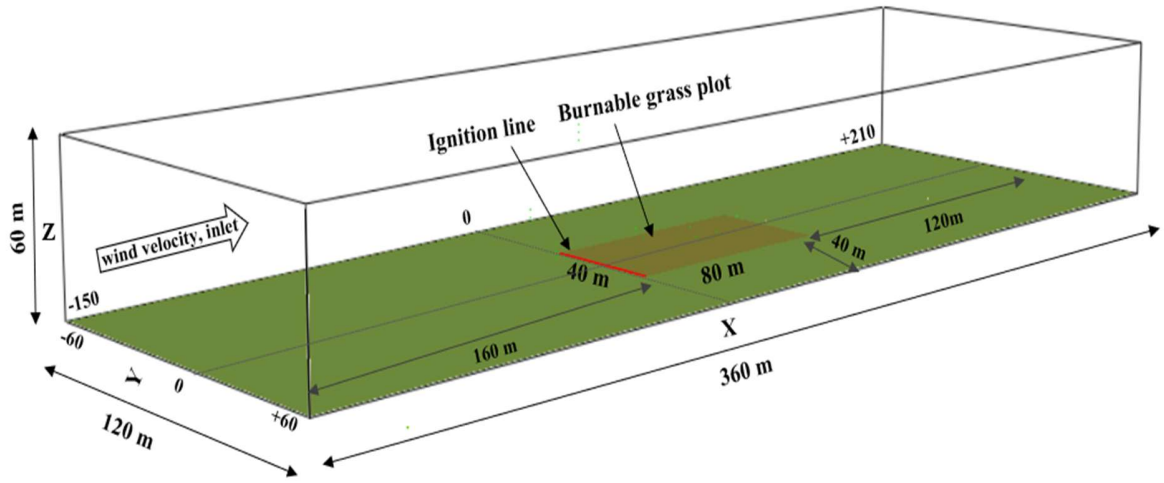

(a) L1- ignition fire line and grass plot width 40 m

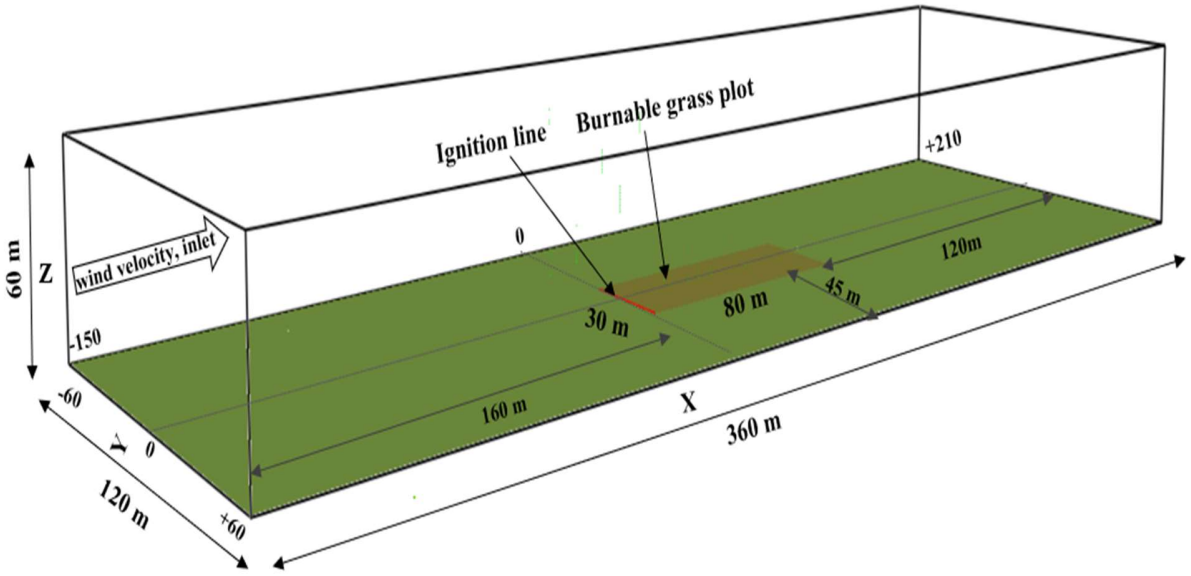

(b) L 2 - ignition fire line and grass plot width 30 m

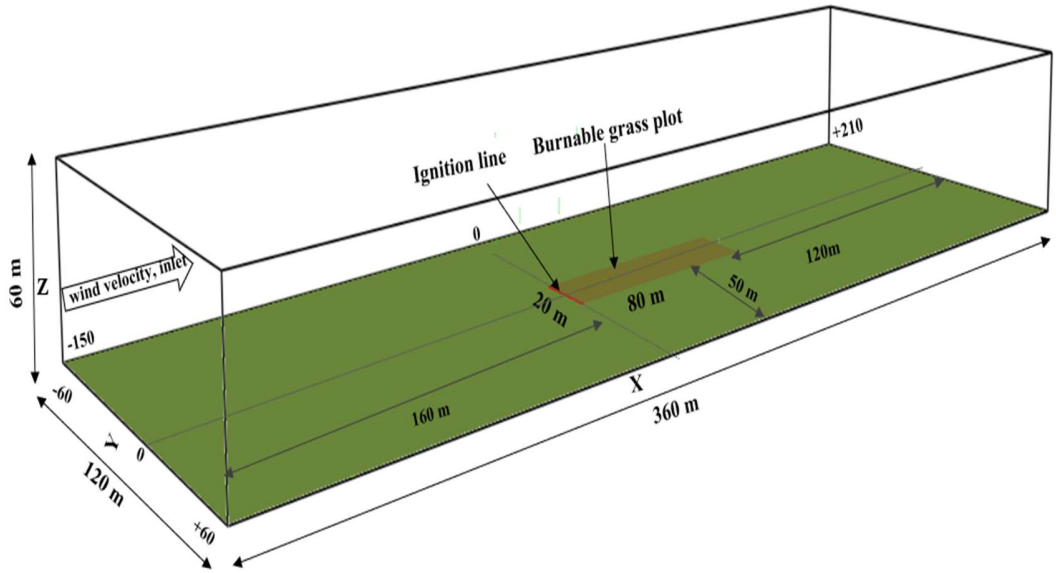

(c) L3 - Ignition fire line and grass plot width 20 m

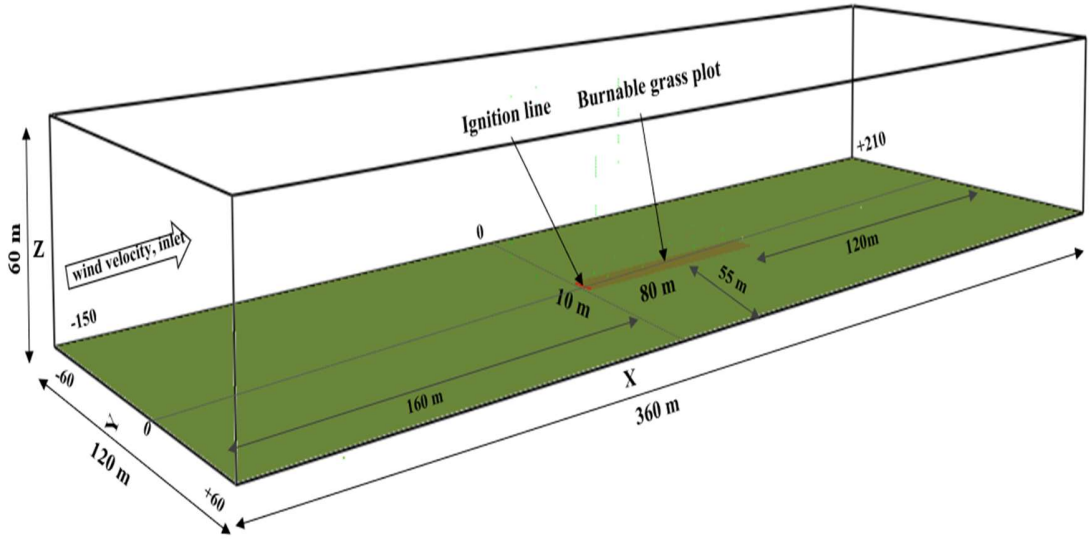

(d) L4 - Ignition fire line and grass plot width 10 m

Figure 6.1 – The geometry of the domain used for the four sets of simulations: 80-m long burnable grass plot, varied ignition fire line and grass plot width (dark green shaded region).

6.1.2 Parameters and variables

The thermo-physical, pyrolysis and combustion parameters for the 'original' fuel detailed in Table 5.2 (Chapter 5, Section 5.2), for lower wind velocity cases, are used for all four sets of simulations.

6.1.3 Results and discussions

The fire isochrones, location of the fire front, *RoS*, fire line intensity and flame length were analysed and the results are presented in the following sections.

6.1.3.1 Progression of isochrones

The fire isochrones resulting from the four sets of simulations at a wind velocity of 1 $m.s^{-1}$ are discussed in this section

The pyrolysis fronts extracted from the boundary temperature are plotted at different times after the ignition starts and when the fire progresses towards the end of the burnable grass plot. The methodology used to extract the data is detailed in Chapter 4 (Section 4.4.1.1). The fire progression

isochrones as a function of time for the four sets of simulations are presented in Figure 6.2. Note that the contours are plotted at the scale of the L1 simulation (with largest width, 40 m). In Figure 6.3, the contours of the four sets are presented scaled to their respective width size to obtain a clear view of the contours with reduced ignition fire lines. The contours for +30° with a 50-m ignition line (L0) are shown in Figure S6.1, Appendix A.

In Chapter 5, we found that for no slope and lower upslope angles at 1 $m.s^{-1}$, fire isochrones progressed very slowly and the fire extinguished rapidly. Hence 0° and +5° cases were not simulated and therefore are not discussed in this chapter.

Slope	40 m (L1)	30 m (L2)	20 m (L3)	10 m (L4)
+10°	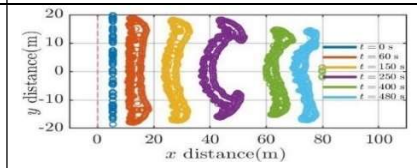 (i)	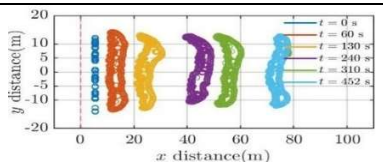 (f)	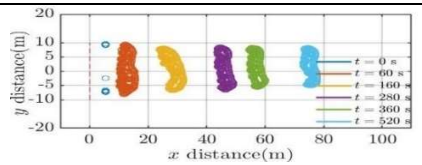 (k)	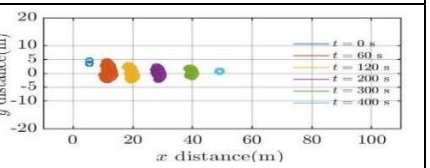 (p)
+15°	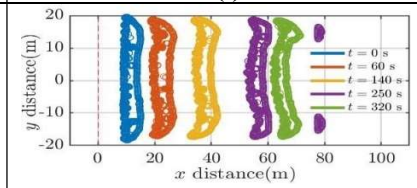 (j)	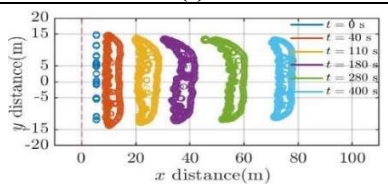 (g)	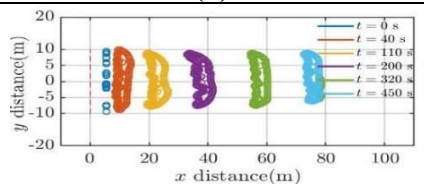 (l)	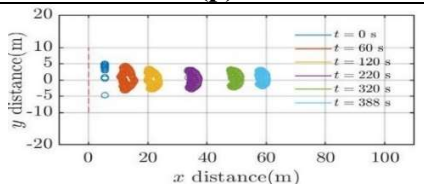 (q)
+20°	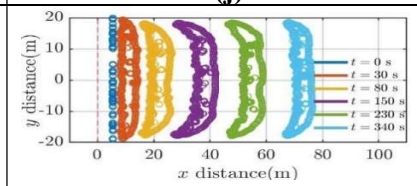 (k)	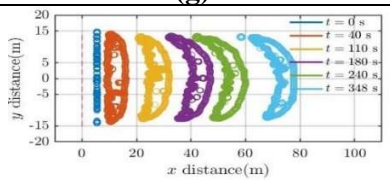 (h)	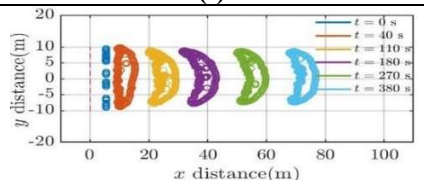 (m)	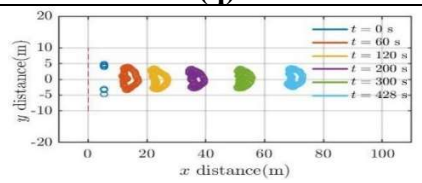 (r)
+25°	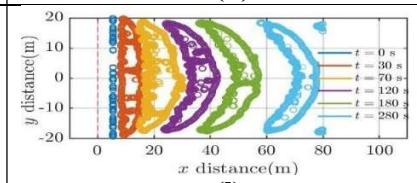 (l)	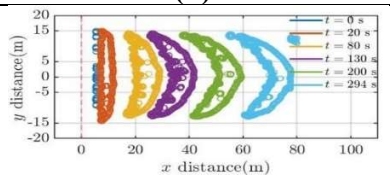 (i)	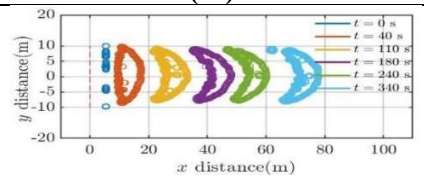 (n)	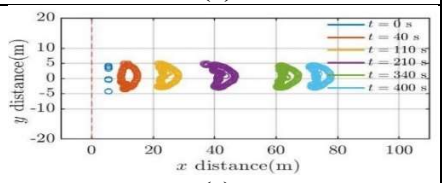 (s)
+30°	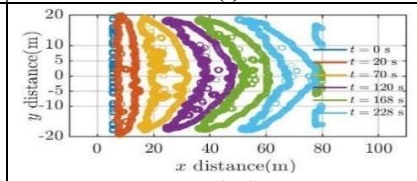 (m)	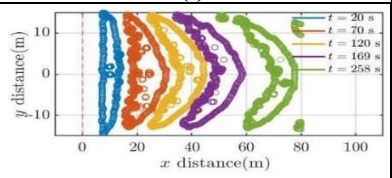 (j)	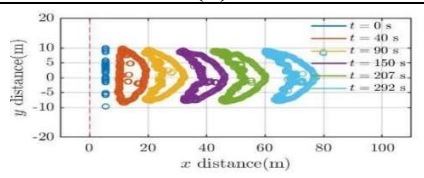 (o)	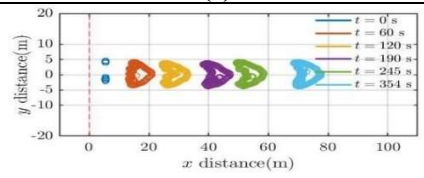 (t)

Figure 6.2 – Progression of isochrones for all four sets, at wind velocity of 1 m.s^{-1}, with varied ignition fire line lengths of : Frames (a–e) 40 m (L1); (f–j) 30 m (L2); (k–o) 20 m (L3); and (p–t) 10 m (L4).

Slope	40 m (L1)	30 m (L2)	20 m (L3)	10 m (L4)
+10°	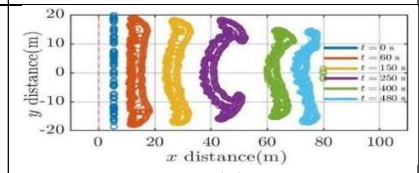 (a)	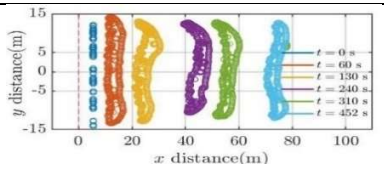 (f)	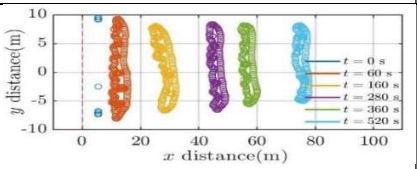 (k)	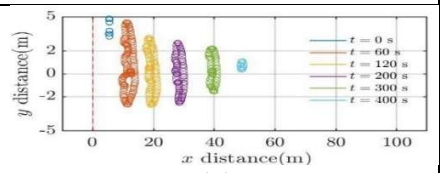 (p)
+15°	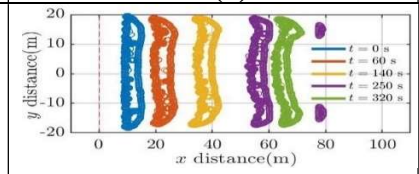 (b)	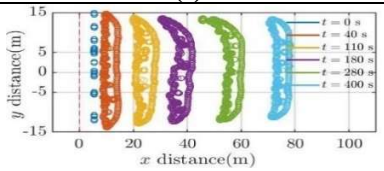 (g)	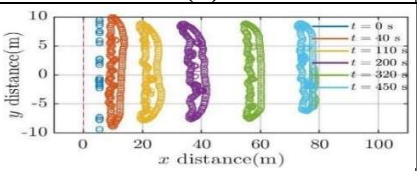 (l)	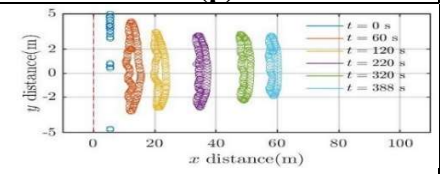 (q)
+20°	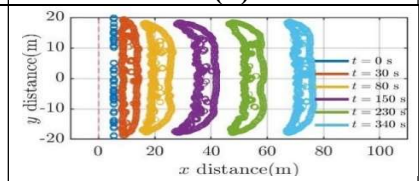 (c)	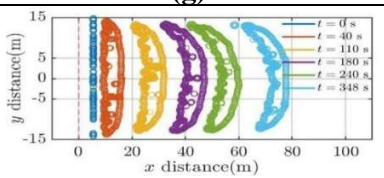 (h)	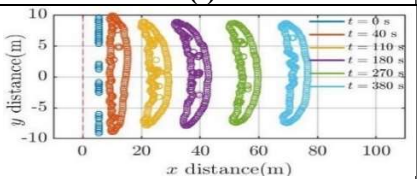 (m)	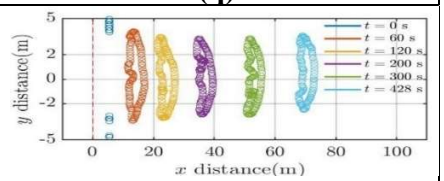 (r)
+25°	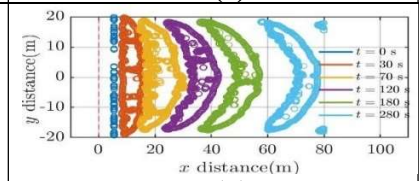 (d)	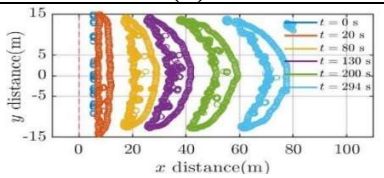 (i)	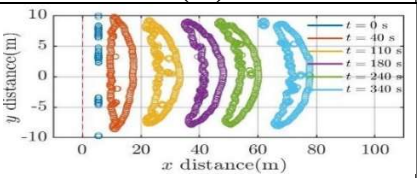 (n)	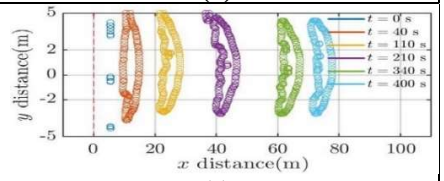 (s)
+30°	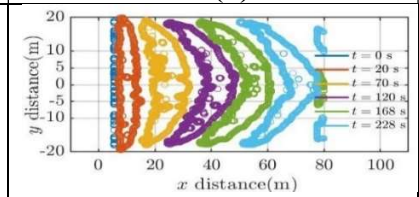 (e)	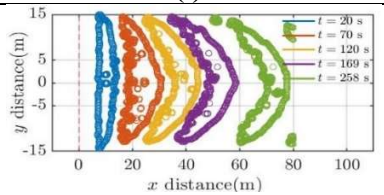 (j)	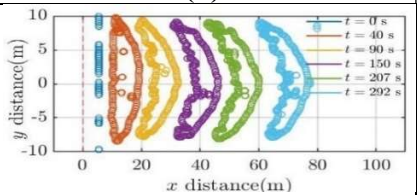 (o)	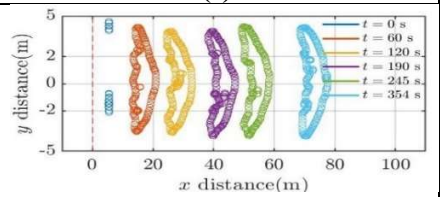 (t)

Figure 6.3 – Progression of isochrones for all four sets, enlarged views (scaled to the respective width dimension): Frames (a–e) 40 m (L1); (f–j) 30 m (L2); (k–o) 20 m (L3); and (p–t) 10 m (L4).

Figure 6.4 shows the fire contour views extracted from the laboratory experimental study of Dupuy *et al.* (2011), detailed in Chapter 2, Section 2.2.1.

(a) Fire-front view from the experimental study of Dupuy *et al.* (2011): +20º, 2 m wide fuel bed

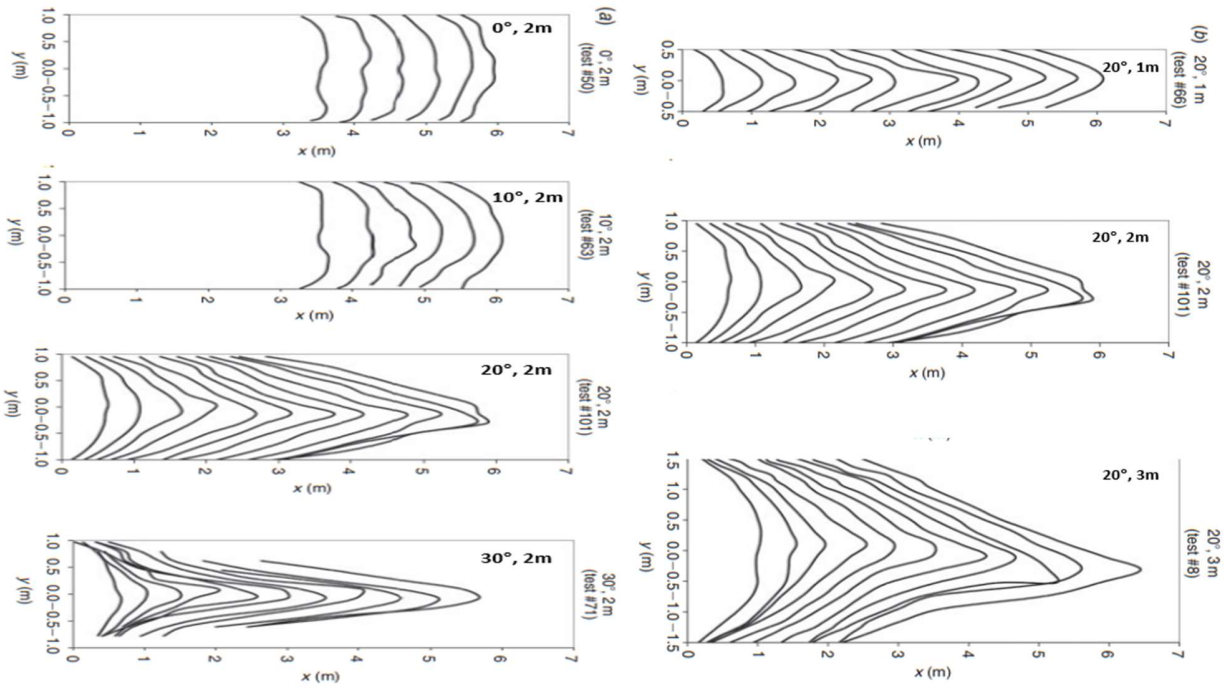

(b) Fire isochrones: 2m wide fuel bed/ignition fire line, varied slope angles.

(c) Fire isochrones: varied fuel bed widths of 1, 2 and 3m, at slope angle of 20º

Figure 6.4 – Fire isochrones extracted from the experimental study of Dupuy *et al.* (2011): (a) fire front view of 20° slope with 2-m wide fire line; (b) fire isochrones with fire line width of 2 m, at slope angles of 0°, 10°, 20° and 30°, and (c) fire isochrones with varied fire line widths of 1, 2 and 3 m for the same slope of 20°.

Figure 6.4(a) shows a photo of the fire front view for a 20° slope with a 2-m wide fuel bed from the experimental study of Dupuy *et al.* (2011). Figure 6.4(b) shows the fire isochrones obtained from a 2-m wide fuel bed (and 2-m ignition fire line) at varied slope angles of 0°, 10°, 20° and 30° (obtained by varying the angle of inclination of the fuel bed) and Figure 6.4(c) the fire isochrones obtained with varied ignition fire lines of 1, 2 and 3 m, at the same slope angle of 20°. These experiments were conducted with no wind imposed. Figure 6.3(c) shows that for the high upslope case of 20°, the width of the ignition fire line does not have a significant effect on the pointiness of the convex curvature.

Figures 6.2 and 6.3 demonstrate that, as observed in Chapter 5 (Section 5.3.1.1), for L1 to L3, the fire isochrones at the lower slope angle +10° generally show an inward or concave shape pattern and occasionally have a straighter shape. This is similar for +15° but with less-pronounced concave isochrones. For these two slope angles, some effect of the shorter fire line ignition width is observed (i.e. less inward curvature for thinner fire lines). For +20°, the isochrones shapes are mostly convex, but did not attain a sharp point, except as seen in Figure 6.2(r) for L4. As the slope angle increases further, the contours evolve with a pointier convex curvature.

Overall, for all four sets, the contours are pointed at higher upslopes, consistent with the experimental study conducted by Dupuy *et al.* (2011). They observed that the fire line shape was greatly influenced by slope, and on +20° and +30° upslope fires with a 2-m ignition width, the isochrones changed to a pointed V- shape, whereas for no slope and +10°, the fires adopted a smooth curved shape.

Comparing contours for varied ignition fire line widths, for higher upslopes, the contour pattern appears to be more pointed with increased ignition line lengths (Figure 6.3(d), (e) and Figure S6.1).

Overall, the present geometry, boundary conditions, size of the fuel bed and fuel type were different from the study of Dupuy *et al*. (2011) but despite this, the fire contour evolution pattern from the simulations showed similarity with the experimentally observed results. Note that the pointed shape of the isochrones starts to occur from +20° slope in the laboratory-scale experiments of Dupuy *et al.* (2011) and from +25° slope in our field-scale simulations.

6.1.3.2 Fire front locations and *RoS* calculation

This section discusses fire front locations, quasi-steady *RoS* calculation and correlations of *RoS* with slope angles for the simulations conducted at a driving wind velocity of 1 m.s^{-1} with varied ignition fire line widths. The quasi-steady *RoS* are then compared with empirically derived values and among different sets of simulations. Figures 6.5 and 6.6 show the temporal fire front locations, determined from the boundary centreline temperature as the fire moves through the grass plot, at the driving wind velocity of 1 m.s^{-1}. Figure 6.5 (a–d) shows fire front location vs time at varied slope angles for L1 = 40 m, L2 = 30 m, L3 = 20 m and L4 = 10 m, respectively (each plot shows fire front location for the same ignition fire line width , however, at varied slope angles).

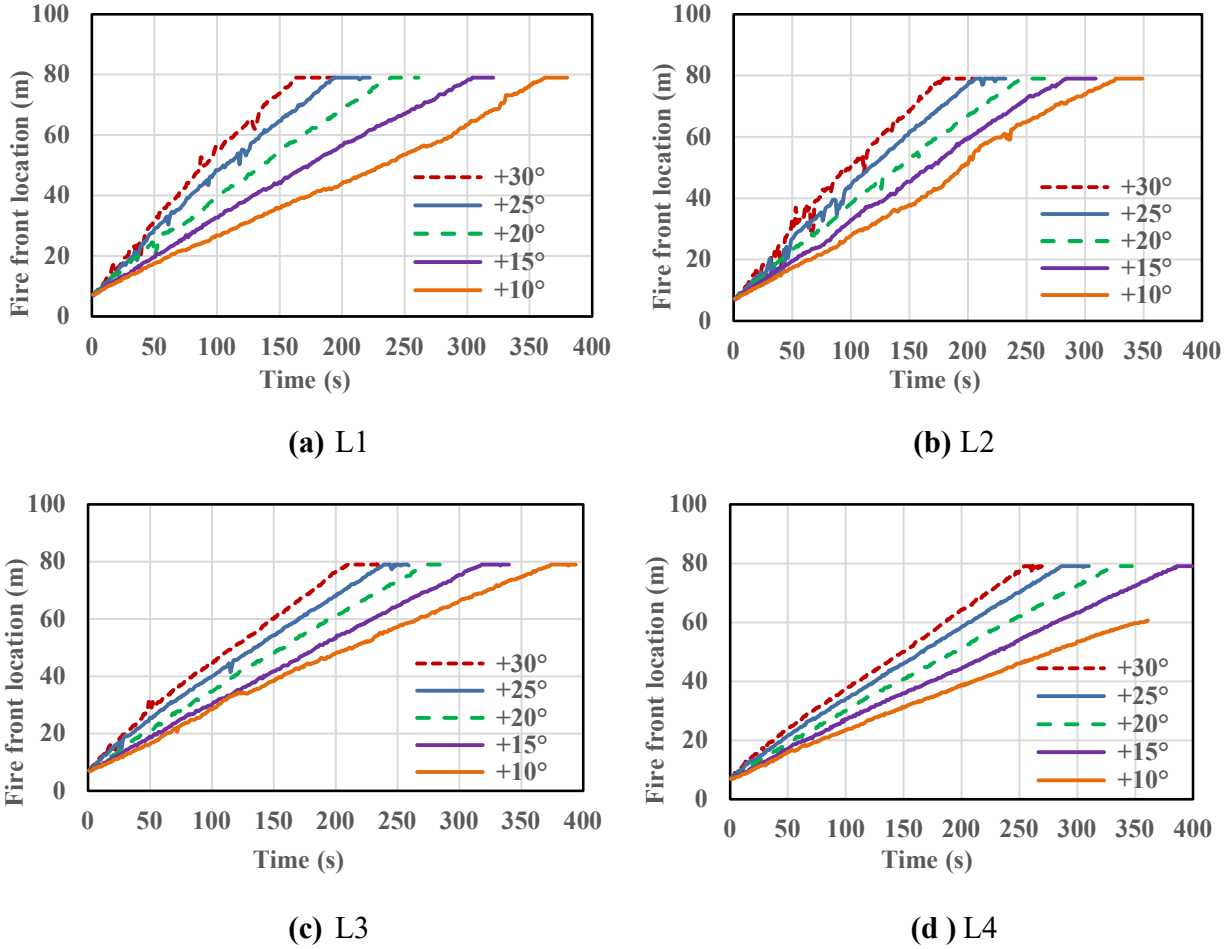

Figure 6.5 – Fire front location vs time for ignition line widths of: (a) L1 = 40 m, (b) L2 = 30 m, (c) L3 = 20 m, and (d) L4 =10 m.

Figure 6.6 (a–e) shows the fire front locations for each of the slope angles (+10° to +30°) with ignition lines of 40, 30, 20 and 10 m (each plot shows fire front location for the same slope angle, however, with varied ignition line widths).

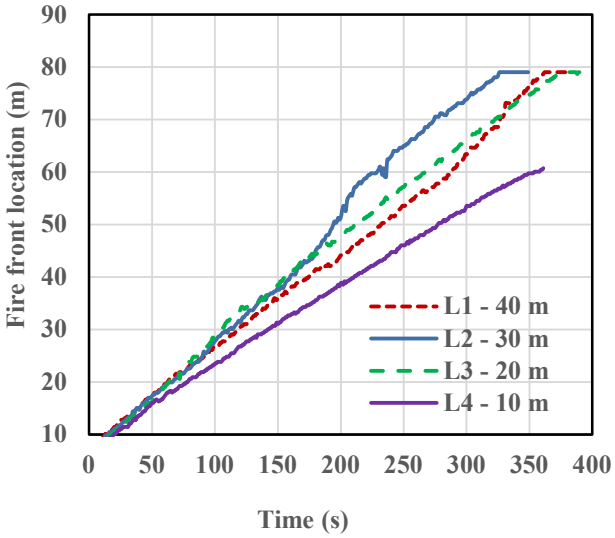

(a) +10°

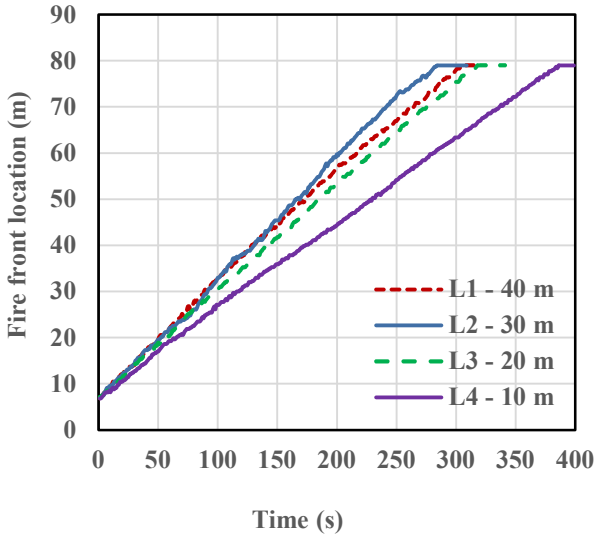

(b) +15°

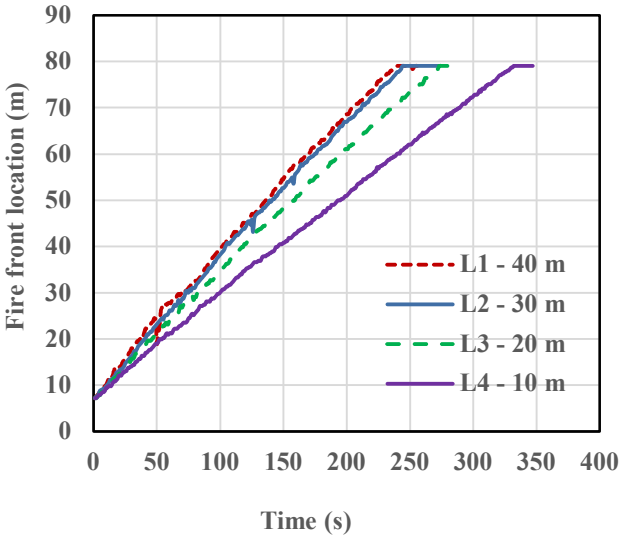

(c) +20°

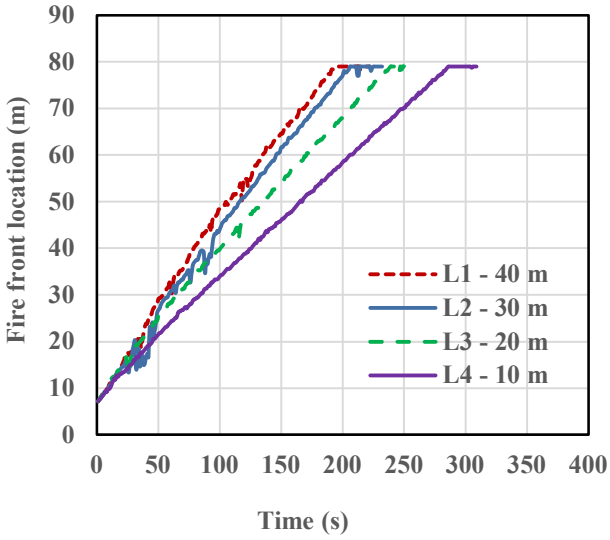

(d) +25°

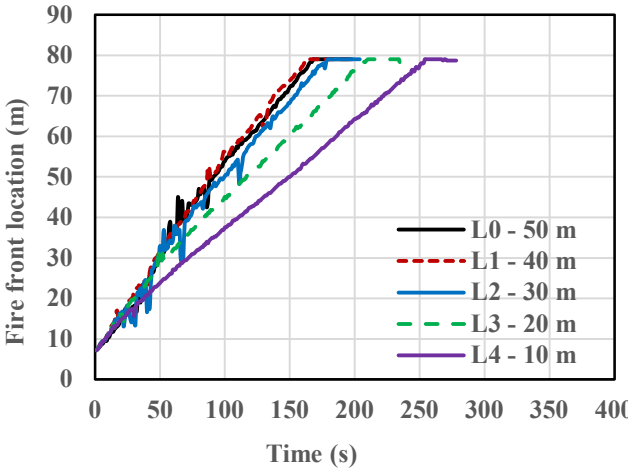

(e) +30°

Figure 6.6 – Fire front location vs time for slopes: (a) +10°, (b) +15°, (c) +20°, (d) +25° and (e) +30°, with ignition lines of 40, 30, 20 and 10 m - (e) includes fire front location for L0 = 50 m.

Figure 6.5(a) shows the same fire front locations as found in Figure 5.9(b) for ignition line width of 40 m (except the fire front location profile for +5° is not included in Figure 6.5(a)). In Figure 6.5(b–c), for a given ignition line width, the fire front moves faster with increase in slope angle as expected. For +10°, fire front does not reach the end of the burnable plot when the ignition length is 10 m, but extinguishes after travelling ~45 m, which may be due to reduced heat flux on the virgin fuel ahead of the fire front with the low HRR (see below, Figure 6.9).

Comparing among the ignition line widths, for a given slope angle, with L4 = 10 m the fire front travels slower for all five slopes. For slope angles +10° and +15°, the fire front is found to be moving nearly the same pace for 40, 30 and 20 m ignition lines (Figure 6.6(a) and (b)). For slope angles ≥ +20° fire front propagates faster with wider ignition line (Figure 6.6(d) and (e)). For wider ignition lines of L = 30, 40 and 50 m, for higher upslopes, the fire propagation is nearly at the same pace indicating it has reached a convergence state.

Following the analysis technique used with higher wind velocity cases (Section 4.4.2.3), the quasi-steady *RoS* values for each slope case are calculated from the fire front location when steady-state conditions are reached. Using the least-squares approximation method, a linear fit is applied to the

instantaneous fire front location plots (shown in Figure 6.5) at steady state for each slope angle. The slope of each linear fit equation represents the quasi-steady *RoS*, which are plotted in Figure 6.7(a) and (b).

Figure 6.7(a) presents the quasi-steady *RoS* values against slope angles (*L* constant and slope varies) for ignition lines of 40, 30, 20 and 10 m and for +30° slope with a 50-m ignition line. Besides the quasi-steady *RoS* values obtained for the four sets of simulations, the *RoS* values for the slope-corrected MKIII model and Rothermel Original and Modified models (derived from the set of equations presented in Section 2.1.1 and 2.1.3) are shown in Figure 6.7(a). The slope-corrected MKV and CSIRO model values are significantly higher for all the slope angles at lower driving wind velocities (as detailed in Chapter 5, Section 5.3.3.3). Therefore, these models are not included in Figure 6.7(a).

Figure 6.7(b) shows the quasi-steady *RoS* values against ignition fire line width (slope constant and *L* varies) for slope angles +10° to +30°.

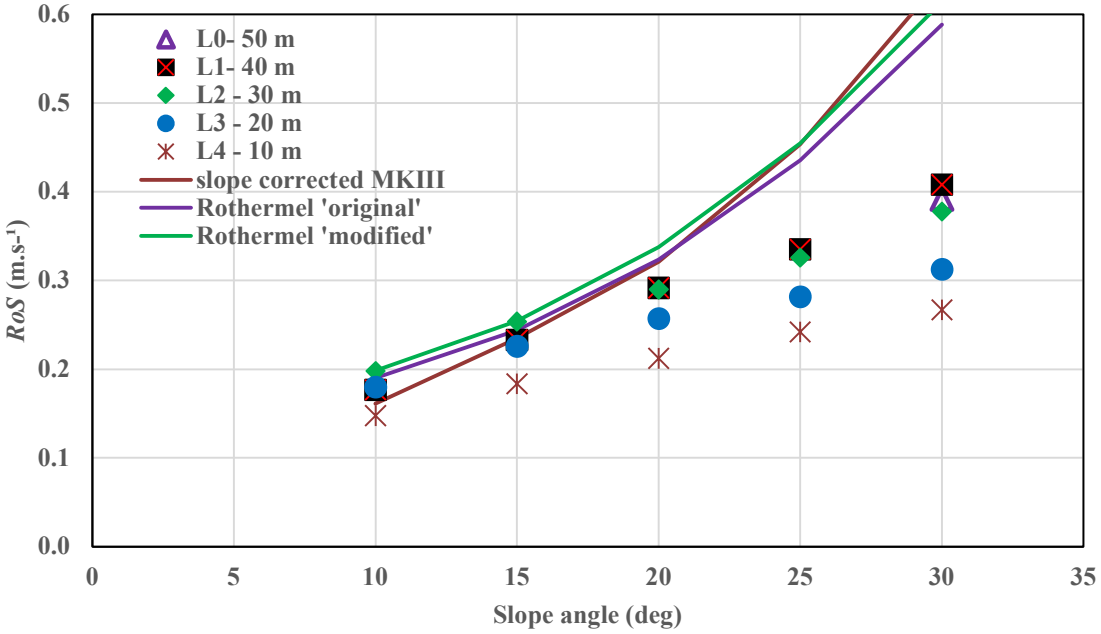

(a) *RoS* vs slope angle for ignition line widths of 40 m (L1), 30 m (L2), 20 m (L3), 10 m (L4) and +30° with 50 m (L0)

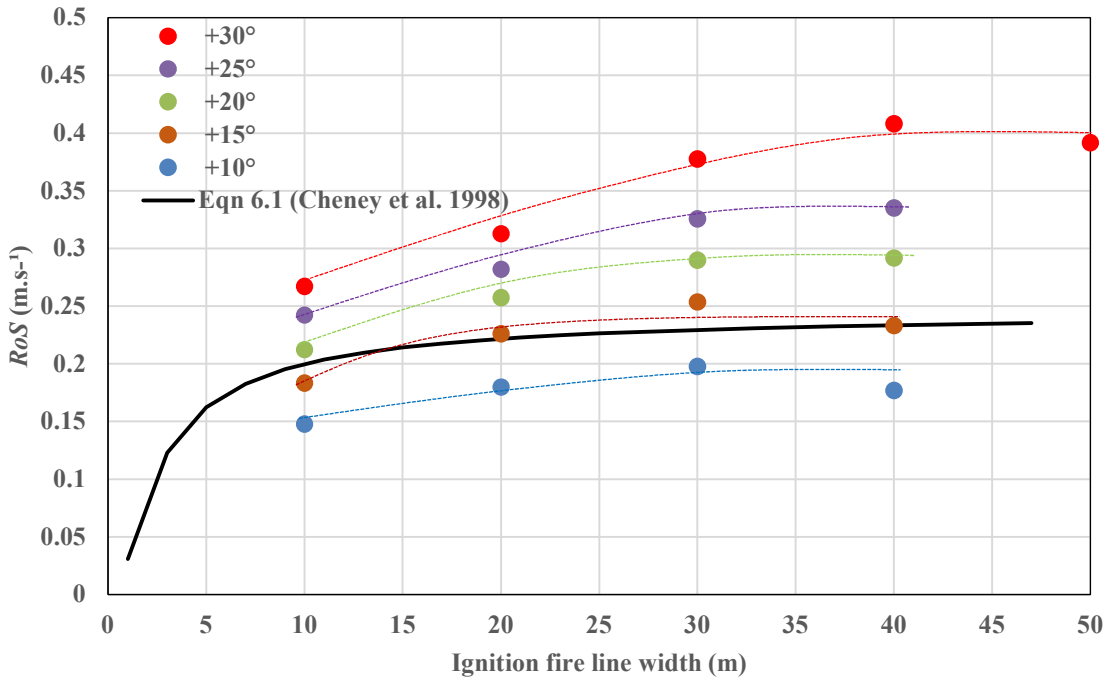

(b) *RoS* vs ignition line widths with slope angles +10°, +15°, +20°, +25° and +30°

Figure 6.7 – Quasi-steady *RoS*: (a) *RoS* vs slope angle for varied ignition line widths; (b) *RoS* vs ignition line width for varied slope angles (the lines are drawn to show the converging nature of *RoS* values and do not represent goodness of fit).

The dynamic *RoS* values are plotted in Appendix A, Figure S6.2. As for lower wind velocity cases, the plots show upward and downward spikes (random fluctuations) in *RoS* values as the fire front moves forward, and the maximum values are observed with +30° slope. Comparing among the ignition line widths, for a given slope angle, the dynamic *RoS* values decrease with ignition line width. In Figure S6.3, average dynamic *RoS* values are plotted (averaged from approximately 50 to 200 s for higher upslopes and up to 250 s for lower slope angles).

Figure 6.7(a) demonstrates that for the same ignition fire line width, the *RoS* changes with the slope angle; as was observed in Chapters 4 and 5, for a given ignition line, *RoS* generally increases with slope angle. Comparing the quasi-steady *RoS* values for different ignition line sizes (Figure 6.7(a)), for lower slope angles +10°, +15° and +20°, the *RoS* values are nearly the same for L1, L2

and L3 and the difference increases as the slope angle increases. This is consistent with the fire front locations plotted in Figure 6.6, where the fire front is found to be moving approximately at the same rate for lower slope angles of +10° and +15°. For the narrow ignition line cases (L4), the *RoS* values are much smaller compared with the other three ignition lines for all slope angles. The narrower fire (L4 = 10 m) moves more slowly and the *RoS* converge at about the 30-m (L2) ignition line. *RoS* values for +30° slope (Figure 6.7 (b)) are nearly the same for 40 and 50 m ignition lines.

Dupuy *et al.* (2011) in their experimental study found that the *RoS* increases with slope angle and with fuel bed width. They found that fuel bed width had a significant effect on *RoS* only at the higher upslopes of 20° and 30° (wider fuel bed, 3 m, had notable effect) and the slope effect was found to be significant for all fuel bed widths. The simulation results shown in Figure 6.7(a) demonstrate similarity up to L2 = 30 m with the experimentally observed results of Dupuy *et al.* (2011). Then, with increase of the ignition line width, the increase of *RoS* becomes nominal. This is also observed in Figure 6.7(b), where quasi- steady *RoS* values are plotted against ignition fire line widths (slope angle constant and *L* varies).

Cheney *et al.* (1998) presented an equation (Eqn 6.1) to determine *RoS* from the head fire width (roughly the ignition line width) based on their grassland fire experiments.

$$RoS = (0.165 + 0.534U_2)\exp([-0.859 - 2.036U_2]/w)\exp(-0.108M_C), \quad (6.1)$$

where U_2 is the wind velocity (m.s^{-1}) at 2-m height, w is head fire width (m) and M_C is the fuel moisture content.

In Figure 6.7(b), *RoS* values obtained from Eqn 6.1 for 0° slope are also presented. Eqn 6.1 shows asymptotic behaviour in *RoS* with increase of the ignition line width. Figure 6.7(b) demonstrates that the *RoS* values converge for slope angles up to +25°. In the Appendix, the dynamic average *RoS* values are plotted against ignition fire line width for the four sets of simulations (Figure S6.4). Similar asymptotic behaviour is noted with average dynamic *RoS* as well. However, on the +30° slope, a difference of 8% in *RoS* is observed between L1 (40 m) and L2 (30 m); the difference does not appear to be significant as shown in the fire front location for +30°, Figure 6.6(e).

6.1.3.4 Relative *RoS*

In Figure 6.8, relative *RoS* (*RoS* on any slope divided by *RoS* at +10°) of WFDS quasi-steady values (from Figure 6.7(a)) are compared among the four ignition line scenarios. The Australian slope correction function values (rule-of-thumb, McArthur models) and the Rothermel model values for a driving wind velocity of 1 m.s^{-1} are also presented in Figure 6.8.

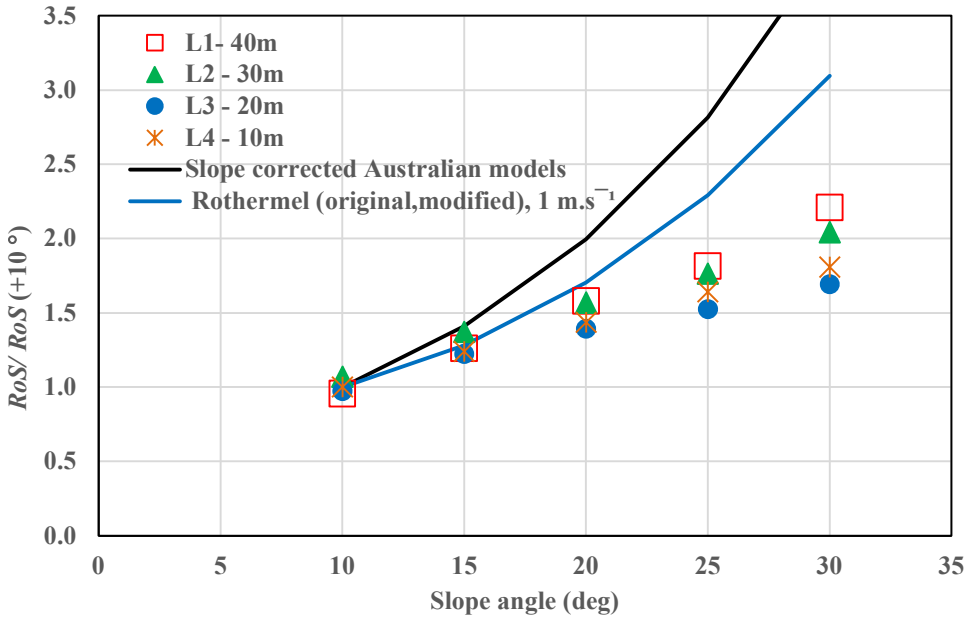

Figure 6.8 – Relative *RoS* vs slope angle- comparison of slope effect with ignition line widths of 40 m (L1), 30 m (L2), 20 m (L3) and 10 m (L4) along with empirical model results.

Like noted in Chapter 5, for 1 m.s^{-1}, the Rothermel model's slope is closer to WFDS quasi-steady results than the Australian (McArthur) model's.

Dupuy *et al.* (2011) in their experimental study compared the spread factor (or relative *RoS*) results from their experimental studies with three empirical and semi-empirical models: the Rothermel model, McArthur model and Canadian Fire Behavior Prediction system (CFBP, based on Rothermel model predictions). They noted that the CFBP system and Rothermel model gave broadly the same spread factor for slope angles 0°, +10° and +20° as their experimental results with 1-m wide ignition fire lines. The McArthur model values were found to be higher than other

models (which is also the case with the WFDS results shown in Figure 6.8). Their experimental relative *RoS* results with the higher upslope angle +30° were higher than all three empirical model values, for all three ignition lines (1, 2 and 3 m). They found that all three models underestimated the spread factor for +30° slope (about 30% for 1-m wide fires and considerably underestimated for wider fires). The difference with the present study may be attributed to the scale factor. This study is conducted at field scale, whereas the study of Dupuy *et al*. (2011) and those from which the empirical models were developed were at laboratory scale.

Our simulation results shown in Figure 6.8 demonstrate similarity with the experimentally observed results of Dupuy *et al.* (2011) for slope angles up to +20° in terms of comparison with the Rothermel model results.

6.1.3.5 Heat Release Rate (HRR) and Fire Intensity

Time series of HRRs obtained from all four sets of simulations are presented in Figure 6.9 for 40-m (L1), 30-m (L2), 20-m (L3) and 10-m (L4) wide ignition lines. In Figure S6.5 in Appendix A, the HRR for +30° slope with 50-m (L0) wide ignition line is plotted. A longer ignition line makes the fire bigger and hence produces a higher HRR. For the same ignition length, higher upslope angles lead to higher HRR, as noted previously in Chapter 5.

As observed in Chapter 5, the HRR generally increases upon ignition, then decreases for a while and surges again. The first peak occurs at ~10 s for all sets, and the second peak occurs at ~65 s for L1, L2 and L3, and at about 40 s for L4. After the second peak, the HRR values reaches a quasi-steady state.

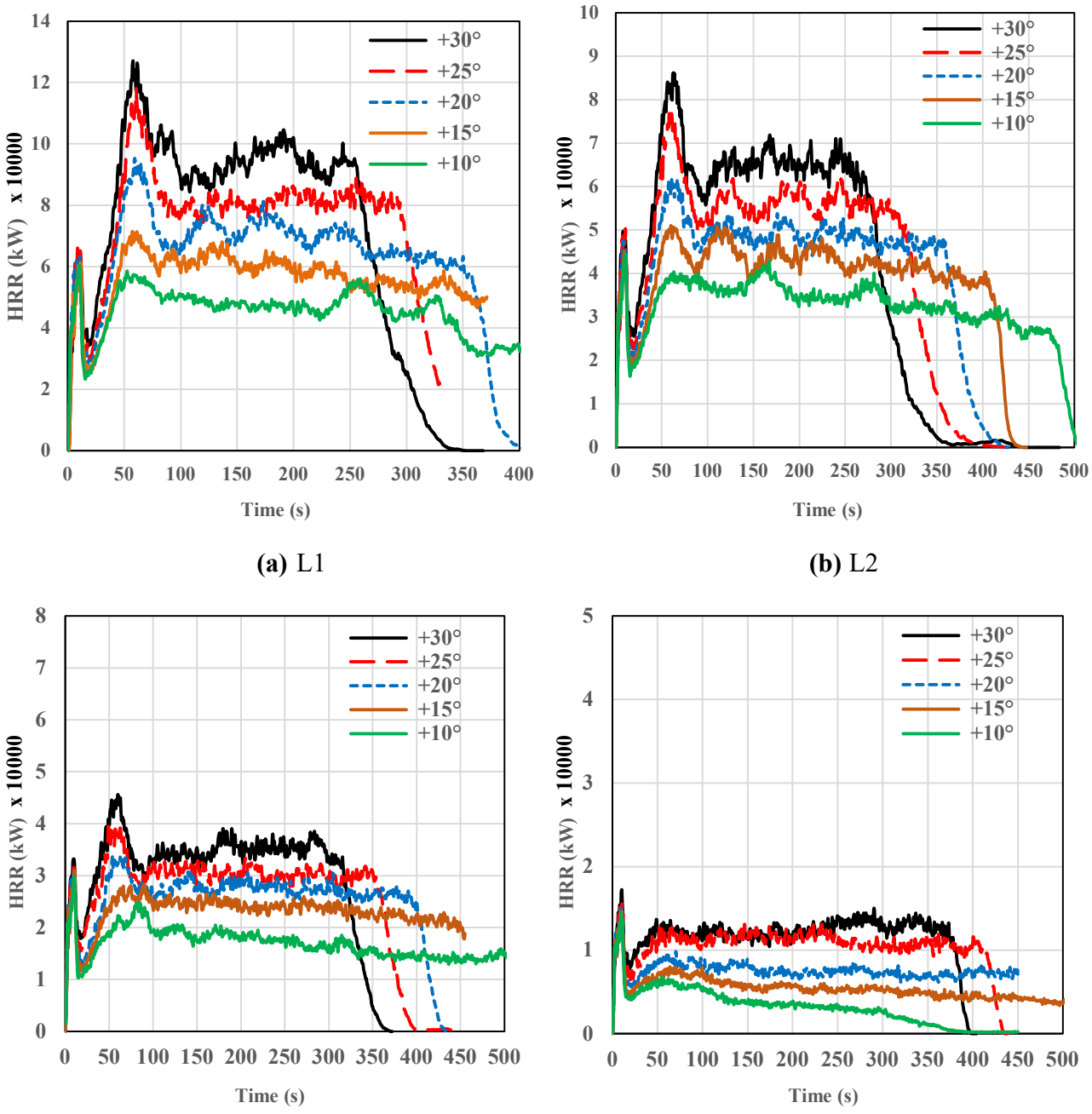

(a) L1

(b) L2

(c) L3

(d) L4

Figure 6.9 – HRR vs time for ignition line widths of: (a) 40 m (L1), (b) 30 m (L2), (c) 20 m (L3) and (d) 10 m (L4). The x-axis has a non-uniform scale to get clear view of HRR values for L3 and L4.

Like the method followed in Chapter 5 to calculate Byram's fire intensity Q (kW.m^{-1}), the instantaneous HRR (kW) values are divided by the measured fire front length (m) at the same instant in time. The fire front length is measured along the centre of the pyrolysis region of fire isochrones every 20 s for the four sets of simulations. The methodology is described in Chapter 4, Section 4.4.3. Again, at the lower upslope angle +10°, the fire isochrones have not attained a curved pattern, and hence, the measured fire front lengths for +10° for the four sets are approximate.

Figure 6.10 shows the measured fire front length against time for each of the slope angles, +10° to +30°, for ignition lines of 40, 30, 20 and 10 m. Figure 6.10(e) for +30° slope includes the fire front length with a 50-m ignition line. For a given ignition line width, for higher upslopes, the contours evolve into a more pointed convex curve (Figure 6.3) and therefore, slightly higher pyrolysis length values are noted for slope angles +25° and +30° at any given time compared with the lower slope angles.

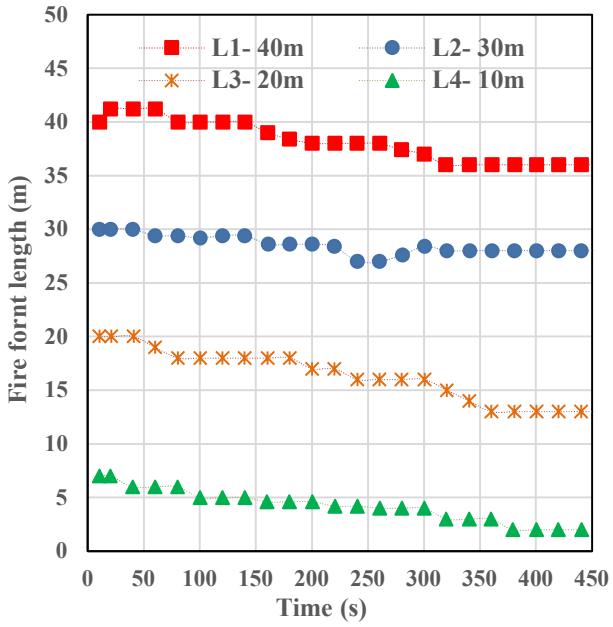

(a) +10°

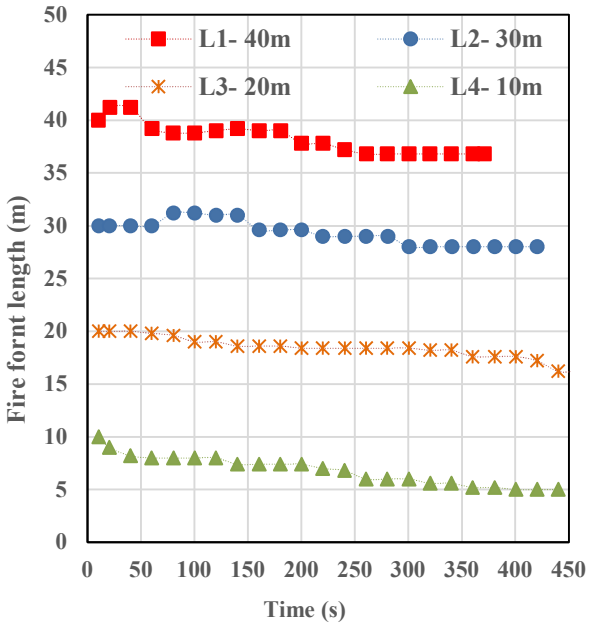

(b) +15°

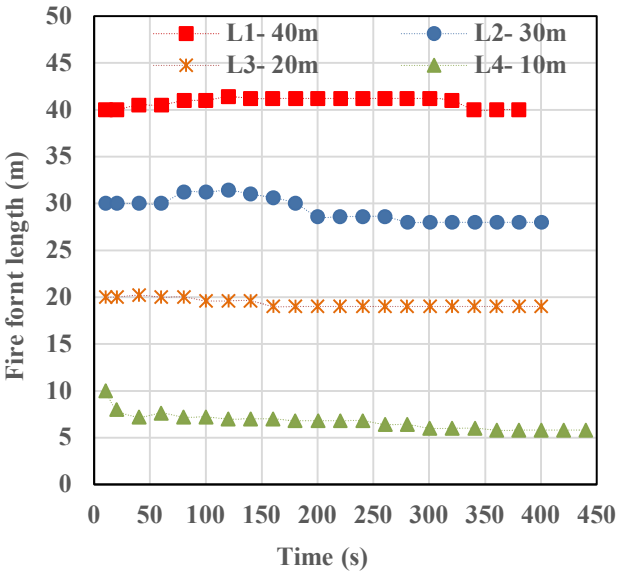

(c) +20°

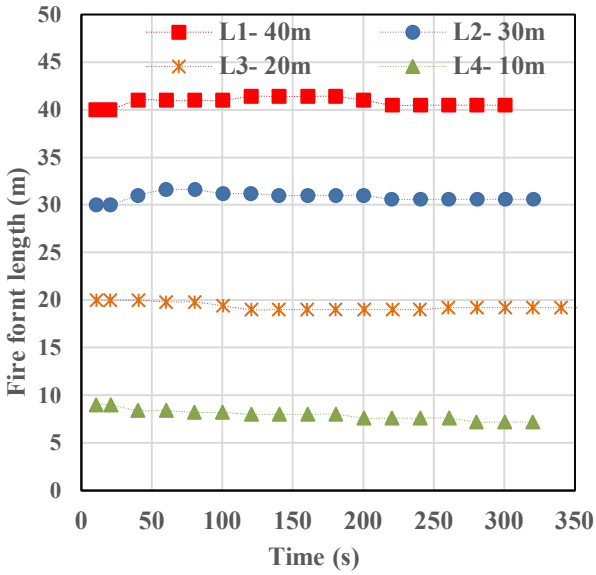

(d) +25°

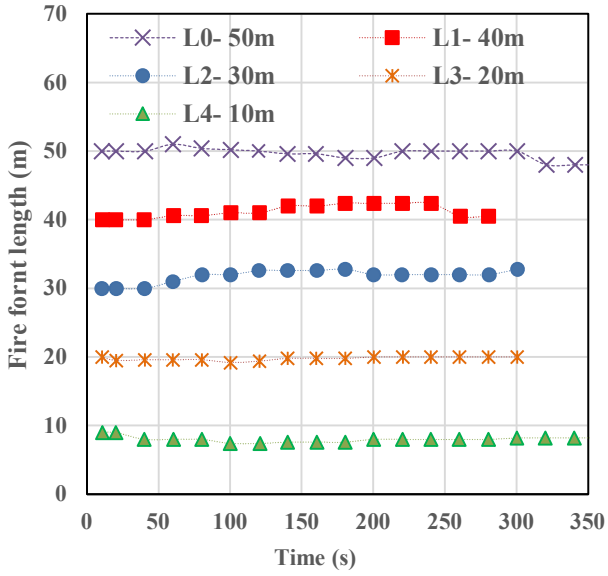

(e) +30°

Figure 6.10 – Fire front length vs time for slope angles: (a) +10°, (b) +15°, (c) +20°, (d) +25° and (e) +30°, with ignition lines of 40, 30, 20 and 10 m. Figure (e) also includes the 50-m ignition line.

Q values obtained by dividing the HRR (kW) values by fire front lengths (m) are presented in Figure 6.11(a–d) for L1, L2, L3 and L4 simulations, respectively. For the 10-m ignition line cases (L4), especially for lower slope angles, the fire did not progress and hence *Q* values are extracted for a shorter period.

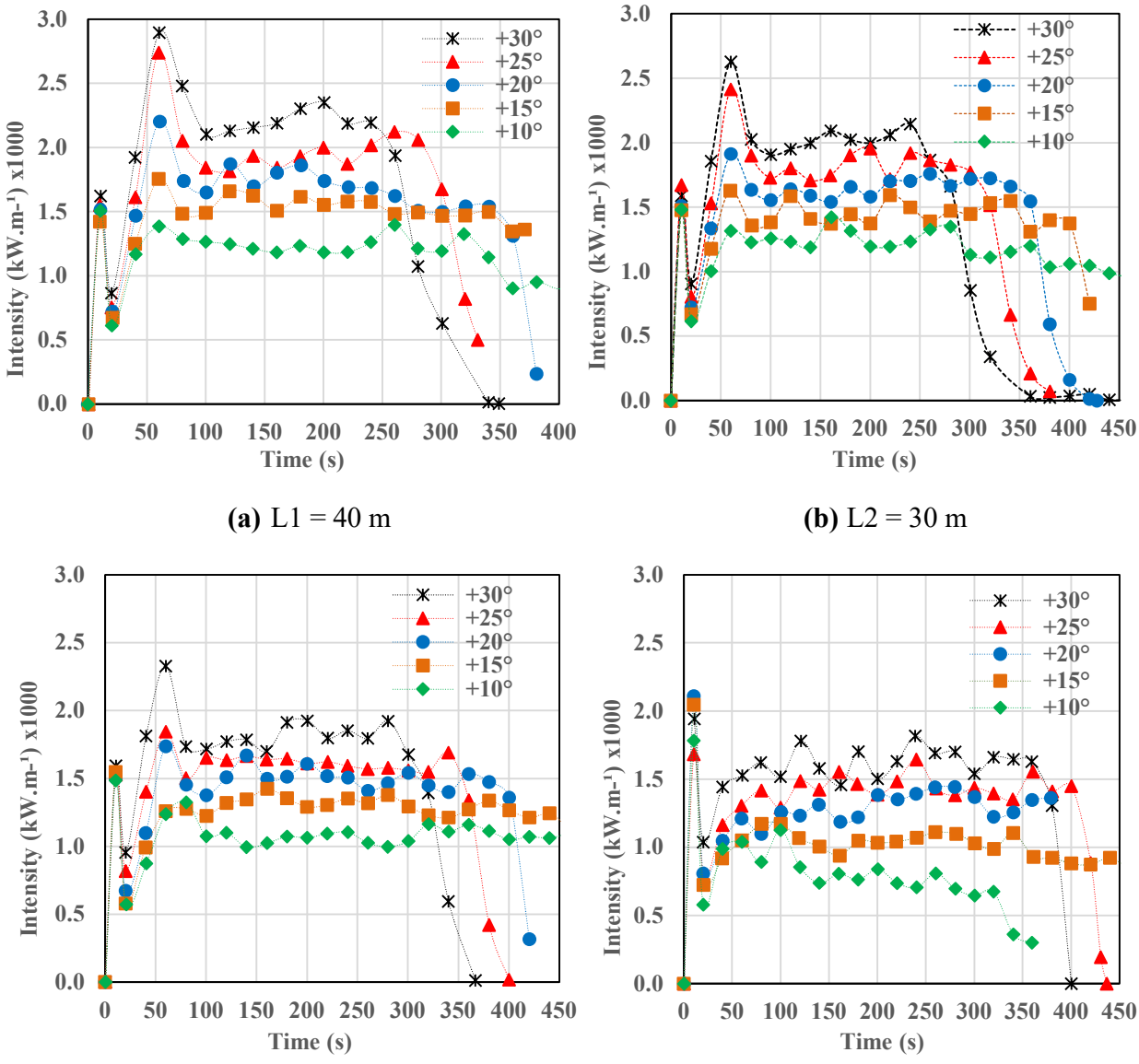

(a) L1 = 40 m

(b) L2 = 30 m

(c) L3 = 20 m

(d) L4 = 10 m

Figure 6.11 – Fireline intensity *Q* vs time for ignition line widths of: (a) 40 m (L1), (b) 30 m (L2), (c) 20 m (L3) and (d) 10 m (L4).

Figure 6.12 presents the quasi-steady Q values for all four sets of simulations. The values are averaged over a period of approximately 80 to 300 s for lower slope angles and approximately 100 to 250 s for higher upslope angles (+25° and +30°).

The Q values are plotted against slope angles in Figure 6.12(a) and against ignition line widths in Figure 6.12(b).

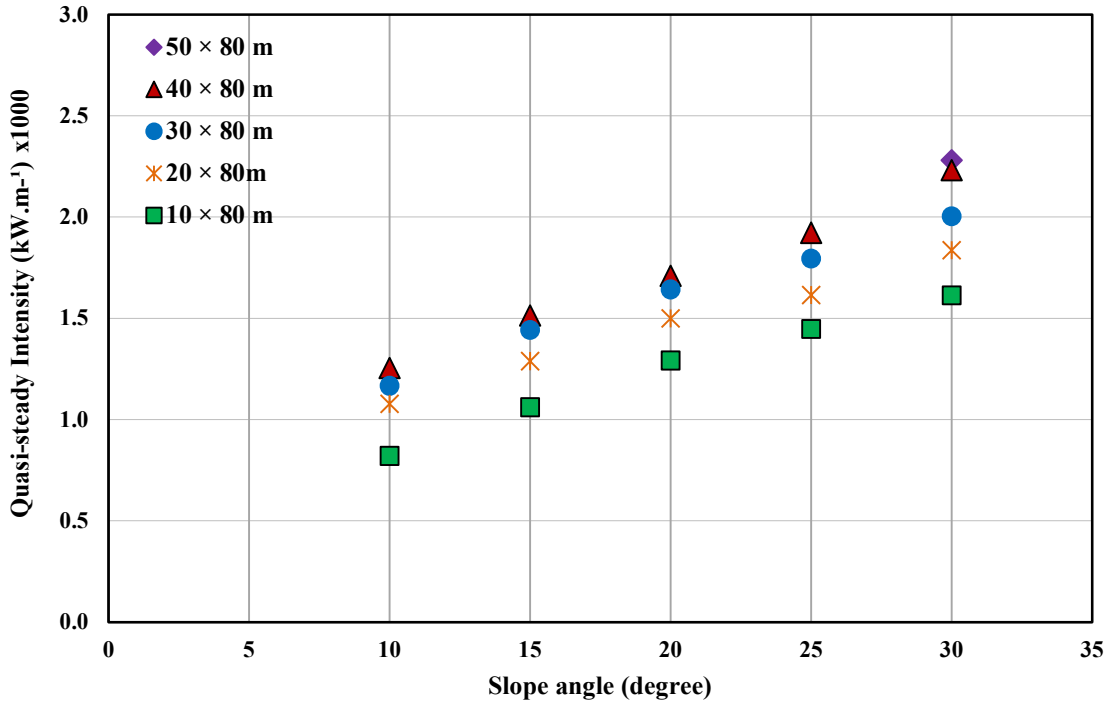

(a) Quasi-steady Q vs slope angle for 40 m (L1), 30 m (L2), 20 m (L3), 10 m (L4) and +30° of 50 m (L0)

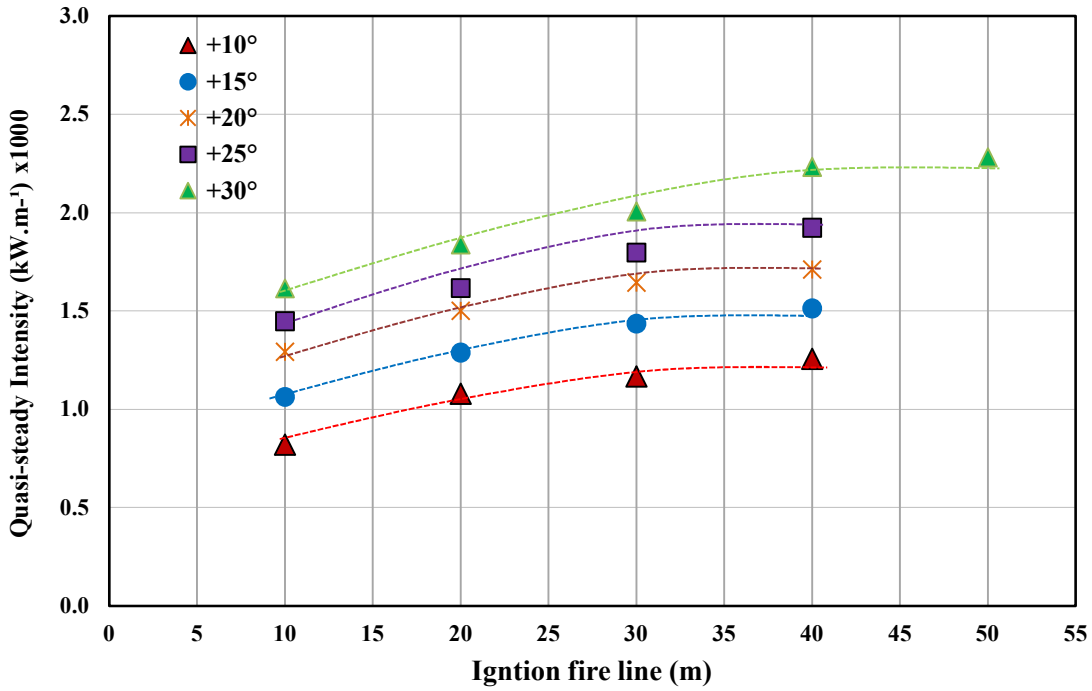

(b) Quasi-steady Q vs ignition line width for slope angles of +10° to +30°

Figure 6.12 – Quasi-steady intensity: (a) Q vs slope angle for 40 m (L1), 30 m (L2), 20 m (L3) and 10 m (L4) ignition lines; and (b) Q vs ignition line width for slope angles +10°, +15°, +20°, +25° and +30° (the lines are drawn to show the converging nature of the values and do not represent goodness of fit).

The Q values increase with slope angle for all ignition line widths (Figure 6.12(a)). For L1, L2 and L3, the quasi-steady Q values increase by approximately 25–40% for every +10° increase in slope, whereas the increase is approximately 40–80% for L4 (10-m ignition line) cases. Figure 6.12(b) shows that the Q values reach an asymptotic or convergence state for up to +25° slope angle, as observed with the *RoS* (Figure 6.7(b)). On the +30° slope, a difference of 16% in Q values is noted between L1 = 40 m and L2 = 30 m.

In Figure 6.13, the quasi-steady intensity Q values are plotted against *RoS* (quasi-steady *RoS* obtained from Figure 6.7) for all sets of simulations.

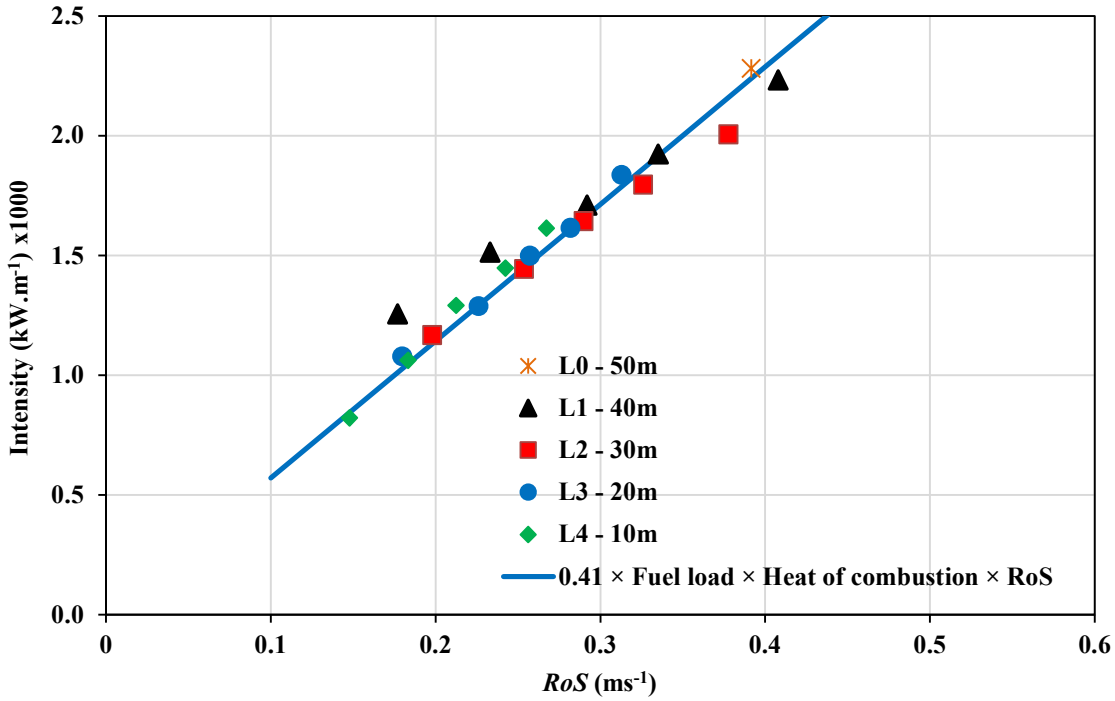

Figure 6.13 – Fire intensity *(Q)* as a function of *RoS* for varied ignition line widths of 40 m (L1), 30 m (L2), 20 m (L3), 10 m (L4) and +30° slope at 50 m (L0).

In Chapter 5 (Figure 5.14), we observed that the *RoS* and intensity value for +30° slope at 1 m.s^{-1} was outlier (falls outside the linear regression fit) and the linear regression for the *Q*–*RoS* relationship was derived without this value. From Figure 6.13, it appears that Byram's intensity (Byram 1959) (*Q* = fuel load × heat of combustion × *RoS*) is reasonably satisfied with ~41% fuel load , instead of 100% fuel load, as for the result obtained with lower wind velocity cases presented in Chapter 5, Figure 5.14. Further, 0.41 × fuel load × heat of combustion × *RoS* also satisfies the values for +30° slope for all four ignition lines (L1, L2, L3 and L4) and +30° slope with L0 = 50 m as well.

6.1.3.6 Flame length

The flame length is computed from instantaneous centreline HRR data using the Matlab software function *regionprops* (https://mathworks.com). The methodology is detailed in Section 4.4.6 for higher wind velocities. Figure 6.14 (a)–(d) shows the flame length vs time plotted for L1, L2, L3

and L4, respectively. The flame length for L0 (50-m ignition line) with +30° slope is shown in Figure S6.6, Appendix A.

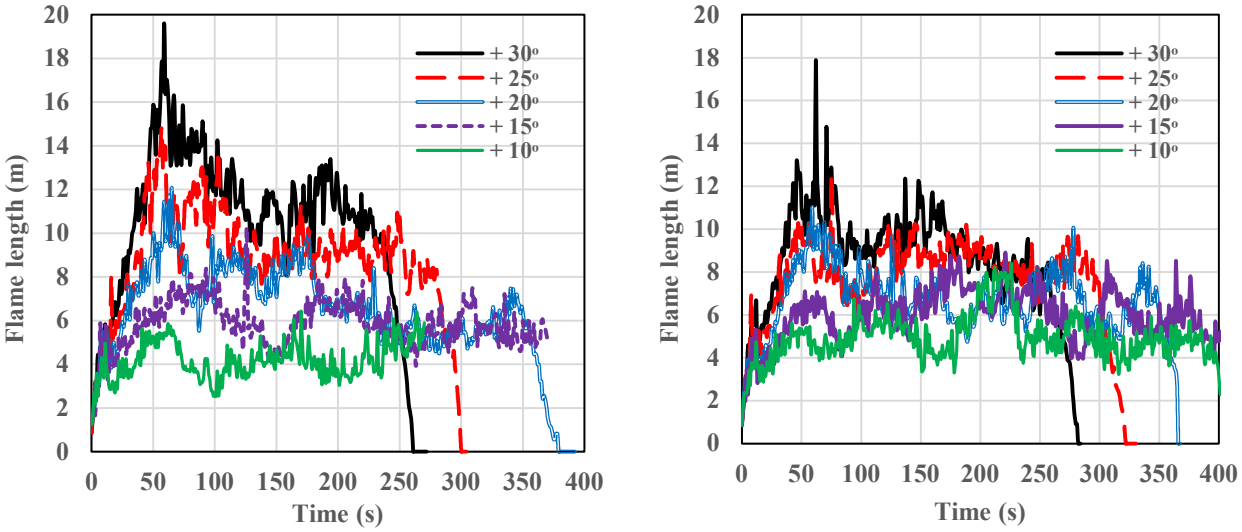

(a) L1 **(b)** L2

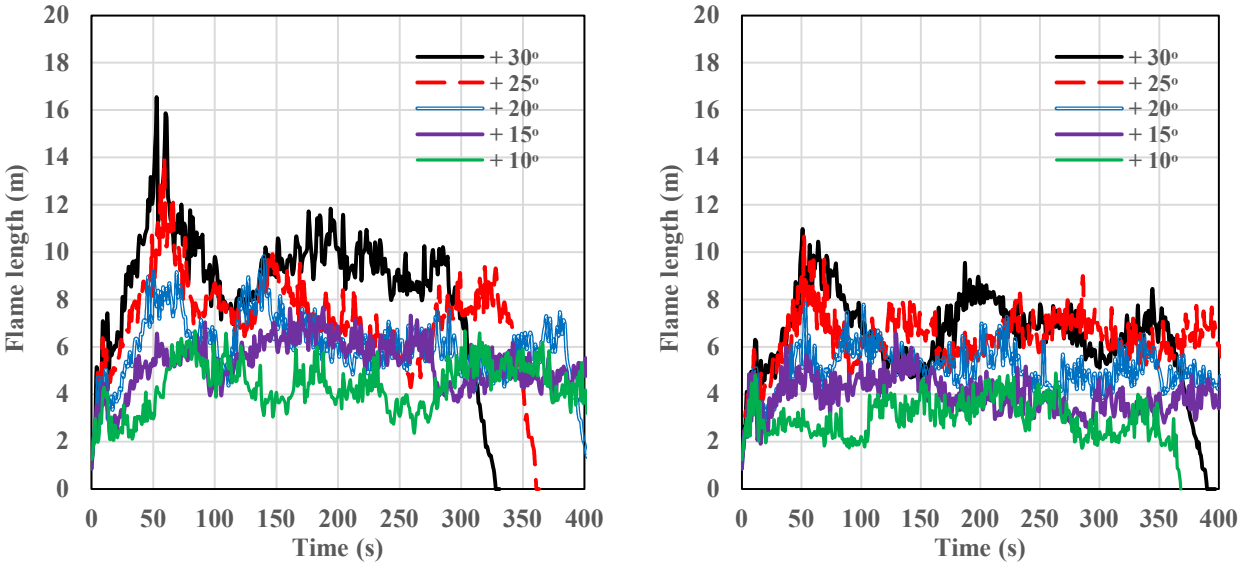

(c) L3 **(d)** L4

Figure 6.14 – Flame length vs time: at wind velocity of 1 m.s^{-1}, for ignition line widths of: (a) 40 m (L1), (b) 30 m (L2), (c) 20 m (L3), and (d) 10 m (L4).

As observed in Chapters 4 and 5, the flame length values do fluctuate and show irregular patterns due to the dynamic nature of fire propagation. For all four ignition lines, the highest flame length is for +30° slope and the flame length decreases as the slope angle decreases. A longer quasi-steady state is observed for lower slope angles for all four sets of simulations.

Figure 6.15(a) shows the quasi-steady flame length vs slope angles plot for the four sets of simulations. The quasi-steady values are extracted from Figure 6.14 (a–d) and from Figure S6.6 when steady-state conditions are reached. For higher upslopes (especially +25° and +30°), where no clear quasi-steady state exists, the flame length is averaged over a short period at the peak of the length. For lower slope angles, the average values are extracted from 100 to 250 s for L1 and L2 cases and from 100 to 350 s for L3 and L4 cases.

In Figure 6.15(b), the quasi-steady flame length values are plotted against ignition line width for each of the slope angles.

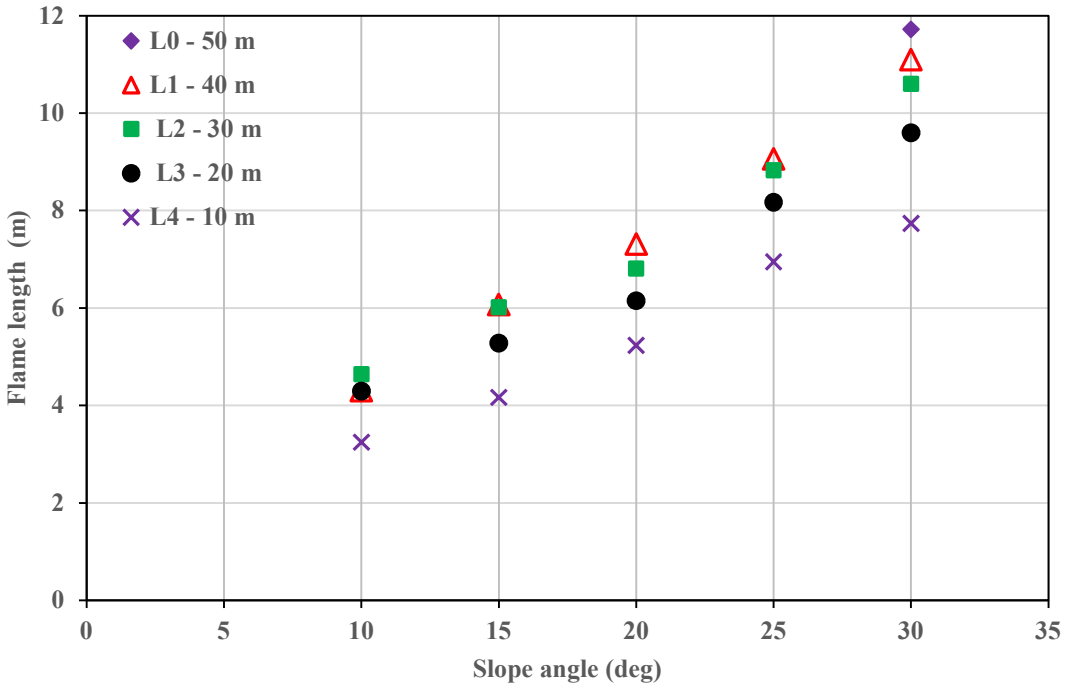

(a) Flame length vs slope angle

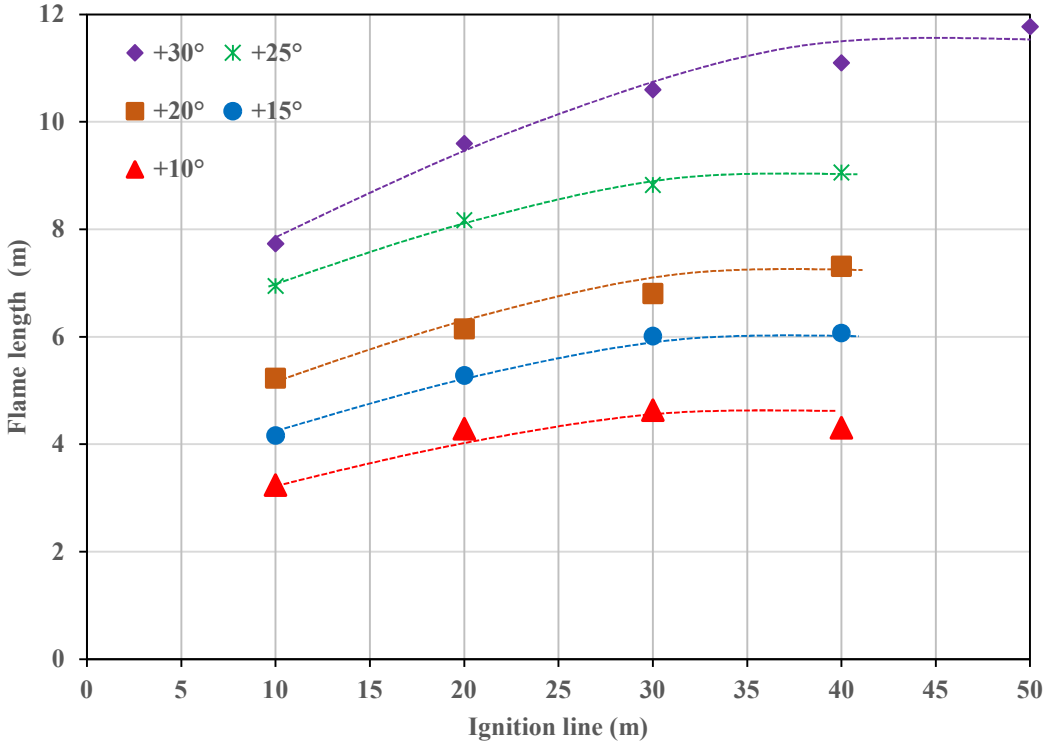

(**b**) Flame length vs ignition line width, at slope angles +10°, +15°, +20°, +25° and +30°

Figure 6.15 – Quasi-steady flame length: (a) flame length vs slope angle for 40, 30, 20 and 10-m ignition lines, and (b) flame length vs ignition line for slope angles of +10° to +30° (the lines are drawn to show the converging nature of values and do not represent goodness of fit).

Comparing the flame lengths (L) among ignition line widths, Figure 6.15(a), for a given slope angle, the flame length increases with ignition line width; however, the difference decreases as the ignition line width increases.

For all four sets, the quasi-steady L value increases by approximately 45–65% for every +10° increase in slope. For a given ignition line width, the flame length increases with slope angle (Figure 6.15(b)). As observed with *RoS* and Q values, the flame lengths reach an asymptotic state for up to +25° slope angle, as shown in Figure 6.15(b). On a +30° slope, a difference of 5% in L values is noted between L1 = 40 m and L2 = 30 m.

In Figure 6.16, flame lengths (L) obtained from this study are plotted against the simulated Q values (from Section 6.1.3.5).

Figure 6.16(a) shows the flame length L vs fire intensity Q for the four ignition lines. For all simulations, the flame length increases with intensity, as shown in Figure 6.16(a). In Figure 6.16(b), the simulated L values are shown against the simulated Q values.

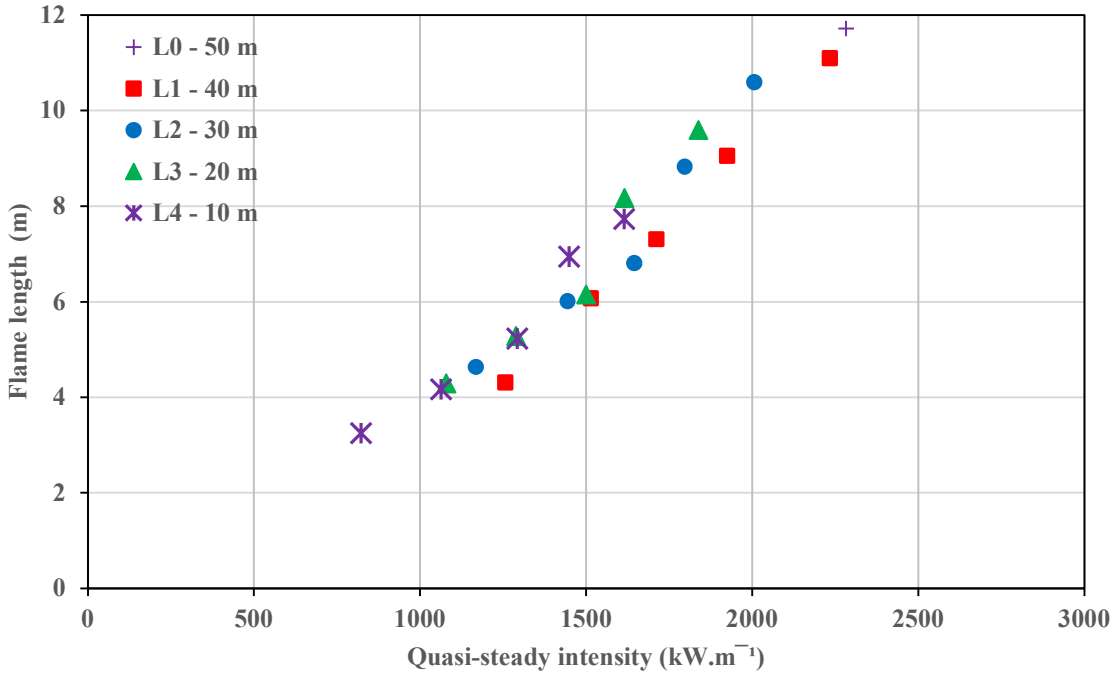

(a) L vs Q for 50, 40, 30, 20 and 10-m ignition lines

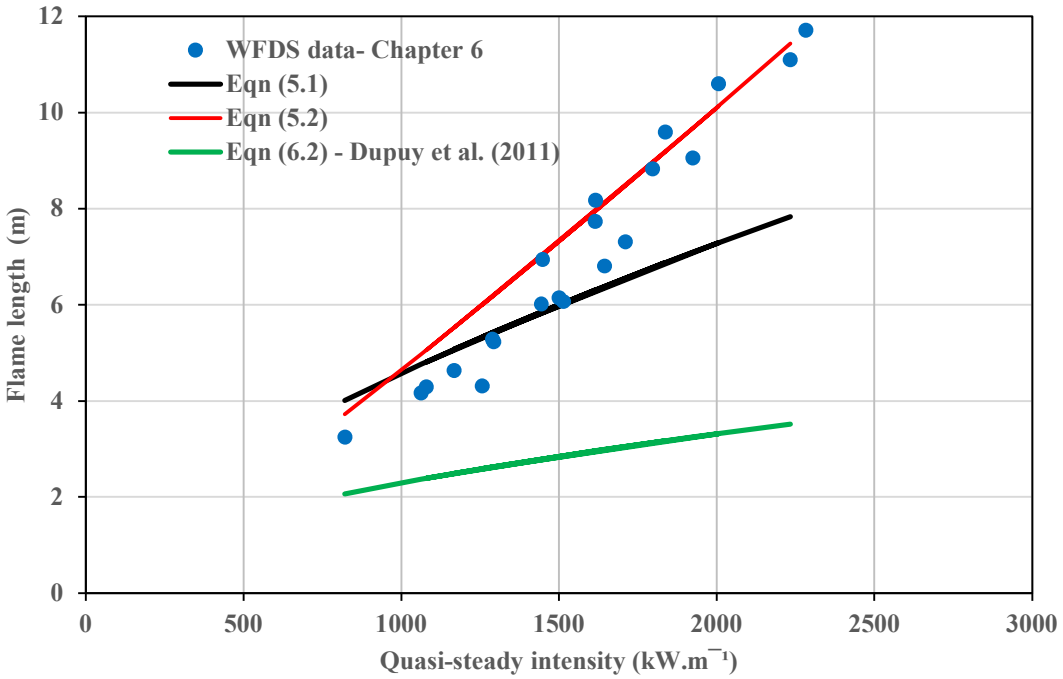

(b) All simulated *L* values vs *Q*

Figure 6.16 – Flame length *(L)* in relation to fire intensity *Q*: (a) flame length vs intensity for all ignition line widths, and (b) all simulated *L* values against *Q* values, plotted with power-law relationship.

The empirical correlation of Anderson *et al.* (1966) for Douglas-fir slash (given as eqn. 5.1 in Chapter 5) matched best with the lower wind velocity cases presented in Chapter 5 (section 5.3.6.). The power-law relationship obtained from the simulated *L* values from this study for lower wind velocity cases were also presented in Chapter 5 (Section 5.3.6), as eqn. 5.2.

In Figure 6.16(b), the results obtained using Eqns 5.1 and 5.2 are presented for all four sets of simulations. eqn 5.2 is valid for the simulations presented in this chapter as well, and eqn 5.1 (empirical correlation of Anderson *et al.* (1966)) is also found to be reasonably in agreement to the simulated *L* values, as observed in Chapter 5.

As mentioned previously, Dupuy *et al.* (2011) analysed flame geometry along with fire isochrone progression, and rate of fire spread in their experimental studies conducted with varied fuel bed

sizes and slope angles. They analysed their experimentally obtained flame length values against intensity and developed a *Q–L* relationship, which is presented as eqn (6.2).

$$L = 0.059\, Q^{0.53} \tag{6.2}$$

Whilst the equation of Dupuy *et al.* (2011) also shows a power-law relationship, eqn (6.2) considerably underpredicts flame lengths (see Figure 6.16 (b)). The difference may be attributed to the fuel type, the scale of the experimental study, and uncertainty in experimental measurements.

The majority of the correlations found in the literature between flame length *L* and *Q* are power-law relationships, where the constant and exponent values are determined from a fit to the data. The simulated flame length results replicate the power-law relationship, and hence we hypothesise that the physics governing flame length appears to be represented sufficiently well.

6.2 Sloped terrain with varied ignition fire line, and constant grass plot size

In this section, grassfire propagation on sloped terrain with varied ignition line widths is investigated, however, keeping the burnable grass plot size constant. The simulations are performed to analyse fire isochrone progression and to further investigate the effect (if any) of these differences on the *RoS* in contrast to the discussions in Section 6.1, in which the grass plot widths were reduced in line with ignition fire line widths.

Two new sets of simulations are conducted with 30, 20 and 10-m ignition fire lines, maintaining the burnable grass plot size of 80 × 40 m. The simulations are conducted at a driving wind velocity (U_{10}) of 1 m.s^{-1}, with a 1-m deep ignition fire line. The simulations are performed at upslope angles of +15° and +20° and are represented as L5, L6 and L7 in the discussions (see Table 6.2). Section 6.1 (Figure 6.7(b)) demonstrated that the *RoS* values for slope angles +15° and +20° clearly reached an asymptotic/convergence state and therefore, only +15° and +20° are analysed in this section to compare *RoS* results between the two scenarios.

Table 6.2: List of Simulations

Slope angle	Simulations			
		L5	**L6**	**L7**
	Burnable grass plot	80 × 40 m	80 × 40 m	80 × 40 m
	Ignition fire line width	30 m	20 m	10 m
+15°		√	√	√
+20°		√	√	√

Figure 6.17 represent the model set-up for L6 with a burnable grass plot size of 80 × 40 m and ignition line widths of 20 m. The model set-up for L5 and L7 are shown in Appendix A, Figure S6.7.

The same thermo-physical, pyrolysis and combustion parameters as shown in Table 5.2 (Chapter 5, Section 5.2) are used for these three sets of simulations.

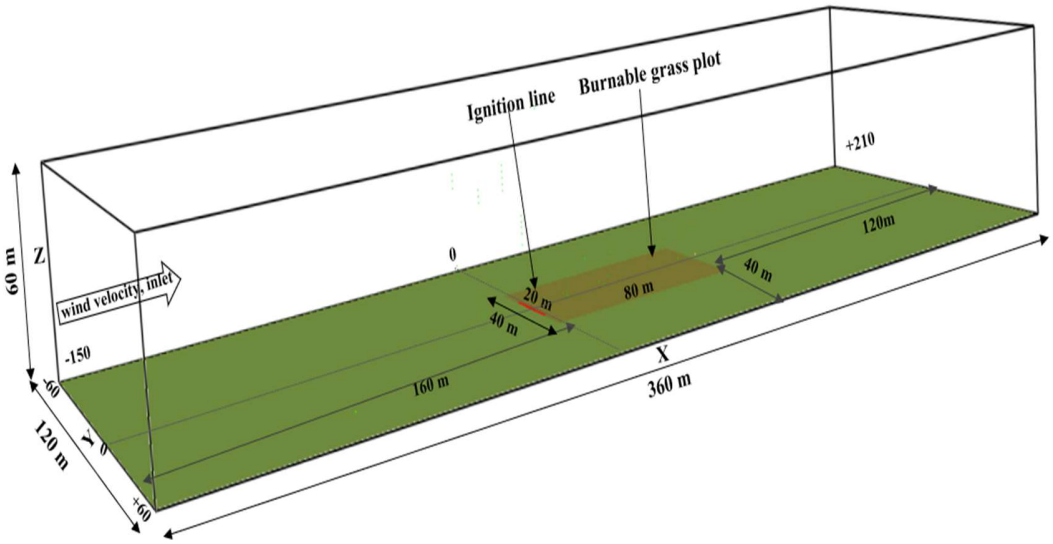

Figure 6.17 **–** The geometry of the domain used in simulation set L6: ignition line width 20 m, burnable grass plot 40 m wide and 80 m long (dark green shaded region).

6.2.1 Results and discussions

The fire isochrones, location of the fire front and *RoS* are analysed and the results are presented in the following sections

6.2.1.1 Progression of isochrones

The fire isochrones from the three sets of simulations (L5 = 30 m, L6 = 20 m and L7 = 10 m – varied ignition line widths, but the same grass plot size) are presented. The results are then compared with the equivalent simulations (L2 = 30 m, L3 = 20 m and L4 = 10 m – varied ignition line widths and grass plot width reduced in line with ignition line) discussed in Section 6.1.3.1

The isochrones of fire progression as a function of time for the three sets of simulations (L5, L6 and L7) are presented in Figure 6.18, along with the isochrone results from the equivalent simulations (L2, L3 and L4), for +15° and +20° slopes. For the same ignition line widths, the contours are extracted at the same time and are shown at an identical scale to obtain a clear view.

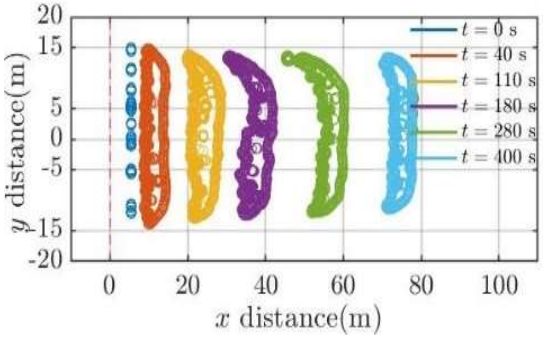

(a) 30 m (L2) - 30 × 80 m grass plot

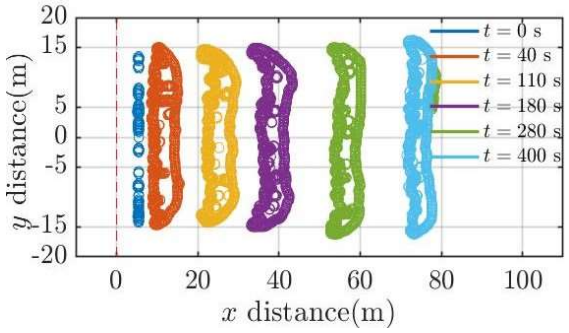

(b) 30 m (L5) - 40 × 80 m grass plot

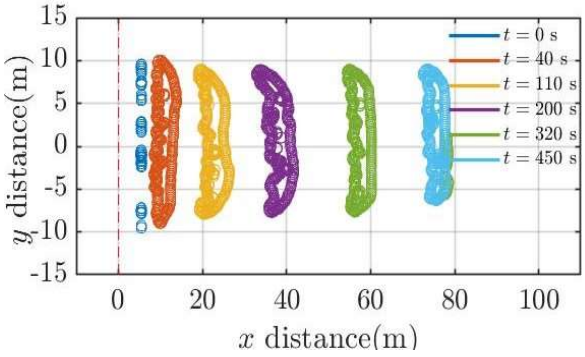

(c) 20 m (L3) - 20 × 80 m grass plot

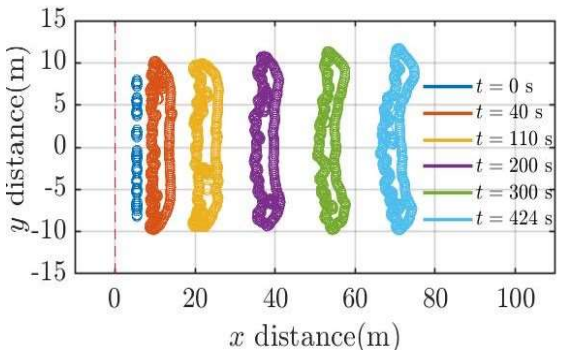

(d) 20 m (L6) - 40 × 80 m grass plot

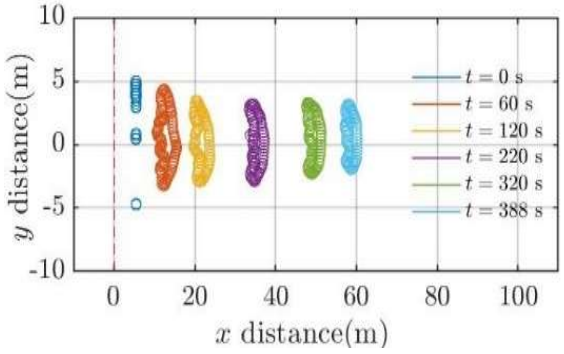

(e) 10 m (L4) - 10 × 80 m grass plot

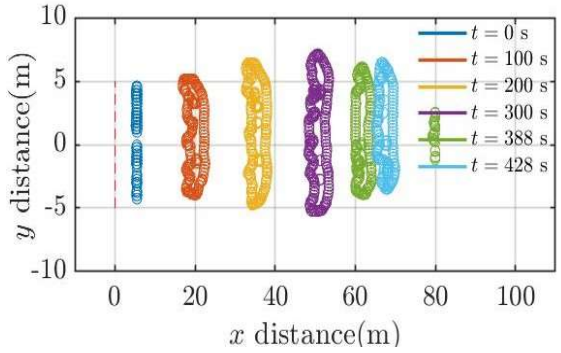

(f) 10 m (L7) - 40 × 80 m grass plot

Frames (a–f): Progression of isochrones at +15° slope

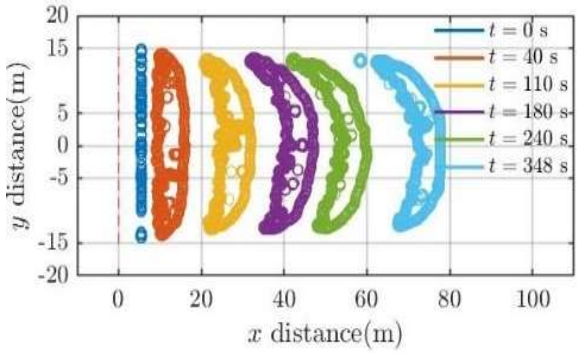

(g) 30 m (L2) - 30 × 80 m grass plot

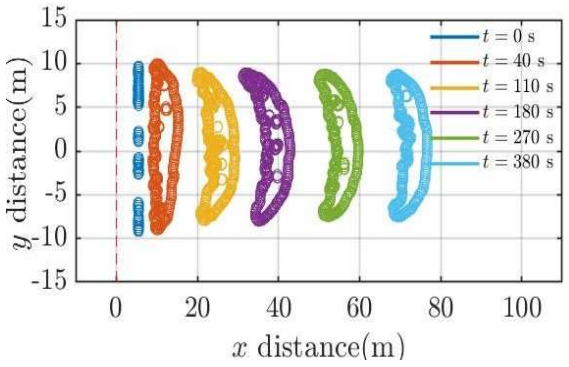

(h) 20 m (L3) - 20 × 80 m grass plot

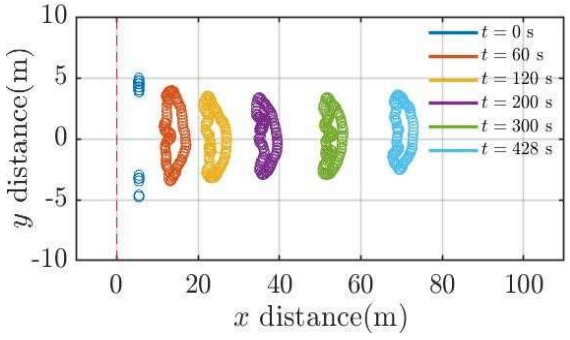

(i) 10 m (L4) - 10 × 80 m grass plot

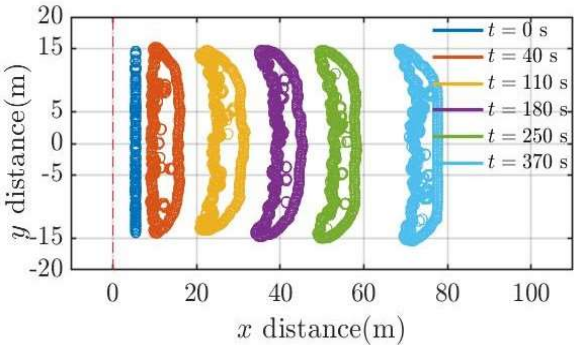

(j) 30 m (L5) - 40 × 80 m grass plot

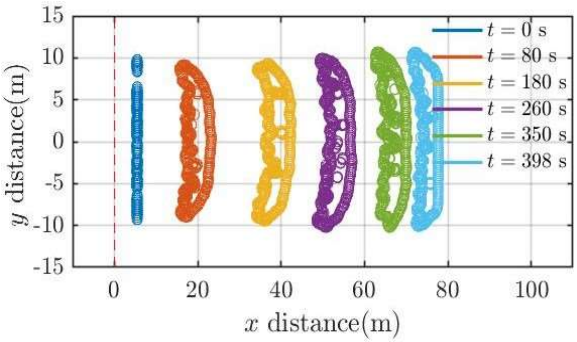

(k) 20 m (L6) - 40 × 80 m grass plot

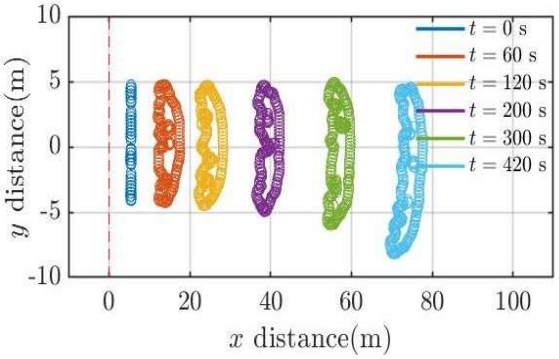

(l) 10 m (L7) - 40 × 80 m grass plot

Frames (g–l): Progression of isochrones at +20°

Figure 6.18 – Progression of isochrones cofor varying ignition line lengths L2, L3, L4, L5, L6 and L7: (a–f) for +15° and (g–l) for +20°.

Comparing the two scenarios (varied and constant grass plot widths), for the respective ignition fire line widths, the fire contour generally demonstrates similar progression patterns. However, for L5, L6 and L7 simulations (Frames (d–f) and (j–l)), as the fire progresses, the isochrones become elongated and the fire front becomes wider than the ignition fire line. This is more visible in the shorter ignition line cases (L6 and L7) for both slope angles +15° and +20°. For the 20-m ignition line (Frames (e) and (k)) as the fire progresses, the length of the contour becomes slightly more than 20 m, whereas for the equivalent simulation L2 (Frames (b) and (h)), as the fire progresses, the fire front length decreases gradually (less than 20 m). A similar pattern is noted for the 10-m ignition line cases L7 (Frames (f) and (l)), where the fire front length increases and exceeds 10 m as the fire progresses (in Frame (f), when the fire front reaches about 50 m and for Frame (l) at about 70 m).

6.2.1.2 Fire front locations and *RoS* calculation

Figure 6.19 shows the temporal fire front locations, determined from the boundary centreline temperature as the fire moves through the grass plot, for simulation sets L2, L3, L4 (ignition line and grass plot with the same width) and L5, L6 and L7 (varied ignition line width, constant grass plot size). Fire front locations against time for +15° cases are presented in Figure 6.19(a) and for +20° in Figure 6.19(b).

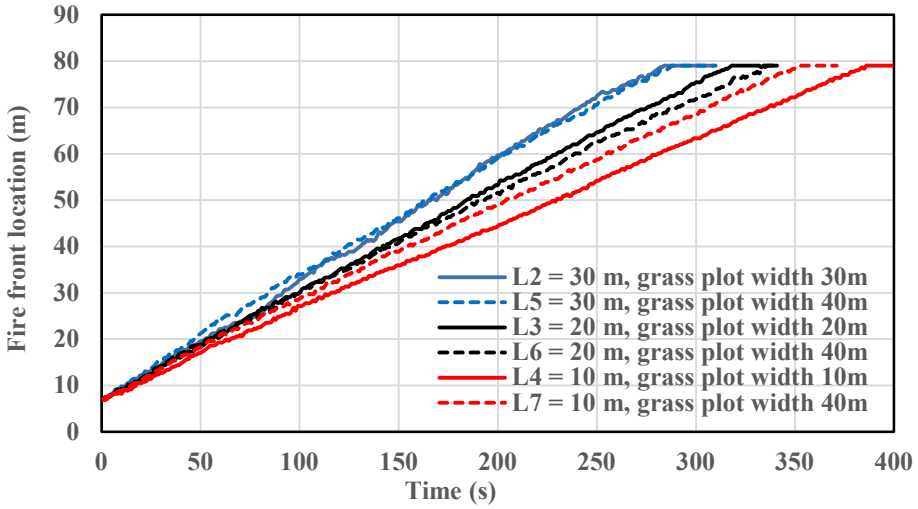

(a) +15°

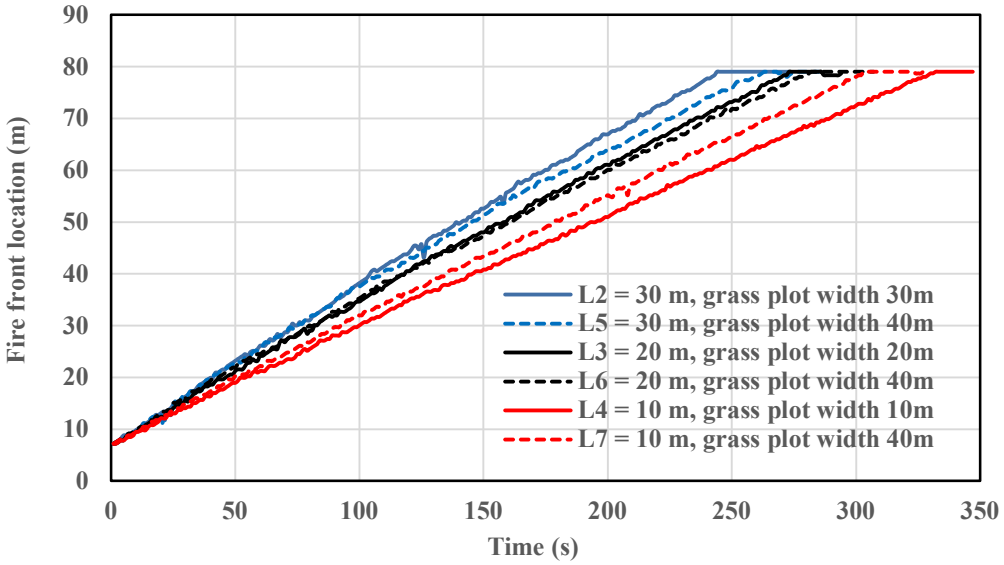

(b) +20°

Figure 6.19 – Fire front location vs time for simulations L2, L3, L4 (ignition line and grass plot with the same width) and L5, L6 and L7 (varied ignition line width, constant grass plot size): (a) +15° and (b) +20°.

At any given time, for +15° and slope, the fire front for L2 and L5 cases (30-m ignition lines) and for +20° slope, L5 and L6 cases (20-m ignition lines) progresses at nearly the same pace. However, with the ignition line length 10 m (L4 and L7 cases), the fire front for L7 travels a bit faster as the time progresses (at a given time after 150 s, the fire front for L7 travels approximately 5-7 m ahead of that of L4), than for L4 cases (both slope cases). In general, for the shortest ignition line (10 m), the fire front progression is slightly faster when the grass plot is wider than the ignition line; however, for longer ignition lines (30 and 20 m), very minimal difference (notably only towards the end of grass plot for 30 m cases) is noted in fire front progression with a thinner or wider grass plot.

The quasi-steady *RoS* values for each slope case are calculated from the fire front location plots, using the least-squares approximation method (Section 4.4.2.3). A linear fit is applied to the instantaneous fire front location plots (shown in Figure 6.19) at steady state and the slope of each linear fit equation represents the quasi-steady *RoS*. The quasi-steady *RoS* values for both +15° and

+20° slopes for ignition lines of 30 m (L2 and L5), 20 m (L3 and L6) and 10 m (L4 and L7) are shown as a bar chart in Figure 6.20. Set 1 data represent the *RoS* values for +15° and Set 2 data for +20° slopes, respectively.

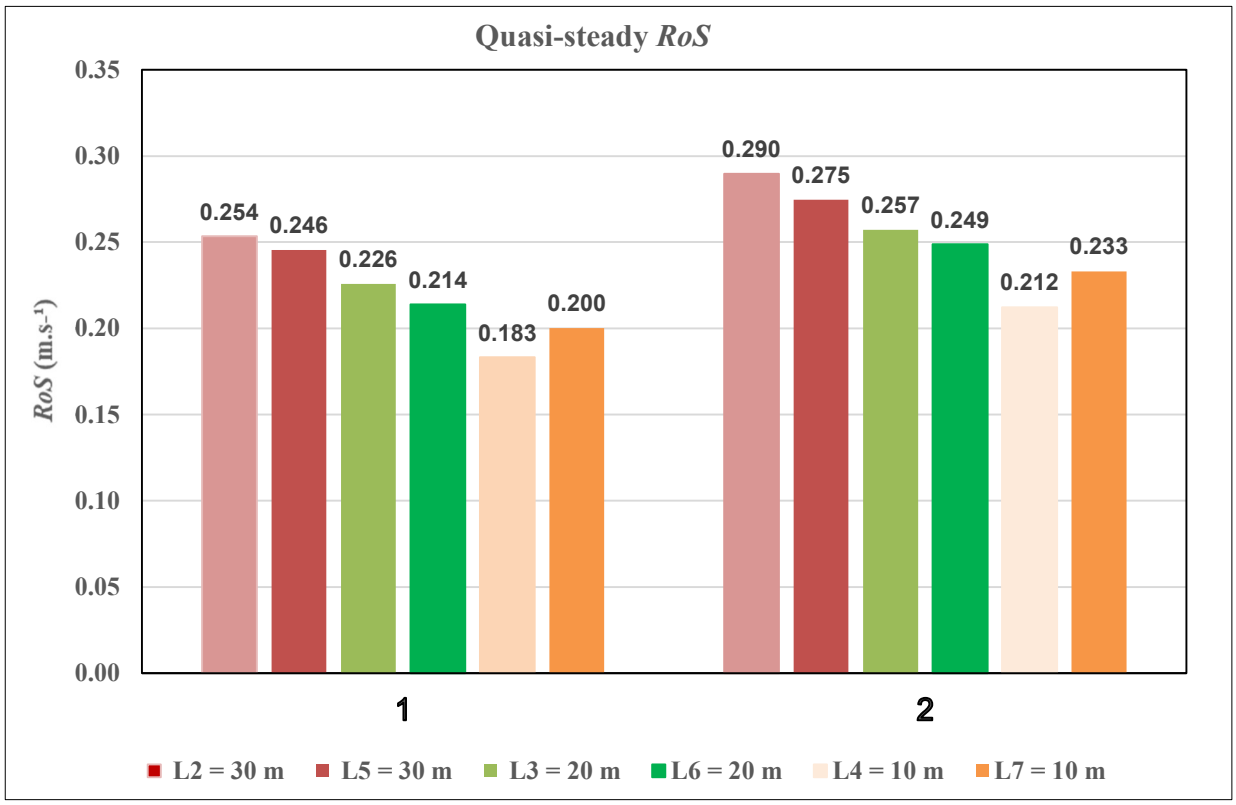

Figure 6.20 – Bar chart showing quasi-steady *RoS* vs slope angle for simulations L2, L3, L4 (ignition line and grass plot with the same width) and L5, L6 and L7 (varied ignition line width, constant grass plot size): Set 1, +15° and Set 2, +20°.

Comparing the quasi-steady *RoS* values for different ignition line sizes, the *RoS* values are nearly the same for wider ignition lines (comparing L2 and L5, and L3 and L6), where the grass plot is of same size as that of ignition line or wider (40 m) than the ignition line. For these cases, comparing the respective ignition lines, the fire fronts move nearly at the same pace (Figure 6.19). However, for the narrow ignition line cases (L4 =10 m and L7 = 10 m), *RoS* values are slightly higher (about 10% higher) for L7 cases (where the grass plot is 10 m wide) compared with L4 cases (where the grass plot is 40 m wide), for both the slope angles. This is consistent with the fire

front location plotted in Figure 6.19. A difference of approximately 9% in *RoS* is noted for both slope angles for the shorter ignition lines (L4 and L7). *RoS* is more sensitive to the grass plot size for the smaller ignition line (10 m). The reason might be, the heat flux ahead of the fire front increases (up to certain limit) as the grass plot width increases compared with the case where the width of the grass plot equals to the fire width. This aspect to be investigated in future studies.

The dynamic *RoS* values for both +15° and +20° slopes for ignition lines of 30 m (L2 and L5), 20 m (L3 and L6) and 10 m (L4 and L7) are plotted in Appendix A, Figure S6.8. As noted in Figure S6.2, the plots show upward and downward spikes in *RoS* values as the fire front moves forward. Comparing the two scenarios, for wider ignition lines (L2 = 30 m, L3 = 20 m where the grass plot width is varied in line with the ignition line and L5 = 30 m, L6 = 20 m where the grass plot width is unchanged), for a given slope angle, generally, in most instances the dynamic *RoS* values are slightly higher for L2 and L3, compared with L5 and L6, though for +20° cases, L5 and L6 surge at few instances than L2 and L3. However, for the narrow ignition line cases (L4 and L7), the dynamic *RoS* values are slightly higher for L7 cases (where the grass plot is 10 m wide) compared with L4 cases (where the grass plot is 40 m wide), for both slope angles. These are instantaneous dynamic values and do fluctuate; despite this, overall, the same trend as for quasi-steady *RoS* is noted.

In general, no significant difference is noted in the *RoS* values when preserving the same grass plot width in contrast to reducing the grass plot width in line with the ignition fire line.

6.2.1.3 Heat Release Rate (HRR) and Fire front length.

The time series of HRR obtained for L5 = 30 m, L6 = 20 m and L7 = 10 m are presented in Figure 6.21, along with the HRR values for L2 = 30 m, L3 = 20 m and L4 = 10 m, which correspond to the same ignition line widths, but with constant and varied grass plot widths, respectively.

As noted in Section 6.1.3.5, the HRR is higher for longer ignition lines for both slope angles. Comparing among the two scenarios – grass plot width reduced (L2, L3 and L4) in line with ignition fire length and fixed grass plot width (L5, L6 and L7) – the HRR values are slightly higher for the cases with a fixed grass plot width of 40 m. As expected, the wider burnable grass plot

releases more heat energy than narrower grass plots. The difference in terms of % or fraction widens as the grass plot width decreases (Figure 6.21(e) and (f)).

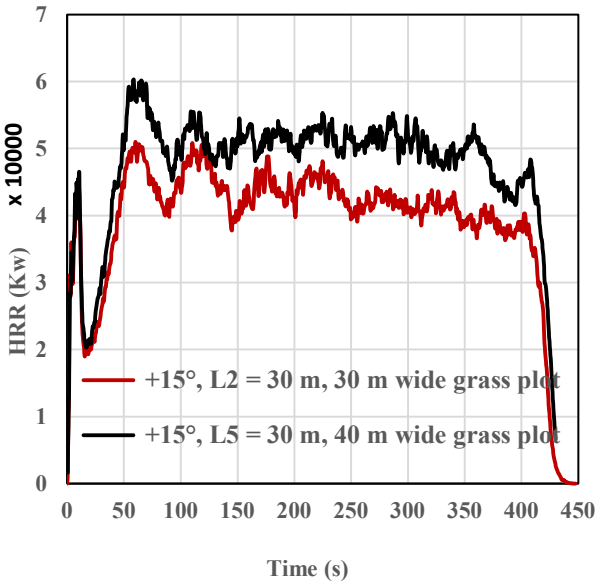

(a) 30 m wide ignition line, +15°

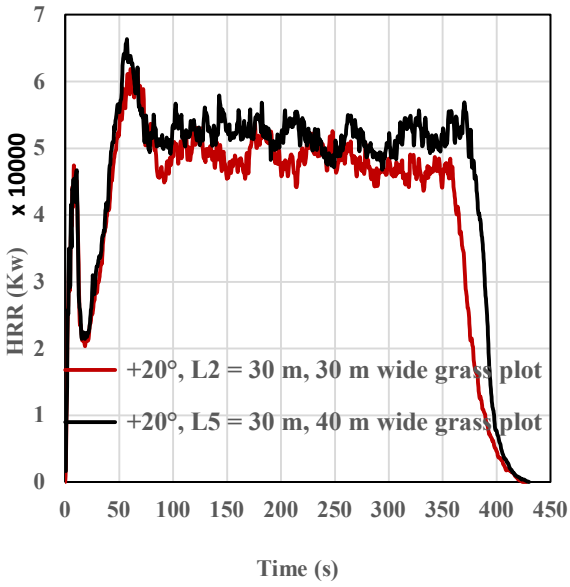

(b) 30 m wide ignition line , +20°

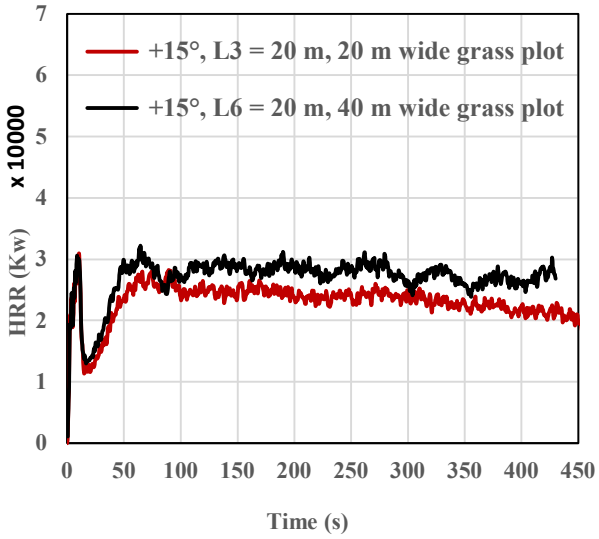

(c) 20 m wide ignition line , +15°

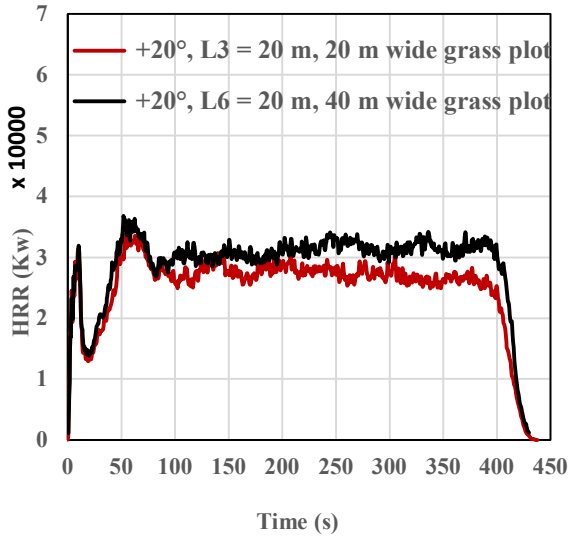

(d) 20 m wide ignition line , +20°

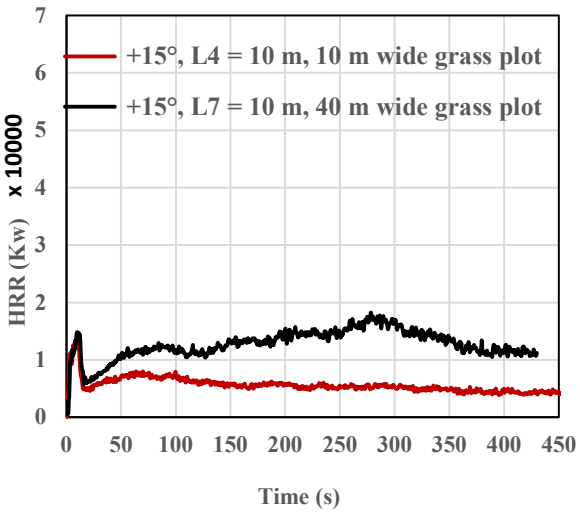

(e) 10 m wide ignition line , +15°

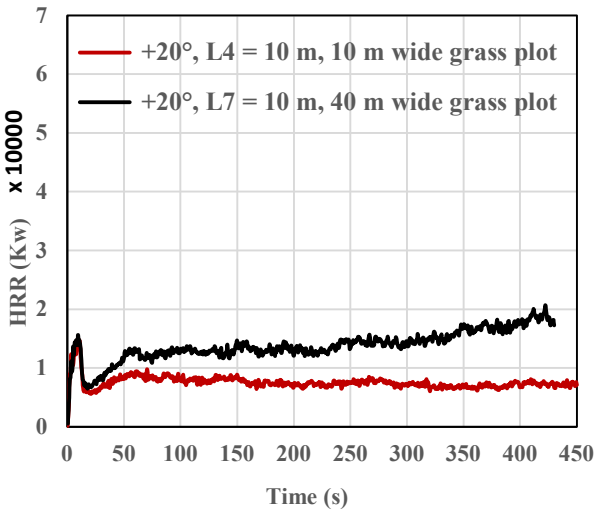

(f) 30 m wide ignition line , +20°

Figure 6.21 – HRR vs time for ignition line widths of 30 m, 20 m and 10 m, for +15° and +20° slope angles.

In Figure 6.22, the measured fire front lengths as a function of time are plotted for +15° to +20° slopes, at varied ignition lines of L5 (30 m), L6 (20 m) and L7 (10 m), preserving the same grass plot width of 40 m. Along with these, the fire front lengths of L2 (30 m), L3 (20 m) and L4 (10 m) – with varied grass plot width in line with ignition fire line – are also plotted for the same slope angles.

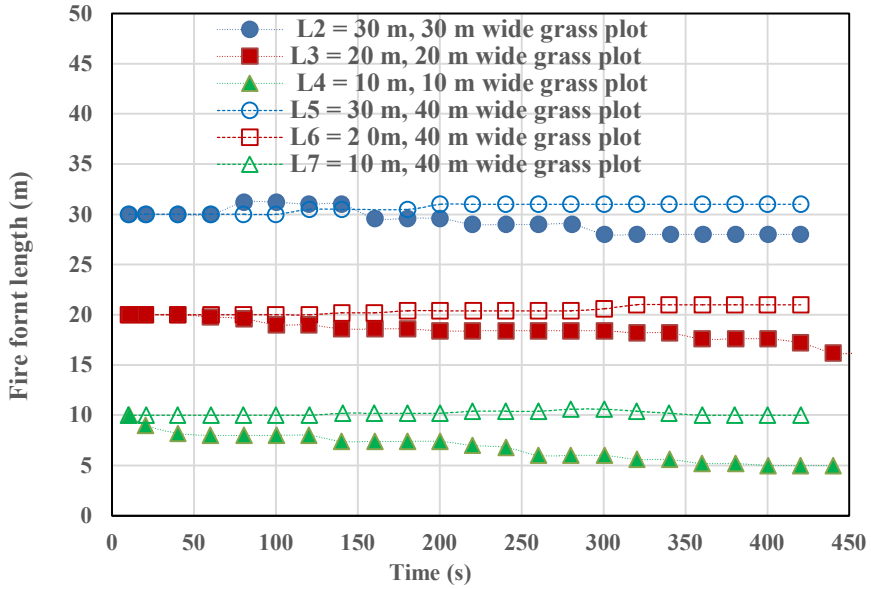

(a) +15°

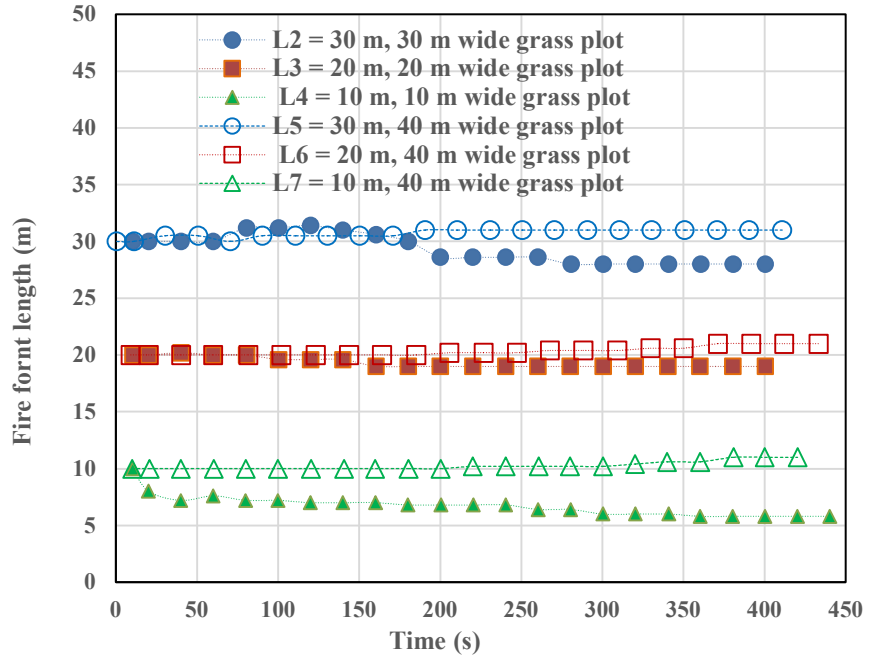

(b) +20°

Figure 6.22 – Fire front length vs time for slope angles with varied ignition lines of 30, 20 and 10 m, for varied and constant grass plot width.

Comparing the two scenarios (varied and constant grass plot widths), as the fire front progresses with time, the fire front gets wider for the large grass plot cases (L5, L6 and L7) compared with the reduced grass plot cases (L2, L3 and L4). For 10 m ignition length, the difference is almost double. This is consistent with the fire isochrones plotted in Figure 6.18, showing that for L5, L6 and L7 simulations, the isochrones become longer than the ignition fire line towards the end of the grass plot.

6.3 *Summary*

This chapter discussed grass fire propagation with varied ignition fire line widths (40, 30, 20 and 10 m) and different upslope angles to assess the effect of varied ignition fire line widths on *RoS* along with other parameters. The simulations were performed at a lower driving wind velocity of 1 $m.s^{-1}$. Two scenarios with varied ignition fire lines were analysed in this chapter: (1) a burnable grass plot width reduced to align with the width of the ignition fire line, and (2) a fixed 40-m grass plot width.

For the first scenario (where grass plot width reduced in line with ignition line width), for all four ignition lines, the contours were found to be sharper for higher upslope angles and more pointed for wider ignition lines. Visually, the fire contour evolution pattern from the simulations was similar to the experimentally observed results of Dupuy *et al.* (2011).

When the ignition line width is the same as the burnable plot, for a given slope angle, the fire front was found to travel more slowly with a narrow ignition line of 10 m compared with wider ignition lines. As a result, fire intensity and flame length are lesser and shorter, respectively. The simulation outcome indicated that results, in terms of *RoS*, fire intensity and flame length, attained convergence at 30 m ignition line width for slope angles up to +25°. For +30° slope, an additional simulation was conducted with 50 m ignition line width and for this slope angle convergence was obtained at 40 m ignition line width. The relative *RoS* results for all four ignition lines demonstrated that WFDS quasi-steady *RoS* values, for up to +20°, are closer to the Rothermel model slope function and WFDS values were lower for +25° and +30° slopes. The experimental

results of Dupuy *et al.* (2011) also showed good comparison with the Rothermel model results for slope angles up to +20°.

For all ignition lines, Byram's intensity was satisfied with ~41% fuel load consumed for all slope angles, as for the result obtained with lower wind velocity cases presented in Chapter 5 (where +30° slope was an outlier). As noted in Chapter 5 for lower wind velocity cases, the empirical correlation (power-law) of Anderson *et al.* (1966) was found to be closer to the simulated flame length (*L)* values; however, we observed that the power-law relationship of Dupuy *et al.* (2011) considerably underpredicted the flame lengths.

Comparing the two scenarios (varied and constant grass plot widths), the fire contours generally demonstrated a similar progression pattern; however, for the constant grass plot cases, the isochrones became elongated as the fire progressed and became slightly wider than the ignition fire line towards the end of the grass plot. It was observed that, for the narrow ignition line (10 m), the fire front was faster when the grass plot was wider than the ignition line. Significant differences were also observed for HRR and instantenous fire front length. However, for the wider ignition lines (30 and 20 m), the differences reduced considerably. Generally, no significant difference was noted in the *RoS* values with constant grass plot width in contrast to the result for grass plot width reduced in line with the ignition fire line.

Chapter 7. Summary and Conclusions

7.1 Introduction

A comprehensive study has been conducted to investigate the combined effect of slope (both upslopes and downslopes) and wind on grassfire propagation and associated behaviour through a set of simulations performed using a physics-based wildland fire model. The overarching objective of this study is to improve the understanding of fire spread in grassland and thereby provide insight into and improvement to current empirical models used for fire behaviour prediction, so that risks and losses associated with bushfires can be reduced.

The contributions to knowledge are,

- This study benefits the research community in developing an understanding of the physics involved in grassfire propagation on sloped terrain under the influence of driving wind.
- provide a comparison of results obtained from this study with existing empirical correlations to evaluate the adequacy of the empirical models which are often developed from experiments conducted at laboratory scale and under benign conditions;
- provide a base for the improvement of current operational models that are used by fire and emergency services for fire behaviour prediction.

The above can subsequently help in developing improved strategies and fire management planning, thereby lowering the risks of wildfire impacts.

7.2 Modelling

The simulations were conducted using the physics-based model Wildland–urban interface Fire Dynamics Simulator (WFDS). The model reliability and accuracy evidence presented in this study and references provided by other studies (Sánchez-Monroy *et al*. 2019, Moinuddin *et al*. 2021) demonstrated that the WFDS model is a reliable research tool that can be applied to study the combined effects of wind and slope on fire propagation in a vegetative fuel bed. In this study, we considered a particular grass type, kerosene grass (represented by specific thermo-physical properties recorded in Tables 4.1 and 5.2 for specified simulation sets) with fixed fuel bed

conditions (fuel load, bulk density and fuel height). Thus, caution needs to be taken in interpreting the results for a wider range of grass species.

A systematic modelling approach was used in this study. This research was performed in a number of phases that commenced with a convergence study that ensured the results were ignition intensity-independent, and grid- and domain-converged. This was followed by model implementation, where we made certain that the atmospheric boundary layer upstream of the burnable grass plot was properly established prior to igniting the fire line. In the second phase, simulations were performed with driving wind velocities of 12.5, 6 and 3 $m.s^{-1}$ with varied slope angles of –30° to +30°, typically on a burnable grass plot of 80 m × 40 m. Simulations with higher upslope angles (+30°, +25° at 12.5 $m.s^{-1}$ and +30° at 6 $m.s^{-1}$) were repeated with an extended burnable grass plot length, ensuring better quasi-steady state results were obtained over a longer period. The *RoS*, head fire width, fire isochrones and location of the fire front, fire intensity, mode of fire propagation, flame dynamics, flame length and heat flux parameters were analysed. *RoS* results were then compared with the results obtained from empirical modelling studies.

In the following phase, simulations were performed with lower driving wind velocities of 0.1 and 1 $m.s^{-1}$ with varied slope angles. The same parameters were analysed and *RoS* results were compared with empirical modelling studies, as well as collated with the results obtained from the higher wind velocity cases. Additionally, two sets of simulations were performed for upslope angles at 1 $m.s^{-1}$ wind velocity, with increased domain size and changed fuel parameters, respectively. The changed fuel was lighter and had a lower FMC, and a higher atmospheric temperature and lower RH were also used. Therefore, it was termed a 'lighter' fuel. We then investigated the fire isochrone progression, fire intensity, fire front locations and *RoS* for these two different scenarios and examined the effect of these variations, particularly on the *RoS.* In the final phase of this study, further simulations were conducted for upslopes at 1 $m.s^{-1}$ with varied ignition fire line widths to examine the effects of varying ignition fire line width on fire isochrone progression, *RoS*, fire intensity and flame length, and we qualitatively compared the findings with experimentally observed results from the literature.

7.3 Conclusions

This section provides a summary of the main findings from this study investigating the combined effect of slope and wind on grassfire behaviour. As mentioned earlier, in this study, we considered a particular surface fuel type with specific thermo-physical properties (presented in Table 4.1 and Table 5.2; some of the fuel characteristics were changed for lower wind velocity cases). Again, these simulations represent an idealised scenario and are at a much smaller scale compared with real wildfire scenarios. Therefore, caution needs to be taken in applying these results for a wider range of grass species and for very large-scale wildfires.

7.3.1 Progression of isochrones and pyrolysis width

The instantaneous temperature contours or fire isochrones (representing the development of the fire) were determined from time-averaged boundary temperature outputs. With increased slope angle, the fire front became wider and reached the end of the burnable grass plot earlier. Comparing among wind velocities, for the same slope angle, with increased wind velocity, the fire front travelled more quickly and reached the end of the burnable grass plot earlier. This was expected behaviour, whereas the fire isochrones moved very slowly for steep downslopes, especially at 3 $m.s^{-1}$ wind velocity.

At lower wind velocities of 0.1 and 1 $m.s^{-1}$, the isochrones showed an inward shape or concave pattern at lower slope angles and often did not attain a convex curvature, in contrast to those observed with higher wind velocities, and as the slope angle increased, the contours evolved into a more pointed convex curve. Again, for lower wind velocities (0.1 and 1 $m.s^{-1}$ and steep downslopes at 3 $m.s^{-1}$), the fire isochrones did not progress for downslopes. In these cases, the fire eventually extinguished because of lower wind enhancement in steep downslope scenarios. Another possibility for extinguishment is due to approximations made in the derivation of the boundary fuel model. These approximations make the model more consistent with conditions in which the flame leans over unburned vegetation. Other reasons for extinguishment may be the physical parameters of the fuel, such as fuel height, fuel load and its thermo-physical properties.

In Chapter 5, we did not observe any notable variations in fire isochrone patterns between the 'original' and 'changed' domain sizes. With the 'lighter' fuel characteristics (with the same driving wind velocity and domain size), generally, the fire isochrones demonstrated similar progression patterns; however, a slightly more convex curvature was noted for the isochrones obtained with 'lighter' fuel parameters.

When the fire isochrones were compared for varied ignition fire line widths (Chapter 6) – with the grass plot width also reduced to match with the ignition fire line width – for higher upslopes, the contour pattern appeared to be more pointed with increased ignition line width. The fire isochrone shape was influenced by the slope and a more pointed shape was noted from +25° slope for wider ignition lines. Overall, the fire contour evolution pattern from the simulations was similar to the experimentally observed results of Dupuy *et al*. (2011), despite the geometry, boundary conditions, size of fuel bed and fuel type being different from the experimental study.

In Chapter 6, we also compared the fire isochrone progression for two different grass plot scenarios: (1) the burnable grass plot width reduced to align with the width of ignition fire line, (2) the burnable grass plot size preserved while the ignition fire line width varied. With the constant grass plot size scenario, as the fire progressed, the isochrones became elongated and fire front became slightly wider than the ignition fire line.

The pyrolysis width (or head fire width) increased with driving wind velocity and slope angle. Like the fire isochrones pattern, the increased domain size (with the same driving wind velocity and fuel characteristics) had an insignificant effect on the pyrolysis width. However, when quasi-steady state widths were plotted against slope angle, a thinner pyrolysis width was noted with the isochrones obtained for 'lighter' fuel. As expected, the fuel characteristics (increased ambient temperature with reduced fuel moisture content, relative humidity and fuel load) affected pyrolysis width. A second-order polynomial relationship was observed between the pyrolysis width and slope angle for higher driving wind velocities (Chapter 4), whereas the relationship was closer to exponential for lower wind velocities (Chapter 5).

7.3.2 Dynamic *RoS*, fire front locations and *RoS* calculations

For all driving wind velocities, we observed evidence of dynamic fire behaviour when the instantaneous *RoS* (obtained by differentiating the fire front location data) was plotted as a function of time. Additionally, the quasi-steady *RoS* values for each case were obtained by applying a least-squares approximation method (with a linear regression formula) to the respective fire front location plot.

For each of the wind velocities, besides the quasi-steady *RoS* values, dynamic maximum, minimum and average (of all instantaneous values) *RoS* were determined. The maximum and minimum dynamic *RoS* values are used as whiskers (i.e. upper bound and lower bound) to present uncertainty to the averaged *RoS* values. These *RoS* values were then compared with empirically derived values (along with slope correction factors) from MKIII, MKV and CSIRO models. In these models, slope correction is multiplied by the atmospheric factor. Comparisons were also made with the Rothermel (Original and Modified) models where slope correction is additive to the atmospheric factor.

Firstly, in Chapter 4, we analysed the quasi-steady *RoS* vs wind velocity results of this study for flat terrain (no slope) and found them to be comparable with the quasi-steady *RoS* obtained from the WFDS simulations of Moinuddin *et al.* (2018) for flat terrain. The *RoS* values were then compared with empirically derived *RoS* values for flat terrain. Overall, the results of the physics-based simulations at different wind velocities with no slope agreed within 5–65% with different empirical models (the highest difference was noted for 3 $m.s^{-1}$ when compared with the MKIII model). As mentioned above, the empirical models were often developed from experiments conducted at laboratory scale and under benign conditions as well as with different types of grass species.

Following this, in Chapter 4, we analysed the *RoS* results for higher driving wind velocities (12.5, 6 and 3 $m.s^{-1}$) with varied slope angles (–30° to +30°) and compared the results with empirically derived slope-corrected *RoS* values. Overall, except for higher slope-corrected Australian model values at 12.5 $m.s^{-1}$ for >+15°, slope-corrected CSIRO values at 6 $m.s^{-1}$ for >+15° and at 3 $m.s^{-1}$ for ≥+30°, all empirical values were found to lie between dynamic minimum and dynamic

maximum *RoS* values for all three driving wind velocities. In those exception cases, the dynamic maximum and in other cases quasi-steady *RoS* values were closer to different empirical model values. On downslopes, dynamic minimum values were closer to slope-corrected MKIII and MKV values and quasi-steady *RoS* values at 6 $m.s^{-1}$ were closer to CSIRO values.

Thereafter, in Chapter 5, we analysed the *RoS* values for lower wind velocities (0.1 and 1 $m.s^{-1}$) and compared them with empirical model values. For 0.1 $m.s^{-1}$ wind velocity, the quasi-steady and dynamic averaged *RoS* values were found to be closer to slope-corrected MKIII and CSIRO models as well as to both the Rothermel model values. For 1 $m.s^{-1}$, the WFDS *RoS* values were closer to slope-corrected MKIII, Rothermel Original and Modified models for slope angles up to +25° (and slightly lower for +30°).

Comparing among the wind velocities, for a given slope angle, *RoS* values with lower wind velocities were lower; however, the difference narrowed with increase in slope angle. With a significant driving wind velocity and the dynamic nature of fire propagation, the trend between quasi-steady *RoS* and slope angles for higher wind velocities fitted to a second-order polynomial relationship better; however, the relationship for 3 $m.s^{-1}$ could also be developed as exponential. With reduced wind velocities (0.1 and 1 $m.s^{-1}$), an exponential relationship was observed between the quasi-steady *RoS* and slope angle. This is consistent with the exponential relationships reported in most of the experimental studies conducted with no or very low wind speeds.

The confidence bounds around the averaged *RoS* estimates (by fitting error bars onto the WFDS quasi-steady *RoS* data for all cases, at all five wind velocites) were presented as a second method to demonstrate uncertainty estimates. Generally, the slope-corrected empirical model values for most of the slope angles at higher wind velocity cases were found to be outside the error bar range, and at lower wind velocity cases (with original fuel parameters), the error bar encapsulated most of the slope-correct empirical model values (except MKV values at both the velocities and CSIRO values at 1 $m.s^{-1}$).

Furthermore, for all wind velocities, we analysed the relative *RoS* values (*RoS* on any slope divided by *RoS* on a reference slope) from the simulation results and compared them with those obtained from the following empirical models: Australian slope function (rule of thumb) and Rothermel

model variations. For higher wind velocities, for upslopes, the relative *RoS* values from WFDS were found to be closer to the Rothermel models than the Australian correlations. The Rothermel models under the influence of strong wind showed minimal slope effect. This is due to multiplicative nature of Australian correlations compared with the Rothermel models' additive nature. However, for lower wind velocity cases, the Rothermel models showed a stronger slope effect. The Australian slope correction under lower or near-zero wind velocities was found to be closer to the WFDS quasi-steady results. However, for higher wind velocities, this was not the case. Hence, the Australian empirical models' multiplicative nature in relation to the slope correction factor, especially for upslopes at higher wind velocities, may need serious scrutiny.

In Chapter 5, we observed that the fuel characteristics influenced fire front movement (and hence the *RoS*). At any given time immediately after ignition, the fire front location with 'lighter' fuel parameters was farther by approximately 30–45% than that with original fuel parameters. The quasi-steady *RoS* values showed that the *RoS* from 'lighter' fuel parameters were higher by approximately 57–60% than that from the original fuel parameters.

Comparing among the ignition line widths (Chapter 6), for slope angles ≥ +20°, the fire front propagated more quickly with wider ignition lines (comparing 10 and 30-m ignition lines). For wider ignition lines (30 m and above), generally, *RoS*, fire intensity and flame length do not change for slope angles up to +25°. It represents that convergence is obtained at 30-m ignition line. Similar convergence is obtained with 40-m ignition line for +30° slope. Insignificant differences were noted in *RoS* values for the constant grass plot size scenario compared with varied grass plot sizes (grass plot width reduced in line with the ignition fire line width) except for 10-m ignition line.

The simulations in this study represent idealised slope scenarios with homogeneous fuel beds, which may be different to real fire scenarios with the existence of fuel inhomogeneity, and wind gusts and directional changes. Taking these into account, measurement of quasi-steady values in outdoor experiments is quite challenging (Mell *et al.* 2018; Sutherland *et al.* 2020a). All these can contribute to any observed differences.

7.3.3 Heat Release Rate (HRR) and Fire Intensity

Time series data of HRR was obtained from all simulations for all driving wind velocities. We then derived Byram's fire intensity by dividing the HRR at various times by the fireline length at the same instant in time.

On sloped terrain, the HRR (and hence intensity, Q) increased with driving wind velocity and slope angle when the fuel characteristics were the same. The values were higher for upslopes at any given location. For downslopes, the HRR decreased with increase in downslope angle. A second-order polynomial relationship was found between Q and the slope angle at 12.5 and 6 $m.s^{-1}$ driving wind velocities, whereas for lower wind velocities, the Q–slope relationship could be constructed as linear or exponential. As noted for other parameters, the Q values decreased with 'lighter' fuel characteristics.

In most cases, we found a linear relationship between Q and *RoS*. This was as expected from Byram's intensity relationship for flat surfaces. However, the relationship deviated from linearity at higher upslopes (this varied for different wind velocities). Generally, the Byram intensity (Q = fuel load × heat of combustion × *RoS)* was satisfied with approximately 42% of the fuel load consumed instead of 100% fuel load.

7.3.4 Flame dynamics and mode of fire propagation

To understand flame behaviour, we extracted the flame contour, temperature contour, detachment location and wind velocity vectors, taken through the centreline of the grass plot at various instants in time.

The plume behaviour analyses demonstrated that the plume was more inclined towards the ground at higher upslopes and at increased wind velocities, whereas on downslopes, the plume rose from the ground earlier (Figure 4.20). For higher wind speeds, plume attachment occurred at much lower slope angles owing to interaction between the sloped terrain and the plume itself. The flame dynamics results at higher wind velocities (12.5, 6 and 3 $m.s^{-1}$) indicated that eruptive growth of fires (which may lead to flame attachment) occurs for higher upslope cases (> +20° slopes), which can result in firefighter casualties (Lahaye *et al.* 2018). For lower wind velocities of 1 and 0.1

$m.s^{-1}$, a clearly detached or rising plume was observed for upslopes (Figure 5.16). At any given slope angle, the plume was found to be rising at a much shorter distance from the ignition line compared with higher wind velocity cases.

The flame dynamics demonstrated that for higher wind velocities, the flame and near-flame appeared to be rising, even though the plume was attached (Figure 4.21), whereas for lower wind velocities (Figure 5.17), the flame as well as the plume appeared to be detached or up-rising. The flame was more vertical at lower slope angles and became deeper/wider as the slope angle increased. Overall, we found similarities with the results of Dold and Zinoviev (2009) and Sharples (2017).

In the simulations conducted in this study, the Byram number (N_c) analysis demonstrated that, for lower wind velocities (3, 1 and 0.1 $m.s^{-1}$), fire propagation upslope was clearly within the plume or buoyancy-dominated regime; however, for higher wind velocities, it was difficult to characterise the near-surface flame dynamics when wind velocity at 2 m (U_2) was used in the Byram number calculation in place of velocity at 10 m (U_{10}). With higher wind velocities, flame behaviour could be different from the overall plume behaviour and the Byram number based upon U_{10} captured plume behaviour, not the flame behaviour.

When the fire propagated upslope, flame length was found to be higher with the flame attached to the ground. For a given slope angle, flame length increased with driving wind velocity. However, the flame length was lower for simulations conducted with 'lighter' fuel characteristics, indicating that 'lighter' fuel characteristics and different atmospheric conditions influenced flame length. For all wind velocities, the flame lengths obtained from this study were found to be reasonably in agreement with the values predicted by the empirical model proposed by Anderson *et al.* (1966). Additionally, a power-law correlation was found to exist between the simulated flame length and fire line intensity, which is in broad agreement with the correlations in the list of empirical models presented in Alexander and Cruz (2012, 2021) and Barboni *et al.* (2012).

7.3.5 The heat fluxes

The convective and radiative heat flux boundary data obtained from the simulations was analysed to understand the role of these heat transfer modes on sloped terrain with varied driving wind velocities. The heat flux contours showed that convective heat flux is the leading heat transfer mechanism for predominantly wind-driven fire propagation. The convective heat fluxes were more significant for higher upslopes in wind-driven fires. However, for lower wind velocities (1 and 0.1 $m.s^{-1}$), where largely buoyancy-driven fire propagation occurred, for higher upslopes > +20°, the radiative heat fluxes were found to lie ahead of the convective heat fluxes as the fire front moves through the burnable grass plot.

Both the total convective and radiative heat flux values increased with slope angle as well as with driving wind velocity. For higher wind velocity cases, for a given slope angle, the total surface radiative heat fluxes were higher than convective heat fluxes. However, the difference between the fluxes narrowed as the wind velocity decreased and both fluxes were found to be equally significant at lower wind velocities. For lower wind velocities and for higher slopes of +25° and +30°, the total convective heat fluxes were found to be higher than the radiative heat fluxes. This finding is consistent with Sánchez-Monroy *et al*. (2019), who reported that for no-wind conditions on slopes above +30º, the convective heat flux is larger. This reinforced the finding that at lower wind velocities, the convective heat flux is more significant at higher slope angles. The same trend was noted when the heat fluxes were compared for 'lighter' fuel characteristics. For the lower wind velocity of 1 $m.s^{-1}$, at +30° slope, the convective heat flux was approximately 20% higher than the radiative heat flux for both the 'original' and 'lighter' fuel parameters.

7.4 Recommendations for future Studies

In the simulations conducted, we noted that the fire did not propagate for steep downslopes at lower driving wind velocities. In these cases, the fire eventually extinguished, and possible reasons have been provided. With improved computational power, the Fuel Element (FE) vegetation sub-model (which needs finer grids to solve the heat transfer between gas and solid phase in a bulk fuel bed) could be used in future studies to investigate this aspect.

Again, for future studies, the Arrhenius thermal degradation sub-model could be used, which requires significantly more user-supplied parameters, where the mass loss occurs at higher temperatures and a finer computational gird. The Arrhenius sub-model works better than Linear with the FE vegetation model.

With the simulated grass plot size, we noted that for higher wind velocities with steep upslopes, the fire travelled more quickly and reached the end of burnable grass plot swiftly. In future studies, with the provision of higher computational resources, we propose to increase the burnable grass plot size (both in lateral and longitudinal directions) to ensure better steady-state results are obtained with the fire progressing for a longer period. The present study is limited to a maximum wind velocity of 12.5 $m.s^{-1}$. In future work, higher wind velocities along with increased domain and grass plot sizes may be explored, representing a more realistic wildfire situation.

The sensitivity to fuel load and fuel height on flat surface was previously investigated by Moinuddin *et al*. (2018, 2021), which we have followed in this study. A detailed sensitivity analyses with different fuel load and fuel height on slope senario could be a subject of future study.

Based on the results from this study and future studies, an improved understanding of combined wind and slope effects can be developed for the operational models. This can be done through improved and refined models for *RoS*, fire intensity and flame length as a function of atmospheric conditions, slope and fuel conditions. In addition, trigger conditions for eruptive fire behaviour can be developed with the ultimate goal of improving resilience to wildfires.

8. REFERENCES

Abu Bakar A. (2015). PhD Thesis report: "Characterization of Fire Properties for Coupled Pyrolysis and Combustion Simulation and their Optimised Use", Victoria University, College of Engineering and Science, Australia.

Alexander M. E. and M. G. Cruz (2012). "Interdependencies between flame length and fireline intensity in predicting crown fire initiation and crown scorch height." International Journal of Wildland Fire 21(1): 95-113.

Alexander M. E. and M. G. Cruz (2021). "Corrigendum to: Interdependencies between flame length and fireline intensity in predicting crown fire initiation and crown scorch height." International Journal of Wildland Fire 30,70(1): 95-113.

Anderson D. H., E. A. Catchpole, N. J. De Mestre and T. Parkes (1982). "Modelling the spread of grass fires." The Journal of the Australian Mathematical Society. Series B. Applied Mathematics 23(4): 451-466.

Anderson H., A. P. Brackebusch, R. W. Mutch and R. C. Rothermel (1966). "Mechanisms of Fire Spread Research Progress Report No.2." U .S . Forest Service Research Paper INT- 28.

Anderson W., E. Pastor, B. Butler, E. Catchpole, J.-L. Dupuy, P. Fernandes, M. Guijarro, J.-M. Mendes-Lopes and J. Ventura (2006). "Evaluating models to estimate flame characteristics for free-burning fires using laboratory and field data." Forest Ecology and Management 234.

Andrews P. L. (2018). "The Rothermel Surface Fire Spread Model and Associated Developments: A Comprehensive Explanation." United States Department of Agriculture Forest Service, General Techncial Report RMRS-GTR-371.

Andrews P. L., M. G. Cruz and R. C. Rothermel (2013). "Examination of the wind speed limit function in the Rothermel surface fire spread model." International Journal of Wildland Fire 22(7).

Apte V. B., R. W. Bilger and A. R. Green (1991). "Wind-aided turbulent flame spread and burning over large-scale horizontal PMMA surfaces." International Fire Journel 85(1-2): 169-184.

AS3959 (2018). Australian Standard AS 3959-2018, Construction of buildings in bushfire prone area. Sydney, Australia.

Barboni T., F. Morandini, L. Rossi, T. Molinier and P.-A. Santoni (2012). "Relationship Between Flame Length and Fireline Intensity Obtained by Calorimetry at Laboratory Scale." Combustion Science and Technology 184(2): 186-204.

Beck J. A. (1995). "EquationsForTheForestFireBehaviourTablesForWesternAustralia." CALMScience.1,325-348.

Burridge H. C. and G. R. Hunt (2017). "From free jets to clinging wall jets: The influence of a horizontal boundary on a horizontally forced buoyant jet." Physical Review Fluids 2(2): 023501.

Burrows N. (1994). Experimental development of a fire management model for Jarrah (Eucalyptus Marginata Donn ex Sm.) forest. Australian National University, Canberra. Australia.

Byram G. (1959). "Combustion of forest fuels." In 'Forest fire: control and use'.(Ed. KP Davis) pp. 61–89. 1959, McGraw-Hill: New York.

Chen T. B. Y., A. C. Y. Yuen, C. Wang, G. H. Yeoh, V. Timchenko, S. C. P. Cheung, Q. N. Chan and W. Yang (2018). "Predicting the fire spread rate of a sloped pine needle board utilizing pyrolysis modelling with detailed gas-phase combustion." International Journal of Heat and Mass Transfer 125: 310-322.

Cheney N. P., J. S. Gould and W. R. Catchpole (1993). "The Influence of Fuel, Weather and Fire Shape Variables on Fire-Spread in Grasslands." International Journel of Wildland Fire 3(l j: 31 - 44,1993.

Cheney N. P. and J. S. Gould (1995). "Fire Growth in Grassland Fuels." International Journal of Wildland Fire 5(4):237-247, 1995.

Cheney N. P., J. S. Gould and W. R. Catchpole (1998). "Prediction of Fire Spread in Grasslands." International Journal of Wildland Fire 8(l):l-13, 1998.

Cobian-Iñiguez J., A. Aminfar, D. R. Weise and M. Princevac (2019). "On the Use of Semi-empirical Flame Models for Spreading Chaparral Crown Fire." Frontiers in Mechanical Engineering 5.

Cruz M. G. and M. E. Alexander (2013). "Uncertainty associated with model predictions of surface and crown fire rates of spread." Environmental Modelling & Software 47: 16-28.

Cruz M. G., M. E. Alexander and A. L. Sullivan (2017). "Mantras of wildland fire behaviour modelling: facts or fallacies?" International Journal of Wildland Fire 26(11).

Cruz M. G., J. S. Gould, M. E. Alexander, A. L. Sullivan, W. L. McCaw and S. Matthews (2015). "Empirical-based models for predicting head-fire rate of spread in Australian fuel types." Australian Forestry 78(3): 118-158.

D.Viegas (2004). "Slope and wind effects on fire propagation." International Journal of Wildland Fire 13(143-156).

Davis T. and K. Sigmon (2005). MATLAB Premier 7th Edition. Florida, USA, CHAPMAN & HALL/CRC. www.dbeBooks.com.

Deardorff J. W. (1972). "Numerical Investigation of Neutral and Unstable Planetary Boundary Layers." National Centre for Atmospheric Research, Colo 80302 (National Science foundation) 91.

Dold J. W. and A. Zinoviev (2009). "Fire eruption through intensity and spread rate interaction mediated by flow attachment." Combustion Theory and Modelling 13(5): 763-793.

Dunn A. and G. Milne (2004). Modelling Wildfire Dynamics via Interacting Automata. School of Computer Science & Software Engineering, The University of Western Australia, 35 Stirling Highway 6009, WA, Australia.

Dupuy J. L., J. Mare´chal, D. Portier and J.-C. Valette (2011). "The effects of slope and fuel bed width on laboratory fire behaviour." International Journal of Wildland Fire 2011, 20, 272–288.

Dupuy J. L. and J. Maréchal (2011). "Slope effect on laboratory fire spread: contribution of radiation and convection to fuel bed preheating." International Journal of Wildland Fire 2011, 20, 289–307.

Eftekharian E., M. Ghodrat, Y. He, R. H. Ong, K. C. S. Kwok and M. Zhao (2019). "Numerical analysis of wind velocity effects on fire-wind enhancement." International Journal of Heat and Fluid Flow 80: 108471.

Eftekharian E., M. Ghodrat, Y. He, R. H. Ong, K. C. S. Kwok and M. Zhao (2020). "Correlations for fire-wind enhancement flow characteristics based on LES simulations." International Journal of Heat and Fluid Flow 82: 108558.

FCFDG (1992). "Forestry Canada Fire Danger Group,Development and structure of the Canadian Forest Fire Behavior Prediction System." Forestry Canada, Science and Sustainable Development Directorate, Information Report.

Finney M. A. (2004). "FARSITE-Fire Area Simulator- Model Development and Evaluation." United States Department of Agriculture U .S . Forest Service Research Paper(RMRS-RP-4).

Fire Protection Research Colloquium (2009). "Proceedings of the Wildland Urban Interface." Fire Protection Research Colloquium, California Polytechnic State University.

Gorrey M. and M. Wade (2019). SGS Economics and Planning report. Australia, sgsep.com.au. 2019.

Gould J. S., W. McCaw, N. P. Cheney, P. F. Ellis and I. K. Knight (2008). "Project Vesta, Fire in Dry Eucalypt Forest: Fuel structure, fuel dynamics and fire behaviour." Csiro Publishing, 2008.(publications.csiro.au).

Hermansen-Baez L. A., J. Seitz and M. C. Monroe (2009). "Wildland Urban Interface: Varied Definitions." School of Forest Resources and Conservation Department, University of Florida FOR225.

Hilton J. E., C. Miller, J. J. Sharples and A. L. Sullivan (2016). "Curvature effects in the dynamic propagation of wildfires." International Journal of Wildland Fire 25(12).

Hoffman C. M., J. Canfield, R. R. Linn, W. Mell, C. H. Sieg, F. Pimont and J. Ziegler (2015). "Evaluating Crown Fire Rate of Spread Predictions from Physics-Based Models." Fire Technology 52(1): 221-237.

Jarrin.N, S.Benhamadouche, D.Laurence and R.Prosser (2006). "A synthetic-eddy-method for generating inflow conditions for large-eddy simulations." International Journal of Heat and Fluid Flow Volume 27, Issue 4, August 2006, Pages 585-593.

Jolly W. M., M. A. Cochrane, P. H. Freeborn, Z. A. Holden, T. J. Brown, G. J. Williamson and D. M. Bowman (2015). "Climate-induced variations in global wildfire danger from 1979 to 2013." Nat Commun 6: 7537.

Kelso J. K., D. Mellor, M. E. Murphy and G. J. Milne (2015). "Techniques for evaluating wildfire simulators via the simulation of historical fires using the AUSTRALIS simulator." International Journal of Wildland Fire 24(6): 784.

Lahaye, S, Sharples, J, Matthews, S, Heemstra, S, Price, O, Badlan, R (2018) How do weather and terrain contribute to firefighter entrapments in Australia? International Journal of Wildland Fire 27,

Linn R., J. Winterkamp, C. Edminster, J. J. Colman and W. S. Smith (2007). "Coupled influence of topgrapy and wind on Wildland fire behavour." International Journal of Wildland Fire 16(2): 183-195.

Linn R. R., J. Reisner, J. J. Colman and J. Winterkamp (2002). "Studying wildfire behaviour using FIRETEC." International Journal of Wildland Fire 11(233-246).

McAlpine R. S., B. D. Lawson and E. Taylor (1991). Fire spread across a slope. In 'Proceedings, 11th Conference on Fire and Forest Meteorology'. M. Society of American Foresters: Bethesda. Bethesda, MD, Society of American Foresters: Bethesda, MD. 16– 19 April 1991**:** 218–225.

McAneney J., K. Chen and A. Pitman (2009). "100-years of Australian bushfire property losses: is the risk significant and is it increasing?" J Environ Manage 90(8): 2819-2822.

McArthur A. G. (1966). "Weather and grassland fire behaviour." Forestry and Timber Bureau, Department of national Development, Commonwealth.

McArthur A. G. (1967). "Fire behaviour in eucalypt forests." Forestry and Timber Bureau, Australia.Department of national Development, Commonwealth.

McGrattan K. B. (2006). "Fire Dynamics Simulator (Verson 4), Technical Reference Guide." National Institute of Standards and Technology Special Publication 1018.

McGrattan K. B., G. P. Forney, S. Hostikka, R. McDermott and C. Weinschenk (2013). "Fire Dynamics Simulator, User's Guide, Sixth edition. (original version 2013, revised version 6.3.2 in 2015)." NIST special publication 1019: 6th Edition,10.6028/NIST.SP.1019.

McGrattan K. B., S. Hostikka, R. McDermott, J. Floyd, C. Weinschenk and K. Overholt (2015). "Fire Dynamic Simulator Technical Reference Guide Volume 1: Mathematical Model." NIST special publication 1018-1(Sixth Edition).

McRae R. (2004). Virtually volvelles. In ‘Proceedings, Bushfire 2004'. S. A. A. Department of Environment and Heritage, SA. Australia.

Mell W., M. Jenkins, J. S. Gould and N. P. Cheney (2007). "A physics-based approach to modelling grassland fires." international Journal of Wildland Fire 2007,16,1-22.

Mell W., A. Maranghides, R. McDermott and S. L. Manzello (2009). "Numerical simulation and experiments of burning douglas fir trees." Combustion and Flame 156(10): 2023-2041.

Mell W., A. Simeoni, D. Morvan, J. K. Hiers, N. Skowronski and R. M. Hadden (2018). "Clarifying the meaning of mantras in wildland fire behaviour modelling: reply to Cruz et al. (2017)." International Journal of Wildland Fire 27(11).

Mendes-Lopes J. M. C., J. M. P. Ventura and J. M. P. Amaral (2003). "Flame characteristics, temperature - time curves, and rate of spread in fires propagating in a bed of Pinus pinaster needles." International Journal of Wildland Fire 12(1): 67.

Metcalfe D. and E. Bui (2016). Topic - Vegitaion land, Australian Government Department of the Environment and Energy. Canberra, Australia, https://soe.environment.gov.au/theme/land/topics. DOI 10.4226/94/58b6585f94911.

Moinuddin K., N. Khan and D. Sutherland (2021). "Numerical study on effect of relative humidity (and fuel moisture) on modes of grassfire propagation." Fire Safety Journal, Vol.125,103422.

Moinuddin K., D. Sutherland and W. Mell (2018). "Simulation study of grass fire using a physics-based model: striving towards numerical rigour and the effect of grass height on the rate-of-spread." International Journal of Wildland Fire 27, 800-814.

Moinuddin K. A. M. and D. Sutherland (2020). "Modelling of tree fires and fires transitioning from the forest floor to the canopy with a physics-based model." Mathematics and Computers in Simulation 175: 81-95.

Morandini F., P. Santoni, J. Balbi, J. Ventura and J. M. C. Mendes-Lopes (2002). "A two-dimensional model of fire spread across a fuel bed including wind combined with slope conditions." International Journal of Wildland Fire 11(doi:10.1071/WF01043): 53-64.

Morandini F. and X. Silvani (2010). "Experimental investigation of the physical mechanisms governing the spread of wildfires." International Journal of Wildland Fire 19(5).

Morandini F., X. Silvani, J.-L. Dupuy and A. Susset (2018). "Fire spread across a sloping fuel bed: Flame dynamics and heat transfers." Combustion and Flame 190: 158-170.

Morvan D., G. Accary, S. Meradji, N. Frangieh and O. Bessonov (2018). "A 3D physical model to study the behavior of vegetation fires at laboratory scale." Fire Safety Journal 101: 39-52.

Morvan D. and J. L. Dupuy (2001). "Modeling of fire spread through a forest fuel bed using a multiphase formulation." Combustion and Flame 127(1-2) 127(1-2):1981-1994

Morvan D. and J. L. Dupuy (2004). "Modeling the propagation of a wildfire through a Mediterranean shrub using a multiphase formulation." Combustion and Flame 138(3): 199-210.

Morvan D. and N. Frangieh (2018). "Wildland fires behaviour :wind effect versus Byram's convective number and consequences upon the regime." International Journal of Wildland Fire CSIRO Publishing, 2018, 27 (9), pp.636(10.1071/Wf18014).

Morvan D., S. Meradji and G. Accary (2007). "Wildfire Behavior Study in a Mediterranean Pine Stand Using a Physically Based Model." Combustion Science and Technology 180(2): 230-248.

Morvan D., S. Meradji and G. Accary (2009). "Physical modelling of fire spread in Grasslands." Fire Safety Journal 44(1).

Morvan D., S. Meradji and W. Mell (2013). "Interaction between head fire and backfire in grasslands." Fire Safety Journal 58: 195-203.

Nelson R. (2002). "An effective wind speed for models of fire spread." International Journal of Wildland Fire 11(doi:10.1071/ WF02031): 153-161.

Nelson R. (2015). "Re-analysis of wind and slope effects on flame characteristics of Mediterranean shrub fires." International journal of wildland fire v. 24(no. 7): pp. 1001-1007-2015 v.1024 no.1007.

Noble I. R., A. Gill and G. Barry (1980). "McArthur's fire-danger meters expressed as equations." Australian Journal of Ecology (1980) 5, 201-203.

Norman B., J. K.Weir, K. Sullivan and J. Lavis (2009). Planning and Bushfire Risk in a Changing Climate. U. o. Canberra. Melbourne, Australia, Bushfire CRC, Victorian 2009 Bushfire research repsone.

Overholt K. J., J. Cabrera, A. Kurzawski, M. Koopersmith and O. A. Ezekoye (2014). "Characterization of Fuel Properties and Fire Spread Rates for Little Bluestem Grass." Fire Technology 50(1): 9-38.

Pagni P. J. and T. G. Peterson (1973). Flame spread through porous fuels. Fourteenth International Symposium on Combustion', Pittsburgh, PA, The Combustion Inst.: Pittsburgh, PA.

Perez-Ramirez Y., W. Mell, P. Santoni and J. B. T. F. Bosseur (2017). "Examination of WFDS in Modeling Spreading Fires in a Furniture Calorimeter." Fire Safety Journal 53(5),1795–1832(2017).

Perry G. L. W. (1998). "Current approaches to modelling the spread of wildland fire: a review." Progress in Physical Geography: Earth and Environment 22(2): 222-245.

Pimont F., J. L. Dupuy and R. R. Linn (2012). "Coupled slope and wind effects on fire spread with influences of fire size: a numerical study using FIRETEC." International Journal of Wildland Fire 21(7).

Porterie B., J. L. Consalvi, A. Kaiss and J. C. Loraud (2005). "PREDICTING WILDLAND FIRE BEHAVIOR AND EMISSIONS USING A FINE-SCALE PHYSICAL MODEL." Numerical Heat Transfer, Part A: Applications 47(6): 571-591.

Porterie B., D. Morvan, M. Larini and J. C. Loraud (1998). "Wildfire propagation: A two-dimensional multiphase approach." Combustion, Explosion and Shock Waves 34(2): 139-150.

Radeloff V., R. Hammer, S. Stewart, J. S. Fried, S. Holocomb and M. J. F (2005). "The Wildland-Urban Interface in the United States." Ecological Applications, Ecological Socitey of America 15(3).

Raithby G. D. and E. H. Chui (1990). "A Finite-Volume Method for Predicting a Radiant Heat Transfer in Enclosures With Participating Media." Journel of Heat Transfer 112(2, May 1990).

Rothermel R. C. (1972). "A Mathematical model for predicting fire spread in wildland fuels." USDA Forest Service, Intermountain Forest and Range, General Technical Report INT-115, Ogden, UT.

Rothermel R. C. and R. E. Burgan (1984). "BEHAVE:Fire Behavior Prediction and Fuel Modeling System." United States Department of Agriculture PMS 439-1,NFES 0275.

Royal Commission (2010). Royal commission report- 2009 Victorian Busfires royal commission. Victoria, Victorian goverment, Australia.

Samgorinsky J. (1963). "General Circulation experiments with the primitive equations;. I.The basic experiment." General Circulation Research Laboratory, U.S Weather Bureau, Washtington D C 91(3).

Sánchez-Monroy X., W. Mell, J. Torres-Arenas and B. W. Butler (2019). "Fire spread upslope: Numerical simulation of laboratory experiments." Fire Safety Journal 108: 102844.

Shamseddin I. (2019). Physics-based simulations of fire development downstream of a canopy. Master of Engineerign in the field of Computational Mechanics. F. n. 143/2018. Labanese University,.

Sharples J. J. (2008). "Review of formal methodologies for wind–slope correction of wildfire rate of spread." International Journal of Wildland Fire 2008, 17, 179–193.

Sharples J. J. (2017). "Risk Implications of Dynamic Fire Propagation, A case study of the Ginninderry region." Preliminary Report, June 2017 Prepared for: Ginninderra Falls Association.

Sharples J. J., V. D.X, M. R.H.D, R. J.R.N and F. H.A.S (2011). "Lateral bushfire propagation driven by the interaction of wind, terrain and fire." 19th International Congress on Modelling and Simulation, Perth, Australia, 2011 pp. 12-16.

S Singha Roy, D Sutherland, N Khan, K Moinuddin, A comparative study of wind fields generated by different inlet parameters and their effects on fire spread using Fire Dynamics Simulator. *Proceedings of the 21st Australasian Fluid Mechanics conference, 2018, paper 763* *(*https://people.eng.unimelb.edu.au/imarusic/proceedings/21/Contribution_763_final.pdf*)*

Stewart S., V. Radeloff, R. Hammer and T. Hawbaker (2007). "Defining the Wildland-Urban Interface." Journal of Forestry, Journal of the Society of American Foresters.

Stull R. B. and C. D. Arhens (2000). "Meteorology for Scientists and Engineers." Brooks/Cole, Pacific Grove, California, 2nd edition.

Sullivan A. L. (2009a). "Wildland surface fire spread modelling, 1990–2007. 1: Physical and quasi-physical models." International Journal of Wildland Fire 2009, 18, 349–368.

Sullivan A. L. (2009b). "Wildland surface fire spread modelling, 1990–2007. 2: Empirical and quasi-empirical models." International Journal of Wildland Fire 2009, 18, 369–386.

Sullivan A. L. (2009c). "Wildland surface fire spread modelling, 1990–2007. 3: Simulation and mathematical analogue models." International Journal of Wildland Fire 2009, 18, 387–403.

Sullivan A. L., I. K. Knight, R. J. Hurley and C. Webber (2013). "A contractionless, low-turbulence wind tunnel for the study of free-burning fires." Experimental Thermal and Fluid Science 44: 264-274.

Sullivan A. L., J. J. Sharples, S. Matthews and M. P. Plucinski (2014). "A downslope fire spread correction factor based on landscape-scale fire behaviour." Environmental Modelling & Software 62: 153-163.

Sullivan A. L., Baker E, Kurvits Tiina. (2022). "Spreading like wildfire, The rising threat of extraordinary landscape fires." A rapid respeonse assesment, GRID-Arendal, UN enviornment programme 5, 1972-2022,

Sutherland, D, Sharples, JJ, Moinuddin, K (2020) The effect of ignition protocol on grassfire development. *International Journal of Wildland Fire* **29**, 70.

Sutherland, D, Sharples, JJ, Moinuddin, K (2022) Simulated flame shape and heat transfer of quai-equilibrium grass fire at transitional Byram numbers. *International Conference on Forest Fire Research* **IX**,

Tang W., G. D.J, M. A. Finney, S. S. McAllister and J. D. Cohen (2017). "An experimental study on the intermittent extension of flames in wind-driven fires." Fire Safety Journal 91,742-748.

Taylor S. W., B. M. Wotton, M. E. Alexander and G. N. Dalrymple (2004). "Variation in wind and crown fire behaviour in a northern jack pine – black spruce forest." Canadian Journal of Forest Research 34(8): 1561-1576.

Tihay V., F. Morandini, P.-A. Santoni, Y. Perez-Ramirez and T. Barboni (2014). "Combustion of forest litters under slope conditions: Burning rate, heat release rate, convective and radiant fractions for different loads." Combustion and Flame 161(12): 3237-3248.

Wadhwani R. (2019). PhD Thesis report: "Physics- based simulation of short -range spotting in wildfires", College of Engineering and Science, Victoria University, Melbourne, Australia.

Weise D. and G. Biging (1997). "A Qualitative Comparison of Fire spread model incorporating wind and slope effects." Forest Science 43, 170-180.

Wilson R. (1980). "Rothermel equations in SI units- Reformulation of Forest Fire Spread Equations in SI units." US Forest Science Research note INT-292.

Wilson R. (1990). "Reexamination of Rothermels Fire Spread Equations in No-wind and No-slope conditions." United States Department of Agriculture, Forest Service Research Paper INT-434.

9. Annexure A: Supplementary Figures and Tables

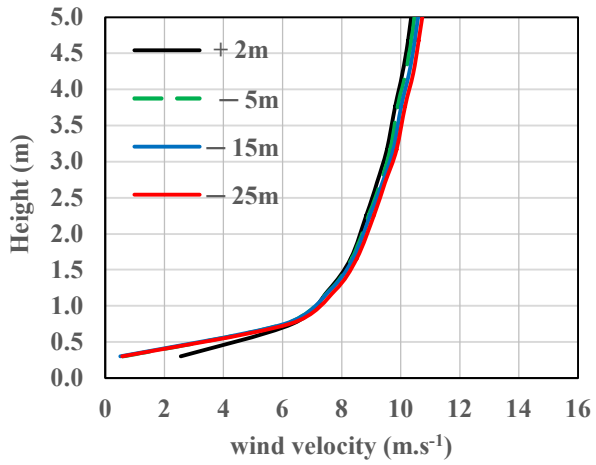

(a)

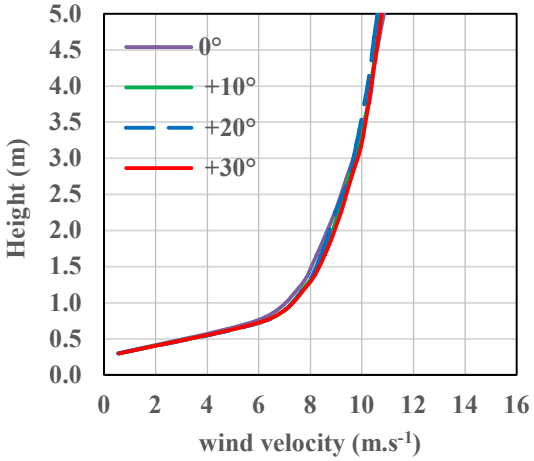

(b)

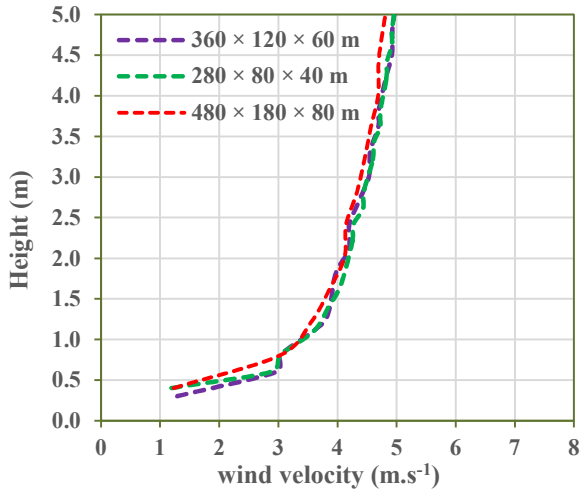

(c)

***Figure S4.1*:** The wind profiles at driving wind velocity of 12.5m.s^{-1} **(a)** enlarged view, upto 5 m, of the wind profiles vs height, taken at different streamwise for 10° upslope **(b)** enlarged view, upto 5 m, of the wind profiles vs height, taken at –25m for 0°, +10°, +20° and +30° **(c)** enlarged view up to 5 m wind profiles vs height for 0° slope at 6 m.s^{-1} for the three domains, taken at the inlet (+2 m) of grass plot.

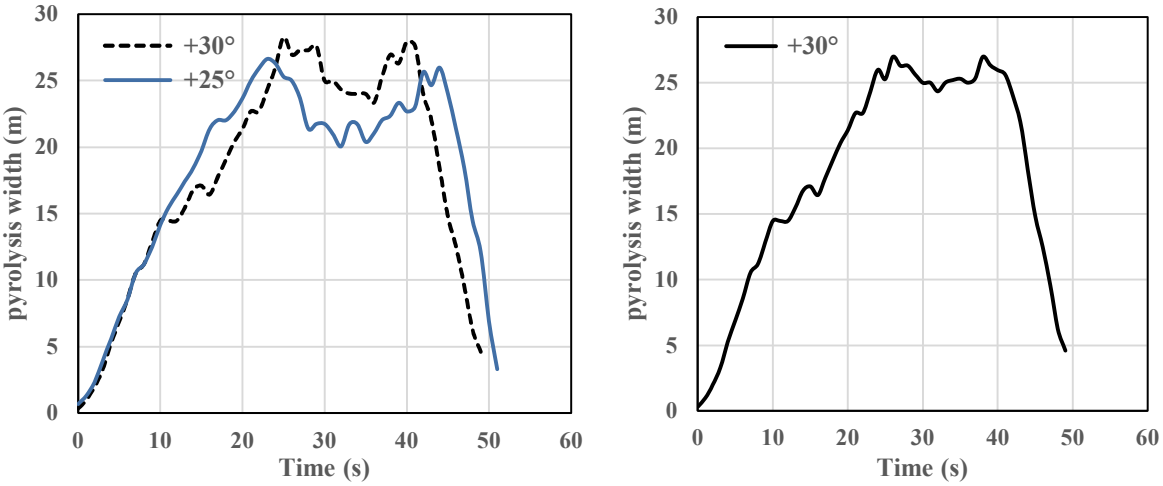

(a) 12.5 m.s^{-1} (b) 6 m.s^{-1}

***Figure S4.2*:** Pyrolysis width vs time with burnable grass plot extended to 120 m in the x-direction): (a) +30°, +25° at 12.5 m.s^{-1}, (b) +30° at 6 m.s^{-1}

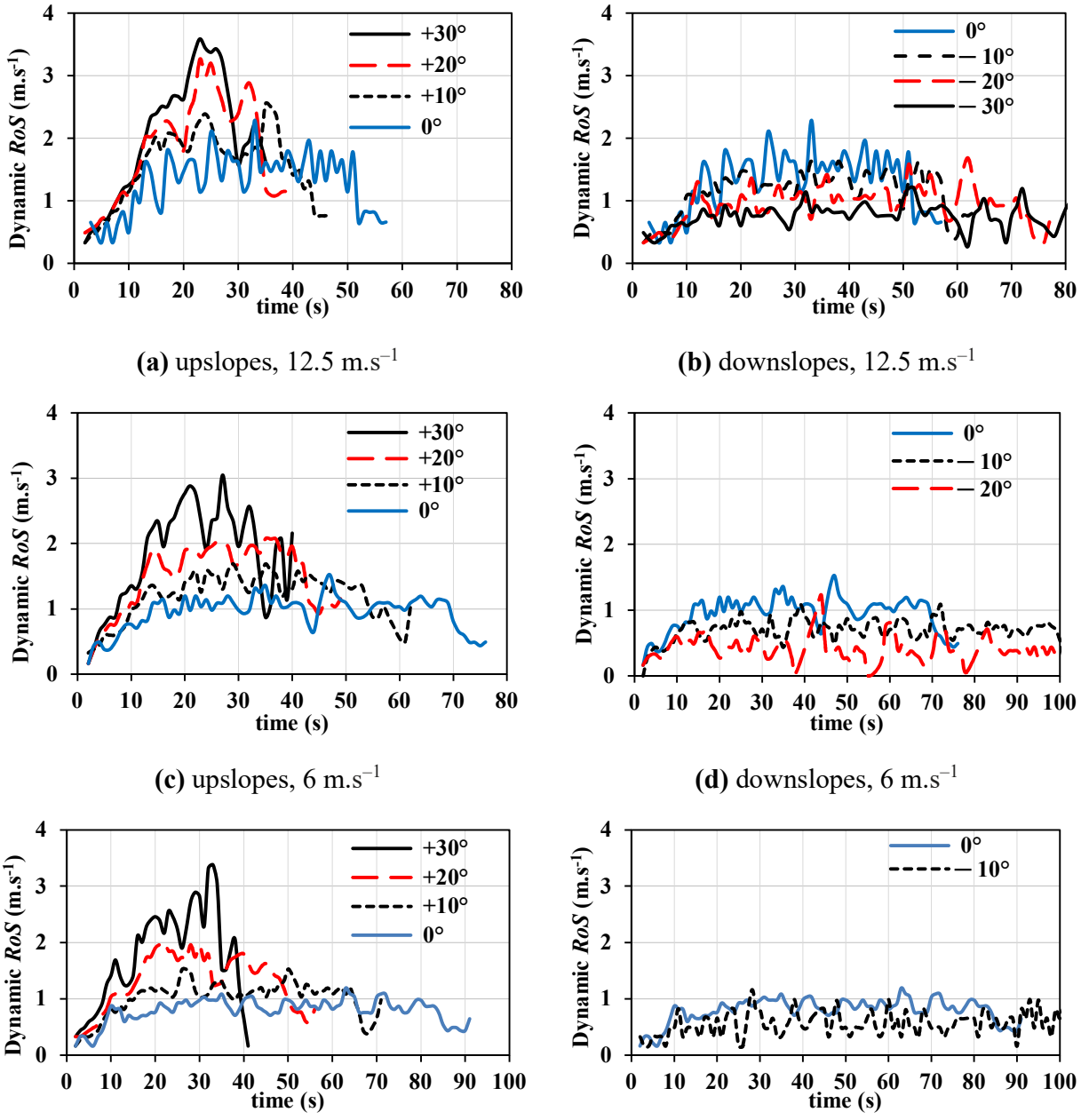

(a) upslopes, 12.5 m.s^{-1}

(b) downslopes, 12.5 m.s^{-1}

(c) upslopes, 6 m.s^{-1}

(d) downslopes, 6 m.s^{-1}

(e) upslopes, 3 m.s^{-1}

(f) downslopes, 3 m.s^{-1}

***Figure S4.3*:** Dynamic *RoS* vs time (smoothed the data and 3-point moving average), at all three wind velocities: (a) upslopes at 12.5 m.s^{-1}; (b) downslopes at 12.5 m.s^{-1}; (c) upslopes at 6 m.s^{-1}; (d) downslopes at 6 m.s^{-1}; (e) upslopes at 3 m.s^{-1}; and (f) downslopes at 3 m.s^{-1}

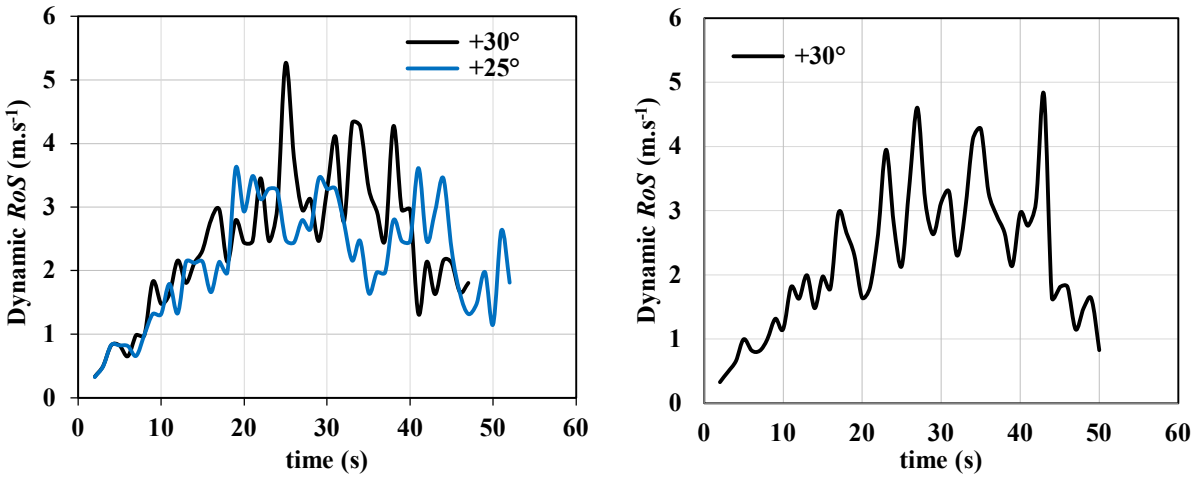

(a) 12.5 m.s^{-1} (b) 6 m.s^{-1}

Figure S4.4 Dynamic *RoS* vs time with burnable grass plot extended to 120 m in the x- direction : (a) +30°, +25° at 12.5 m.s^{-1}, (b) +30° at 6 m.s^{-1}

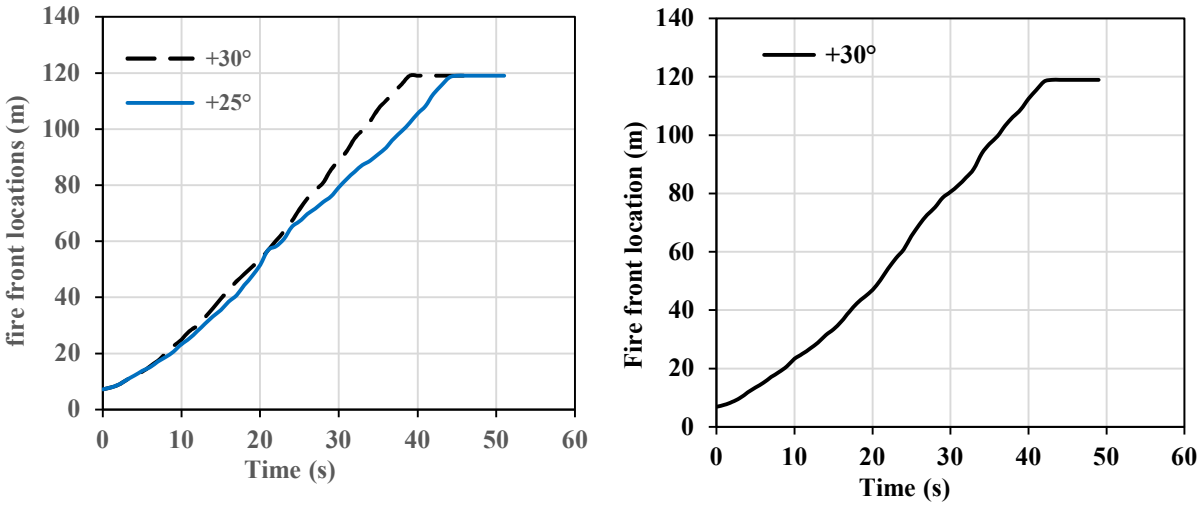

(a) 12.5 m.s^{-1} (b) 6 m.s^{-1}

Figure S4.5 Fire front vs time with burnable grass plot extended to 120 m in the x- direction : (a) +30°, +25° at 12.5 m.s^{-1}, (b) +30° at 6 m.s^{-1}

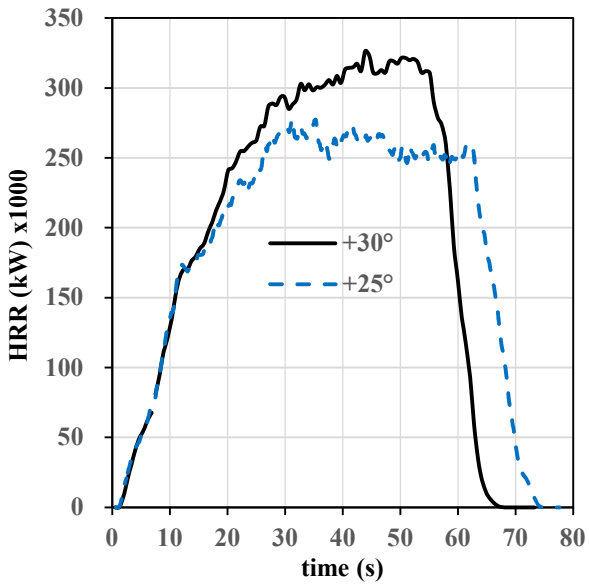

(c) 12.5 m.s^{-1}

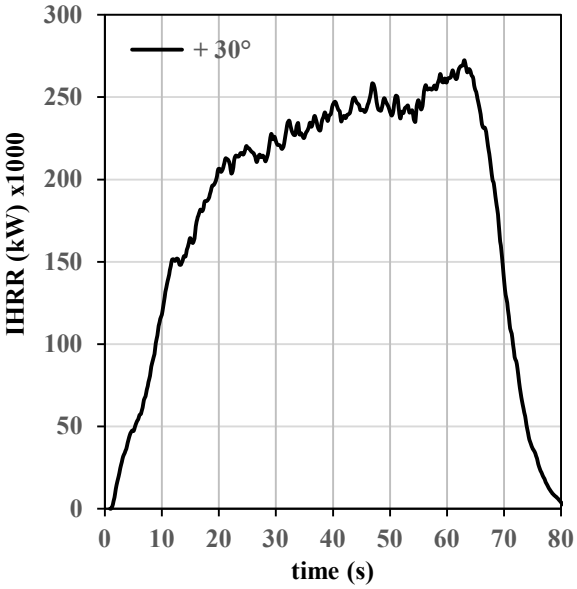

(d) 6 m.s^{-1}

Figure S4.6. Heat release rate (HRR) as a function of time with longer domain (burnable grass plot extended to 120m in the x- direction) for; (a) +30°, +25° slopes at 12.5m.s^{-1} wind velocity (b) +30° slope at 6 m.s^{-1} wind velocity.

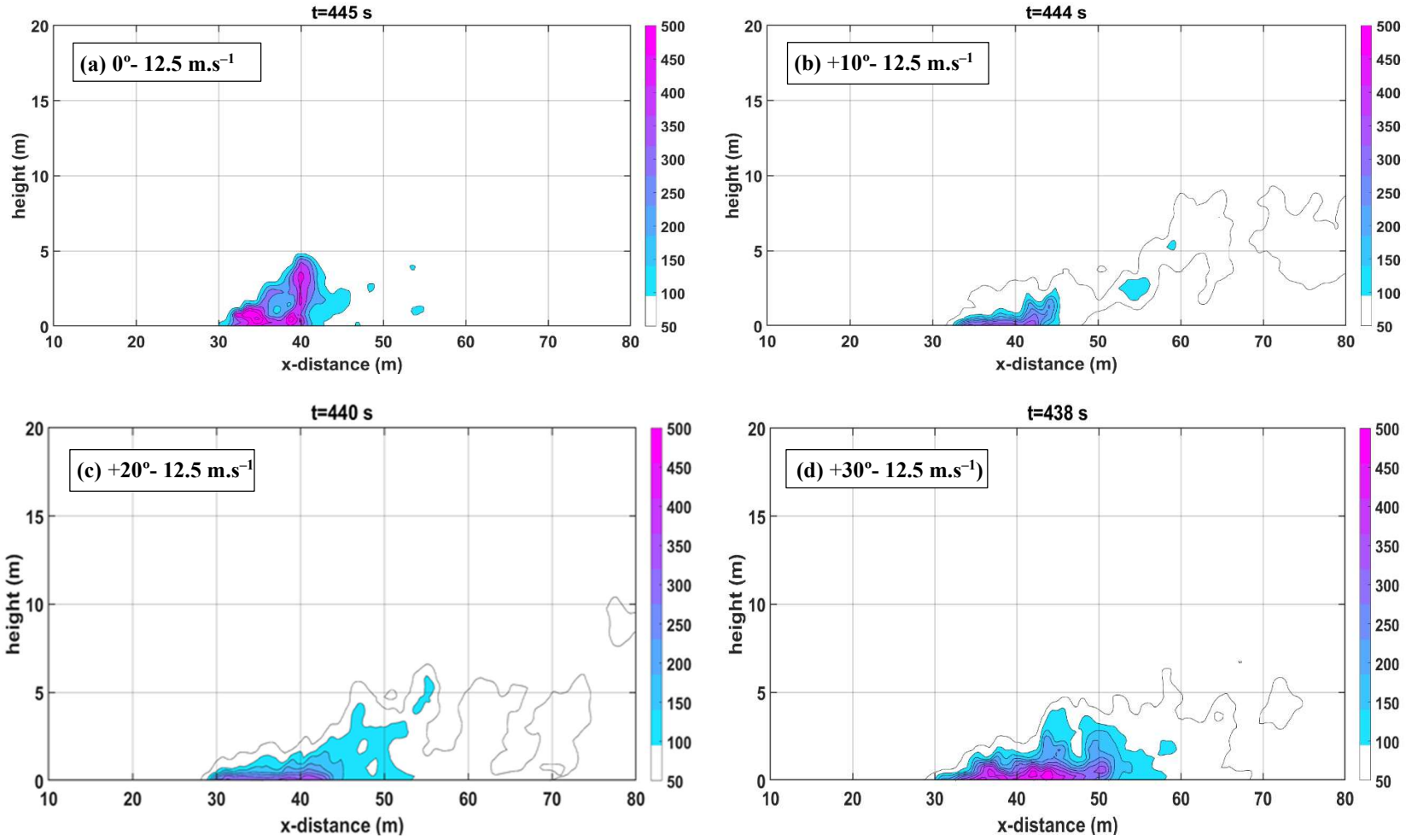

Figure S4.7 (a-d): Temperature contours (representing plume) at the same firefront location, at wind velocity 12.5 m.s^{-1} : 0°, +10°, +20° and +30° slopes

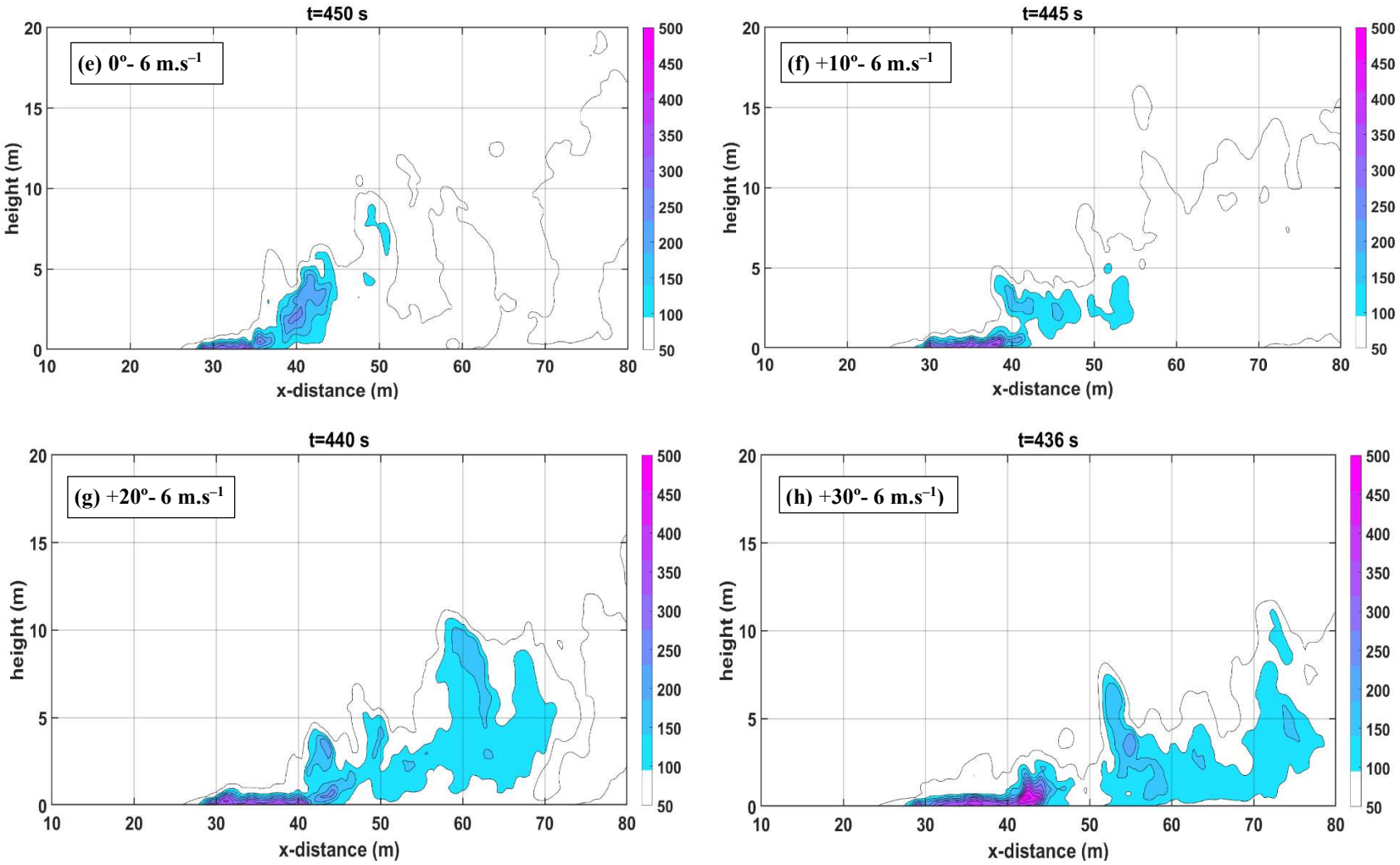

Figure S4.7 (e-h): Temperature contours at the same firefront location, at wind velocity 6 m.s^{-1} : 0°, +10°, +20° and +30°

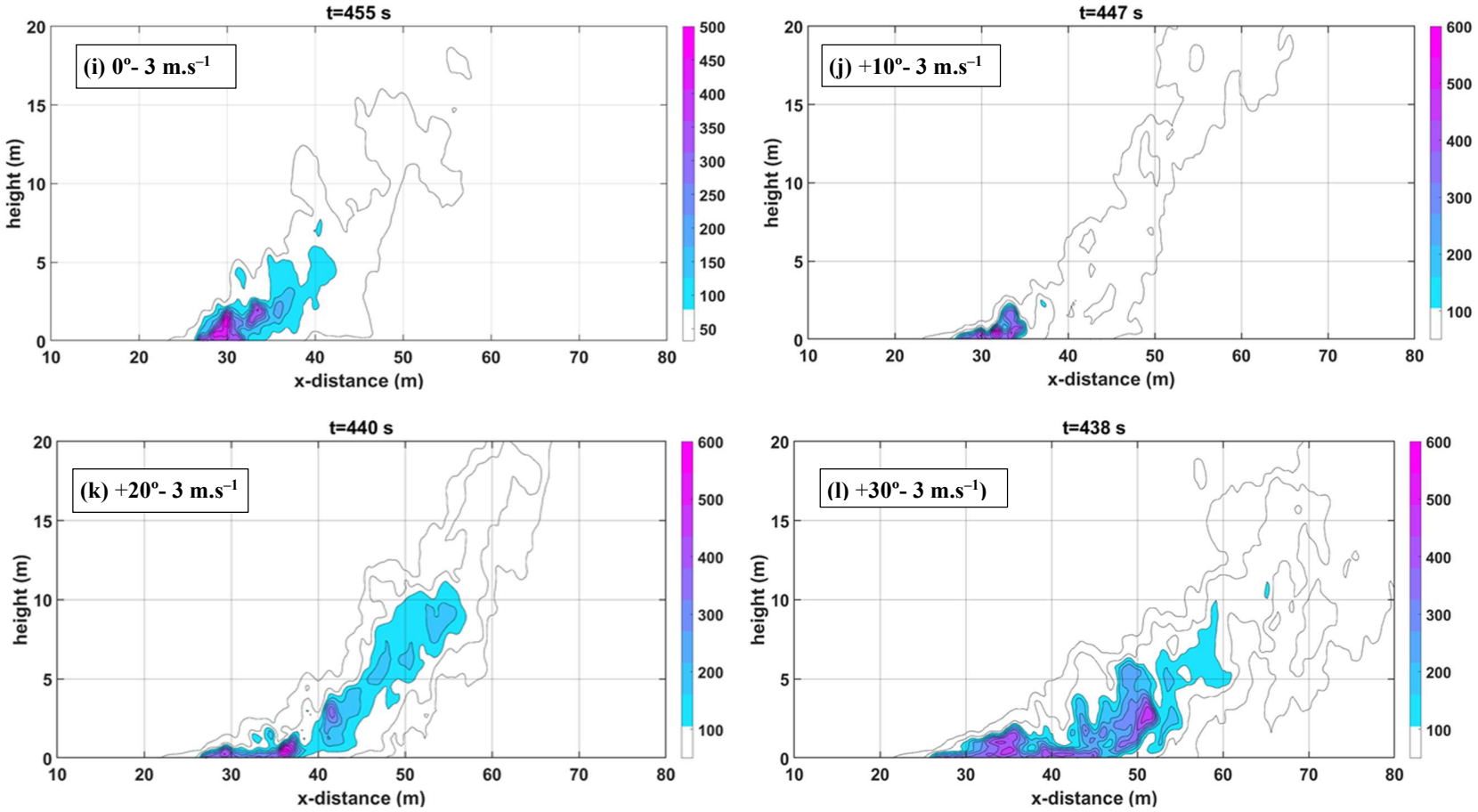

Figure S4.7*:* Temperature contours (representing plumes) along the geometric centreline of the grass plot, at the same fire front location from ignition line: Frames (a-d) - 0°, +10°, +20°, +30° at 12.5 m.s^{-1}; Frames (e-h) - 0°, +10°, +20°, +30° at 6 m.s^{-1}; Frames (i-l)- 0°, +10°, +20°, +30° at 3 m.s^{-1}

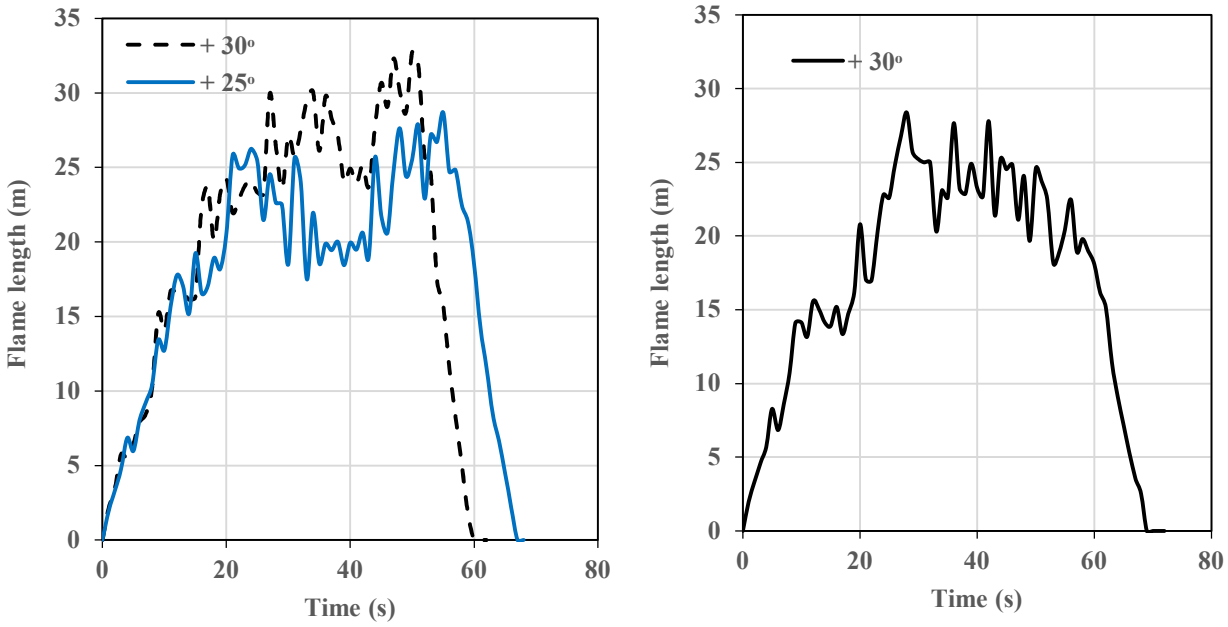

(a) 12.5 m.s^{-1} (b) 6 m.s^{-1}

Figure S4.8: Flame length with extended burnable grass plot (120 × 40 m grass plot): (a) +30°, +25° at 12.5 m.s^{-1}, (b) +30° at 6 m.s^{-1}

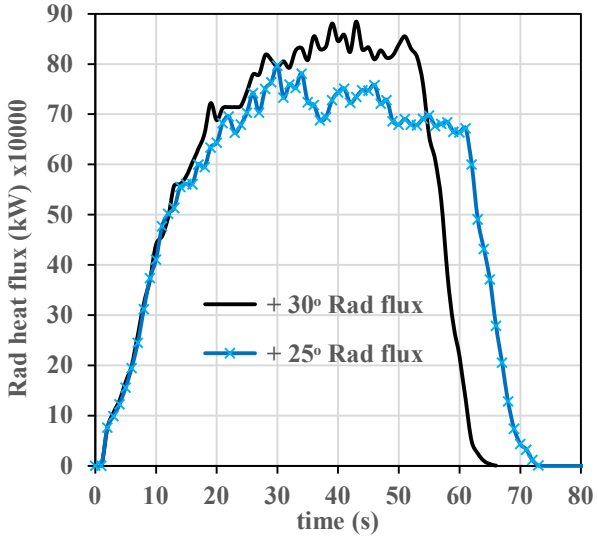

(a) Radiative heat flux vs time- 12.5ms^{-1}

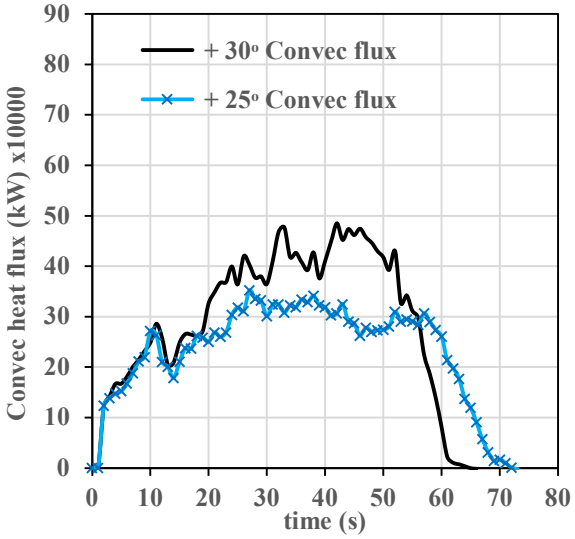

(b) Convec heat flux vs time- 12.5ms^{-1}

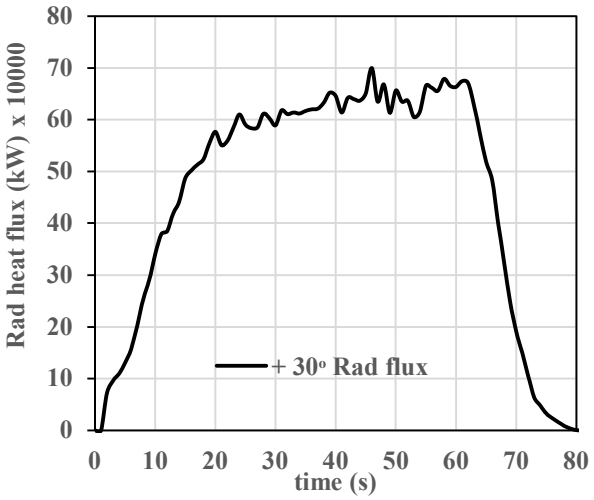

(c) Radiative heat flux vs time: 6 ms^{-1}

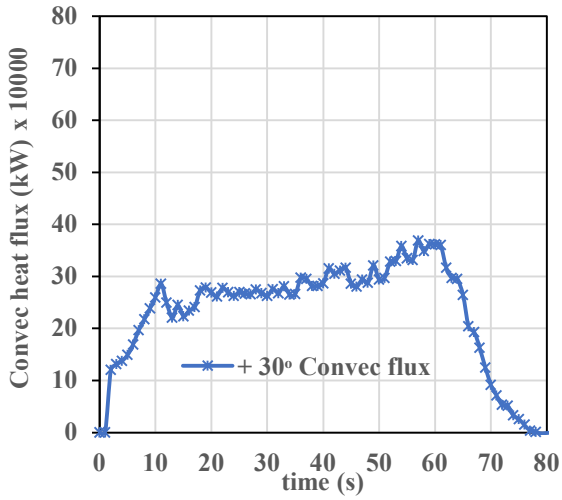

(d) Convective heat flux vs time: 6 ms^{-1}

Figure S4.9*:* Heat flux as a function of time for 120 × 40 m burnable plot simulation for higher upslopes +30°, +25° at 12.5 m.s^{-1} and +30° at 6 m.s^{-1} : (a) Radiative heat flux vs time 12.5 ms^{-1}, (b) convective heat flux vs time 12.5 ms^{-1}, (c) Radiative heat flux vs time 6 ms^{-1}, (d) convective heat flux vs time 6 ms^{-1}

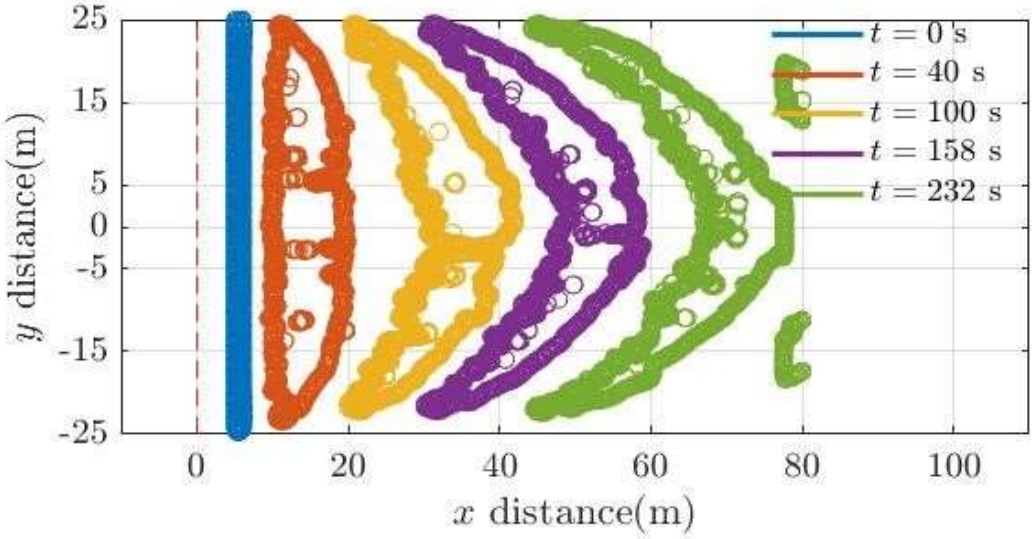

Figure S6.1 – Progression of isochrones: +30° slope with ignition line width of 50 m (L0)

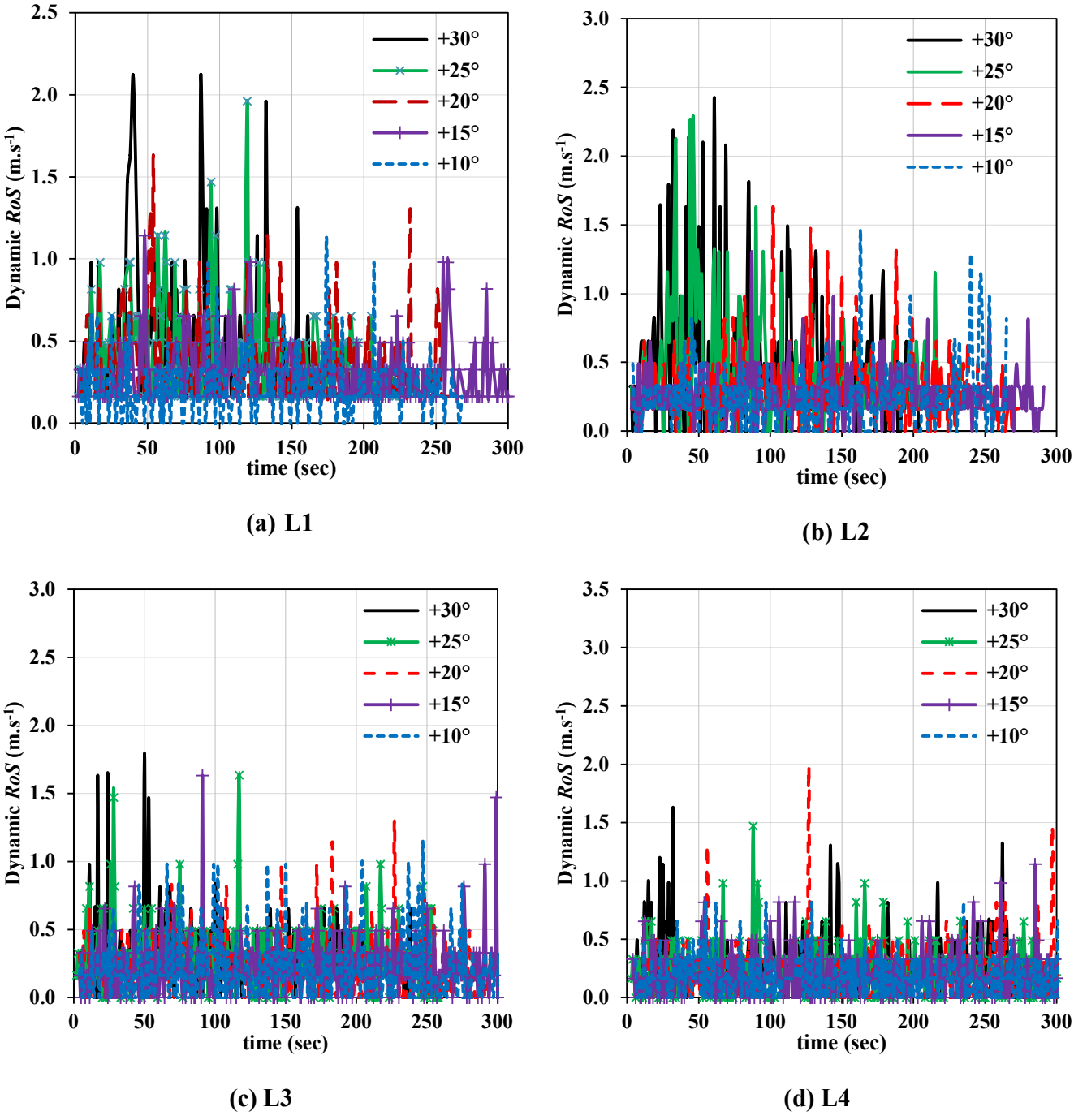

Figure S6.2 – Dynamic *RoS* with wind velocity of 1 m.s^{-1} and ignition line widths of: (a) 40 m (L1), (b) 30 m (L2), (c) 20 m (L3), and (d) 10 m (L4).

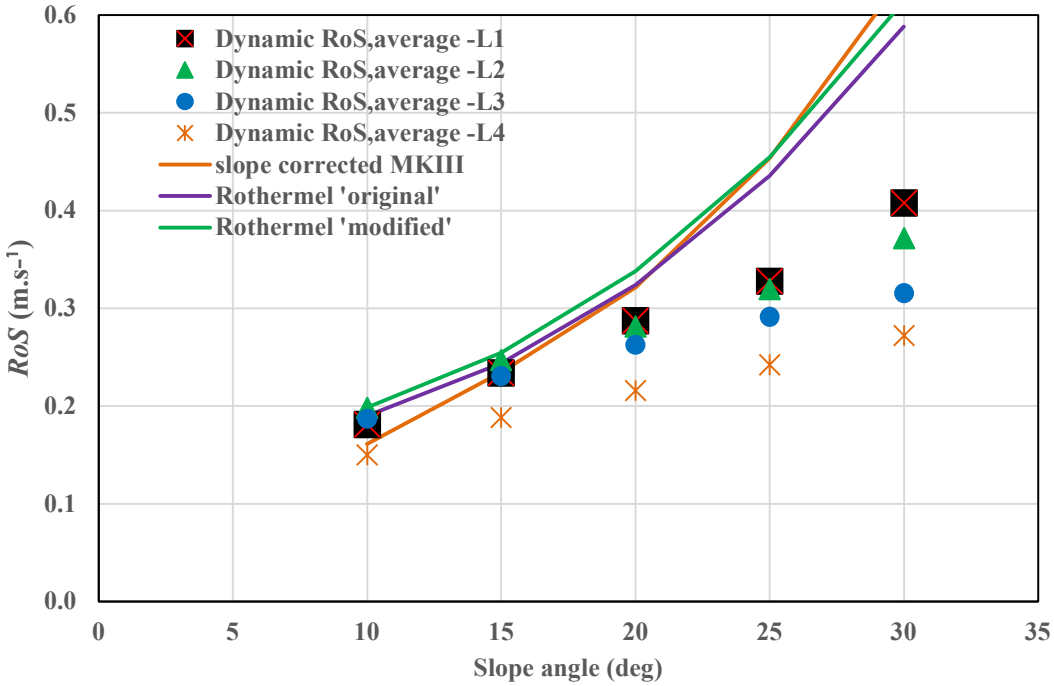

Figure S6.3 – Dynamic *RoS* average vs slope angle for ignition line widths of 40 m (L1), 30 m (L2), 20 m (L3), and 10 m (L4).

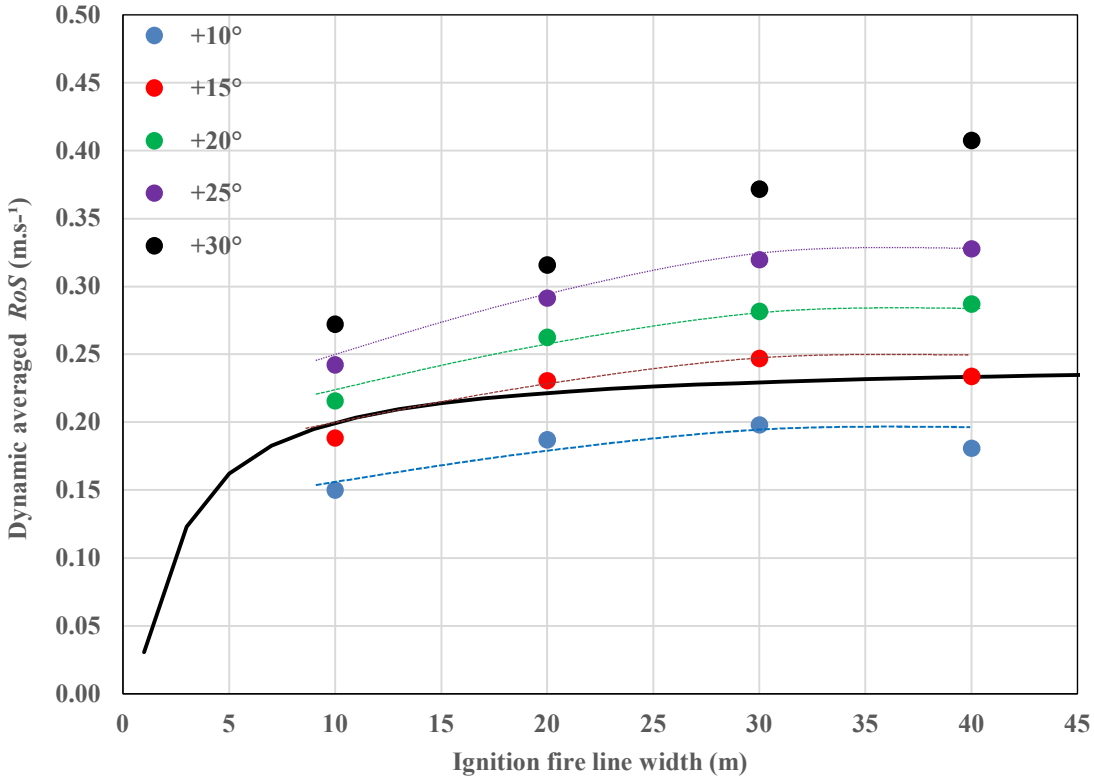

Figure S6.4 – Dynamic *RoS* vs ignition line widths for slope angles of +10°, +15°, +20°, +25° and +30° along with empirically derived *RoS* values (Eqn. 6.1) (the lines are drawn to show the converging nature of *RoS* values and do not represent goodness of fit).

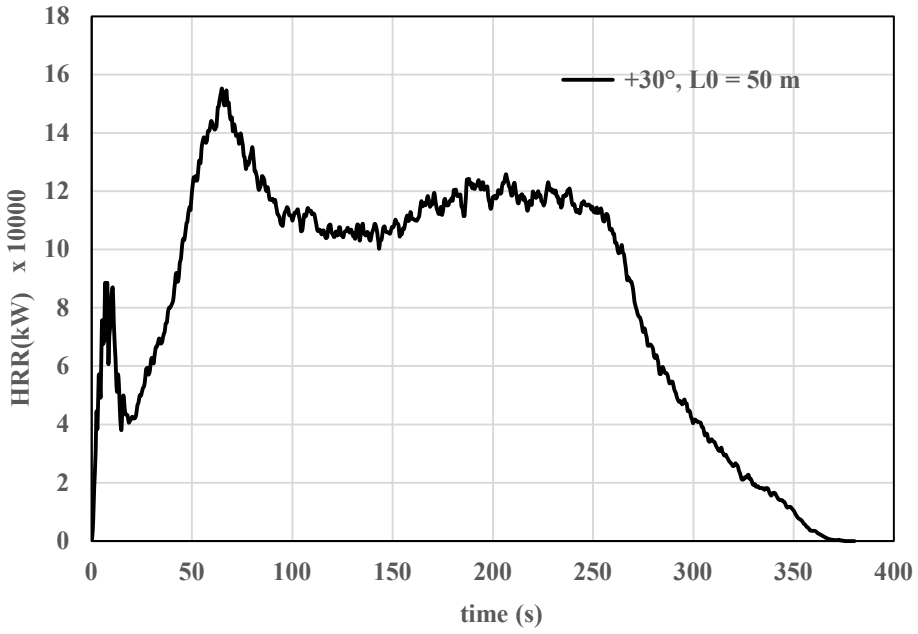

Figure S6.5 –HRR vs time : +30° slope at ignition line width of 50 m (L0)

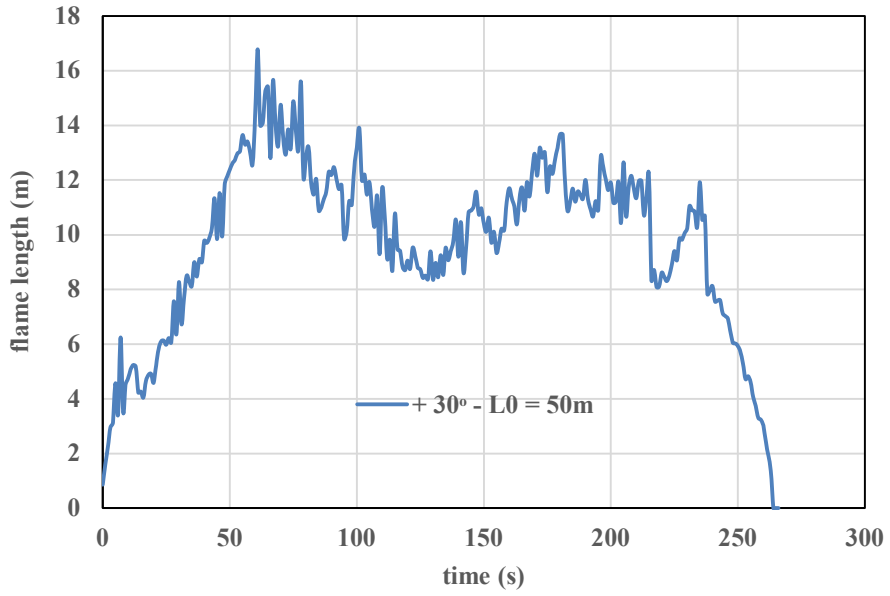

Figure S6.6 – Flame length vs time : +30° slope with ignition line width of 50 m (L0)

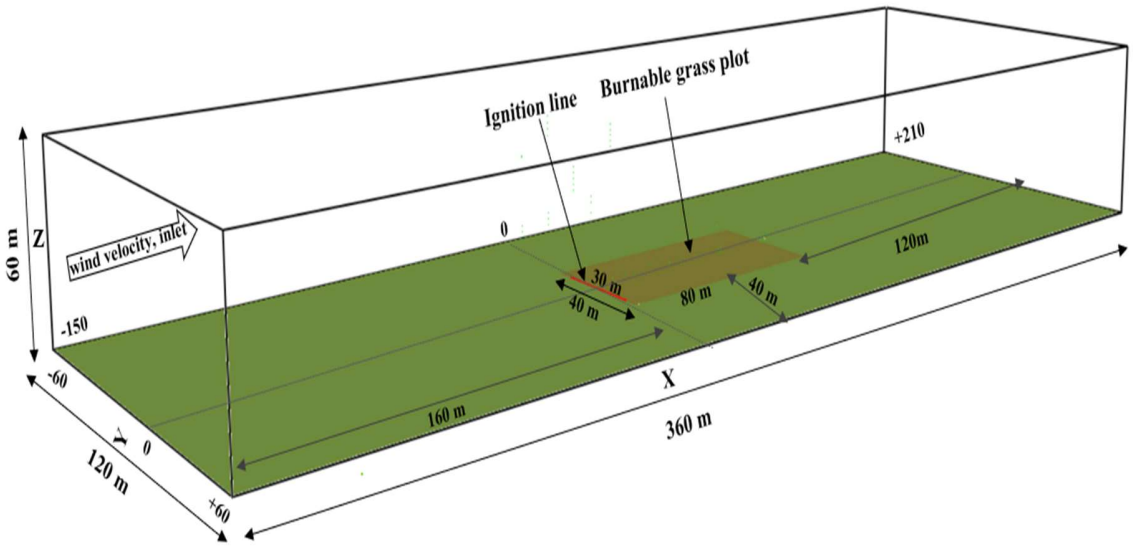

(a) L5: ignition fire line 30 m, grass plot width 40 m

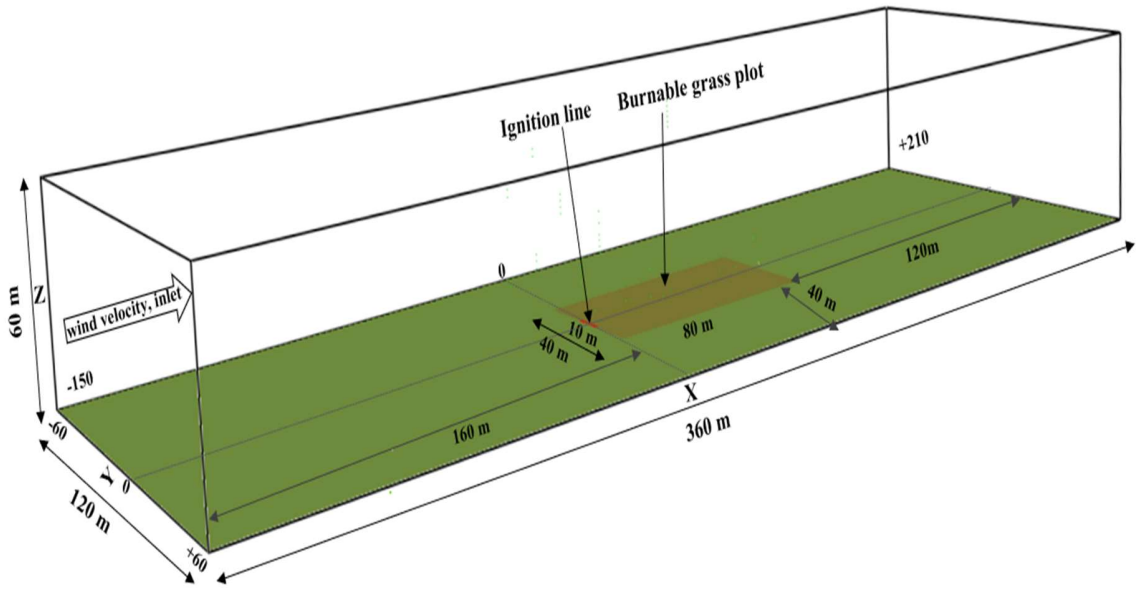

(b) L7: Ignition fire line 10 m, grass plot width 40 m

Figure S6.7 – The geometry of the domain used with L5 and L7: with burnable grass plot 40 m wide and 80 m long (dark green region).

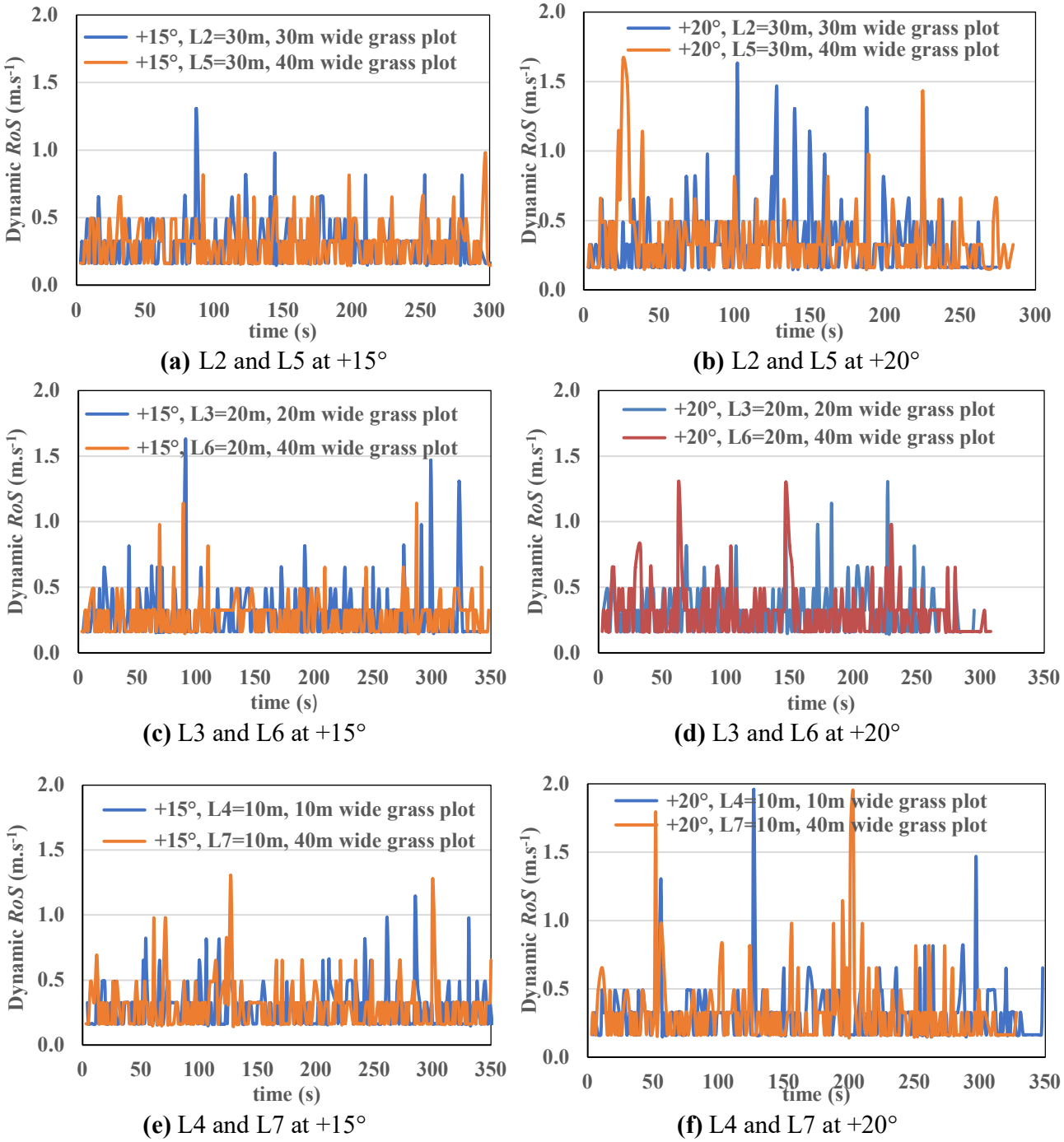

(a) L2 and L5 at +15°

(b) L2 and L5 at +20°

(c) L3 and L6 at +15°

(d) L3 and L6 at +20°

(e) L4 and L7 at +15°

(f) L4 and L7 at +20°

Figure S6.8– Dynamic *RoS* vs time: simulations where grass plot width is varied in line with ignition line and grass plot width unaltered: (a) L2 and L5 at +15°, (b) L2 and L5 at +20°, (c) L3 and L6 at +15°, (d) L3 and L6 at +20°, (e) L4 and L7 at +15°, (f) L4 and L7 at +20°

Table S4.1. Measured fire front length and *Q* values

Slope	Measured fire front length (m) (@10, 20, 30, 40, 50, 60, 70, 80……s)			Measured *Q* (MW.m^{-1}) (@10, 20, 30, 40, 50, 60, 70, 80……s)		
	12.5 m.s^{-1}	6 m.s^{-1}	3 m.s^{-1}	12.5 m.s^{-1}	6 m.s^{-1}	3 m.s^{-1}
–30°	40,42,42,42.5,43,44,44,44.2,45,45,45.5,46,46,46,46	Not applicable	Not applicable	2.6,1.6,1.6,1.7,1.6,1.6,1.5,1.5,1.3,1.1,1.2,1.2,1.1	Not applicable	Not applicable
–20°	40,41.5,42,42,43.5,43.5,43.8,43.5, 44,44,44	44,45,45,44,44,42.5,42,42, 42,42,42,41,41,40,40,	Not applicable	2.8,2.1,2.2,2.3,2.1,2.2,2.2,2.0,2.1, 1.8,0.4	1.9,0.92,0.76,0.82,0.89,0.86,0.87, 0.84,0.79,0.81,0.79,0.75,0.86,0.8	Not applicable
–10°	41,41,42,42,42.5,42.5,43.2,43.2	41,41,42,42,42.5,43,43.5,44,44.5,45,45, 45,45,	44,44,45,45,45,45,46,46,46, 46,46, 46	3.0,2.7,2.9,2.9,2.8,2.8,2.9,2.7,0.18	2.44,1.54,1.58,1.61,1.63,1.61,1.5, 1.5,1.5,1.5,1.42,	1.4,0.99,0.94, 1.02,1.0,1.1,1.1,1.1,1.1,1.1, 1.1,
0°	41.5,41.5,42,42.5,42.5,43,43.5	43,43.5,45,45,46.2,46.2,47, 47,47.5,48,49	42.5,43,43,40.5,39,39,39,37,38,38,38,34,34	2.4,3.1,3.4,3.4,3.2,3.2,2.9	2.5,2.1,1.96,2.15,2.14,2.14,2.1,1.97,2.1,1.55	1.7,1.56,1.6,1.78,1.85,1.85, 2.0,2.1,2.1,2.1,2.0,2.0,2.0, 0.7
+10°	41.5,43,43,43.5,44.5,44.5	43,45.5,46,46.5,47.5,47.8,48,48,48	40,41,39,36,36,36,38,37,34, 34,30	3.4,4.1,4.3,4.1, 4.0,2.2	2.8,2.7,2.6,2.8, 2.8,2.8,2.7,0.92	2.2,2.2,2.3,2.3,2.45,2.5,2.6,2.5, 2.6,1.9,0.57
+20°	42,43.8,44.5,45,45,45	44,46.8,48,48.5,49,49.5,49.5	40,43,37,34.5,34,34,32,32, 31,31	3.8,4.8,5.2,5.2, 3.2,0.14	2.87,3.44,3.28,3.4,3.68,2.79,0.16	2.6,2.9,4.1,3.1,3.0,3.5,2.3, 0.79, 0.23
+30°*	42.5,45,47,47.2,47.5,47.5,46	43,46,48,49,49.5,49.5,49.5, 50	41,42,39,38,36,30,28,28,28	3.9,5.7,6.4,6.6,6.5,2.5,0.23	3.21,4.6,4.6,4.9, 5.0,5.3,2.2	3.01,3.92,3.83,3.4,3.75,1.65,0.97,0.39

* data for +30° cases for 12.5 m.s^{-1} and 6 m.s^{-1} are from extended grass plot simulations

10. Annexure B: WFDS input file for a case

Wildland–Urban Interface Fire Dynamics Simulator (WFDS) version svn 9977 (developed by Dr. Ruddy Mell at US Forest Department) is used here. This is compatible with FDS (Fire Dynamic Simulator) version 6.0 released by National Institute of Standards and Technology (NIST), USA. The source code is supplied by Dr. Mell.

WFDS Simulation script for a case (upslope10 - 6m/s)

```
&HEAD CHID='upslope10-6msec', TITLE='upslope 10deg, burnable grass 40mx80m ,VEL=-6.0m/sec' /

&TIME T_END=660/,

&MISC PROJECTION=.TRUE.,WIND_ONLY=.FALSE.,TMPA=32.,GVEC=-1.703,0.0,-9.661,/
INITIAL_UNMIXED_FRACTION=0/ RESTART=.TRUE.

&DUMP
DT_SLCF=1.0,DT_BNDF=1,DT_ISOF=1,DT_PL3D=50,PLOT3D_QUANTITY(1:5)='TEMPERATURE','U-
VELOCITY','V-VELOCITY','W-VELOCITY','HRRPUV',DT_DEVC=1,
DT_DEVC_LINE=300,/UVW_TIMER(1)=405./

---for 16 meshes

&MESH IJK=60,120,60, XB=-150,-90,-60,60,0,60 /mesh 1

&MESH IJK=180,80,120, XB=-90,0,-20,20,0,60 /mesh 2

&MESH IJK=80,160,240,XB=0,20,-20,20,0,60 /mesh 3,

&MESH IJK=80,160,240,XB=20,40,-20,20,0,60 /mesh 4,

&MESH IJK=80,160,240,XB=40,60,-20,20,0,60 /mesh 5,

&MESH IJK=80,160,240,XB=60,80,-20,20,0,60 /mesh 6,

&MESH IJK=140,80,120, XB=80,150,-20,20,0,60 /mesh 7,

&MESH IJK=60,120,60, XB=150,210,-60,60,0,60 /mesh 8

&MESH IJK=120,80,120,XB=-90,-30,-60,-20,0,60 /mesh 9

&MESH IJK=120,80,120,XB=-30,30,-60,-20,0,60 /mesh 10

&MESH IJK=120,80,120,XB=30,90,-60,-20,0,60 /mesh 11
```

&MESH IJK=120,80,120,XB=90,150,-60,-20,0,60 /mesh 12

&MESH IJK=120,80,120,XB=-90,-30,20,60,0,60 /mesh 13

&MESH IJK=120,80,120,XB=-30,30,20,60,0,60 /mesh 14

&MESH IJK=120,80,120,XB=30,90,20,60,0,60 /mesh 15

&MESH IJK=120,80,120,XB=90,150,20,60,0,60 /mesh 16

-- Boundary conditions

&SURF ID='INFLOW',PROFILE='ATMOSPHERIC',Z0=10,PLE=0.143,VEL=-6.00/,RAMP_V='rampv' /

&VENT XB = -150,-150, -60,60,0,60, SURF_ID = 'INFLOW',N_EDDY=200,L_EDDY=6.0,VEL_RMS=0.6 /

&VENT XB =210,210, -60,60,0,60, SURF_ID = 'OPEN' /outflow

&VENT XB = -150,210, -60,-60,0,60, SURF_ID = 'MIRROR' /RIGHT SIDE

&VENT XB = -150,210, 60,60,0,60, SURF_ID = 'MIRROR' /LEFT SIDE

&VENT XB = -150,210, -60,60,60,60, SURF_ID = 'OPEN' /TOP

!--devices simulating thermocouples on OBST

&OBST XB =80,80,-0.25,0.25,1.25,1.75, SURF_ID='INERT'/

&DEVC XYZ=80,0,1.5, ID='RADI-FRONT', IOR=-1, QUANTITY='RADIATIVE HEAT FLUX'/

&DEVC XYZ=80,0,1.5, ID='CONV-FRONT',IOR=-1, QUANTITY='CONVECTIVE HEAT FLUX'/

&REAC ID='WOOD'

FUEL='WOOD'
FYI='Ritchie, et al., C_3.4 H_6.2 O_2.5, Overholt 2014, dHc = 16.4MW/kg, Ariza, 2016 soot .008 pine'
SOOT_YIELD = 0.008
O = 2.5
C = 3.4
H = 6.2
HEAT_OF_COMBUSTION = 16400 /

&SPEC ID='WATER VAPOR' /

- Boundary fuel GRASS C064 of Cheney *et.al*

&SURF ID = 'GRASS', VEGETATION = .TRUE.,VEG_DRAG_COEFFICIENT = 0.125, VEG_LOAD = 0.283,VEG_HEIGHT = 0.21,VEG_MOISTURE = 0.065,VEG_SV = 9770, VEG_CHAR_FRACTION= 0.17, VEG_DENSITY = 440,EMISSIVITY = 0.99, VEG_DEGRADATION =

'LINEAR',FIRELINE_MLR_MAX = 0.15, VEG_H_PYR= 200, VEG_HCONV_CYLRE = .TRUE., RGB = 122,117,48 ,ROUGHNESS=0.9/

!-- BURN GRASS

&VENT XB=5,20,-20,20,0,0,SURF_ID='GRASS' /Grass plot within 3

&VENT XB=20,40,-20,20,0,0,SURF_ID='GRASS' /Grass plot 4

&VENT XB=40,60,-20,20,0,0,SURF_ID='GRASS' /Grass plot 5

&VENT XB=60,80,-20,20,0,0,SURF_ID='GRASS' /Grass plot 6

!-- NO BURN GRASS

&SURF ID = 'NO BURN GRASS',VEGETATION = .TRUE.,VEG_NO_BURN = .TRUE.,VEG_DRAG_COEFFICIENT = 0.125,VEG_LOAD = 0.283, VEG_HEIGHT = 0.21, VEG_MOISTURE = 0.065, VEG_SV = 9770, VEG_DENSITY= 440, EMISSIVITY = 0.99, VEG_HCONV_CYLRE = .TRUE., RGB = 110,139,61, ROUGHNESS=0.9/

&VENT XB=-150, 4,-60,60,0,0,SURF_ID='NO BURN GRASS' /

&VENT XB= 80, 150,-20,20,0,0,SURF_ID='NO BURN GRASS' /

&VENT XB= 150,210,-60,60,0,0,SURF_ID='NO BURN GRASS' /

&VENT XB= 4,150,-60,-20,0,0,SURF_ID='NO BURN GRASS' /

&VENT XB= 4,150,20,60,0,0,SURF_ID='NO BURN GRASS' /

- Ignitor fire. Delayed for 410s to allow wind to sweep through domain

&SURF ID='LINEFIRE',HRRPUA=1000,RAMP_Q='RAMPIGN',RGB=255,0,0,VEG_DRAG_COEFFICIENT = 0.125,VEG_LOAD = 0.283, VEG_HEIGHT = 0.21, VEG_MOISTURE = 0.065, VEG_SV = 9770, VEG_DENSITY= 440, EMISSIVITY = 0.99, VEG_HCONV_CYLRE = .TRUE. ,ROUGHNESS=0.9/

&RAMP ID='RAMPIGN',T= 0,F=0 /

&RAMP ID='RAMPIGN',T=410,F=0 /

&RAMP ID='RAMPIGN',T=412,F=1 /

&RAMP ID='RAMPIGN',T=420,F=1 /

&RAMP ID='RAMPIGN',T=422,F=0 /

&VENT XB=4,5,-20,20,0,0,SURF_ID='LINEFIRE'/

- Outputs

-- slice files

&SLCF PBY=20.0, QUANTITY='TEMPERATURE',VECTOR=.TRUE. /

&SLCF PBY=20.0, QUANTITY='VELOCITY'/

&SLCF PBY=20.0, QUANTITY='HRRPUV' /

&SLCF PBY=0.0, QUANTITY='TEMPERATURE',VECTOR=.TRUE. /

&SLCF PBY=0.0, QUANTITY='VELOCITY'/

&SLCF PBY=0.0, QUANTITY='HRRPUV' /

&SLCF PBY=-20.0, QUANTITY='TEMPERATURE',VECTOR=.TRUE. /

&SLCF PBY=-20.0, QUANTITY='VELOCITY'/

&SLCF PBY=-20.0, QUANTITY='HRRPUV' /

&SLCF PBZ=2.4, QUANTITY='TEMPERATURE',VECTOR=.TRUE. /

&SLCF PBZ=2.4, QUANTITY='VELOCITY'/

&SLCF PBZ=1.2, QUANTITY='TEMPERATURE',VECTOR=.TRUE. /

&SLCF PBZ=1.2, QUANTITY='VELOCITY'/

-- Boundary files

&BNDF QUANTITY='WALL TEMPERATURE'/

/&BNDF QUANTITY='WALL THICKNESS'/

&BNDF QUANTITY='BURNING RATE'/

&BNDF QUANTITY='CONVECTIVE HEAT FLUX'/

&BNDF QUANTITY='RADIATIVE HEAT FLUX'/

-- Device files (gas phase point measurement)

&DEVC ID='U_0x0y2x', XYZ=0,0,2,QUANTITY='U-VELOCITY' / at x,y,z=0m,0m,2m

&DEVC ID='qr_0x0y2x',XYZ=0,0,2,QUANTITY='RADIATIVE HEAT FLUX GAS',ORIENTATION=-1,0,0 /

-- Device files -VELOCITY PROBE TREE to calculate velocity profile at various streamwise station

&DEVC XB=-25,-25,0,0,0,60, ID='VELOCITY_TREE_minus-25M', QUANTITY='U-VELOCITY',POINTS=200 / at x=-25m

&DEVC XB=-15,-15,0,0,0,60, ID='VELOCITY_TREE_minus15M', QUANTITY='U-VELOCITY',POINTS=200 / at x=-15m

&DEVC XB=-5,-5,0,0,0,60, ID='VELOCITY_TREE_minus5M', QUANTITY='U-VELOCITY',POINTS=200 / at x=-5m

&DEVC XB=2,2,0,0,0,60, ID='VELOCITY_TREE_2M', QUANTITY='U-VELOCITY',POINTS=200 / at x=2m

&DEVC XB=10,10,0,0,0,60, ID='VELOCITY_TREE_10M', QUANTITY='U-VELOCITY',POINTS=200 / at x=10m

&DEVC XB=20,20,0,0,0,60, ID='VELOCITY_TREE_20M', QUANTITY='U-VELOCITY',POINTS=200 / at x=20m

-- Device files -VELOCITY PROBE TREE to calculate velocity profile - in the x-direction, Z heights,

&DEVC XB=0,80,0,0,2.0,2.0, ID='Z VELOCITY_TREE_2M', QUANTITY='U-VELOCITY',POINTS=200 / at z=2.0m

&DEVC XB=0,80,0,0,6.0,6.0, ID='Z VELOCITY_TREE_6M', QUANTITY='U-VELOCITY',POINTS=200 / at z=6.0m

&DEVC XB=0,80,0,0,10.0,10.0, ID='Z VELOCITY_TREE_10M', QUANTITY='U-VELOCITY',POINTS=200 / at z=10.0m

&TAIL /
